Texture-induced hydrophobicity, and some collective effects in granular matter and economics

Pierre Lecointre

INSTITUT POLYTECHNIQUE DE PARIS

NNT : 2019IPPAX009

Thèse de doctorat

À la recherche de la texture hydrophobe

Et quelques effets collectifs dans les milieux granulaires et en économie

Thèse de doctorat de l'Institut Polytechnique de Paris
préparée à l'École polytechnique

École doctorale n°626 École Doctorale de
l'Institut polytechnique de Paris (ED IP Paris)

Spécialité de doctorat : Mécanique des Fluides

Thèse présentée et soutenue à Paris, le 18 décembre 2019, par

PIERRE LECOINTRE

Composition du Jury :

Jean-François Joanny Professeur, Collège de France	Président
Cécile Cottin-Bizonne Directeur de Recherche, Institut Lumière Matière	Rapporteuse
Thierry Ondarçuhu Directeur de Recherche, IMFT	Rapporteur
Stephan Herminghaus Professeur, Max Planck Institute for Dynamics and Self-Organization	Examinateur
Ioannis Papakonstantinou Professeur, University College London	Examinateur
David Quéré Directeur de Recherche, ESPCI Paris	Directeur de thèse
Christophe Clanet Directeur de Recherche, École polytechnique	Co-directeur de thèse
Michael Benzaquen Chargé de Recherche, École polytechnique	Invité
Gaëlle Lehoucq Chercheuse, Thales Land & Air Systems	Invitée

Résumé de la thèse

Dans cette thèse, nous avons principalement abordé le problème de la condensation sur des surfaces superhydrophobes et comment repousser efficacement la buée. Deux sujets indépendants sont aussi étudiés: la capture de poussière par des fibres mouillées d'huile ainsi que l'équation de Slutsky, communément rencontrée en microéconomie.

Dans le **chapitre 1**, nous introduisons la tension de surface ainsi que le mouillage de surfaces texturées. Des surfaces pourvues de textures hydrophobes ont la capacité de pouvoir repousser l'eau. Dans ces conditions, le liquide repose sur le haut des textures et demeure donc en contact sur un coussin d'air, ce qui explique sa grande mobilité. Cependant, une buée ou de l'eau chaude peuvent détruire le caractère superhydrophobe d'une surface texturée, du fait de la condensation à l'intérieur des textures. Néanmoins, il a été observé que des matériaux couverts de cônes nanométriques, à l'image des ailes de cigales, peuvent résister à la buée; les gouttes issues de la condensation étant éjectées à l'occasion de leur coalescence par transfert d'énergie de surface en énergie cinétique.

Dans le **chapitre 2**, nous montrons tout d'abord expérimentalement par des images de microscopie électronique que la forme conique des nanotextures permet bien aux gouttelettes d'eau d'être en "état fakir", y compris à très petite échelle, *i.e.* pour des rayons de goutte allant jusqu'au micron. A l'aide de deux caméras synchronisées, nous étudions ensuite au **chapitre 3** la trajectoire des gouttes de buée éjectées et observons un maximum de vitesse pour des rayons de l'ordre de 4 μm et une immobilité des gouttes aux rayons inférieurs au micron. Nous montrons que la viscosité joue un rôle majeur dans leur balistique. En effet, les effets visqueux durant la coalescence entre deux gouttes peuvent dissiper assez d'énergie pour limiter le saut des gouttes. Nous notons qu'au moment de leur retour sur la surface, les gouttes de buée n'ont pas assez d'énergie pour rebondir et restent collées, et montrons que le ralentissement causé par la friction dans l'air est à l'origine de cet effet.

Le **chapitre 4** est consacré à l'étude de différentes familles de surfaces à cônes en variant l'espacement et la hauteur des textures. Aux nanoéchelles, nous montrons que l'effet anti-buée est peu influencé par la taille des textures, et que ses limites proviennent plutôt des propriétés de l'eau elle-même, sa viscosité en particulier. Aux microéchelles, nous décrivons des situations nouvelles où l'on observe l'éjection spontanée de la buée malgré un piégeage local de l'eau. Nous montrons que le rayon minimum de saut des gouttes éjectées est directement corrélé à la taille des textures. Nous mettons ensuite en évidence que le troncage des cônes peut diminuer de manière drastique le pouvoir anti-buée d'une surface.

Enfin, dans le **chapitre 5**, nous nous intéressons à la capacité des surfaces superhydrophobes à repousser des gouttes d'eau chaude, montrant l'existence de deux recettes distinctes pour parvenir à un tel effet. Une première solution consiste à utiliser des textures nanométriques qui vont limiter la taille des ponts d'eau entre les textures et la goutte. Une deuxième solution consiste, quant à elle, à recourir à des grandes surfaces aux tailles de l'ordre de la dizaine de microns. Dans ce cas, la buée n'a pas le temps de remplir les textures et la goutte n'est pas donc pas sensible aux ponts d'eau et peut donc être repoussée efficacement pour toutes les gammes de température d'eau chaude.

Dans la seconde partie de la thèse (**chapitre 6**) consacrée aux milieux granulaires, nous abordons le problème du pouvoir de capture de poussière de fibres mouillées d'huile. Nous montrons que la quantité de particules capturées est seulement influencée par la quantité d'huile déposée sur la fibre et non par la configuration adoptée par l'huile (film ou goutte), contrairement à la dynamique de croissance de l'agrégat, au cours de laquelle, de larges différences apparaissent entre les deux configurations.

Enfin, la dernière partie de la thèse (**chapitre 7**) est consacrée à l'équation de Slutsky, communément rencontrée dans le domaine de la microéconomie. Nous décrivons comment la matrice de Slutsky est modifiée en présence d'hypothèses non rencontrées en économie classique telles que l'irrationalité, l'hétérogénéité des agents ou l'interaction entre produits; et comment celles-ci font apparaître des résultats surprenants non prédits par la théorie classique du consommateur. Les trois parties peuvent être abordées de manière indépendante.

Contents

Les grands voyages ont ceci de merveilleux que leur enchantement commence avant le départ même. On ouvre les atlas, on rêve sur les cartes. On répète les noms magnifiques des villes inconnues...

La vallée des rubis, Joseph Kessel

Foreword

After completing a Master's degree in Naval Architecture at University of California, Berkeley, I decided to pursue in the field of Hydrodynamics but dive instead into smaller scales. Water and especially liquid interfaces have always been fascinating to me for its complexity and variety of phenomena. Thus, I engaged in a PhD under the supervision of D. Quéré and C. Clanet at LadHyX (École polytechnique) and PMMH (ESPCI Paris). My doctorate has mainly been devoted to the understanding of anti-fogging surfaces and issues related to condensation and followed the work of T. Mouterde [1] with whom I had the pleasure to collaborate. Most of the time, fog can destroy the water-repellency of hydrophobic textured materials and my aim was to investigate the conditions under which a material covered with certain structures could instead resist fog. This study involved the development of experimental procedures to study condensation on surfaces, as well as theoretical works to model the observed phenomena. One of the experimental tools we have resorted to is Environmental Scanning Electron Microscopy (ESEM), which has been made possible thanks to the collaboration with A. Tanguy at the Laboratoire de Mécanique des Solides at École polytechnique.

Furthermore, because of their complexity in fabrication, we have engaged in many collaborations with groups that could design the materials on which we performed experiments. Producing surfaces composed of nanostructures at the size of hundreds of nanometers requires equipments and knowledge that were beyond my skill set. Consequently, for the production of nanostructures, we set up a collaboration with a group led by I. Papakonstantinou at University College London that has proved extremely fruitful. Similarly, for larger features (microcones) and to complement our understanding, we have continued our long-standing collaboration with Thales Research & Technology and its team led by G. Lehoucq.

However, setting up these collaborations as well as finding the good parameters for designing the materials were an intricate business: for instance, the nanostructures only arrived during my 3$^{\text{rd}}$ year of PhD. I took advantage of these rather quiet periods to discover new fields and undertake two side projects in the areas of granular matter and complex economics. For the former, we engaged a collaboration with Saint-Gobain Recherche in the team led by M. Lamblet. This cooperation has focused on dust produced by glass wool deterioration. This industrial concern led the firm to incorporate oil in their fabrication method of glass wool in order to capture the dust made of broken glass wools. My work was aimed at understanding how much quantity of dust particles could be captured by oil and was undertaken in close cooperation with the industrial team, which made the project even more stimulating, because of its direct practicality.

Another project I have embarked on involves econophysics. A new researcher at LadHyX, M. Benzaquen, was starting the EconophysiX group, in close collaboration with Capital Fund Management, a hedge fund led by J.-P. Bouchaud. Econophysics is a rather new discipline that notably aims at challenging the ubiquitous *Homo economicus* hypothesis which considers perfect economic agents within classical economics. The idea is instead to implement more realistic behavioral hypotheses combining statistical physics tools. Willing to discover this new approach, I have had the chance to work with the group and have mainly focused on the Slutsky equation which describes changes in demand in response to price variations for a given basket of goods. We have introduced agent irrationality, heterogeneity and interactions to examine how classical outcomes are perturbed. This theoretical study has enabled me to discover an entire new field, far from liquid interfaces, but with a great impact on real-life economics and financial markets. Our next step is now to confront our theoretical framework to available data.

My manuscript is organized as follows: the first part of this thesis gathers our work on liquid interfaces. **Chapter 1** introduces the physics of wetting and how water can be repelled at different scales. We present the properties of textured hydrophobic materials and how their water-repellency can be destroyed in the presence of fog. Finally, we consider the particular case of nanostructures and the influence of texture shape on the ability to repel dew. To produce a systematic study on condensation, we present in **Chapter 2** the different materials we have used during the thesis, followed by the technique of ESEM, which we perform on our samples. Based on the observations made in the previous chapters, we study in **Chapter 3** the trajectory of ejected condensed drops after coalescence on a surface covered with nanocones. In **Chapter 4**, the effect of cone size (spacing and height) on antifogging efficiency is discussed, at a scale ranging from tens of nanometers to few microns. Finally, we focus in **Chapter 5** on the ability of superhydrophobic surfaces to repel hot water. In a second part dedicated to granular matter, we present in **Chapter 6** our results on dust capture on oily fibers. The last part on complex economics (**Chapter 7**) discusses our work on the Slutsky equation and how realistic hypotheses on agents can reveal features absent from classical economic theory. The three parts can be addressed independently.

Different scales, different materials, different behaviours. Sources: [2, 3].

Il comprit que le monde était d'une ampleur infinie et d'une substance difficile pour l'homme. Il connut le prix du soleil, l'interdiction terrible des ténèbres, la magie de l'eau, le sang précieux des nourritures.

Fortune carrée, Joseph Kessel

PART I

LIQUID INTERFACES

1

Introduction : Repelling water

In this chapter, we first present the basics of surface tension and how animals or objects can float on water. We then introduce the wetting of textured materials and the properties of superhydrophobic surfaces as well as the basics of condensation. We later discuss the behaviour of such materials in the presence of micrometric drops, as produced by fog. Repelling water at a micrometer-scale is challenging and we list some conditions to promote dew-repellency. To that end, we finally introduce the influence of different texture shapes on the antifogging efficiency for structures at the size of hundreds of nanometers.

Fakir in Benares, India. Photography taken by Herbert Ponting (1907) [4].

Contents

1.1 Introduction

"And when Moses' hand was stretched out over the sea, the Lord with a strong east wind made the sea go back all night, and the waters were parted in two and the sea became dry land. And the children of Israel went through the sea on dry land: and the waters were a wall on their right side and on their left."(Exodus 14:21-22). This miracle related in the Book of Exodus, when Moses opened the Red Sea, enabled the Jews to flee and escape from Egyptians eventually struck when "the waters came back". The power of water is in everyone's mind, which makes this legendary event even more extraordinary and how Moses managed to break the sea into two parts with an opening width of 5 km over a distance of 3 km!

Figure 1.1: Moses opening the Red Sea. Source: [5].

A closer look at the interactions between water molecules can help to realize the magnitude of Moses' power. In a liquid phase, molecules are attracted by each other, which generates cohesion. Hence, a molecule situated at the interface is in a state unfavourable compared to a molecule inside the medium. This energetic cost per surface area is named surface tension γ, and it explains why liquids tend to minimize their surface: soap or water drops are observed spherical as this shape yields the lowest surface area for a given volume. Surface tension only depends on the liquid nature, and it is low for oils, on the order of 20 mN/m, while it reaches 72 mN/m for water. Taking an average depth of 2 km for the Red Sea, it yields an energy on the order of 1 MJ for Moses to open the sea, in the same magnitude as the energy liberated by 1 kg of TNT!

Capillary force opposes gravity force and it becomes predominant below a certain distance named the capillary length. Let us consider a drop with radius R and weight $P = mg$, where m is the drop mass and g the gravity. P scales as $\rho g R^3$, denoting ρ as the density of liquid. The capillary force derived from the surface energy γR^2 scales as γR, so that equating the two expressions yields the capillary length κ^{-1}, that is, the threshold below which capillarity dominates gravity:

$$\kappa^{-1} = \sqrt{\frac{\gamma}{\rho g}} \, . \tag{1.1}$$

For water on Earth, the capillary length is found around 2.7 mm, a quantity that drops to 1.5 mm for oil. Moses repelled water at a large scale but the trick is not written in the Old Testament! There are fortunately other ways of repelling water, at smaller scales, which we now discuss.

Ponds or lakes are often covered with multiple insects that can walk at the water surface. These creatures can float on water or other liquids using curvature forces, namely the capillary force, and provided it can bear their weight. A body of mass M and liquid-solid

contact length L can float on water provided [6, 7]:

$$\frac{Mg}{2\gamma L \sin\theta} < 1 \ . \tag{1.2}$$

We here introduce θ the angle of the free surface with the horizontal (Figure 1.2a). Using Eq. (1.2), Hu *et al.* managed to explain the behaviour of more than 300 species of water-striders [6] (Figure 1.2b). These centimetric insects can repel water using the fact that their legs are millimeter-size and taking advantage of capillarity.

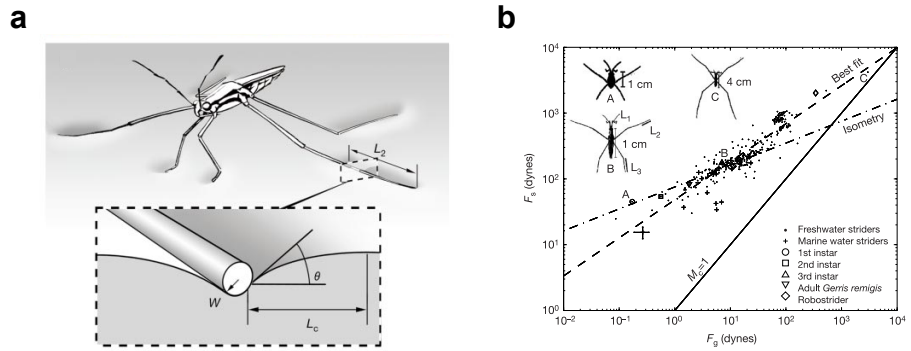

Figure 1.2: (a) Sketch of the free surface between a gerris leg and water. It makes an angle θ with the horizontal. (b) Maximum curvature force as a function of the weight for 342 gerris species. Eq. (1.2) is verified. Extracted from [6].

1.2 Physics of Wetting

We now look at the liquid configuration when deposited on a solid surface.

1.2.1 Contact angle

1.2.1.1 Young-Dupré law

Surface energies govern the shape of the liquid. They include the surface energy at a solid-liquid interface (γ_{SL}), at a vapour-solid interface (γ_{SV}) and at a liquid-vapour interface (γ). A quantity, namely the spreading parameter S, determines the state of liquid. It is given by:

$$S = \gamma_{SV} - \gamma_{SL} - \gamma \ . \tag{1.3}$$

A positive S implies a lower energy if the liquid completely spreads (Figure 1.3a), a situation observed when pouring ethanol on glass for instance. Conversely, a negative S means that the liquid does not spread totally and makes a contact angle θ with the surface (Figure 1.3b). Young and Dupré managed to calculate this angle [8]. If we project the three tensions over the horizontal (Figure 1.3b), one obtains at equilibrium $\gamma\cos\theta + \gamma_{SL} - \gamma_{SV} = 0$, hence:

$$\cos\theta = \frac{\gamma_{SV} - \gamma_{SL}}{\gamma} \ . \tag{1.4}$$

On a flat surface, this quantity can span from 0 to $\sim 120°$ for water. When $\theta < 90°$, a surface is called hydrophilic and hydrophobic for the opposite case.

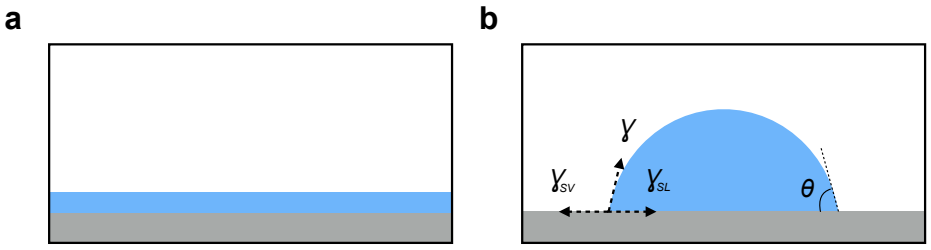

Figure 1.3: (a) For positive S (Eq. (1.3)), liquid totally spreads on the surface. (b) For negative S instead, liquid makes an angle θ with the surface, a quantity given by the equilibrium between the three surface tensions (Eq. (1.4)).

1.2.1.2 Contact angle hysteresis

Most solids are not flat, even at a molecular scale. Their roughness is then induced by defects which can pin the contact line [9]. Therefore, the contact angle of liquid is not constant at a fixed location and ranges between two extreme values: θ_r and θ_a, the receding and advancing contact angles. These two contact angles are observed when depositing a drop on a inclined surface: because of contact angle hysteresis ($\theta_a - \theta_r$), the liquid can be stuck. At the onset of motion, the front and back lines respectively wet the surface with contact angles θ_a and θ_r.

1.2.2 Rough surfaces

Repelling millimetric drops requires the design of water-repellent surfaces. Although water contact angle cannot exceed 120° on a flat surface, texturing a solid can dramatically increase θ.

1.2.2.1 Wenzel model

When deposited on a textured solid, liquid can impregnate the structures in the Wenzel wetting state [10, 11]. The roughness r_f of a solid, *i.e.* the quotient of the real surface over the apparent surface ($r_f \geq 1$), can modify the contact angle. We can estimate the energy change $\mathrm{d}E$ by unit length for a drop with contact angle θ_W to move by $\mathrm{d}x$:

$$\mathrm{d}E = \gamma \mathrm{d}x \cos\theta_W + r_f \mathrm{d}x(\gamma_{SL} - \gamma_{SV}) \ , \tag{1.5}$$

where the first part of the right hand side corresponds to the increase of liquid-vapour interface and the second part to the replacement of a solid-vapour interface by a solid-liquid interface over the length $r_f \mathrm{d}x$. At equilibrium, $\mathrm{d}E = 0$ and using Eq. (1.4), one obtains:

$$\cos\theta_W = r_f \cos\theta \ . \tag{1.6}$$

For a hydrophobic surface ($\theta > 90°$), roughness increases the contact angle. However, the increase in solid-liquid contact also increases the contact angle hysteresis, because of the numerous defects, that generates pinning and adhesion.

1.2.2.2 Cassie-Baxter model

A second configuration for liquid is to rest at the top of the texture. Then, air pockets are formed below the drop that contacts the solid with a fraction ϕ_s, and air with $1 - \phi_s$.

Eq. (1.5) can be modified and it now reads:

$$\mathrm{d}E = \gamma \mathrm{d}x \cos\theta_C + \phi_s \mathrm{d}x(\gamma_{SL} - \gamma_{SV}) + (1 - \phi_s)\gamma \mathrm{d}x \ , \tag{1.7}$$

which yields the Cassie-Baxter contact angle [12]:

$$\cos\theta_C = -1 + \phi_s(1 + \cos\theta) \ . \tag{1.8}$$

For low ϕ_s and θ close to 120°, this law predicts a contact angle close to 180°: the drop adopts a quasi-spherical shape, which makes the surface superhydrophobic. This wetting state is all the more advantageous as it exhibits small contact angle hysteresis, a necessary condition for water-repellency. Such surfaces are found in nature and the most famous one is the lotus leaf, that is covered with an assembly of micrometric posts [13] (Figure 1.4a). The combination of roughness and hydrophobicity, through a natural wax coating on the texture, makes lotus highly hydrophobic and explains why water is so mobile when deposited on its leaves. Smaller texture is also present in nature, such as on moth eyes that are covered with nanostructures at the scale of 100 nm (Figure 1.4b). Such small features present the double advantage of being superhydrophobic and anti-reflective, as their size ($\sim$ 100 nm) is smaller than the wavelength of light [14].

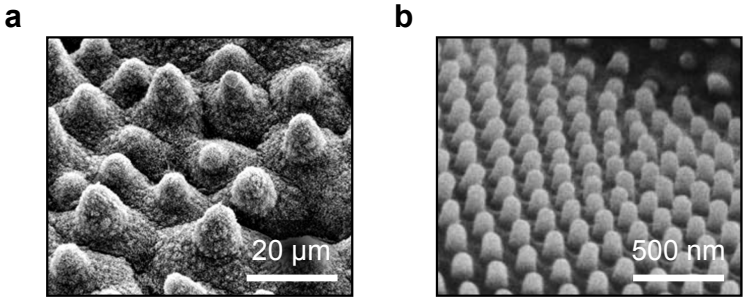

Figure 1.4: (a) Scanning electron microscopy (SEM) image of a lotus leaf. It is covered with posts with size of tens of μm. Adapted from [13]. (b) SEM image of a moth eye structure. Texture is smaller, on the order of 100 nm. Adapted from [14].

Inspired by natural surfaces, nano and microtextured surfaces can be fabricated with different feature shapes (pillar, cone, mushroom). They are rendered superhydrophobic by applying a hydrophobic treatment than can lead to static angle up to 120°.

For other liquids such as oil, where the surface tension is low, the contact angle θ is generally smaller than 90°. In that case, resorting to pillar-textured surfaces is impossible because the Cassie state is not stable. However, Herminghaus first showed that particular texture shapes can induce oil-repellency [15]. Thus, the use of mushroom shape features or nanobeads have proved efficient for designing oleophobic/alcoholphobic surfaces [16, 17].

1.2.3 Properties of superhydrophobic surfaces

1.2.3.1 Condition for superhydrophobicity

Pillar-textured surfaces

The Cassie-Baxter state is favoured over the Wenzel state provided the energetic cost of creating air pockets is smaller than the one required to wet the solid. Equating the two elementary energies associated with these two situations (Eqs. (1.5) and (1.7)) yields the

critical angle θ_{cr} [9]:

$$\theta_{cr} = -\frac{1-\phi_s}{r_f-\phi_s} \ . \tag{1.9}$$

A static angle θ larger than θ_{cr} ensures that liquid remains at the top of the texture. For very rough solids ($r_f \gg 1$), this condition is always satisfied since θ_{cr} approaches 90°, a value smaller than the observed angles on hydrophobic surfaces ($\sim 100-120°$). For materials covered with cylindrical pillars with pitch p, height h and radius a disposed in a square array, the roughness factor r_f is given by:

$$r_f = 1 + \frac{2\pi a h}{p^2} \ . \tag{1.10}$$

This relation shows for instance, that increasing p, keeping all other parameters constant, will induce a transition from the Cassie to the Wenzel state.

Cone-textured surfaces

Surfaces composed of cones contrast with those made of pillars. The sharp tip of the texture forces the contact line in a unique stable position [18], contrary to pillars where the contact line can adopt different positions owing to the texture roundness.

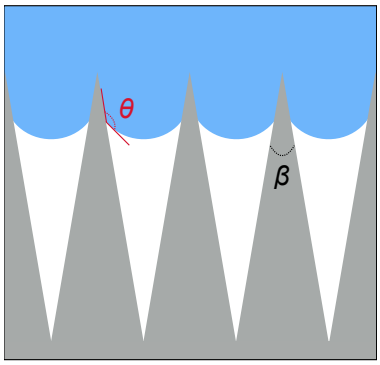

Figure 1.5: Sketch of liquid in Cassie state on a cone-textured material (with cone angle β). Water makes a contact angle θ with the surface and the contact line can adopt only one stable position.

In order to be superhydrophobic, surface tension forces must be oriented upwards to counter the pressure induced by liquid (Figure 1.5). The force exerted by the solid on the surface makes an angle $\pi - \theta + \beta/2$ with the vertical, where β is the cone angle, and it must be smaller than $\pi/2$, which finally yields the condition for superhydrophobicity:

$$\beta < 2\theta - \pi \ . \tag{1.11}$$

For high β, the force is exerted downwards, which pushes the liquid inside the texture and induces a Wenzel state: water wets totally the structures. After a hydrophobic treatment, the contact angle on a flat surface is $\theta \approx 120°$, which yields a critical cone angle $\beta_c = 2\theta$ - $\pi \approx 60°$.

1.2.3.2 Anti-rain efficiency

Owing to their large contact angle and low hysteresis, superhydrophobic surfaces have the remarkable ability to repel millimetric drops impacting them [19]. Figure 1.6 shows

different snapshots of a water drop impacting and rebounding a superhydrophobic material: after impact, liquid expands and later retracts, like a spring, before leaving the surface.

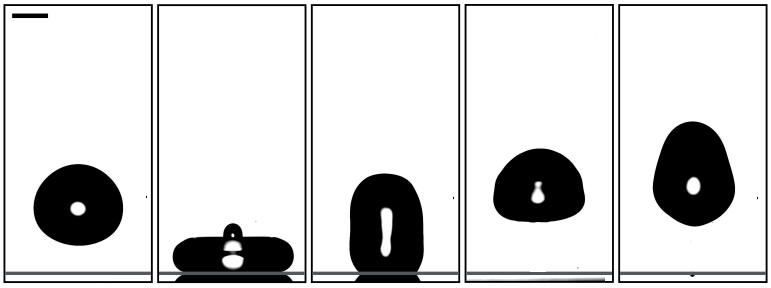

Figure 1.6: Snapshots of a water drop impacting a superhydrophobic surface. Images are spaced of 6.9 ms. The scale bar indicates 1 mm.

The water-repellency of millimetric drops may be destroyed at large impact velocity U, as the liquid pressure ($\sim \rho U^2$) becomes large enough to curve this interface at the top of the structures ($\rho U^2 > \gamma h/p^2$) and connect their bottom, hence inducing a Wenzel state. Another scenario occurs when the contact line at impact reaches the angle θ_a (advancing angle on the flat surface) and sinks in the cavities. These two situations were described by Reyssat *et al.* and Bartolo *et al.* and provided the threshold velocity $U^\star$ for a transition between bouncing and sticking. For pillars with height h, pitch p, radius a and solid fraction $\phi_s = \pi a^2/p^2$, the threshold reads [20, 21]:

$$U^\star = \min\left(\sqrt{\frac{\gamma}{\rho}\frac{h}{p^2}}, \sqrt{\frac{2\phi_s}{1-\phi_s}|\cos\theta_a|\frac{\gamma}{\rho a}}\right) . \tag{1.12}$$

For a texture of tens of microns, the critical velocity $U^\star$ for millimetric drops is found around 3 m/s, on the order of the speed of millimetric raindrops. This speed increases for nanotextured surfaces and even more for the ones textured with cones. In that case, the pressure to push liquid inside the texture increases with the sinking height because of the cone shape. Thus, for surfaces with cones of 100 nm, the threshold velocity $U^\star$ is found around 50 m/s [1], a speed much larger than that of raindrops.

The metastability of the Cassie state on microtextured surfaces during water impact and its transition to the Wenzel state can also occur in other situations such as drop evaporation [22], compression of a liquid droplet between two plates [23] or exposure to fog, which we now discuss.

1.3 Micrometric scale

We reported the exceptional water-repellency of superhydrophobic materials at the millimeter-scale. However, one may wonder what happens when exposed to tiny drops, as encountered in fog or humid environments, which generate drops at a micrometer scale.

1.3.1 Condensation

1.3.1.1 Definition

Condensation occurs during the change of water from the vapour to the liquid phase. It can happen owing to a temperature difference between air and a solid surface. If a cold surface contacts hot air, air cools down and contains more water vapour than the value

allowed by equilibrium. In that case, water spontaneously transfers from vapour to liquid and condensation starts.

The vapour partial pressure P_v is defined as the pressure exerted by vapour alone. The saturated vapour pressure P_{sat} is the vapour partial pressure when vapour is at equilibrium with liquid. We can also define the relative humidity RH at a defined temperature as:

$$RH = \frac{P_v}{P_{\text{sat}}} \ , \tag{1.13}$$

and a saturated air corresponds to a humidity RH of 100%. The empirical Rankine formula provides an approximation of the saturated vapour pressure with temperature T:

$$P_{\text{sat}} = P_0 \ \exp(13.7 - \frac{5120}{T}) \ . \tag{1.14}$$

We here denote P_0 as the atmospheric pressure. Furthermore, when air at temperature T is in contact with a surface at temperature T_s, the supersaturation S can be introduced:

$$S = \frac{P_v(T)}{P_{\text{sat}}(T_s)} \ . \tag{1.15}$$

To promote condensation, S must be larger than 1 and a phase change between vapour and liquid can be triggered. The temperature for which $S = 1$ is defined as the dew point temperature T_r and condensation happens when $T_s \leq T_r$.

1.3.1.2 Nucleation

The formation of the initial dew drop is a typical nucleation process from a bulk vapour phase. A thermodynamic model was adopted to discuss the conditions of nucleation and named as Classic Nucleation Theory (CNT) [24]. The nucleation process is influenced by numerous factors such as the surface wettability, temperature and the nano/micro structures of the solid surface. Creating a water nucleus is possible when the energy difference of system with or without a nucleus is favourable. The CNT model predicts that the energy variation depends on two parameters: (1) the energetic cost for creating the different nucleus interfaces and (2) the energetic cost of transferring molecules from the vapour to the liquid phase.

The Gibbs free energy barrier $G^\star$ that has to be overcome to form a nucleus of critical radius $r^\star$ can finally be expressed, as well as $r^\star$ [24]:

$$\begin{cases} G^\star = \dfrac{\pi\gamma r^{\star 2}}{3} f(\theta) \\ r^\star = \dfrac{2\gamma}{n_L \, k_B T \ln(S)} \ . \end{cases} \tag{1.16}$$

We introduce here n_L the number of molecules per unit volume of condensed liquid, k_B the Boltzmann constant and $f(\theta) = 2 - 3\cos\theta + \cos^3\theta$ an increasing function of the contact angle θ. From Eq. (1.16), $r^\star$ is observed to be independent of the surface wettability, unlike the energy barrier $G^\star$ that increases with hydrophobicity. A nucleus with a radius smaller than $r^\star$ is not stable and evaporates. Besides, water is assumed to be incompressible and vapour an ideal gas. In normal conditions ($T = 25°\text{C}$ and $P_0 = 10^5$ Pa), we find $r^\star \sim 1 - 5$ nm for a surface temperature of $\sim 5°\text{C}$ and $RH \sim 40\%$.

Nuclei form on the surface with a nucleation density n that depends on the surface wettability (because of the dependence of $G^\star$ on θ), the saturation S and the substrate roughness [25]. For superhydrophobic surfaces, the hydrophobic treatment makes the energy

barrier high compared to an hydrophilic material and n is observed to vary between 10^{-4} to 1 μm^{-2} [1].

1.3.1.3 Superhydrophobicity failure

Although superhydrophobic materials can repel millimetre-size drops, fog or humid conditions generally destroy the repellency. Water nucleation occurs both on top and within the texture. As water nuclei grow by condensation, droplets can fill the cavities that gives water its high mobility. This phenomenon was reported on lotus leaves and micrometric features [26, 27, 28]: water is strongly pinned in the features and these materials can even exhibit a hydrophilic behaviour in the receding state, a manifestation of the Wenzel state.

1.3.2 Scale effect

Enright *et al.* developed a thorough study of condensation on textured materials with sizes ranging from 100 nm to 10 μm [29]. They were able to report different droplet behaviours during condensation, which are influenced by the texture size and condensation conditions.

1.3.2.1 Influence of nucleation density

Upon cooling the solid, water nuclei form with a nucleation density n. We can introduce l the mean separation distance between nuclei and this quantity depends on n as $l \sim n^{-1/2}$. Enright *et al.* considered surfaces composed of square array pillars that are spaced by p, a quantity that must be confronted with l, which defines two cases:

(1) If $l/p > 1$, water nuclei do not fill all cells and the Cassie state is possible (Figure 1.7a).

(2) Conversely, if $l/p < 1$, every cell encloses a water nucleus and condensation growth will lead to the Wenzel state (Figure 1.7b).

From typical values of n, l usually varies between 1 and tens of μm. Therefore, microtextured surfaces have a great chance of being filled with water as l can be smaller than p, as observed on lotus [26]. This study shows that nanostructured surfaces have greater abilities in the presence of condensation: l/p is usually larger than 1 and droplets can develop in Cassie state.

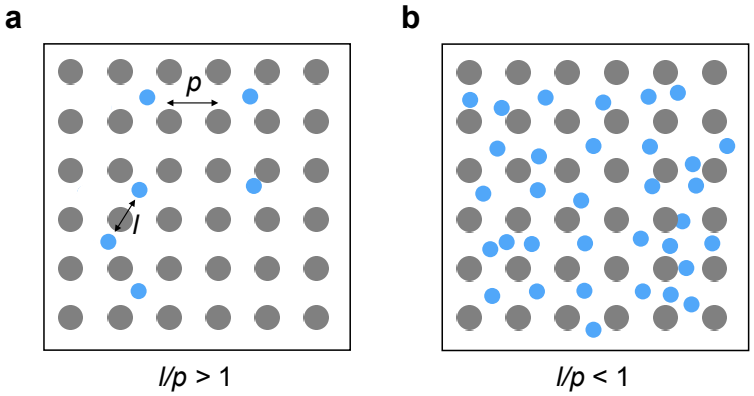

Figure 1.7: Mean separation distance l between nuclei vs pitch p. (a) For $l/p > 1$, water nuclei do not form in every unit cell which makes the Cassie state possible. (b) Conversely, for $l/p < 1$, every cell encloses at least a nucleus, hence inducing the Wenzel state. Adapted from [1].

1.3.2.2 Energy criterion

Provided the condition $l/p > 1$ is satisfied, a second criterion must yet be fulfilled to ensure Cassie state. It involves the energies for a condensed drop to grow either sideways in the structures or beyond them. Two situations can emerge after a nucleus develops inside the structures (Figure 1.8a):

(1) A first case concerns a condensed droplet growing above the texture after being constrained by the neighbouring pillars. Liquid attains the top of the texture and extends upwards, which favours a partial Cassie state where a unit cell is filled with water (Figure 1.8b).

(2) The second scenario concerns growth inside the structures. The condensed droplet wets the pillars and extends sideways, which is typical of a Wenzel state (Figure 1.8c).

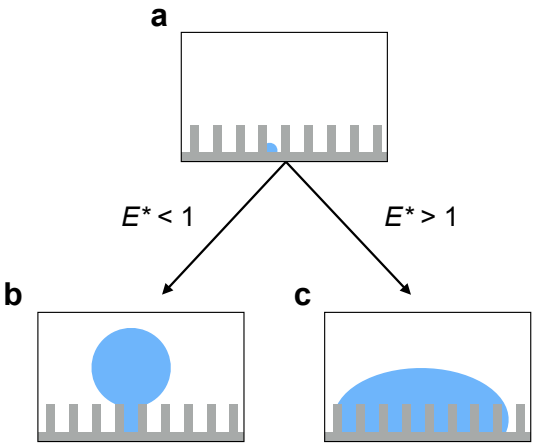

Figure 1.8: Two situations after a nucleus grows within a unit cell. For $E^\star < 1$ (Eq. (1.17)), the droplet grows beyond the structures while, for the opposite case, it expands sideways in the stuctures, hence promoting a Wenzel state. Adapted from [1].

The elementary energy $\mathrm{d}E$ to extend an interface by a distance $\mathrm{d}x$ can be defined as $\mathrm{d}E = \gamma \cos\theta_{WS}\, \mathrm{d}x$ where θ_{WS} is the angle associated with the wetting state. Enright considers $\theta_C = 180°$ for the Cassie state (situation 1) and the Wenzel angle $\cos\theta_W = r_f \cos\theta$ (situation 2) [29]. Comparing the two energies yields the energy criterion $E^\star$:

$$E^\star = -\frac{1}{r_f \cos\theta} \,. \tag{1.17}$$

To prevent water from invading texture, one must have $E^\star < 1$, which promotes a Cassie state, while the opposing case generates the Wenzel wetting state. The criterion given by Eq. (1.17) directly depends on the roughness factor r_f (Eq. (1.10) for pillar-textured surfaces). From this law, tall pillars with small pitch make high r_f and should promote Cassie morphology, as indeed observed in [29].

1.3.2.3 Phase diagram

Based on these two criteria, a phase diagram can be obtained as a function of the two quantities l/p and $E^\star$ [29]. From Figure 5.14, the partial Cassie state is only observed for $l/p > 1$ and $E^\star < 1$. This study enables us to rationalize the observations made on lotus and microtextured sufaces [26, 27, 28]. As texture have sizes on the order of tens of μm, l/p is generally smaller than 1, which favours Wenzel state.

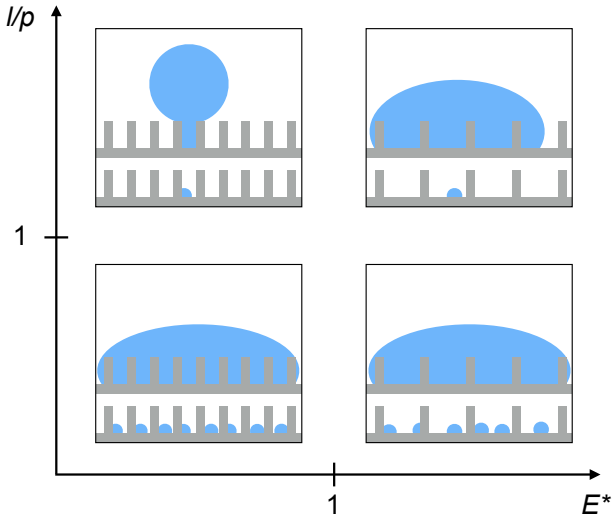

Figure 1.9: Phase diagram of wetting morphologies as a function of l/p and $E^{\star}$. Adapted from [1].

1.3.2.4 Wetting states

During condensation on textured hydrophobic materials, a condensed droplet can exhibit three wetting morphologies:

(1) A Cassie state where the droplet rests on the top of the texture (Figure 1.10a). On surfaces composed of pillars, this state was rarely observed and occurred when a nucleus develops at the top of the posts [30, 31]. We will show later that this state can also be obtained for the majority of droplets condensing on nanocones. For most of the droplets condensing on pillars, two other states are encountered: the partial Cassie and Wenzel states (Figures 1.10b and c).

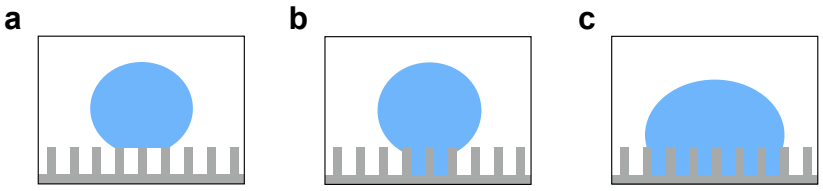

Figure 1.10: Droplet morphologies observed during condensation. (a) Cassie state when the nucleus develops at the top of the texture. (b) Partial Cassie state where the droplet is pinned in a certain number of wetted unit cells. (c) Wenzel state where the droplet grows within the structures, which yields a high adhesion.

(2) Partial Cassie concerns a droplet that grows beyond the texture after filling a certain number of cells below it (Figure 1.10b). Enright and Mulroe have focused on the prediction of the number of wetted cells [29, 32]. There has been a debate over the growth behaviour: Enright *et al.* postulates that a unit cell is first filled until water reaches the top of texture. At this point, it can either wet the neighbouring cells or grow out above the structures. Conversely, Mulroe *et al.* stipulates that liquid can grow sideways in numerous unit cells until reaching the top of the posts, which is followed by either upward or sideways growth. In this partial Cassie state, droplets are pinned at their base.

(3) The final wetting state concerns the case where water extends sideways in the texture

so that droplets emerge in a Wenzel state (Figure 1.10c).

Repelling water at the micrometer-scale is challenging as water can invade the stuctures during condensation. However, for materials where Cassie and partial Cassie states are favoured, one could expect a certain form of water-repellency.

1.3.3 Antifogging efficiency

1.3.3.1 Spontaneous droplet departure

In 2009, Boreyko and Chen discovered a new phenomenon that can occur during condensation on nanostructured or hierarchical superhydrophobic surfaces [33]: condensed droplets can coalesce and depart the surface by taking advantage of the excess of surface energy liberated during coalescence. Spontaneous droplet departure has since been observed on a variety of superhydrophobic surfaces, mainly composed of nanostructures. Most microtextured surfaces do not enable droplet ejection because drops mainly grow in the Wenzel state. For other surfaces where Cassie or partial Cassie wetting states are favoured, adhesion does not impede vertical motion and droplets can take off from the surface.

As expressed in Figure 5.14, nanostructured surfaces are preferable for promoting non-wetting states, *i.e.* partial Cassie and Cassie states, because their texture size is usually smaller than the mean separation distance between nuclei. Condensation on such surfaces reveals indeed a high antifogging repellency. For instance, after being exposed to foggy conditions, the mosquito eye and the cicada wing remain dry of water (Figures 1.11a and b). Scanning electron microscope (SEM) images reveal materials covered with nanostructures at a scale of $\sim$ 100 nm [34, 35]. Hence, small scale texture can exhibit antifogging abilities and repel micrometric drops. Furthemore, the cicada wing's structure reveals an array of nanospikes, which led Mouterde *et al.* to study the influence of texture shape, at the nanoscale, on antifogging efficiency [36].

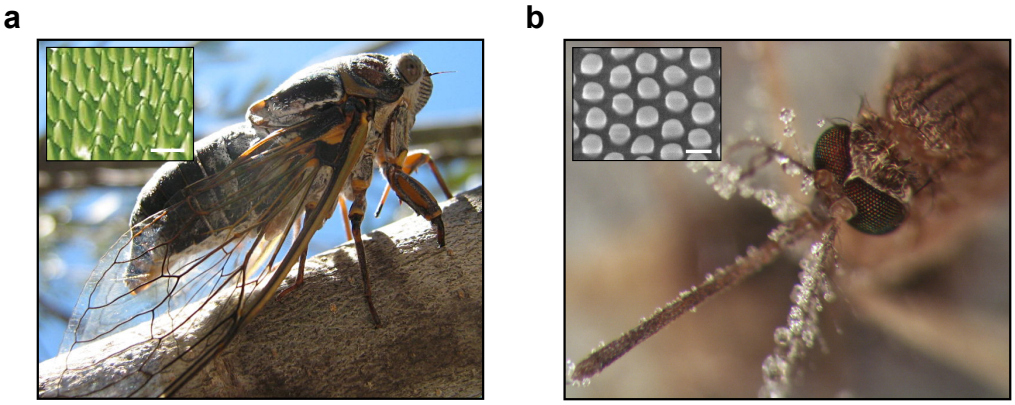

Figure 1.11: (a) Picture of a *Psaltoda claripenni* cicada resting on a branch. Inset: scanning electron viewgraph of the cicada wing structure. It is covered with an array of nanocones [35]. Scale bar = 200 nm. (b) Mosquito exposed to a foggy environment. Its eyes remain dry and SEM images reveal structures at the scale of hundreds of nanometers (inset) [34]. Scale bar = 100 nm.

1.3.3.2 Towards antifogging surfaces

While the influence of texture size on repelling water at a micrometer-scale was ascertained, the feature shape can also dramatically modify the antifogging properties of a

material. To that end, Mouterde *et al.* studied condensation on two surfaces A and N1 with similar size but with different texture shape [36]: surface A is made of silicon pillars spaced of 52 nm and with a height of 88 nm (Figure 1.12a) while surface N1, inspired by the cicada wing's structure (Figure 1.11a), is composed of cones with similar pitch and a height of 115 nm (Figure 1.12b).

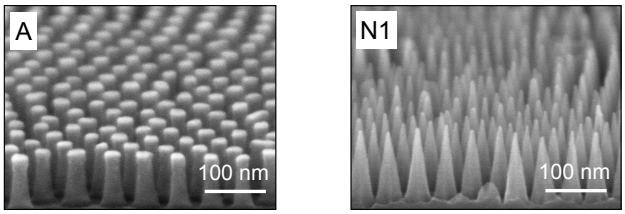

Figure 1.12: Materials used in [36]. Surface A is composed of a hexagonal array of cylindrical nanopillars with pitch $p = 52$ nm, height $h = 88$ nm and radius $a = 15$ nm. Surface N1 is instead covered with jointed nanocones with same pitch and a height $h = 115$ nm.

The two materials are cooled down and subsequent condensation is observed under an optical microscope. Using statistical tools, the authors measured the proportion N of ejected drops. As evidenced in Figure 1.13a, the two quantities are found constant with time but markedly different between the two surfaces. While material A exhibits only few droplet jumps, as noted by the low value of N ($N \approx 0.2\%$), this quantity jumps to $\sim 90\%$ for nanocones. Droplet ejection was also observed on other nanostructures but the maximum measured N was $\sim 30\%$ [37]. To rationalize these observations, Mouterde *et al.* suggested that droplets condensing on nanocones are kept in a Cassie state (Figure 1.10a), the conical shape of texture preventing them from being pinned in cells, unlike pillars (Figure 1.10b). This hypothesis will be discussed in the next chapters where we provide images of micro-droplets condensing on nanocones.

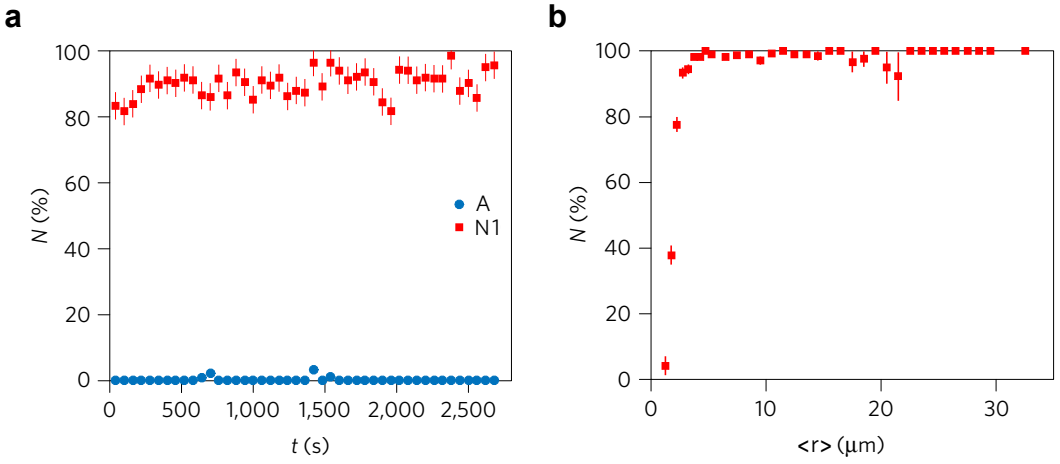

Figure 1.13: (a) Time evolution of the jumping rate N (proportion of ejected drops after coalescence) for materials A and N1. For the latter surface, N jumps to 90% and falls to 0.2% for nanopillars. Each point is obtained after averaging for 1 minute. (b) Jumping rate N as a function of the common radius $< r >$ for 2-droplet-symmetric coalescences. Extracted from [36].

If we now only consider coalescences involving two symmetric droplets with respective radii r' and r ($r'/r > 0.8$), the jumping rate N can be plotted in Figure 1.13b as a func-

tion of the common radius $< r >$ ($< r >= (r' + r)/2$). N approaches its maximum value ($N \approx 99\%$), even at the scale of drops of a few micrometers, before falling down critically for $< r >$ ranging from 1 to 3 μm. Droplets smaller than $\sim$ 1 μm never depart the surface, a value that highlights the ability of nanocones to promote antifogging. Furthermore, nanostructured surfaces with texture of hundreds of nanometers also have anti-reflection properties [14, 38, 39] because their size is smaller than the visible wavelengths, which makes them advantageous for designing optical systems.

Repelling water at different scales from centimeter to micrometer-size has evidenced the importance of superhydrophobic surfaces as well as their texture size. Nanometric features have been reported to promote water-repellency even for condensing drops, that is, at the size of μm. The influence of texture shape also seems to play a dramatic role as conical features tend to induce high antifogging efficiency. However, to that point, little is known on the behaviour of condensed droplets on such materials and it is the aim of the thesis to address this question.

Take home message of Chapter 1

1. Surface tension. The energetic cost for a liquid to create an interface generates an additional energy, that is the product of surface tension γ with the interface area. For sizes smaller than the capillary length, capillary force is dominant. For partial spreading, the Young-Dupré law dictates the value of the contact angle made by the drop with the material. However, because of irregularities, the contact angle, in fact, varies between the receding and the advancing angles.

2. Textured materials. When deposited on a rough solid, liquid can adopt two wetting states: the Wenzel state where the drop impregnates the structures, which generates high adhesion, and the Cassie state where the drop lies on the top of the features.

3. Superhydrophobicity. Superhydrophobic materials are Cassie stable surfaces. They can trap air, which renders water extremely mobile on them and enables to repel liquid at the millimeter size, that is rain for instance.

4. Antifogging ability. Most micro-textured surfaces lose their superhydrophobicity in humid conditions as water nuclei condensing in the texture are at the scale of the structures and can fill the air layer. However nanostructured surfaces, especially those covered with cones, can repel these micrometric droplets: they can spontaneously take off the surface after coalescence by taking advantage of the excess of surface energy.

2

Observations of condensation droplets

Observing micrometric and even nanometric condensation droplets on superhydrophobic surfaces has recently been achievable thanks to Environmental Scanning Electron Microscopy (ESEM). A recent study reported the exceptional antifogging efficiency of a nanocone-textured surface, which was assumed to promote a non-adhesive state for droplets, namely the Cassie state. First, we present here all the samples used in the thesis. Then, the general principles of ESEM are recalled as well as their drawbacks when imaging. Finally, the results of our ESEM experiments on three samples are shown and dramatic differences are observed between cone and pillar-textured materials.

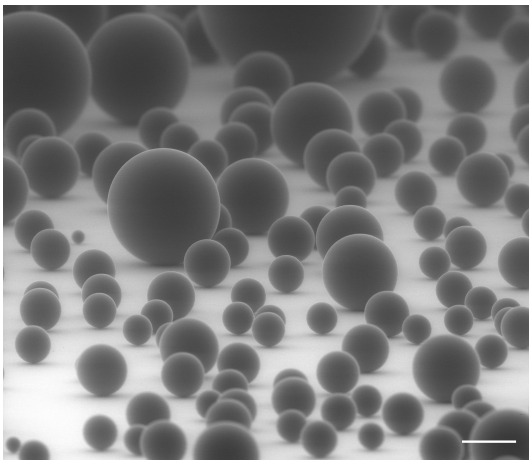

Condensed drops on a nanocone texture. The scale bar indicates 20 μm.

Contents

For this study, I do particularly thank Alexandre from LMS without whom the ESEM images would have not existed! Besides, many people contributed to the fabrication of the samples I used: Gaëlle, Julie and Raphaël from TRT, Ioannis, Tao, Sophia and Martyna from UCL. I thank you for the remarkable surfaces you created.

2.1 Presentation of the different materials

We first introduce the samples used in our work. In order to have a consistent study, different families of samples are fabricated, mainly covered with cones as this shape has proved to be the most antifogging-efficient [36]. We performed experiments on nanometric and micrometric cones with different spacings and heights, as well as on truncated cones.

2.1.1 Dimensions

Most of the samples used for experiments are textured surfaces composed of cones. As presented in Figure 2.1a, they have a base diameter denoted as d, a height h and a pitch p. The cone angle β is defined as $\beta = 2\tan^{-1}(d/2h)$. We name N and M cones that are nanometric and micrometric, respectively. The letter is followed by a number that denotes the relative size of the texture: surfaces are ranked from lowest to highest pitch p. Samples that have same p are ranked from lowest to highest cone height h. Surfaces N are disposed in a dense hexagonal array while surfaces M have a square array. We also introduce a surface named A, that is, the surface made of nanopillars presented in Chap. 1. It is composed of cylindrical pillars disposed in hexagonal array with diameter d, height h and pitch p. All surfaces along with their dimensions h, p and d are reported in Table 2.1. Besides, all surfaces N have jointed cones, *i.e.* $d = p$. For surfaces M, a small separation distance equal to $p - d$ exists between two neighboring cones.

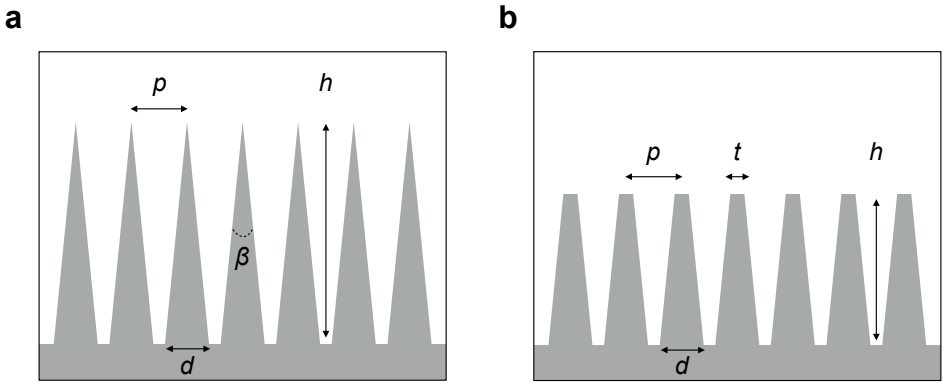

Figure 2.1: (a) Sketch of a surface textured with cones. They are spaced with pitch p and have height h and diameter d. The cone angle is defined as $\beta = 2\tan^{-1}(d/2h)$. (b) Sketch of a surface textured with truncated cones. They are spaced with pitch p and have height h and diameter d. The diameter of the upper part is denoted as t.

Families of samples are created in order to study the influence of several parameters such as pitch, height, cone angle and spacing between cones. For example, samples N3-7 have same pitch ($p = 110$ nm) but different heights. Similarly, N1, N2 and N5 are homothetic, *i.e.* with the same cone angle β, which enables one to study the influence of texture size, keeping all other parameters constant.

Truncated cones are also considered, as sketched in Figure 2.1b. They are cut from the top and their top diameter is denoted as t ($t < d$). We name them NT and they are ranked from smallest to largest t. Their pitch p is close to 100 nm, in order to compare them with the N3-7 family (Table 2.2).

Sample	Pitch p (nm)	Height h (nm)	Diameter d (nm)	Cone angle β (°)
A	52	88	30	n/a
N1	52	115	52	25.5 ± 1
N2	56	133	56	23.8 ± 2
N3	110	101	110	57.1 ± 2
N4	110	220	110	28.0 ± 2
N5	110	250	110	23.3 ± 2
N6	110	284	110	20.8 ± 2
N7	110	420	110	14.9 ± 2
M1	500	2000	400	11.4 ± 1
M2	1600	6000	1500	28.0 ± 1
M3	2400	7200	2100	32.5 ± 1

Table 2.1: Characteristics of our cone-textured surfaces. As an exception, surface A is covered with cylindrical nanopillars. We denote as N and M surfaces where cones are nanometric and micrometric. The surfaces are ranked from lowest to largest pitch p. Samples with the same p are ranked according to their height h.

Sample	Pitch p (nm)	Height h (nm)	Diameter d (nm)	Diameter t (nm)
NT1	93	162	93	42
NT2	105	107	105	53
NT3	115	117	115	60

Table 2.2: Characteristics of the truncated cones family NT.

2.1.2 Fabrication

We briefly describe here the fabrication processes of the different samples.

2.1.2.1 Samples A and N1

Both samples A and N1 were produced at *Brookhaven National Laboratory* by A. Checco, A. Rahman and C. T. Black during T. Mouterde's PhD [1]. They have been fabricated by combining block-copolymer self-assembly with anisotropic plasma etching in silicon, which provides large-area (cm^2) textures with $\sim$ 10 nm feature size and long-range order, as described in [40]. Block-copolymers are chains composed of alternating blocks of two monomers. The following fabrication steps for surface A are applied [40]:

(1) Polystyrene-block-poly(methylmethacrylate) (PS-b-PMMA) is deposited on a flat silicon surface.

(2) Thermally annealing the sample for 12 hours at 200°C enables block-copolymer self assembly via microphase separation.

(3) Tri-methyl aluminum (TMA) is incorporated into the PMMA (polymethacrylate) layer.

(4) An exposure to oxygen-plasma removes all the organic material and it remains aluminum pill-shaped nanostructures in a hexagonal array.

(5) These nanostructures finally provide a mask for nanotexturing the underlying silicon by plasma etching. Surface N1 is fabricated by using the exact same method but the only difference comes during the etching step by using a hydrogen bromide:chlorine:oxygen ($HBr:Cl_2:O_2$). Both surfaces are shown in Figure 1.12 in Chap. 1.

2.1.2.2 N2-N7 and NT1-3 Families

These two families of samples were fabricated at *University College London* by S. Laney, M. Michalska, T. Li and I. Papakonstantinou. We detail here the following fabrication steps:

(1) 100 nm SiO_2 is deposited on a silicon wafer by plasma-enhanced chemical vapour deposition. The block copolymer (BCP) Poly(styrene-*block*-2-vinyl pyridine) (PS-b-P2VP) is self-assembled in *m*-xylene and subsequently spin-cast at 4000 rpm for 30 seconds to give a thin film. The resultant film comprises a well ordered monolayer of packed micelles, in which the molecular weight of each block dictates the distance between neighboring micelles (pitch).

(2) A polymer breakthrough etch is performed in a PlasmaPro NGP80 Reactive Ion Etcher (RIE) at 20°C under Oxygen plasma in order to remove the polymer matrix. The remaining micellar bumps act as a topographic contrast for the subsequent SiO_2 etch.

(3) The micelle pattern is registered into the SiO_2 layer using CHF_3/Ar plasma etching. The SiO_2 pattern acts as a hard mask for etching into the underlying Si.

(4) Dry Si etching is performed in an Advanced Silicon Etcher using chlorine plasma and under low plasma power in order to achieve slow lateral etching and undercutting of the SiO_2 mask.

(5) The remaining SiO_2 mask is stripped using hydrofluoric (HF) acid, to produce sharp tipped or truncated cones, depending on the point at which the Si etching is stopped, as shown in Figure 2.2.

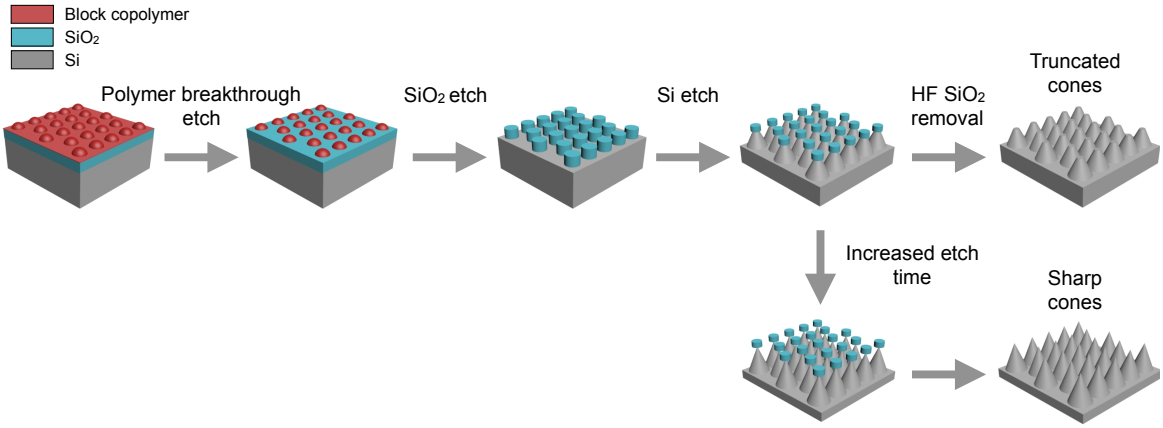

Figure 2.2: Schematic of the fabrication process starting from the block copolymer micelle deposition on a Si wafer with 100 nm layer of SiO_2. From left to right: removing the polystyrene matrix through a polymer breakthrough etch; etching the underlying SiO_2 layer using the micelles as a soft mask; etching the silicon layer using the SiO_2 pillars as a hard mask, with the degree of cone sharpness being a function of etching time; removal of the remaining SiO_2 via an HF etch.

2.1.2.3 M1-3 Family

The production of the M family requires the fabrication of nano/micrometric patterns, using classical fabrication processes for microelectronics. These three materials were developed at *Thales Research & Technology* by R. Guillemet, J. Cholet and G. Lehoucq. The technological processes, shown in Figure 2.3 and described below, are followed:

(1) After a cleaning step, a metallic mask is deposited by sputtering (a) and patterned with high-resolution lithography and etching steps (b) and (c).

(2) Patterns are transferred into the substrate (silicon or germanium) with a reactive

ion-etching-based process (d).

(3) The metallic mask is removed in an acid solution and the samples are cleaned up (e).

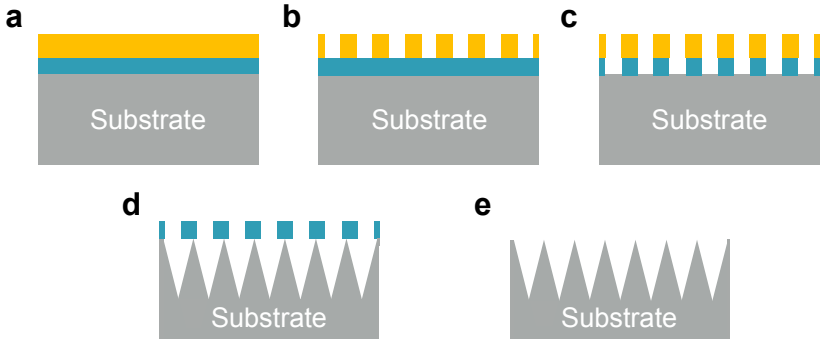

Figure 2.3: Process steps for the productions of family M samples. The yellow layer is a resin and the blue one a metallic layer.

Scanning electron micrographs of the resulting three surfaces are displayed in Figure 2.4. All three samples exhibit sharp tips and cones are disposed in a regular square array. The cone angle β is observed to increase with the size in our family: cones on surface M1 are extremely steep (Figure 2.4a), as indicated by the low value of the cone angle, $\beta = 11°$ (see Table 2.1). In contrast, β is found three times larger on M3 ($\beta = 32°$), as evidenced in Figure 2.4c.

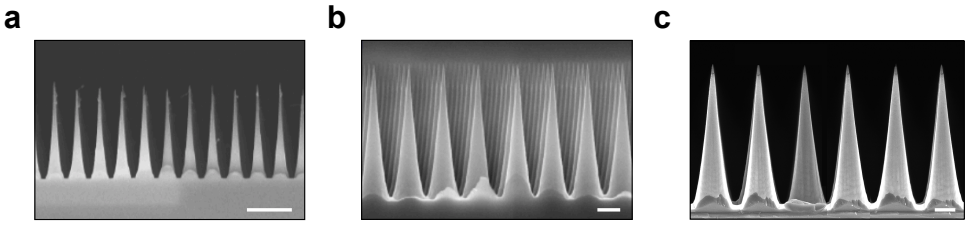

Figure 2.4: Scanning electron microscopy (SEM) images of surfaces M1 (a), M2 (b) and M3 (c). The scale bars indicate 1 μm on the three images.

2.1.3 Silanization

Surfaces are finally rendered hydrophobic after silanization. Chemical vapour deposition of 1H,1H,2H,2H-perfluorodecyltrichlorosilane is achieved by first activating the surface in a plasma cleaner for 45 s. The activated surface is then enclosed in a Petri dish close to a plastic well containing typically $\sim$ 20 μL of silane and desiccants to avoid reaction with water contained in the air. This treatment on flat silicon gives an advancing water contact angle $\theta_0 = 120 \pm 2°$. Because they are textured, most of our surfaces are rendered superhydrophobic ($\theta > 150°$) and their resulting advancing and receding angles will be reported in Chap. 4.

2.2 General principles of Environmental Scanning Electron Microscopy (ESEM)

2.2.1 Introduction

Over the past decade, Environmental Scanning Electron Microscopy (ESEM) has received considerable attention for the study of condensation on superhydrophobic surfaces. The willingness to observe sub-10 μm phenomena such as droplets condensing on texture has pushed one to resort to electron microscopy. Many studies used optical microscopy to observe phenomena with sizes ranging from the millimeter to the tens of μm but diffraction of light makes it tricky to go below this limit. However, the imaging of micrometer-size phenomena was found to be essential to understand the condensation dynamics and the shape of micrometric droplets, a key aspect when studying nanotexture. Electrons have a much shorter wavelength ($\sim 10^{-11}$ m for accelerating voltages of $\sim$ 30 kV) than that of light, which yields a significant increase in resolution; modern SEM can have maximum resolution better than 1 nm. Our study concerns nanotextured surfaces with condensing micrometric droplets possibly ejected after coalescing with their neighbours. Therefore, we have decided to resort to ESEM to understand the fundamental aspects of condensation when performed on these nanostructures (droplet shape, dynamics). We first present the principles of ESEM.

2.2.2 Principles of ESEM

Electron microscopy consists in focusing an electron beam on a sample. Interactions between the electrons and the atoms constituting the sample will generate different signals, that are collected thanks to an attractive electrical field and used to produce an image. As sketched in Figure 2.5, various signals are produced because of the interactions and the principal ones in SEM are secondary electrons (SE) and reflected or back-scattered electrons (BSE). Other signals include characteristic X-rays and light (cathodoluminescence) (CL), absorbed current (specimen current) and transmitted electrons.

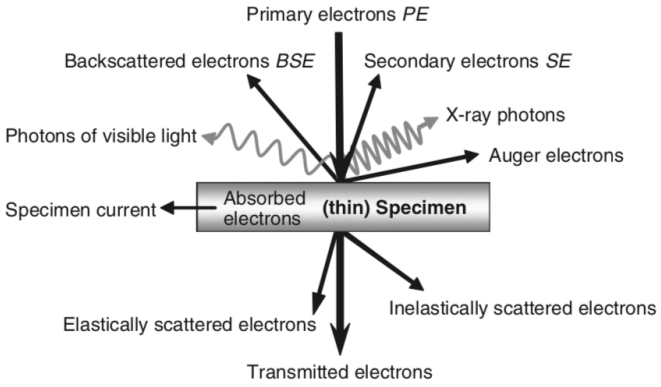

Figure 2.5: Signals generated by the interactions between an electron beam and a sample. Extracted from [41].

Secondary electrons are generated as ionization products and they are emitted close to the sample surface (Figure 2.6a). Their energy is smaller than 50 eV (region III in Figure 2.6b). Back-scattered electrons are instead, primary electrons reflected from the sample by elastic scattering and emitted with a higher angle (Figure 2.6a). Their energy can be up to the primary beam energy E_0 (Figure 2.6b) and down to the level of secondary electron energy

($\sim$ 50 eV). The beam of electrons is produced after a high voltage is applied to a filament.

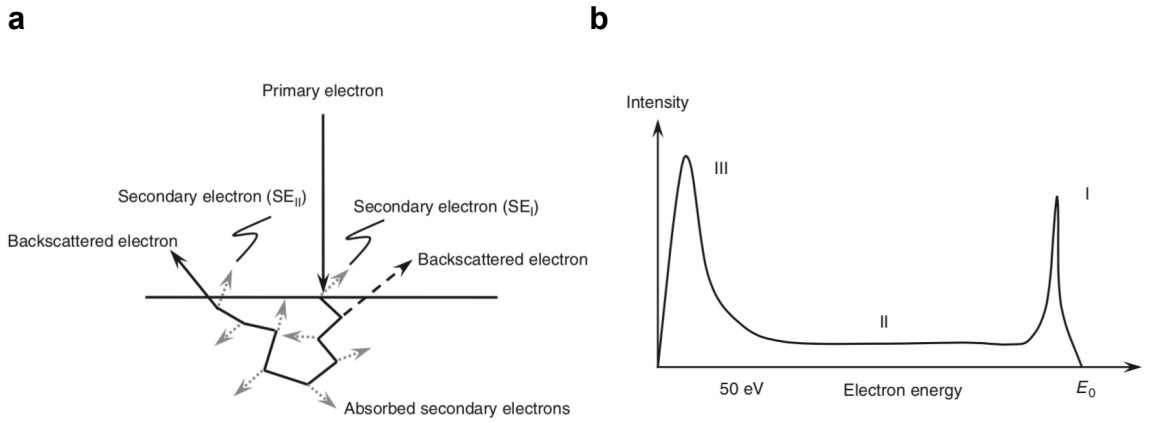

Figure 2.6: (a) Schematic diagram showing the path of a primary electron and the emission of backscattered electrons and secondary electrons. (b) Distribution of electron signals and their relative energies, for a given primary beam energy. Regions I and II refer to the backscattered electron contributions, while Region III corresponds to the secondary electrons signal. Extracted from [41].

The primary electrons of energy ranging from 0.2 to 40 keV are then focused by condensers, that are followed by deflectors so that the beam can scan a rectangular area. After the beam interacts with the sample, the signals are collected by detectors: for SE, it consists in attracting them with an electrically positive grid and accelerating them. For BSE, as they are emitted with a higher angle compared to SE, other detectors are used. Contrary to SEM where the sample is held into a high vacuum environment, ESEM enables one to operate with pressure in the chamber up to 2.7 kPa and the pressure control is ensured through mechanical pumps and apertures (Figure 2.7). The pressure being in the range of hundreds of Pa, water condensation can be achieved by affixing the sample to a Peltier stage and decreasing the sample temperature below the saturation temperature: $\sim 0-10°C$, which corresponds to chamber vapour pressure of $\sim 700-1300$ Pa. Despite its promising advantages, ESEM presents some limitations and electron beam can induce several issues, as discussed further.

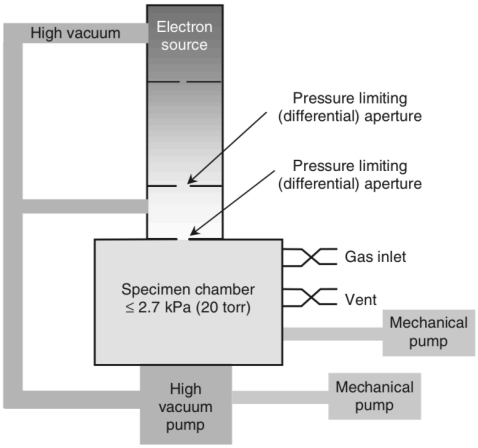

Figure 2.7: Schematic diagram showing the arrangement of different zones and pressure-limiting (differential) apertures of a typical ESEM instrument. Extracted from [41].

2.3 Limitations of ESEM

During ESEM observations, electrons can interact no only with water but with the sample too. These interactions can lead to serious issues in the imaging that we present here and that were widely discussed in [42, 41, 43].

2.3.1 E-beam contamination

Textured surfaces are rendered superhydrophobic by the use of a hydrophobic coating. Prolonged direct electron beam exposure of a superhydrophobic surface can lead to the carbonization of the sample irradiated area (amorphous carbon film formation) [44, 45] or dissociation of the silane coating on our materials [46]. These wettability changes happen when the area is exposed for a "long time" to the electron beam. Figure 2.8 shows such a degradation on the nanocone surface N1. It reveals a darker square area which was exposed for few minutes to a beam with an energy of 15 keV. The dark stains show condensation and evidence that water wets totally the surface, as shown by its filmwise configuration. This morphology is in stark contrast with the expected behaviour on a superhydrophobic surface where droplets are observed to exhibit large contact angles, even during condensation [29]. Thus, the observed "hydrophilic" behaviour underlines the degradation of the hydrophobic coating. To avoid this predicament, one must use low-energy electron beam (< 15 keV) and change exposed areas over the whole condensation experiment. After long exposure, hydrophobicity is regenerated by cleaning the surface with ultrasounds, hence removing the products of degradation. In extreme cases, a new hydrophobic coating is necessary to regenerate the hydrophobic layer.

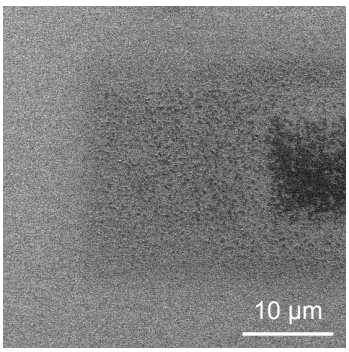

Figure 2.8: Possible effect of e-beam on hydrophobic coating. Long exposure to e-beam results in the surface degradation, as revealed here during water condensation on a superhydrophobic nanotexture (sample N1). The dark square area was exposed for few minutes to an e-beam of energy 15 keV. Dark stains show filmwise water condensation, in contrast with the expected behaviour on a superhydrophobic behaviour where droplets exhibit high contact angles. This observation then strengthens a possible silane coating deterioration.

2.3.2 E-beam radiology

Radiation damage is a serious concern and it can hinder the ESEM imaging of condensation. The use of water vapour as imaging gas can indeed induce inelastic e-beam scattering, which forms ionized or excited water molecules. As evidenced in [47], the excited water molecules can decay into free radicals or ions. The reaction of water with an electron e^- produces an excited water molecule $H_2O^\star$, which is followed by these two reactions for

instance:

$$\begin{aligned} H_2O^\star &\rightarrow H\cdot + \cdot OH \\ H_2O^\star &\rightarrow H^+ + OH^- \ . \end{aligned} \tag{2.1}$$

The hydroxyl free radical ·OH is found to be the most aboundant [48, 47]. Water radiolysis can induce damage to the solid (change of wettability, for instance), as well as decrease the signal quality. To cope with this issue, a low energy electron beam is preferable since it will decrease the concentration of damaging species [47].

2.3.3 E-beam electrical charging

The electron beam-sample interaction can generate an accumulation of the net charge of the solid surface, a result of nonzero balance between incoming and outgoing electrons. The sample charge can either be positive or negative. If negative, the incoming primary electron beam can lose energy, hence causing a reduction in the penetration of the beam and an increase in SE emission. In extreme cases, the electric field at the sample surface is so high that the primary beam is actually deflected by the sample, which provides a deterioration of the image [49, 50]. Besides, Stokes *et al.* evidenced a dynamic liquid charging during ESEM experiments [49] which can modify the water wettability on the surface. We have observed during our condensation experiments that changing the electrostatic potential (bias), that is the potential imposed to the detector to collect electrons, can induce dramatic changes in wettability. A high potential induces a high wettability of condensation droplets, a scenario not predictable on our superhydrophobic samples, which could originate in electrowetting [51]. To prevent e-beam electrical charging, a low beam energy (< 15 keV) is required, as well as a low detector potential, even if the latter may decrease the quality of images.

2.3.4 E-beam heating

Electron beam can also cause a significant heating and evaporation of water, especially when imaging a small area ($< 5\ \mu$m $\times$ $5\ \mu$m). Imaging at high magnification implies a large energy density that can heat droplets and cause their evaporation. Besides, even for larger imaging areas, evaporation can be observed after long beam exposure. For instance, snaphots of Figure 2.9 show the fast evaporation of a Cassie droplet on a superhydrophobic surface covered with micrometric cones (sample M2).

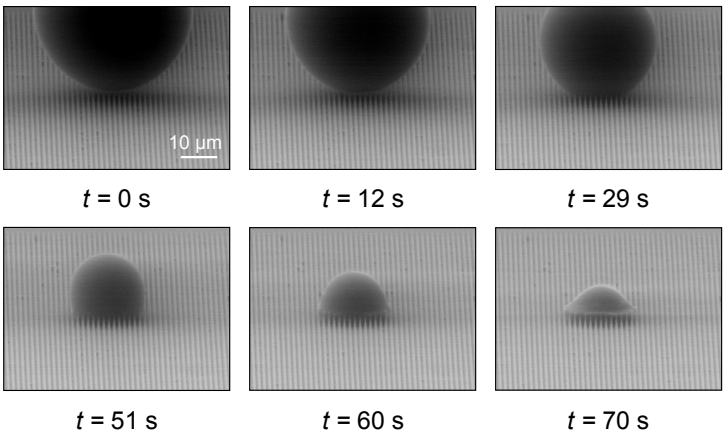

Figure 2.9: Snapshots of the fast evaporation of a Cassie droplet on hydrophobic microcones caused by e-beam heating (sample M2). The e-beam energy is 10 keV, surface temperature $T_s = -3.5°$C and chamber pressure $P = 615$ Pa.

At initial time ($t = 0$ s), the drop is quasi-spherical, with a low contact area with its substrate, which can be associated with a Cassie state on the cone tops. The drop volume decreases with time, a consequence of intense evaporation. Its apparent contact angle drastically decreases as evaporation takes place, passing from a value of order 170° at short time to 90° after 50 s, and even to acute angles (of order 45°) after 70 s, keeping a constant base radius. In the corresponding movie, we see in addition that the drop abruptly modifies its contact angle after typically 10 s, and this conjuntion of sudden decrease in contact angle and strong pinning evidences a transition from the Cassie to the Wenzel state. Evaporation could be a way to measure the receding angle θ_r of a microdrop. However, as illustrated in Figure 2.9, measuring θ_r during ESEM was rendered impossible on microdroplets because of the quick transition to Wenzel state, which exhibits low receding angles and much smaller than on Cassie droplets ($\theta_r = 163°$ for millimetric drops on M2). E-beam heating is a major issue for imaging nanostructures because micrometric drops are difficult to observe with a high magnification and the mechanisms of nucleation, where droplets are of nanometer size, are nearly inaccesible. Rykaczewski *et al.* developed a thorough study on heating effects caused by primary electrons [52]. The authors suggested to use a beam energy of 10 keV and a current of 0.036 nA with a field of view greater than ~ 4 μm by 4 μm.

Heating effects have been the major issue encountered during our experiments, which prevented us from observing the nucleation and growth of a water nucleus inside a nanotexture. However, we have managed to produce images that could enhance our understanding of condensation occurring on nanostructures, which is the subject of the next section.

2.4 Experimental set-up

2.4.1 Goal of the study

As reported by Mouterde *et al.*, superhydrophobic materials made of cylindrical nanopillars perform remarkably well when exposed to hot water [36]. However, under dew conditions generated by sample cooling, these surfaces are rapidly filled with water. Yet, a material composed of nanocones with the same size as pillars exhibits remarkable anti-fogging abilities (see Chap. 1). This effect was assumed to be caused by the the texture shape that would promote a Cassie state for condensation droplets. Because these surfaces have cones at a scale of hundred nanometers, the use of ESEM imaging could prove useful as it enables one to observe sizes down to the nanometer. Our aim here is to study the wetting states of droplets condensing on nanopillars and nanocones, the latter being never studied in ESEM. As illustrated in Chap. 1 (Figure 1.10), different wetting morphologies of condensation droplets were already reported during ESEM imaging, such as the Cassie (C) and Wenzel (W) states, as well as a Partial Cassie state (PC) where droplets locally wet the substrate [12, 52, 53, 30]. Miljkovic *et al.* evidenced the two states where droplet ejection can occur (C and PC), using ESEM on a sample textured with tall micrometric pillars [31]. While most of the droplets are in PC state, a consequence of the nuclei locations inside the texture, few droplets, with radii larger than 2.5 μm, were instead found in Cassie state, because of their nucleation on the top of pillars.

Furthermore, dynamics of microdroplets formation has also been extensively studied experimentally and theoretically. Rykaczewski studied the growth of droplets formed by condensation [54] and he evidenced two growth modes. One is the constant base area growth (CB) where the contact angle increases while keeping the base area constant. The other, named constant contact angle growth area (CCA), concerns the growth of the base area while keeping the contact angle constant. For a droplet condensing on textured materials, an alternation between the two modes happens: at the beginning of the growth, water fills the texture and the droplet subsequently grows by increasing either its base area or its

contact angle. Different growth dynamics were also found for partial Cassie and Cassie drops [31]. Our aim here is to image water condensation by ESEM on the different nanostructured surfaces presented in Table 2.1.

2.4.2 Principle of the experiment

The dynamics of water condensation is imaged using an FEI Quanta 650 field emission gun (FEG) environmental scanning electron microscope that belongs to the *Laboratoire de Mécanique des Solides* at École polytechnique. The sample is mounted on a horizontal bracket for top images and a 60°-tilted copper bracket for tilted images. The support can be inclined up to 90° to provide a clear view of water droplets. The bracket is mounted on a cooled thermoelectric (Peltier) cooling stage and both temperature and chamber pressure are controlled. Before every experiment, five purging cycles are performed, consisting in varying the pressure between 150 and 600 Pa, in order to remove any non-condensable gas. After this procedure, the sample is chilled at around -2 ± 1°C for 2 min at a vapour pressure of 200 Pa. Water condensation is later achieved by increasing the chamber pressure to about 500-700 Pa. Low beam energies (10 keV) and spot size of 3.5 are used to minimize heating, contamination and radiation damage. A SE detector (GSED) is selected for imaging as it yields better results than BSE detector. Besides, the detector potential is set at 330 ± 30 V (bias between 55 and 65) to prevent e-beam charging: the electric field magnitude increases with the bias, hence surface potential is more important for high bias. This parameter was found to be central for limiting wettability changes during condensation. Higher bias led to the complete wetting of droplets condensing and may be due to electrowetting. Finally, the electron beam working distance is set around 5 mm. During image processing, the contact angles θ of micrometric drops are computed after measuring the drop radius r and its contact radius l (radius of the contact area of the drop with the surface), since θ is simply given by $\sin\theta = l/r$.

2.4.3 Samples used

For this study, three samples are used, namely A, N1 and N7; their corresponding SEM images are displayed in Figure 2.10. Other samples are tested as well under ESEM and shown in Chap. 4. Samples A, N1 and N7 are rendered superhydrophobic after silanization and they have respective advancing angles $\theta_a = 167°$, 167° and 164° and receding angles $\theta_r = 140°$, 157° and 153°. Surface A has the largest contact angle hysteresis $\Delta\theta = \theta_a - \theta_r$, owing to its pillar geometry that favours contact line pinning, hence a significant decrease of the receding angle of water.

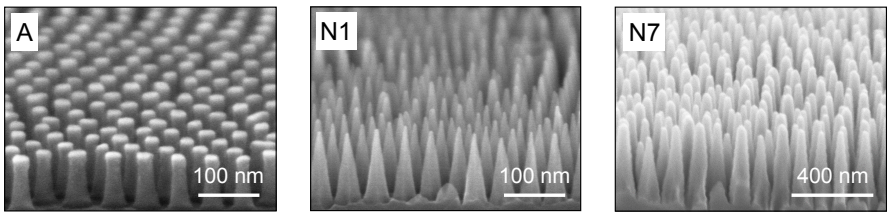

Figure 2.10: SEM images of the samples A, N1 and N7.

2.5 Observation of condensation droplets

2.5.1 Comparison between A and N1

Our first aim is to compare condensation droplets on materials with similar texture size but with different shapes, hence the use of samples A (pillars) and N1 (cones). Figures 2.11a and b present ESEM snapshots of condensation occurring on the two samples after cooling the surface and increasing the chamber pressure. The left images are wider viewpoints while right ones are closer looks at droplets. Despite the difference of tilting angles (60° for N1 and 85° for A), differences can be noted between the two surfaces: on sample N1, drops appear spherical with a very low surface area and they exhibit large contact angles ($160 - 170°$) for all sizes, a plausible manifestation of a Cassie state. In contrast, drops on sample A seem to adhere much more to the texture and drop contact angles approach 140° (Figure 2.11b right) - a value usually observed for droplets in a partial Cassie state [54, 29]. Although images differ between the two surfaces, it was hard to get a clear view of droplets on sample N1 as it was the first surface used in our experiments. At that time, our experimental set-up was not perfectly efficient and with some practice, the good set of parameters (beam energy, bias, tilt angle) were obtained. These new parameters were tested on samples A and N7 and in those cases, tilt angles approached more $80 - 85°$ for both samples, hence giving us good access to the surface contact area and drop contact angle.

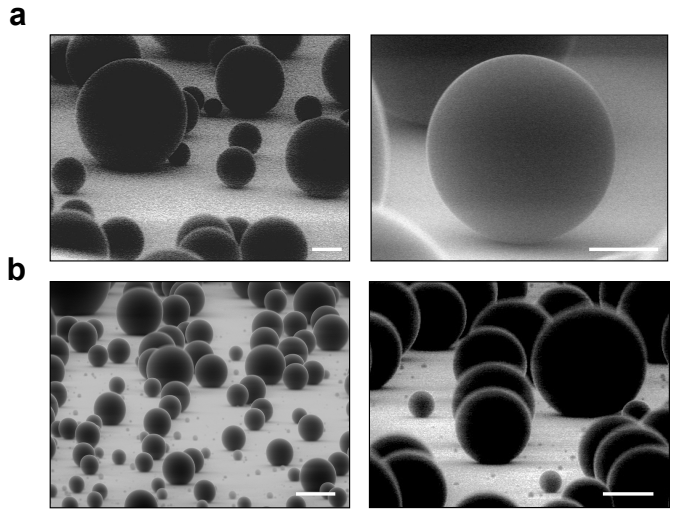

Figure 2.11: ESEM images of water drops condensing on samples N1 (a) and A (b). Right images show closer look at droplets. The tilt angles are respectively 60° for N1 and 85° and condensation experiments are both performed with $T_s = -2 \pm 1°C$ and $P = 560 \pm 50$ Pa. Differences of contact angle can be noted between the two surfaces: on surface A, drops have larger contact areas with the solid. The scales indicate 10 μm except for the bottom right image where it is 2 μm.

2.5.2 Comparison between A and N7

Two ESEM images of droplets condensing on materials A and N7 are shown respectively in Figure 2.12a and b. Samples are tilted by an angle of 85° for surface A and 80° for N7, which allows one to get a clear view of the droplets. On material A, all drops meet the surface with an apparent angle significantly smaller than that on material N7. Contact angles on A vary between drops: while large drops ($r \gtrsim 2$ μm) exhibit angles θ as high as 140°, smaller drops can have θ of around 120°. This image dramatically differs from that

of sample N7 displayed in Figure 2.12b. In contrast with sample A, drops condensing on nanocones all seem to "levitate" and exhibit contact angles close to 175°, much larger than the maximum value measured on nanopillars. For some droplets, it is even hard to define a contact area as their shape approaches that of a sphere. This behaviour strongly suggests a Cassie state for drops condensing on nanocones as contact angles close to $170 - 175°$ are observed for nearly all droplet sizes ($r \gtrsim 1$ μm), contrasting with nanopillared surfaces where only a few drops lie in a fakir state [31]. The Cassie state is observed for all drops condensing on surface N7, with radii spanning from $r = 1$ μm to 23 μm (a value close to the maximum radius of 24 μm observed on sample N1 [36]).

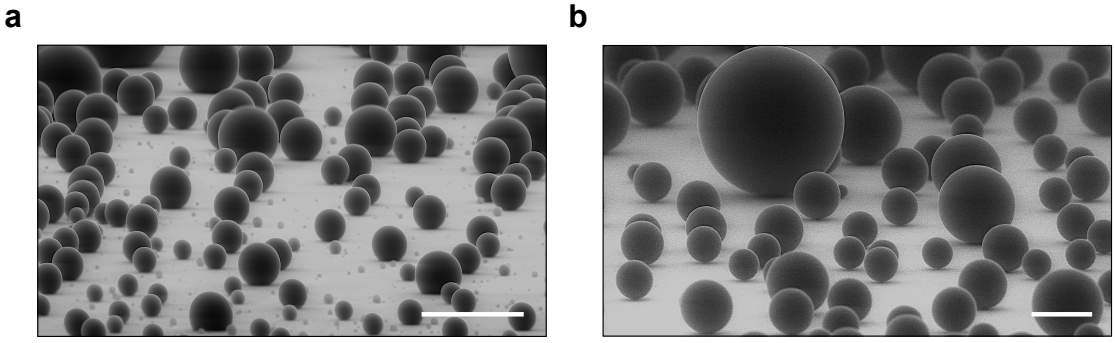

Figure 2.12: ESEM images of drops condensing on samples A (a) and N7 (b). Surface A is covered with nanopillars with $p = 52$ nm and $h = 88$ nm, while N7 is composed of nanocones with $p = 110$ nm and $h = 420$ nm. On sample A, drops adhere to the surface with contact angles no larger than 140°. Conversely, contact angles on sample N7 are found close to $170 - 175°$ for all drops' radii r (1 μm $\leq r \leq 23$ μm). The quasi-spherical shape of drops as well as the low contact with the solid suggests a Cassie state. Both scales indicate 20 μm.

2.5.2.1 Growth dynamics

ESEM experiments also enable to capture the condensation dynamics. The different phases of a droplet growing on material A are shown in Figure 2.13. During condensation, the drop experiences two growth modes, as predicted in [54]: for $0 < t < 3.8$ s (images 1 and 2), the drop grows with a constant contact angle of $120 \pm 5°$ and its radius varies from 850 nm to 1.1 μm, while for 3.8 s $< t <$ 7.6 s (images 2 and 3), it exhibits a constant base area. Subsequently ($t > 7.6$ s), the drop grows with a quasi-constant contact angle of $140° \pm 5°$ until reaching a radius of 2.8 μm in the last image. The maximum value of the contact angle is also observed for even larger drops (see Figure 2.12a). Enright *et al.* observed that condensed drops on pillar-textured surfaces can exhibit three wetting states [29]: Wenzel or partial Cassie states, and even sometimes Cassie state [31]. As mentioned in the Chap. 1, the two first states will occur depending both on the criterion $E^\star$ (see Eq. (1.17)), that compares Cassie to Wenzel energies, and on the comparison between the nucleation site spacing and pillar spacing. Most droplets on material A appear in partially wetting state, as evidenced by the values of their contact angle.

Drops on material N7 have shapes that largely differ from those observed on material A, as evidenced in Figure 2.14, that presents different snapshots of a droplet growth induced by condensation. At $t = 1.8$ s (2^{nd} image), the drop has a low contact angle ($\approx 130 \pm 7°$) for a radius $r \approx 600$ nm. Yet, very rapidly, the drop exhibits a quasi-spherical shape as r approaches 1 μm. For larger radii ($t > 5.4$ s), that is $r > 1.2$ μm, the measured advancing contact angle remains constant and equal to $170 \pm 4°$, while the drop radius keeps increasing until reaching 1.6 μm at $t = 9$ s (constant contact angle growth mode).

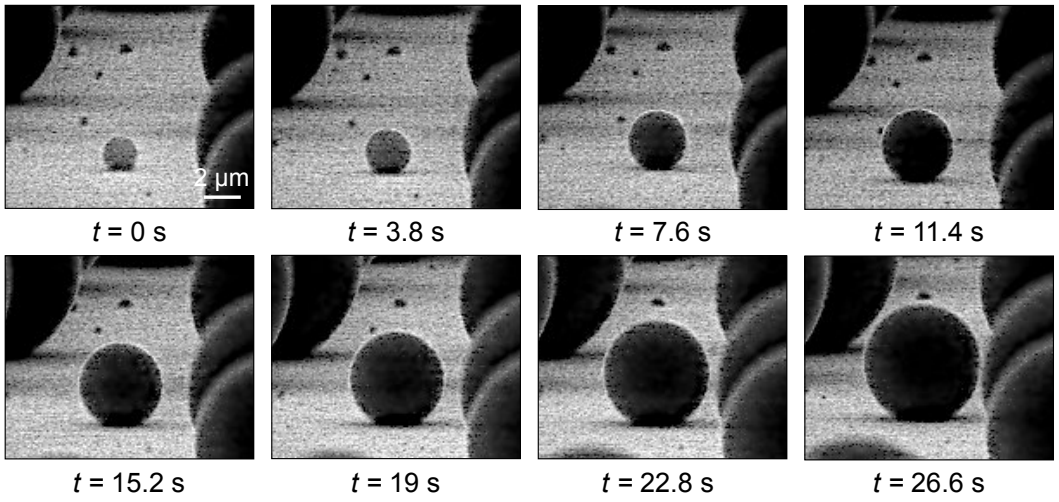

Figure 2.13: Snapshots of droplet growth on material A (nanopillars). During its expansion, the drop exhibits two growth modes characterized by constant base area and constant contact angle. Between the first and last images, the advancing contact angle θ_a varies from 120 to 140°. Images are separated by 3.8 s, temperature is $T_s = -2.5$°C and chamber pressure $P = 600$ Pa. The scale bar indicates 2 μm.

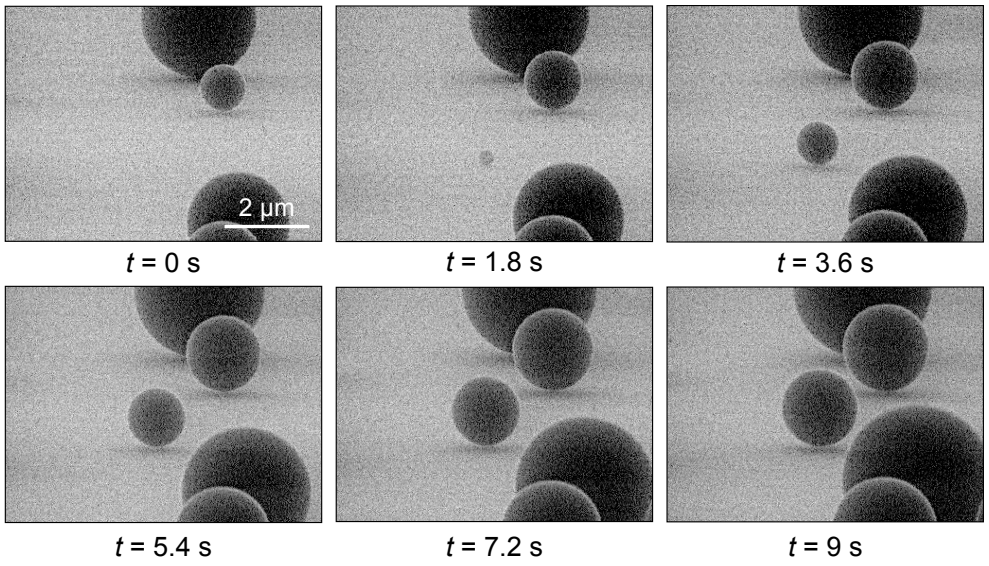

Figure 2.14: Snapshots of droplet growth on material N7. At small radius ($r < 1$ μm, $t = 1.8$ s), the advancing contact angle θ_a equals 130 ± 7°. For larger radii, the drop approaches the shape of a sphere with θ_a around 170°, a manifestation of a possible Cassie state. Images are separated by 1.8 s, temperature is $T_s = -1.5$°C and chamber pressure $P = 700$ Pa.

Values of advancing contact angles θ_a for the two samples are reported in Figure 2.15 as a function of droplet radius r. Much information can be extracted from this plot. Firstly, the values of contact angle markedly differ between the two surfaces, the angles being about 30° smaller on nanopillars than on nanocones. Secondly, a size effect can be noted for both samples: θ_a increases with radius r until $r \approx 2$ μm and then converges towards a constant value, $\theta_a = 141 \pm 3$° for sample A and $\theta_a = 171 \pm 3$° for sample N7. The maximum value of

θ_a on sample A is much lower (25°) than that for millimetric drops in a Cassie state where $\theta_a = 167°$ (red dashed line in Figure 2.15). It strengthens the observations made earlier: drops condensing on sample A do not exhibit Cassie state and rather lie in a partial Cassie with a pinned area, owing to the wetting of unit cells (see Chap. 1). Besides, the increase of θ_a for $r < 2$ μm can be interpreted as the manifestation of the constant base area growth mode: the contact line is pinned on pillars and the contact angle keeps increasing.

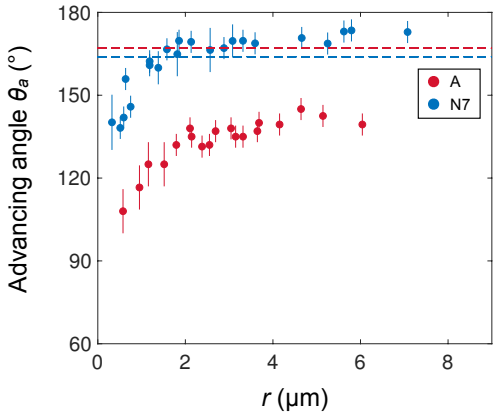

Figure 2.15: Advancing contact angle θ_a as a function of drop radius r for materials A (red dots) and N7 (blue dots). For both surfaces, θ_a converges towards a constant value equal to 141 ± 3° for substrate A and 171 ± 3° for substrate N7, slightly larger than the measured one on millimetric drops, $\theta_a^{app} = 164 \pm 3°$ (blue dotted line). For substrate A, the maximum value of θ_a markedly differs from that for millimetric drops in Cassie state ($\theta_a^{app} = 167 \pm 3°$), drawn in red dotted line. It shows that drops condensing on nanopillars do no exhibit a Cassie state but rather a partial Cassie state. For $r < 2$ μm, θ_a is observed to increase with r for both materials: from 110 to 140 ± 3° on nanopillars while from 140 to 171 ± 3° on nanocones.

For material N7 instead, it is the first report of such high contact angles for radii as small as 1 μm. Previous studies measured contact angles as high as 170°, but for droplets with larger radii and in partial Cassie state [29, 54]. Contrary to the case of sparse Cassie droplets [31], all droplets formed by condensation have here large contact angles on material N7, independently of their size. For drops in partial Cassie state and with radii much larger than the wetted area, the apparent advancing contact angle can be high. Enright *et al.* indeed observed contact angles up to 170° for partially wetted drops with radii as high as 20 μm [29]. In those cases, ESEM imaging clearly evidenced a pinned wetted area below the droplet. However, in our case, drops do not exhibit any wetted area and for radii as small as 1 μm, they still have high contact angle. Besides, one can note that the limit value of θ_a ($\theta_a = 171 \pm 3°$) is found to be larger than that for millimetric drops ($\theta_a = 164 \pm 3°$, blue dotted line in Figure 2.15). For millimetric drops, gravity can play a role and tends to flatten the drop, hence decreasing its apparent contact angle. In that case, for a high non-wetting substrate, the radius l of the liquid-surface area is no more equal to $r \sin\theta$, but to r^2/κ^{-1} [55], denoting $\kappa^{-1} = (\gamma/\rho g)^{1/2}$ as the capillary length and where γ and ρ are respectively the surface tension and density of water and g the gravity. Weight can be neglected when $r \sin\theta > r^2/\kappa^{-1}$, which yields $r < 400$ μm, a condition always verified for micrometric drops. The size effect of θ_a where θ_a increases with r for $r < 2$ μm is the subject of the next section.

2.5.2.2 Arrangement of Cassie droplets

Figure 2.16a skteches the shape of the contact line of a droplet being in a Cassie state on an array of hydrophobic cones.

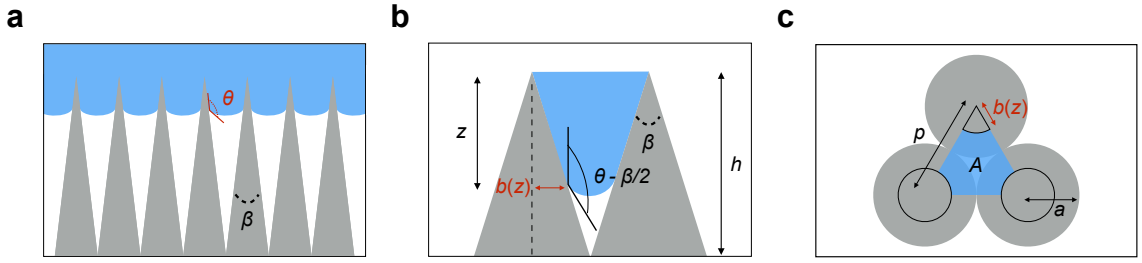

Figure 2.16: (a) Cassie state for a drop resting on an array of cones. (b) Side view of liquid inside the cones. The contact line sinks at the depth z and makes a contact angle with the vertical equal to $\theta - \beta/2$, where β is the cone angle. The radius of solid-liquid contact is denoted as $b(z)$. (c) Top view of an elementary triangular cell delimited by three cones. The liquid occupies an area $\mathcal{A}$. Adapted from [1].

Contrasting with pillars where a contact line can exhibit different contact angles at a same position, owing to the roundness of the pillars' edge, the contact line along a cone has only one eligible position. The depth z to which water can go inside the texture (Figure 2.16b) is dictated by the equilibrium between the Laplace pressure inside the droplet and the tension exerted on the contact line. The contact line perimeter being $3 \times \pi b(z)/3$ (Figure 2.16c), surface tension exerts a force equal to $-\pi b(z)\gamma\cos(\theta - \beta/2)$, where we denote $b(z)$ as the contact radius, γ the surface tension of water and θ the contact angle of water on flat silicon. The force divided by the area of the air-water interface $\mathcal{A} = \sqrt{3}p^2/4 - \pi b^2/2$ (Figure 2.16c) yields the pressure $\Delta P(z)$ [56, 1] :

$$\Delta P(z) = -\gamma\cos(\theta - \beta/2)\frac{4\pi b(z)}{\sqrt{3}p^2 - 2\pi b^2(z)} \ . \tag{2.2}$$

At equilibrium, this pressure equals the Laplace pressure $\Delta P_L = 2\gamma/r$, so that we obtain a relation between $b(z)$ and r. Besides, the cone geometry enables us to link $b(z)$ and the depth z with the relation $z = 2hb(z)/p$. Finally, solving $\Delta P(z) = \Delta P_L$, one obtains the depth z as a function of r:

$$z(r) = \frac{hr|\cos(\theta - \beta/2)|}{p}\left[\sqrt{1 + \frac{2\sqrt{3}p^2}{\pi r^2|\cos(\theta - \beta/2)|^2}} - 1\right] \ , \tag{2.3}$$

where $\theta = \theta_0 \approx 120°$ the advancing angle of water on flat silicon as it concerns droplet growth. The sinking depth z is observed to decrease with radius r as the Laplace pressure decreases, hence the contact line will rest closer to the top of the cones. For $r \gg p$, Eq. (2.3) simplifies as $z(r) \approx \sqrt{3}hp/\pi r|\cos(\theta - \beta/2)|$. It is drawn in Figure 2.17a as a function of the drop radius r for the material N7 parameters (Table 2.1). The depth z is indeed observed to be a decreasing function of r and for 500 nm $< r <$ 1 μm, one finds 122 nm $> z >$ 67 nm. Therefore, for our observed radii (Figure 2.15), drops can sink up to more than one fourth of the cones' height. Our previous observations have pushed us to suggest that drops condensing on nanocones lie in a Cassie state because of the high measured contact angles. We now try to understand the low contact angles reported for $r <$ 1 μm (Figure 2.15). Assuming that drops are resting on cones and writing that the contact base radius is equal to $r\sin\theta_a$ (inset of Figure 2.17a), the advancing contact angle

θ_a can be approximated as:

$$\theta_a \approx \pi - \cos^{-1}\left[\frac{r - z(r)}{r}\right] \quad . \tag{2.4}$$

Measuring the contact angle of Cassie drops presents some issues as it does not reflect the real shape of droplets [57]: indeed, for Cassie droplets resting on cones, the contact line lying below the top of the cones is not visually accessible. The only characteristic that can be measured is the contact angle, that is the angle between the drop and the top of the surface. Droplets with radii smaller than 1 μm have large depth z, hence their apparent contact angle will appear to be low (inset of Figure 2.17a). Finally, Eq. (2.4), along with Eq. (2.3) for $z(r)$, is plotted in Figure 2.17b in solid line as a function of droplet radius r for sample N7, together with the experimental data (blue dots). The model captures well the behavior of θ_a with r, in particular for radii smaller than 1 μm, and tends to validate our hypothesis of low contact angles for nanodroplets. It is worth noting that the resolution of our ESEM and electron beam effects prevented us from imaging droplets with radii smaller than 300 nm.

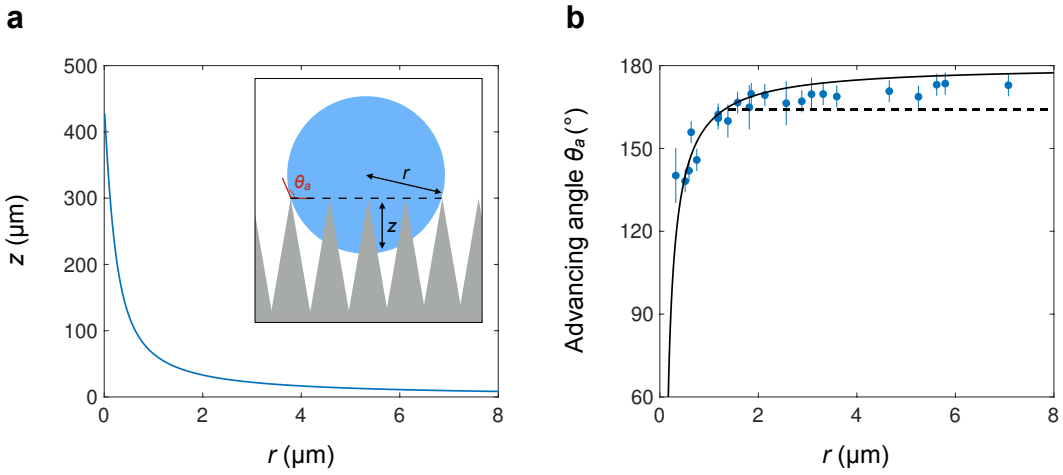

Figure 2.17: (a) Sinking depth z for a drop (radius r) in a Cassie state on an array of hydrophobic cones (inset). The solid line is Eq. (2.3) plotted for sample N7 : $p = 110$ nm, $d = 110$ nm and $h = 420$ nm. The depth decreases with radius r. (b) Advancing contact angle θ_a as a function of the drop radius r for sample N7. The solid line represents Eq. (2.4) and the dashed line the advancing angle measured on millimetric drops, $\theta_a = 164°$. A good agreement is observed betwen experimental data (blue dots) and the model. For drops with $r < 1$ μm, the apparent advancing contact angle θ_a decreases owing to the liquid configuration in the nanocones (inset).

Take home message of Chapter 2

1. Families of materials. To provide a consistent study on antifogging abilities, two families of samples are tested: first, a set of surfaces covered with nanocones and composed of homothetic ones and constant pitch ones. Micrometric cones are also considered as well as truncated nanocones to further understand the influence of cone shape.

2. ESEM imaging. Despite its success in imaging submicrometric droplets issued from condensation, the use of ESEM presents several limitations due to e-beam exposure than can hinder the imaging. Good sets of parameters are found to properly image water condensation.

3. Water condensing on nanocones. Water droplets condensing on nanocones are quasi-spherical, which suggests a possible non-wetting Cassie state, even for radii smaller than 1 μm. In this state, nanodroplets can sink deeply in the features, which impacts the value of their apparent contact angle. On the contrary, on nanopillars with same size, droplets adhere to the surface and exhibit lower contact angles.

3

Ballistics of self-jumping microdroplets

Water-repellent materials ideally operate at very different liquid scales - from centimeter-size for bugs living on ponds through millimeter-size for anti-rain functions to micrometer-size for anti-fogging solids. In the latter situation, it was recently evidenced that microdrops condensing on a highly non-adhesive substrate can take advantage from coalescence to jump off the material, even if the dynamical characteristics of the jump were not established at such microscales. We first experimentally report the jumping velocity of drops condensing on a conical nanotexture and then quantitatively describe its evolution with their radius. Finally, we study the ballistics of these jumping microdrops, from the height they reach to their behaviour at landing.

Tartaglia trajectory of a cannonball. Source: [58] extracted from [59].

Contents

As for many parts of this thesis, this work has been the result of my collaboration with Timothée Mouterde and was performed as we were both PhD students. He can be thanked for all his help and his (large) contribution to my PhD. This study has been published in *Physical Review Fluids* (see Appendix B)

3.1 State-of-the-art review

Although humid conditions can often destroy the superhydrophobic properties of a textured surface, if suitably designed, *i.e.* nanotextured or hierarchical, these materials can lead to droplets jumping away from the surface. This suprising effect was first reported by Boreyko and Chen in 2009 [33]: they observed spontaneous jumping on droplets coalescing and the minimum evidenced jumping droplet radius was 5 μm. According to them, droplets are able to take off by benefiting from the excess of surface energy that can be transferred into kinetic energy. The typical surface energy gained at coalescence scales as γr^2, denoting γ as the surface tension of water and r as the radius of the coalescing droplet. Similarly, the kinetic energy for a jumping droplet with velocity U scales as $\rho r^3 U^2$ where ρ is the density of water. If the transfer of energy were fully efficient, it would provide the following scaling:

$$U \sim (\gamma/\rho r)^{1/2} \ , \tag{3.1}$$

where we denote $U^\star = (\gamma/\rho r)^{1/2}$. There has been a strong debate on the dependence of the jumping velocity U on $r^{-1/2}$, as well as on the correct prefactor in front of U. For two symmetric droplets with radii r, a proper energy analysis yields $U = (3[2-2^{2/3}])^{1/2}\, U^\star \approx 1.11\, U^\star$. This law has been tested in different situations: Leidenfrost droplets by Liu *et al.* [60] or superhydrophobic surfaces by Boreyko *et al.* [33]. For droplets large enough to be above the cutoff radius (that depends on texture) for which jumping is no longer observed, the scaling in $r^{-1/2}$ is nicely obeyed but the prefactor tends to overestimate by a factor 5 the measured jumping velocities: the experimental jumping velocities U measured are indeed found around $0.2\, U^\star$. As pointed out by Enright *et al.*, the energy transfer is in fact inefficient as coalescence generates strong oscillations that can absorb up to $\sim$ 90% of the initially available energy [61]. Internal viscous dissipation during coalescence was first proposed to account for no jumping for radii below 5 μm [62, 63].

However, recent experimental and numerical studies have demonstrated that jumping could occur at a much smaller scale, $r \approx 1$ μm [36, 32] and even $r \leq 500$ nm [64, 60, 65, 66]. Both this threshold and the jumping velocity are material-dependent [63, 62, 65, 32], and modelling them requires to consider both viscous and adhesive effects at such microscales. To promote jumping-droplet condensation on a textured material, droplets must be in either the two wetting states which generate the least adhesion: the Cassie state where they rest on top on the texture or partial Cassie state where some texture cells below the droplet are filled with water. These two states, as well as the number of wetted cells, depend on the texture shape (cone or pillar), their size and their arrangement. Two thorough studies were performed to predict the number of wetted cells below a condensation droplet, so as to predict the minimum jumping radius [29, 32]. In the latter study, Mulroe *et al.* compared the energies for a nucleus to grow above or inside the texture in order to predict the number of wetted cells and deduce the threshold for jumping. In Chap. 1 was introduced the case of a texture covered with jointed nanocones where spontaneous jumping is observed as well [36], that is surface N1 (Table 2.1 and Figure 2.10). As noted by the previous cited authors, the jumping velocity U is an interesting quantity to study, which has led us to measure this quantity on our materials. In Chap. 2, ESEM images of sample N1 have revealed quasi-spherical droplets during condensation (Figure 2.11), suggesting that they are in Cassie state, even for $r \approx 1$ μm. We assume that this state is promoted by the conical shape of texture thanks to the Laplace pressure that pushes the growing nucleus to the top of the structures. As they mainly rest on air, their mobility is favoured, hence explaining the high antifogging ability of this texture generated by jumping-droplet condensation (see Chap. 1). Contrary to the previous cases where droplets are pinned [61, 65, 32], the scenario induced by nanocones is different since one would expect adhesion to be less significant. In order to model the jumping velocity for drops condensing on this nanotexture, it is yet essential to

understand the mechanisms of droplet-jumping after coalescence for drops in Cassie state.

Mouterde *et al.* had the idea of depositing drops on a superhydrophobic surface, making them coalesce and measuring the jumping velocity of the resulting drop [67]. This study will be crucial for our modelling of U with r and we expose here the principal results. The authors filmed the coalescence of two drops with different sizes on a superhydrophobic surface. The material is connected to a MEMS sensor than can determine the force exerted on the surface. It enables then to measure the momentum of the jumping drop. Because coalescence is not an energy-efficient process, resorting to momentum equilibrium is a way to neglect the effect of drop oscillations. Several drop volumes were used, as well as drop asymmetries $\varepsilon = r'/r$, where we have denoted r' and r ($r' < r$) as the two drops radii. Similarly, in an asymmetric situation, an energy analysis would yield the corresponding jumping velocity U:

$$U = U^\star \sqrt{\frac{6[\varepsilon^2 + 1 - (\varepsilon^3+1)^{2/3}]}{(\varepsilon^3+1)}} \,. \tag{3.2}$$

This law is found to largely overestimate the measured speed U and predicts a maximum for $\varepsilon \approx 0.85$ whereas U is instead observed to decrease monotically as ε decreases, which led the authors to develop a model based on each drop momentum.

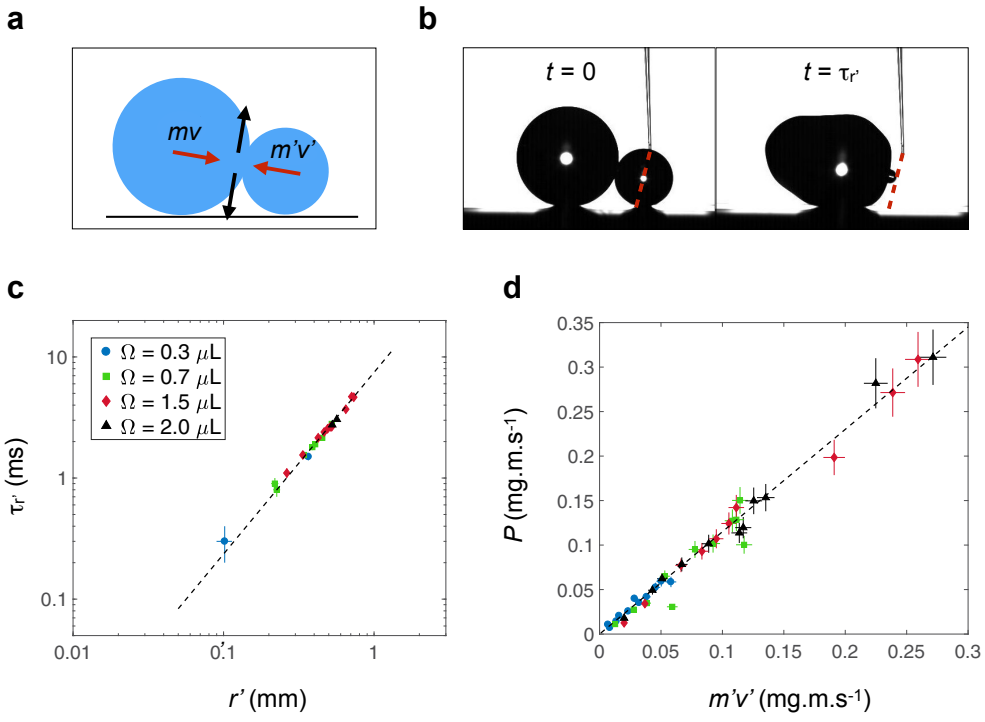

Figure 3.1: (a) Schematic describing the transfer of quasi-horizontal momentum of the small drop into quasi-vertical momentum. (b) Snapshots illustrating the small radius retraction time $\tau_{r'}$, defined as the time needed for the edge of the small drop to move by its own radius r'. (c) Retraction time $\tau_{r'}$ as a function of r' for different large drop volumes Ω. The black dashed line shows $\tau_{r'} \approx 2(\rho r'^3/\gamma)^{3/2}$. (d) Force P integrated over the jumping time as a function of the measured momentum $m'v' = mr'/\tau_{r'}$ of the small drop. The dashed line has a slope 1.15. Adapted from [67].

During coalescence between two asymmetric drops, the smaller drop (with mass m') retracts the fastest with a velocity v' and a time $\tau_{r'}$ (Figure 3.1a). Mouterde *et al.* measured this retraction time and found $\tau_{r'} \approx 2(\rho r'^3/\gamma)^{3/2}$ (Figure 3.1b and c), the same scaling as the one found when balancing inertial and capillary forces [68]. The smaller drop has thus a retraction velocity $v' \approx r'/\tau_{r'} \approx (1/2)(\gamma/\rho r')^{1/2}$. During coalescence, the smaller drop first retracts with a momentum $m'v'$, then, the larger drop opposes an equivalent momentum and the flow incompressibility ensures that each horizontal momentum is deviated upwards and backwards: the smaller drop having the smaller momentum, $m'v'$ is the resulting drop momentum $(m+m')U$, where m is the mass of the larger drop. This momentum is equal to P, the measured force integrated over the jumping time and Figure 3.1d confirms the linear relation between P and $m'v'$. Finally, one can obtain the velocity $U = m'v'/(m+m')$ of the jumping drop:

$$U = \frac{1}{2}U^\star \frac{\varepsilon^{5/2}}{1+\varepsilon^3} \ . \tag{3.3}$$

This equation is drawn in solid line in Figure 3.2 and found to match well the experimental data. It predicts a jumping velocity $U = 0.25\,U^\star$ for symmetric drops ($\varepsilon = 1$), a value close to the measured one on condensed droplets ($U \approx 0.2\,U^\star$). The overestimation can originate in residual adhesion (contact angle hysteresis) that is not taken into account in the model and could dissipate energy. This momentum balance model has thus managed to predict a correct estimation of the jumping velocity. However, it concerns an ideal case where droplets are deposited and have a size much larger than that of condensed droplets, that are micrometric. Besides, at a millimeter scale, adhesion and viscous effects are marginal unlike at a micrometer scale, where they can impede the motion and impose a threshold in radius for jumping. Therefore, we now focus on the jumping velocity for droplets condensing on a material covered with nanocones (material N1), as well a their ballistics after departure from the surface.

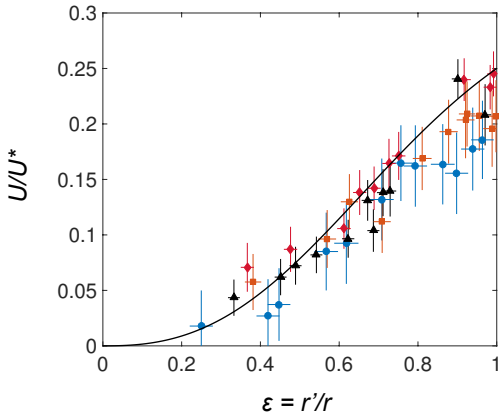

Figure 3.2: Normalized jumping velocity $U/U^\star$ as a function of the asymmetry ratio ε and where $U^\star = \sqrt{\gamma/\rho r}$. Colours indicate different volumes of the large drop. The solid line shows Eq. (3.3) drawn without any adjustable parameter. Adapted from [67].

3.2 Experimental set-up

Our goal is to determine the jumping velocity of condensing droplets on a superhydrophobic material. Surface N1 is tested and one reminds here its principal characteristics: it is covered with jointed cones with a pitch $p = 52$ nm and a height $h = 115$ nm, The advancing and receding angles are respectively $\theta_a = 167 \pm 2°$ and $\theta_r = 157 \pm 2°$, which entails a modest

hysteresis $\Delta\theta = \theta_a - \theta_r = 10 \pm 4°$. Condensation of water from the atmosphere is triggered by affixing the substrate on a Peltier module, and setting the temperature at $T_s = 3 \pm 1°C$, a value below the dew point in the laboratory conditions (temperature $T = 25 \pm 1°C$, relative humidity $RH = 39 \pm 1\%$ and supersaturation $S = 1.63 \pm 0.26$). To determine the jumping velocity, the coalescence of pairs of neighboring condensed droplets is filmed from above and from aside. The two synchronized high-speed videocameras (Photron Mini UX 100) capture images at a respective rate of 1 and 40 kHz, for top and side views. The camera for top view is connected to a microscope (Infinitube In-line and Nikon ELWD 20x) attached to an optical fiber that enables one to film at a high frame speed. As sketched in Figure 3.3, the radii of the merging droplets, r' and r ($r' < r$) are determined using top view and it ensures us that only two-droplet coalescences are considered: indeed, many recent studies [61, 69] measured the jumping velocities of drops without knowing the initial number of coalescing droplets and their size, while asymmetry can, for instance, dramatically change the jumping velocity (Figure 3.2), hence the need for top view imaging. Besides, side view (Figure 3.3) allows us to measure the jumping velocity U of the departing water drop with radius $R = (r^3 + r'^3)^{1/3}$, the value of which obtained using volume conservation.

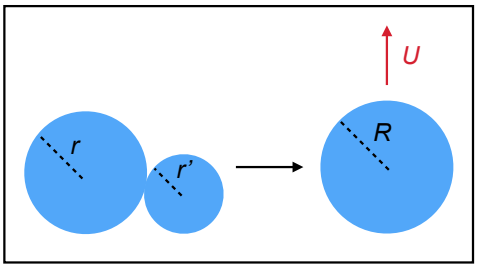

Figure 3.3: Schematic of the experiment: The coalescence of two droplets with respective radii r and r' ($r' < r$) is filmed from above. The resulting drop with radius R, simultaneoulsy filmed from aside, departs with a jumping velocity U.

Droplets departing on sample N1 have radii r ranging from 1 to 24 μm, owing to the high antifogging ability of our substrate [36] (see Figure 1.13 in Chap. 1). To get a larger span of radii, a second experiment is performed and consists of measuring the coalescence of needle-dispensed drops with radii ranging from 150 to 1100 μm, in the same manner as in [67]. The glass needles are rendered superhydrophobic by coating them with a Glaco solution (hydrophobic silica nanobeads in isopropanol) and drying the solution at 250°C for half an hour. Two droplets are deposited using the needles and their merging is recorded from the side at a rate of 4 kHz.

3.3 Jumping velocity

3.3.1 Symmetric merging

We first focus on symmetric merging for which the radii ratio $\varepsilon = r'/r$ is larger than 0.95.

3.3.1.1 Experimental observations

The chronophotography of Figure 3.4a shows the takeoff of a water drop with radius $R = 11.3 \pm 0.1$ μm resulting from the symmetric coalescence of a pair of droplets with $r = 8.9 \pm 0.1$ μm. Images are separated by 0.125 ms and one notices a quick deceleration

of the drop with time. The side images enable one to compute the drop position $z(t)$, hence providing us with the drop velocity $\dot{z}$, that is displayed as a function of time t in Figure 3.4b. As noted in the image and the plot, $\dot{z}$ decreases monotically with time. The jumping (or departure) velocity U is taken as the maximum of $\dot{z}(t)$. A layer of microdroplets sometimes hides the beginning of the jump, which generates an uncertainty on U on the order of 10%. For this particular case (Figures 3.4a and b), we measure a jumping velocity $U = 55 \pm 5$ cm/s. Besides, the initial acceleration of the drop is observed to be extremely strong (with a value on the order of 100 g) and the small size of the drop makes it highly sensitive to air (quick deceleration, slight deviation from the vertical).

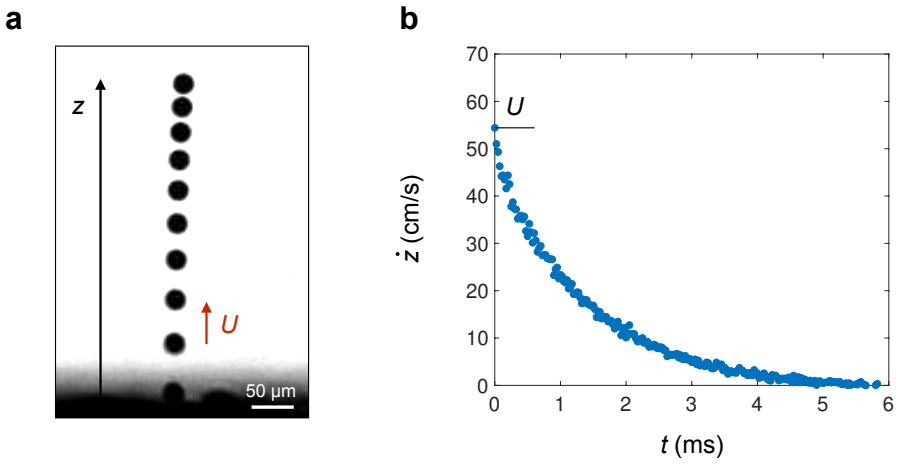

Figure 3.4: (a) Side-view chronophotography of a jumping drop with radius $R = 11.3 \pm 0.1$ μm resulting from the coalescence of a pair of droplets with $r = 8.9 \pm 0.1$ μm. Images are separated by 0.125 ms. The drop takes off with a vertical jumping velocity $U = 55 \pm 5$ cm/s. (b) Plotting the drop velocity $\dot{z}$ as a function of time t provides our definition of the jumping velocity U: it is taken as the maximum of $\dot{z}$.

In contrast, for bigger drops ($r > 150$ μm), the departing velocity is observed to be much smaller: snapshots of Figure 3.5 shows the takeoff after merging of two drops with radii $r = 580 \pm 5$ μm and the measured jumping velocity is $U = 7 \pm 1$ cm/s. In addition, we notice strong persistent droplet deformations after coalescence, another consequence of the much larger scale. We now report the jumping velocities measured for the two ranges of radii.

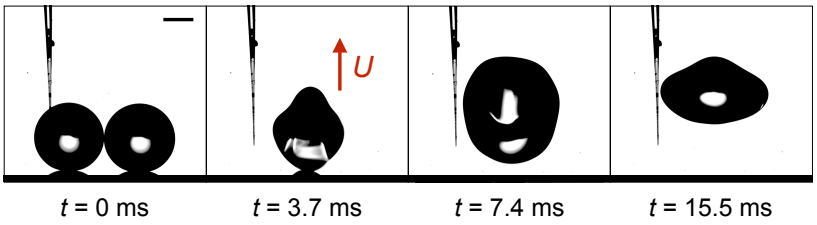

Figure 3.5: High-speed photography of a symmetric coalescence of two drops with $r = 580 \pm 5$ μm. Images are separated by 3.7 ms, except the last one which is at 15.5 ms, when the drop reaches its maximum height. The first snapshot shows the beginning of the coalescence while the second one corresponds to takeoff; the measured jumping velocity is $U = 7 \pm 1$ cm/s. The scale bar indicates 500 μm.

3.3.1.2 Quantitative results

Figure 3.6 displays the jumping velocity U after symmetric coalescence of two drops with radii r. Two families of data are plotted, that correspond to the two observation modes: condensed ($r \leq 24$ μm) and deposited droplets ($r \geq 150$ μm). For $r > 5$ μm, U decreases as r increases and data are well described by the dotted line with slope -0.5 in the log-log plot: the velocity indeed scales with the inertio-capillary velocity $U \sim \sqrt{\gamma/\rho r}$, as reported by previous authors [33, 60, 64], a law extended here down to 5 μm. The jumping velocity U deduced from the energy analysis, $U \approx 1.11\,U^\star$, is drawn in solid line in Figure 3.6: it is observed to overestimate the observed speed by a factor 5 and experimental data are found to align more on a line with a factor of around 0.22, a value close to the one measured by several authors [33, 60]. The maximum jumping velocity is observed for radii r around 4-5 μm and drops can depart as fast as 75 cm/s. However, drops smaller than 5 μm take off slower than predicted by the inertiocapillary scaling and U tends to 0 as r approaches 1 μm, in agreement with the cutoff radius of jumping measured on the same substrate in [36].

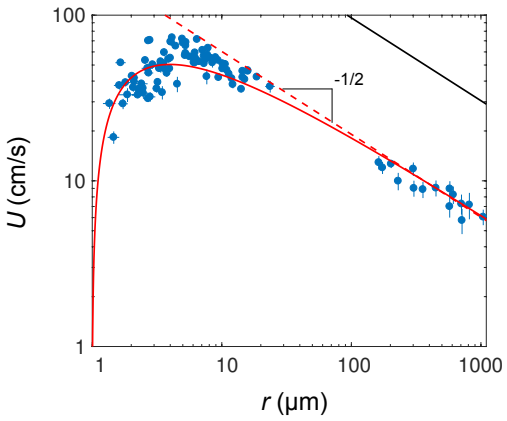

Figure 3.6: Velocity U for symmetric coalescence ($\varepsilon > 0.95$) as a function of the radius r of the two merging drops. Black line shows the speed resulting from energy conservation ($U = 1.11\,U^*$) and red dashes correspond to $U = 0.22\,U^*$, denoting $U^* = \sqrt{\gamma/\rho r}$. The red line shows the velocity $U = (U^*/4)\,[\alpha - 4.9\,Oh]$ (Eq. (3.8)), where $\alpha = 1 - 6\sin^2\theta_r(1+\cos\theta_r)$ and $Oh = \eta/\sqrt{\rho\gamma r}$ is the Ohnesorge number with η the water viscosity. The coefficient 4.9 is close to 4 the one predicted in Eq. (3.8).

3.3.1.3 Quantitative model

For drops in Cassie state, Eq. (3.3) yields $U = U^\star/4$ ($\varepsilon = 0$), and the factor 0.25 is 10% higher than the observed one in our data $U \approx 0.22\,U^\star$ (red dotted line in Figure 3.6). As observed in Chapter 2, ESEM images on nanocones suggest that water remains in a Cassie state despite condensation and even at microscales ($r \approx 1$ μm). It was proposed that the conical shape of texture manages the water nuclei to be brought at the top of the structures. As a consequence, in that case, the adhesion energy E_a, that is the energy needed to detach each droplet from the substrate, can be written as:

$$E_\mathrm{a} = \pi r^2 \gamma \sin^2\theta_r(1+\cos\theta_r)\ , \tag{3.4}$$

where θ_r is the receding angle. Previous studies determined adhesion based on the number of filled cells below each condensed droplet that lies instead in a partial Cassie state and the magnitude of adhesion energy would be much more significant in that scenario, because

of the additional energy needed to create air-water interfaces, as some water remain pinned inside the cells when drops take off the substrate [65, 32]. A water droplet condensing on a conical nanotexture is assumed to be sitting at the top of cones (inset of Figure 2.17). However, the contact line can be inside the texture, which generates adhesion. For droplets with $r \approx 100$ nm, one expects that they sink to a depth of around 70 nm (see Eq. (2.3) in Chap. 2), that is more than half of the cones height ($h = 110$ nm). On the contrary, droplets with $r \approx 1$ μm sink to a depth as low as 10 nm. This sinking depth decreases with increasing radius and varies from 10 to 2 nm as r ranges from 1 to 5 μm. Therefore, adhesion effects must only play a key role for nanodroplets and should not be the main cause of the decrease in mobility at low radius r. The results of next chapter (Chap. 4) confirm this assumption: after varying height and pitch for conical nanotexture, the same threshold and jumping velocites are obtained, which suggests that texture sizes at these scales have a low impact on limiting spontaneous droplet ejection.

Following the expression of the adhesion energy E_a, the corresponding momentum P_a can be written as $P_\mathrm{a} \approx E_\mathrm{a}\,\tau_r/r$, where we remind that τ_r is the retraction time of the merging droplets. Using momentum balance, one gets:

$$2mU = mv - 2P_\mathrm{a} \ , \tag{3.5}$$

where the factor 2 refers to the number of merging droplets, and it modifies the takeoff velocity in:

$$U = \frac{U^*}{4}\left[1 - 6\sin^2\theta_r(1+\cos\theta_r)\right] \ . \tag{3.6}$$

A numerical coefficient of 0.22 corresponds to a receding angle of 154°, a value comparable to the measured angle $\theta_r = 157 \pm 2°$. The calculated value of P_a suggests as well that water adhesion remains marginal in our system. Conversely, the takeoff velocity U of droplets smaller than 5 μm strongly deviates from the dashes in Figure 3.6. In the absence of significant adhesion, we interpret this decrease in mobility by the effect of viscosity. The flow during coalescence generates a dissipative force per droplet $F_\mathrm{v} \approx \eta\,\Delta v\,\Omega$, where η is the viscosity of water and Ω the droplet volume. Since Δv scales as v/r^2, we deduce:

$$F_\mathrm{v} \approx \frac{2\pi\eta}{3}\sqrt{\frac{\gamma r}{\rho}} \ , \tag{3.7}$$

an expression that depends on both viscosity and radius. The resulting loss of momentum $P_\mathrm{v} \approx F_\mathrm{v}\,\tau_r$ is found to be $(4\pi/3)\eta r^2$. For $r \approx 5$ μm and $U \approx 50$ cm/s, the ratio P_v/mU is of order unity and it decreases as $1/\sqrt{r}$, which suggests viscous dissipation as the main cause of loss at microscales. This result qualitatively agrees with numerical simulations that showed that water should be fully immobilized at a scale smaller than 300 nm [60, 64].

Finally, the momentum balance becomes: $2mU = mv - 2P_\mathrm{v} - 2P_\mathrm{a}$. Hence we get a modified expression for the jumping velocity U:

$$U \approx \frac{U^\star}{4}\left[\alpha - 4Oh\right] \ . \tag{3.8}$$

We introduce here the Ohnesorge number $Oh = \eta/(\rho\gamma r)^{1/2}$ and $\alpha = 1 - 6\sin^2\theta_r(1+\cos\theta_r)$ is a numerical coefficient close to unity at large θ_r. It is interesting to note that an energy conservation argument leads to a normalized velocity U/U^* scaling as $\sqrt{1-Oh}$ [63, 62, 70], a power law different from the one obtained with momentum transfer. Eq. (3.8) is drawn in Figure 3.6 (red solid line), where $\alpha \approx 0.93$ is not adjusted, since it corresponds to the measured value $\theta_r = 157°$; yet we use to best fit the data a coefficient 4.9 instead of 4 in front of the Ohnesorge number, which corrects the coefficient calculated with a scaling argument.

We used $\eta = 1.62$ mPa.s, $\rho = 1000$ kg/m^3 and $\gamma = 75.3$ mN/m, all quantities considered for water at 3°C. Eq. (3.8) nicely captures the decrease of the departing velocity for $r \lesssim 5$ μm, *i.e.* for $Oh \gtrsim 0.1$, showing how viscosity affects the inertio-capillary kinetics. In addition, this expression predicts a critical jumping radius of 1 μm and a maximum jumping velocity U for $r \approx 4$ μm, in good agreement with the experiments. For $r \geq 150$ μm, the predicted velocity approaches $U = 0.22\,U^*$, the asymptotic behaviour drawn with a dotted line.

It is worth focusing a little on the momentum balance model. When two drops coalesce, a liquid bridge develops at the contact point due to differences in curvature between the drop (with radius r) and the bridge (with radius r_b). For $Oh < 1$, droplet coalescence is shown to occur in two distinct regimes [71, 72]: first, an inertially limited viscous regime where $r_b = \gamma t/\eta$, followed by an inertial regime where $r_b \sim (\gamma r/\rho)^{1/4}\, t^{1/2}$. Cha *et al.* demonstrated the predominance of the inertial regime, except for $r \lesssim 1$ μm where the viscous regime can represent more than 50% of the total coalescence time [65]. However, the coalescence time τ_r was measured for $r > 3$ μm and the authors found that the capillary-inertial scaling time stills holds. In our momentum balance, we assume that inertial effects dominate the motion. However, at small scale (≈ 1 μm), the Reynolds number $Re = \rho v r/\eta$ being of order unity and the viscous regime being not negligible, one can legitimally assume that viscosity plays a role. We recognize that our approach is a bit simplistic as coalescence is a complicated process but Eq. (3.6) yet manages to provide a good estimation of the jumping velocity and its variation with r. We now consider the case of asymmetric merging, *i.e.* for $r'/r < 0.95$.

3.3.2 Asymmetric merging

Condensing droplets are often asymmetric when they merge, due to the randomness of the condensation process. In Figure 3.7, the takeoff velocity U/U^* is drawn as a function of the degree of symmetry $\varepsilon = r'/r$, for different radii r varying between 2 μm and 22 μm, which makes Ohnesorge number vary between 0.13 and 0.04. We observe that U/U^* is sensitive both to the Ohnesorge number Oh (as expressed by Eq. (3.8)), and to the parameter ε: the larger the asymmetry (that is, the smaller ε), the slower the takeoff. A change in ε by typically 25 % modifies the jumping velocity by a factor 2. Hence, asymmetry impacts the dynamics of jumping much more than adhesion (found in Eq. (3.8) to decrease U by only 7 %). For simplicity here, we first analyze asymmetry effects by taking $\alpha = 1$ (negligible adhesion). In addition, if we also neglect viscosity, we can obtain Eq. (3.3), a prediction drawn with a black dashed line in Figure 3.7. This behavior is found to capture asymptotically the data at large r (black symbols). Smaller droplets are slower, which we understand mostly as a consequence of the viscous dissipation described above. We generalize Eq. (3.8) to the case of asymmetric merging by rewriting the momentum balance as:

$$(m + m')U = m'v' - P'_{\mathrm{v}} - P_{\mathrm{v}} \ , \tag{3.9}$$

using the same notations as previously. On the one hand, one has $P'_{\mathrm{v}} \approx F'_{\mathrm{v}}\tau_{r'}$, where the viscous force $F'_{\mathrm{v}} \approx \eta \Delta v' \Omega'$ is integrated over the small droplet merging time $\tau_{r'}$. On the other hand, we assume $P_{\mathrm{v}} = P'_{\mathrm{v}}$ because the small drop induces fluid motion in the large one at its own scale, as shown in simulations by Eiswirth *et al.* (Figure 3.8) [73]. Hence, we get an analytical expression for the jumping velocity U in an asymmetric configuration:

$$U \approx U^* \left[\frac{\varepsilon^{5/2}}{2(1+\varepsilon^3)} - 2Oh \frac{\varepsilon^2}{1+\varepsilon^3} \right] \ . \tag{3.10}$$

Despite the small size of droplets, the Ohnesorge number $Oh = \eta/(\rho\gamma r)^{1/2}$ remains small (< 0.2), so that U/U^* simply increases with ε at fixed r, and with r at fixed ε, as observed

in Figure 3.7. As asymmetry vanishes ($\varepsilon \to 1$), Eq. (3.10) reduces to Eq. (3.8) (with $\alpha = 1$ since we neglected adhesion). Drawn in Figure 3.7 for three ranges of increasing radii that is, three ranges of Oh (red, blue and black areas), Eq. (3.10) is observed to show a fair agreement with the data.

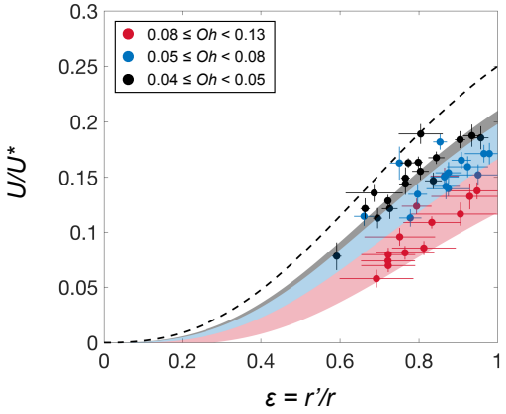

Figure 3.7: Jumping velocity of droplets after an asymmetric coalescence; U is normalized by $U^* = \sqrt{\gamma/\rho r}$ and plotted as a function of the degree of symmetry $\varepsilon = r'/r$. The three sets of data correspond to three ranges for the larger radius: 2 μm $< r \leq$ 5 μm (red) corresponding to $0.08 \leq Oh < 0.13$, 5 μm $< r \leq$ 13 μm (blue) corresponding to $0.05 \leq Oh < 0.08$ and 13 μm $< r \leq$ 22 μm (black) corresponding to $0.04 \leq Oh < 0.05$. The dashed line shows Eq. (3.3) which provides an asymptotical behaviour for the data. Red, blue and black areas show Eq. (3.10) drawn with the corresponding colours for each range of Ohnesorge numbers.

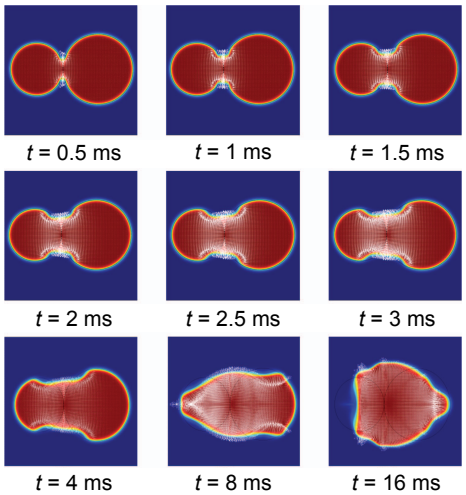

Figure 3.8: Snapshots of a simulated coalescence between two asymmetric drops. Internal motion mainly occurs during the small radius retraction time $\tau_{r'}$ at the scale of the small drop. Extracted from [73].

If we now take into account adhesion in our model and assume that it occurs during each coalesence time $\tau_{r'}$ and τ_r, momentum balance yields:

$$U \approx U^* \left[\frac{\varepsilon^{5/2}}{2(1+\varepsilon^3)} - \frac{3}{2}\sin^2\theta_r(1+\cos\theta_r)\frac{1+\varepsilon^{5/2}}{1+\varepsilon^3} - 2Oh\frac{\varepsilon^2}{1+\varepsilon^3} \right] . \tag{3.11}$$

This law is drawn for the same ranges of radii as for Eq. (3.10) in Figure 3.9. For $\varepsilon = 1$, one recovers Eq. (3.8). The model is found to match relatively well the data except for high radii where it tends to underestimate the normalized jumping velocity.

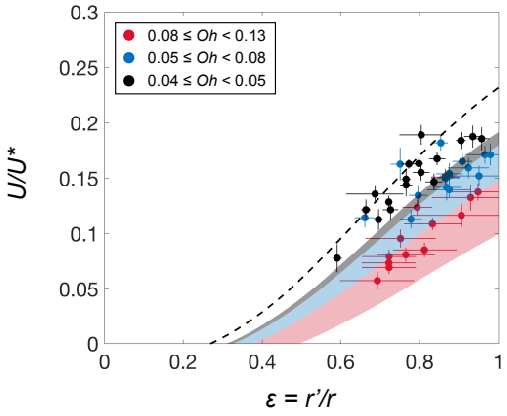

Figure 3.9: Jumping velocity of droplets after an asymmetric coalescence; U is normalized by $U^* = \sqrt{\gamma/\rho r}$ and plotted as a function of the degree of symmetry $\varepsilon = r'/r$. The three sets of data correspond to three ranges for the larger radius as in Figure 3.7. The dashed line shows Eq. (3.3) and red, blue and black areas show Eq. (3.11) drawn with the corresponding colours for each range of Ohnesorge numbers. It provides a good agreement but slightly underestimates the normalized velocities.

3.4 Droplet flight

After takeoff, drops follow quasi-vertical paths until falling back to the substrate. We discuss here the flight of microdrops ($r \leq 17$ μm) formed after coalescence. We denote their radius as $R = (r^3 + r'^3)^{1/3}$ (volume conservation), and we report in Figure 3.10a the temporal evolution of the vertical position $z(t)$ for a drop with radius $R = 12.9 \pm 0.7$ μm departing at $U = 29 \pm 2$ cm/s. The function $z(t)$ is observed to be highly asymmetric. While the ascending phase occupies 20 % of the flight time, the descending phase takes much longer, a consequence of the action of air viscosity at microscales. This friction is also responsible for the modest maximum height ($H = 740$ μm) reached by the drop after less than 6 ms. The Reynolds number in air is $Re = \rho_a U R/\eta_a$, with U the jumping velocity, ρ_a and η_a the air density and viscosity. At microscales, Re is smaller than unity and Stokes drag $F = 6\pi\eta_a R\dot{z}$ is the main source of friction [60]. Hence, the successive phases of rise and descent can be expressed by a balance between drag, inertia and gravity and using Newton's first law, one obtains an equation for the speed $\dot{z}$:

$$M\frac{\mathrm{d}\dot{z}}{\mathrm{d}t} = -6\pi\eta_a R\dot{z} - Mg , \tag{3.12}$$

where $M = (4\pi/3)\rho R^3$ is the drop mass. Integrating Eq. (3.12) yields the speed $\dot{z}$ as a function of time t:

$$\dot{z}(t) = (U + g\tau_a)e^{-t/\tau_a} - g\tau_a \ , \tag{3.13}$$

where the braking time τ_a is equal to:

$$\tau_a = \frac{2}{9}\frac{\rho R^2}{\eta_a} \ . \tag{3.14}$$

Microdrops ballistics markedly differs from that of drops larger than 100 μm. For these, the drag force becomes negligible compared to weight, which classically yields the parabolic motion resulting from a balance between inertia and gravity: $z(t) = -gt^2/2 + Ut$. Figure 3.10b shows it for a drop with radius $R = 287 \pm 3$ μm departing at $U = 11 \pm 2$ cm/s, together with its parabolic fit drawn in red.

We can estimate the threshold for which the trajectory transfers from a "Tartaglia" (Figure 3.10a) to a parabola (Figure 3.10b). As evidenced by Cohen and Clanet [74, 75], the ratio of the drag force over weight scales as U/U_∞ where $U_\infty = (2/9)\rho g R^2/\eta_a$. If $U > U_\infty$, the trajectory is a Tartaglia, while for $U < U_\infty$ it becomes a parabolic motion. The threshold radius R_t, that governs the transition between the two regimes, is obtained after taking $U = U_\infty$. Besides, as we consider radii larger than 5 μm, the jumping velocity U can be approximated as the inertio-capillary velocity $U = \alpha U^\star/4$, where $\alpha \approx 0.93$ (Eq. (3.8)). The threshold radius R_t finally reads:

$$R_t = \left(\frac{9 \times 2^{1/6}}{8}\frac{\alpha\eta_a\gamma^{1/2}}{\rho^{3/2}g}\right)^{2/5} \ . \tag{3.15}$$

The threshold radius is found on the order of 50 μm, a value larger than the jumping drops radii where $R \lesssim 30$ μm, hence all condensed drops that take off from our material follow a Tartaglia trajectory.

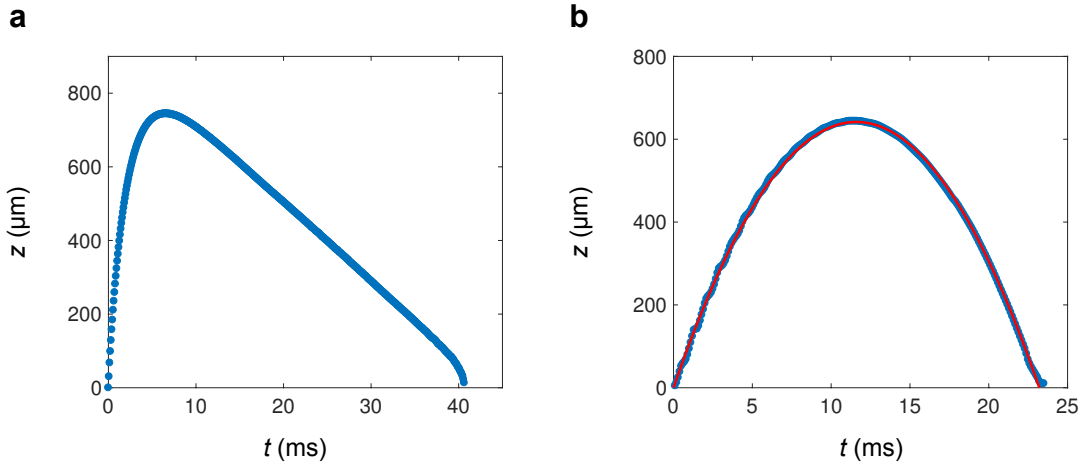

Figure 3.10: (a) Vertical trajectory $z(t)$ of a drop with radius $R = 12.9 \pm 0.7$ μm after its ejection at a velocity $U = 29 \pm 2$ cm/s. (b) Same plot for a drop with radius $R = 287 \pm 3$ μm departing at $U = 11 \pm 2$ cm/s. The function $z(t)$ is nicely fitted by a parabola (red solid line).

Furthermore, at small time, Eq. (3.13) reduces to $\dot{z}(t) = Ue^{-t/\tau_a}$, as indeed observed in Figure 3.11a and in its inset, where the line shows an exponential decrease with $\tau_a = 1.8$ ms,

comparable to the expected value of this braking time given by Eq. (3.14): 2 ms for $R = 13$ μm. The measured braking time τ_a is plotted with radius R in Figure 3.11b and found to be well described by the expected parabolic behaviour (Eq. (3.14)), drawn with a dashed line without any adjustable parameters. At later times ($t \gg \tau_a$), Eq. (3.13) predicts a constant descent velocity $\dot{z}(t) = -g\tau_a$, as observed in Figure 3.11a and stressed by a dashed line. For this particular example, we measure an absolute descent velocity of 2.1 $\pm$ 0.1 cm/s, close to the prediction $g\tau_a = 2$ cm/s. One can also note that the drop accelerates during the last milliseconds of its descent, contacting the substrate at a velocity of 4.5 cm/s. Similar accelerations were recently reported by Miljkovic *et al.* and attributed to electrostatic effects [76]. This surprising observation will be further discussed in Sec. 3.6.

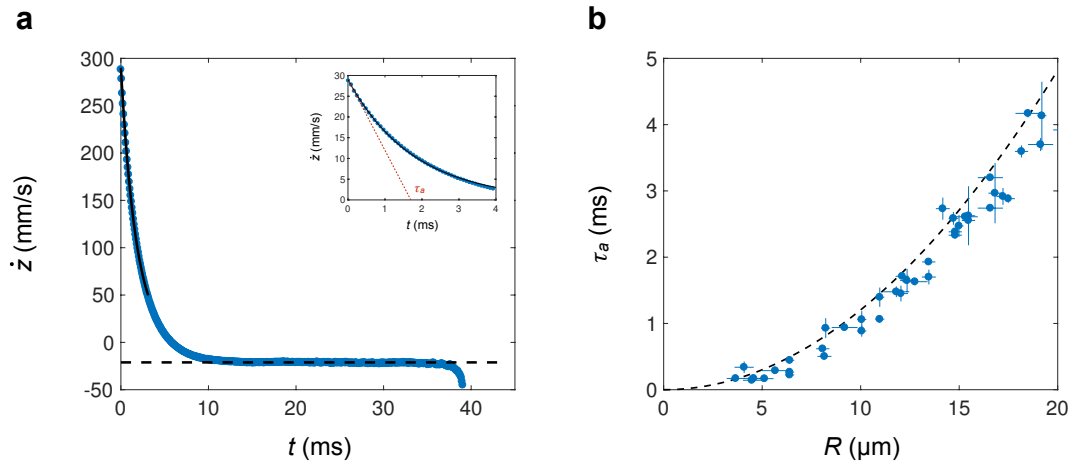

Figure 3.11: (a) Velocity $\dot{z}$ of a drop with radius $R = 12.9 \pm 0.7$ μm as a function of time t. The jumping velocity is $U = 29 \pm 2$ cm/s. $\dot{z}$ decreases with time and fits with an exponential (solid black line in the inset). (b) Measured braking time τ_a as a function of drop radius R. The black dashed line shows the theoretical braking time τ_a given by Stokes drag, $\tau_a = (2/9)\rho R^2/\eta_a$, $\eta_a = 1.84 \times 10^{-5}$ Pa.s at $T = 25$°C.

From our observations, we can also extract a useful, practical quantity, namely the maximum height H reached by the drop and plotted in Figure 3.12a [77, 78, 79]. Integrating Eq. (3.13) yields $z(t) = \tau_a(U + g\tau_a)(1 - e^{-t/\tau_a}) - g\tau_a t$, whose maximum is:

$$H = U\tau_a - g\tau_a^2 \ln(1 + \frac{U}{g\tau_a}) \ . \tag{3.16}$$

The main parameter in the latter equation is the radius R, both contained in the departing velocity U (Eq. (3.8)) and in the braking time τ_a (Eq. (3.14)). At microscales, τ_a is small so that H increases with R, as $R^{3/2}$. Eq. (3.16) predicts that $H(R)$ reaches a maximum around $R \approx 50$ μm, a size larger than that of condensing drops. Drawn with a dashed line in Figure 3.12a without adjustable parameter, Eq. (3.16) nicely describes the data. In the presence of a wind, in the range of 1-10 m/s, the air boundary layer, at a centimeter size L from the edge of the solid surface expelling dew, has a thickness δ of about 0.1-1 mm (using $\delta \sim L/\sqrt{Re}$), showing that most drops can escape this layer and be entrained by the wind - an interesting property if the substrate is horizontal for avoiding the redeposition of dew. For vertical substrates, H is the typical distance of ejection, after which droplets can fall under the action of gravity.

On descent, drops quickly reach their terminal velocity V, plotted in Figure 3.12b as a function of the radius R and compared with the prediction $V = g\tau_a$ (dashed line). The fit is convincing except at small radius ($R \leq 8$ μm) where V can be as much as ten times

larger than predicted. This discrepancy may originate from a charge effect [76] adding an electrostatic attractive contribution to the force balance, which is dominant at small substrate distances (*i.e.* at small R). This supplementary attraction is found to become significant at a distance of about 200 μm, which corresponds (in Figure 3.12a) to a radius of about 7.5 μm, the size below which the gravitational prediction does not apply.

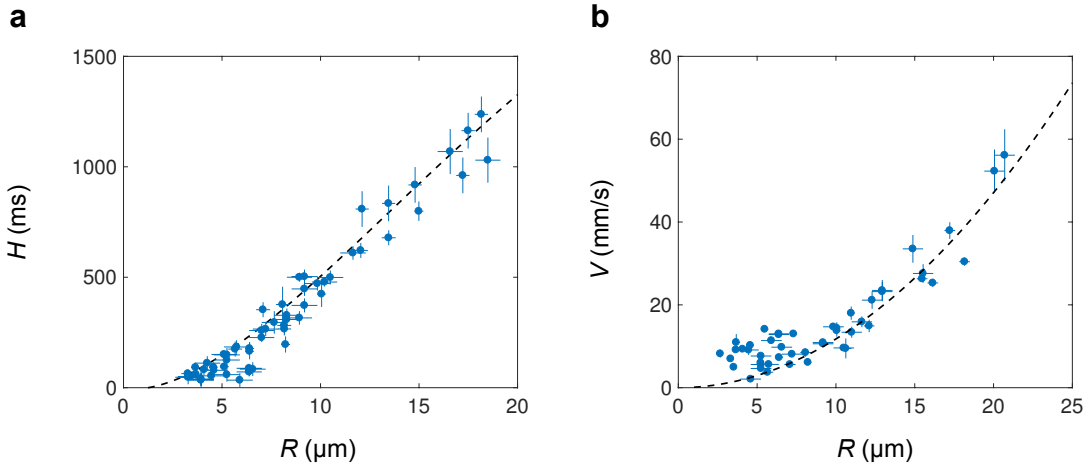

Figure 3.12: (a) Maximum measured height H reached during flight as a function of radius R. The dashed line represents the theoretical height $H = U\tau_a - g\tau_a^2 \ln(1 + U/g\tau_a)$ (Eq. (3.16)). (b) Absolute terminal velocity V as a function of radius R. The dashed line corresponds to the velocity given by the equilibrium between gravity and Stokes drag, $V = (2/9)\rho g R^2/\eta_a$.

3.5 Droplet landing

Droplets finally return to the substrate, which they impact at the velocity V. We study the landing for both condensed drops (2.7 μm $\leq R \leq$ 22.7 μm and 2 cm/s $\leq V \leq$ 15 cm/s) and water sprayed onto the surface using a water atomizer (25 μm $\leq R \leq$ 160 μm and 2 cm/s $\leq V \leq$ 100 cm/s), and report in Figure 3.13 the behaviour of drops after impact: either they bounce (green data), as expected on a repellent material, or they stick (red data split between sprayed (squares) and condensed droplets (empty circles)). Only drops with large size R and velocity V are observed to bounce. Conversely, none of the droplets formed by condensation get reflected by the material from which they were ejected: dew repellency is found to be more demanding than dew ejection, which we now comment.

Our experiments probe the very unusual situation of microdrops impacting a solid at a small velocity (red circles). The corresponding Reynolds number $Re = \rho RV/\eta$ is of order unity or even smaller. Therefore, even in the limit of a strictly non-adhesive material ($\theta_r = 180°$), drops should stick when the viscous dissipation at impact exceeds the kinetic energy. $Re = 1$ provides the threshold V_l above which we leave this regime:

$$V_l = \eta/\rho R \ . \tag{3.17}$$

This frontier is marked with a dashed line in Figure 3.13 and it is found to enclose all the data for dew. Being above this dashed line does not guarantee bouncing either. The Weber number $We = \rho V^2 R/\gamma$ controlling liquid deformation at impact in this domain remains modest, on the order of 0.1. Hence, for the sake of simplicity, we consider that impacting water contacts the substrate with a radius of order R, with a contact line dissipation of order $\pi R^2 \gamma(1 + \cos\theta_r)$. Drops will stick if this quantity exceeds the kinetic energy at impact

$2\pi R^3 \rho V^2/3$. The balance between these two energies yields a minimum velocity V^* required for repellency:

$$V^* \approx \sqrt{\frac{3\gamma}{2\rho R}(1+\cos\theta_r)}\ . \tag{3.18}$$

Drawn with a solid line in Figure 3.13, Eq. (3.18) nicely captures the frontier between bouncing and sticking. More generally, if we model the behaviour of droplets after ejection using Eq. (3.13), we find $g\tau_a > V^*$ as a criterion for bouncing. Both the dependencies of τ_a and V^* with R being known, we deduce a minimum radius R^* for bouncing:

$$R^* = \left[\frac{243}{8}\,\frac{\eta_a^2\,\gamma\,(1+\cos\theta_r)}{\rho^3 g^2}\right]^{1/5}\ . \tag{3.19}$$

This quantity is found around 60 μm. Such drops are larger than that obtained after condensation, which confirms the unability of condensed drops to bounce. It may seem surprising that an antifogging surface is unable to reflect the water ejected from it, but this is mainly a consequence of their slowness at impact. The only possibility for such a drop to bounce is to meet another one at impact [80, 81].

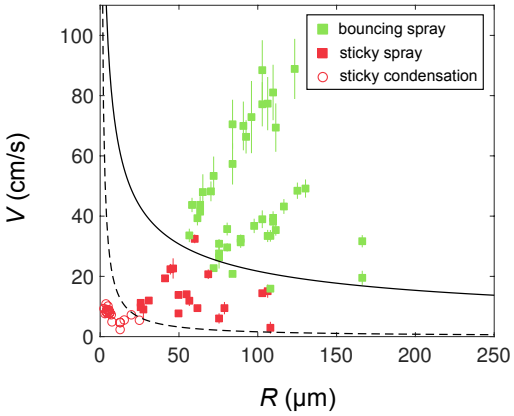

Figure 3.13: **Phase diagram of droplets at landing.** The drop radius and velocity are denoted as R and V. Green color indicates bouncing and red color indicates sticking. Dots and squares mean that drops are made from condensation or from a spray, respectively. The solid line expresses the balance between adhesion and inertia (Eq. (3.18)). The dashed line represents the threshold of bouncing dictated by viscosity, $V_l \approx \eta/\rho R$ (Eq. (3.17)).

3.6 Extensions

3.6.1 Jumping velocity

Two effects were proposed to account for the decrease of the jumping velocity U for drop radii below 5 μm: adhesion and viscous effects. Our model suggests that adhesion remains marginal because condensed droplets are in Cassie state. However, as suggested in Chap. 2, droplets with $r \lesssim 1$ μm can sink deeply inside the structures, which decreases their apparent advancing angle. One could imagine the same scenario for the receding angle θ_r and assume that it varies with r. Using our model for the advancing angle (see Eq. (2.4) in Chap. 2), we assume the same evolution for θ_r and first take a constant contact angle hysteresis $\Delta\theta$ with r, $\Delta\theta = 10°$, the one measured on millimetric drops. For this configuration, θ_r is plotted in

green solid line in Figure 3.14a along with θ_a (black solid line). We also take the maximum values $\theta_a = 167°$ and $\theta_r = 157°$ when the computed values are above these values, that is for $r > 650$ nm.

Considering only adhesion, we plot in green solid line in Figure 3.14b the jumping velocity $U = (U^\star/4)\left[1 - 6\sin^2\theta_r(1+\cos\theta_r)\right]$ (Eq. (3.6)) with $\theta_r = f(r)$ as a function of drop radius r. The model is confronted with the experimental data (blue dots), the model with viscosity and adhesion (Eq. (3.8), red dotted line) and Eq. (3.6) (constant $\theta_r = 157°$, black dotted line). The new model captures the decrease of U below a threshold radius but predicts no jumping for $r \leq 200$ nm, far from the observed data largely overestimates U for 400 nm $< r <$ 5 μm.

One can instead assume that $\Delta\theta$ is not constant with r but grows higher when r decreases. It yields a receding angle plotted in Figure 3.14a in red solid line, which maximum value is also $\theta_r = 157°$. This model, along with Eq. (3.6), is drawn in red solid line in Figure 3.14b. Again, it predicts a cutoff radius of 450 nm, much lower than the observed one of 1 μm and does not capture the evolution of U with r. These two models suggest that viscosity must play a significant role in jumping-droplet dynamics for droplets condensing on nanocones.

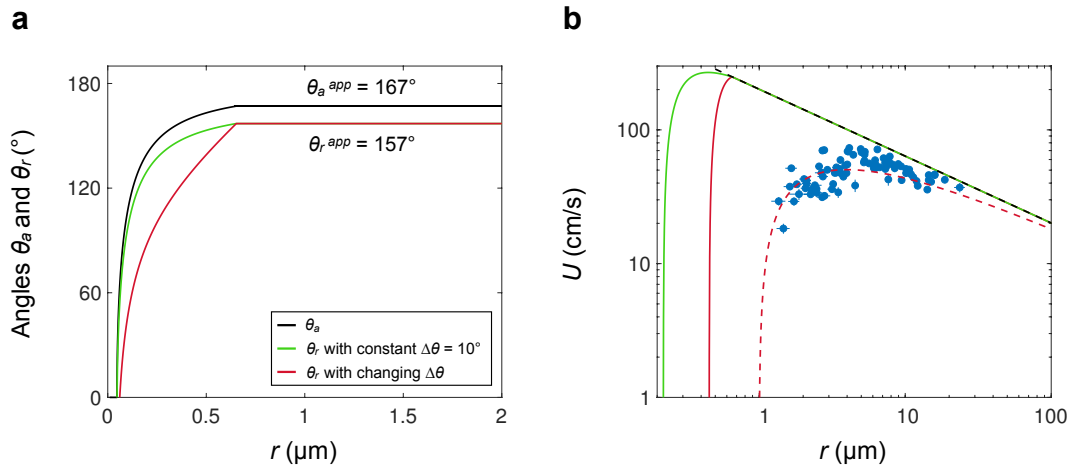

Figure 3.14: (a) Evolution of the advancing θ_a and receding angles θ_r with drop radius r on sample N1. The black solid line shows θ_a given by Eq. (2.4) (see Chap. 2) and drawn with the N1 parameters. Its maximum value is the angle measured on millimetric drops, $\theta_a = 167°$. The green solid line denotes the receding angle θ_r given by Eq. (2.4) and lowered by a constant contact angle hysteresis $\Delta\theta = 10°$. Finally, the red solid line is θ_r with a changing $\Delta\theta$: it decreases with r and reaches 10° for $r > 650$ nm when θ_r equals 157°. In both models, the maximum value of θ_r is 157°. (b) Velocity U for symmetric coalescence ($\varepsilon > 0.95$) as a function of the radius r of the two merging drops. Black dashes correspond to $U = 0.22\,U^*$, denoting $U^* = \sqrt{\gamma/\rho r}$. The red dotted line shows the velocity $U = (U^*/4)\,[\alpha - 4.9\,Oh]$ where $\alpha = 1 - 6\sin^2\theta_r(1+\cos\theta_r)$ and $Oh = \eta/\sqrt{\rho\gamma r}$ is the Ohnesorge number with η the water viscosity. The green and red solid lines present the velocity $U = \alpha(r)U^*/4$ with $\theta_r(r)$ given in (a). Both models do not capture correctly the evolution of U with r.

3.6.2 Self-propulsion of water-glycerol drops

To further illustrate the influence of viscous dissipation, we have considered the coalescence of deposited water-glycerol drops on our material. Varying the percentage of glycerol increases the viscosity while keeping roughly constant the surface tension, hence

superhydrophobicity is preserved even at high glycerol concentration. We consider two water-glycerol mixtures: one has viscosity $\eta = 11$ mPa.s and density $\rho = 1150$ kg/m^3, while the second $\eta = 22$ mPa.s and density $\rho = 1180$ kg/m^3. We perform the same experiments as for our large drops (see Sec. 3.2) where two drops are deposited using glass needles. Figure 3.15a shows the normalized velocity $U/U^\star$ as a function of the asymmetry ratio ε for three large drop radii r and $\eta = 11$ mPa.s. For these ranges, one has $0.05 < Oh < 0.06$ and Eq. (3.10) agrees well with the data. The normalized velocity is also displayed for a large drop radius $r = 520$ μm and the two viscosities: Oh is up to 0.11, in the same range as the ones measured on our small radii during condensation ($r < 5$ μm). Again, Eq. (3.10) manages to capture the evolution of the normalized velocity with the Ohnesorge number Oh. However, a more thorough study would be necessary to check the minimum jumping radius as a function of the Ohnesorge number for different viscosities.

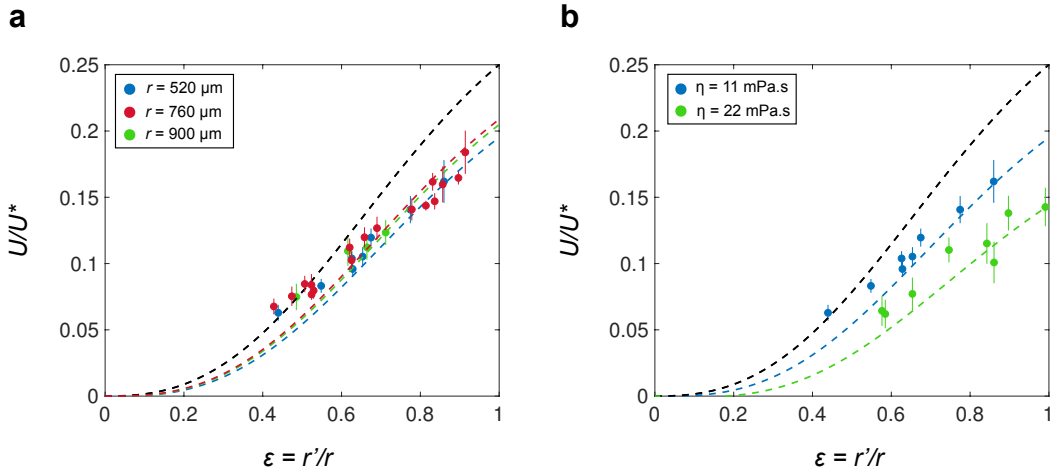

Figure 3.15: (a) Normalized jumping velocity of droplets after an asymmetric coalescence for water-glycerol mixtures; U is normalized by $U^* = \sqrt{\gamma/\rho r}$ and plotted as a function of the degree of symmetry $\varepsilon = r'/r$. The viscosity of the mixture is $\eta = 11$ mPa.s. The three sets of data correspond to three values of the large radius: $r = 520$ μm (blue), $r = 760$ μm (red) and $r = 900$ μm (green). The dashed line displays Eq. (3.3) which provides an asymptotical behaviour for the data. Blue, red and green dotted lines show Eq. (3.10). (b) Normalized jumping velocity $U/U^\star$ as a function of $\varepsilon = r'/r$ for two water glycerol mixtures and large drop radius $r = 520$ μm: $\eta = 11$ mPa.s (blue data) and $\eta = 22$ mPa.s (green data). Blue and green dotted lines show Eq. (3.10) drawn with the corresponding Ohnesorgue numbers and they are observed to nicely fit the data.

3.6.3 Droplet flight

3.6.3.1 Final droplet acceleration

Figure 3.12b reports, for $R < 8$ μm, values of terminal velocities V much larger than the ones predicted by the balance between drag and gravity ($V = g\tau_a$). Similarly, for even larger drops, the final phase of descent is the stage of a sudden acceleration, as displayed in Figure 3.11a. In the presence of water, hydrophobic surfaces tend to absorb the ions OH^- in the immobile Stern layer and form a electrical double layer in the fluid (Figure 3.16) [82, 83]. It implies then that most hydrophobic coatings have a negative zeta potential, that is the electrical potential at the plane of shear between the Stern and the Gouy-Chapman layers (Figure 3.16). Miljkovic *et al.* first reported the acceleration of jumping droplets at landing [76]. By showing that the time required for a mobile OH^- anion to transport to

the bulk liquid droplet during coalescence is much larger than the coalescence time between two droplets, they evidenced a gained positive charge for the jumping droplet. Hence, at its descent, the falling droplet will be accelerated in the presence of the zeta potential. Another explanation for the acceleration might lie in the electrical properties of water. The permittivity of a medium represents how an electric field influences the organization of electric charges in it. The dielectric constant of water ε_r being significant ($\varepsilon_r = 81$), before touching the substrate, the droplet may be affected by the zeta potential and charge migration could occur: a dipole could then be created in the landing droplet, which could generate an electrical attractive force during its descent.

3.6.3.2 Cunningham slip correction

For small droplets ($R < 10$ μm), air could not be considered as a continuous medium and Stokes drag is modified. One must then compare the mean free path λ of the gas molecules and the droplet diameter $d = 2R$ using the Knudsen number $Kn = \lambda/2R$. Assuming that air is an ideal gas, one has $\lambda = k_B T/\sqrt{2}\pi d^2 P$, where k_B is the Boltzmann constant, T the outside temperature and P the saturated pressure. For $R \approx 2$ μm, one finds $\lambda \approx 80$ nm and $Kn \ll 1$. The drag force is divided by the Cunningham correction factor C that depends directly on Kn. In our case, C is roughly equal to 1 [84], hence no modification in the Stokes force expression.

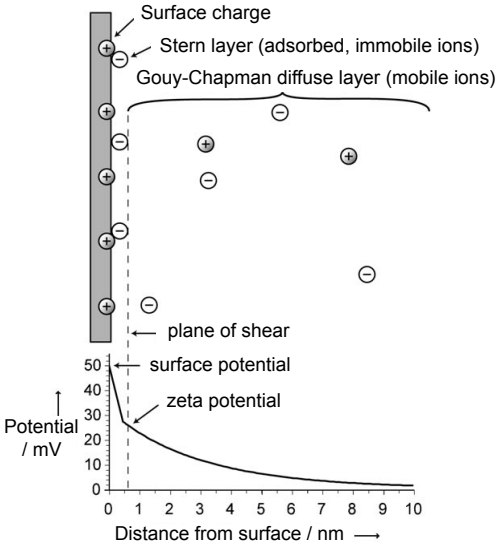

Figure 3.16: Schematic of the interface between a charged solid and an aqueous solution and calculated average electrostatic potential with respect to the distance from surface. Extracted from [82].

Take home message of Chapter 3

1. Jumping velocity. On a conical nanotexture, microdroplets condensing on the substrate can take advantage from coalescence to jump off the material. Their jumping speed is found non-monotonic with the drop size, showing a maximum around 5 μm and scales with the inertio-capillary velocity above this size.

2. Adhesion and viscous effects. For radii smaller than 5 μm, the jumping velocity decreases until 1 μm where it is found null. Viscous dissipation during coalescence and adhesion impede the motion and the evolution of the jumping velocity with droplet radius can be understood by considering these two effects.

3. Ballistics. After jumping, microdrops ballistics is governed by an equilibrium between inertia, gravity and viscous drag. Their trajectory is a "Tartaglia" one and upon their return to the substrate, retakeoff is suprisingly found to be nearly unachievable despite the extreme non-wettability of the material.

4

Antifogging abilities

Materials covered with hydrophobic nanocones have recently been shown to exhibit remarkable antifogging abilities. A systematic study is developed here to understand the influence of texture sizes on antifogging properties. We present the results of condensation experiments on two families of nanocones, either homothetic or having a constant pitch, which enables us to confirm previous assumptions. We then consider the case of micrometric cones and propose a model to understand how antifogging characteristics are modified on such texture. Finally, we present the intermediate case of nanometric truncated cones.

Condensation on a mosquito. Its eyes remain dry compared to the rest of the body. Source: [34].

Contents

This chapter is the result of my collaboration with colleagues from University College London, Thales Research & Technology and my friend Timothée Mouterde. Once again, I thank all of them.

4.1 Introduction

Spontaneous jumping of condensing droplets has recently been found to be a promising solution for antifogging [33, 78, 79], among many other applications. To promote self-propulsion, drops formed by condensation must lie in a highly non-wetting state, namely the Cassie (or partial Cassie) state, in order to exhibit large contact angles, a necessary condition for taking off [54]. As stated in Chap. 1, Enright *et al.* recently discovered that these states can be achieved under two conditions: (1) the Cassie state must be energetically favorable compared to the Wenzel state and (2) the mean separation distance between nuclei must be smaller than the features' spacing [29]. These two conditions are statisfied when using nanostructures, hence the willingness to use features smaller than 100 nm [85, 30, 29, 54]. A central parameter in jumping-droplet condensation is the critical jumping radius r_c, that is, the radius above which most droplets jump: a surface will be all the more antifogging as r_c is small. Recent studies on nanopillar-textured surfaces proposed models to predict r_c, based on the number of wetted cells under the growing condensing droplet [29, 32]: this structures' shape indeed favours a partial Cassie morphology where a constant number of cells are filled with water. The authors showed that r_c is surface dependent as the pinned radius of droplet is directly proportional to the feature spacing p.

The recent discovery of the exceptional antifogging ability of materials textured with nanocones has opened a new path for the design of antifogging materials [86, 36]. Compared to pillars, where the proportion of ejected droplets was found to be at most 30% [37], more than 90% of droplets are ejected on substrates textured with nanospikes [36]. This remarkable antifogging ability is assumed to originate from the conical shape of texture that may promote a Cassie state, even at small drop size, as evidenced by ESEM experiments (Chap. 2). Yet, a systematic study is required to understand the relation of r_c with texture sizes, as well as the proportion of ejected drops. We have proposed in Chap. 3 a model based on adhesion and viscosity to predict r_c on material N1; yet more surfaces need to be tested. Thus, to further our understanding, we now study condensation on different nanostructures with same pitch p or same height h.

Previous reports on surfaces covered with pillars concern highly disordered samples, making difficult the understanding of the influence of each parameter (pitch, height) on the antifogging efficiency [29, 32]. Our samples N1-7 have instead either the same pitch p (N3-7) or are homothetic (same aspect ratio h/p or cone angle β) such as N1, N2 and N5. We first present the results of condensation experiments performed on these surfaces. Furthermore, we complement our study with larger features, at a micrometric scale (M1-3, Table 2.1 in Chap. 2). Finally, it is known that cone-textured surfaces exhibit small contact angle hysteresis because pinning is reduced, unlike on pillar-textured ones where it can be significant owing to the pinning on the pillar tops. We study here the intermediate case of truncated cones (NT1-3, Table 2.2) with pitch equal to 110 nm (same as samples N3-7). Therefore, our study enables us to perform experiments on cones with pitches of two orders of magnitude difference, ranging from 50 nm to 2.4 μm, and possibly truncated.

4.2 Experimental set-up

4.2.1 Principle of the experiment

To observe condensation, samples are placed upside down on a Peltier module and brought to a temperature below the dew point (Figure 4.1) [1]. We observe the breath figures using an inverted microscope (Nikon Eclipse Ti-U) with a camera attached to it (Hamamatsu C11440). To have comparable experiments, the supersaturation S (ratio between vapour pressure at laboratory temperature and saturated vapour pressure at surface

temperature) is kept constant for all experiments, at a value $S = 1.6 \pm 0.2$. The experiment lasts 30 minutes and images, with a size of 700 μm $\times$ 700 μm, are recorded every 2 seconds. The long duration of the experiment provides a quantitative study on the condensation process. We use the algorithm developed in [1]: taking the difference between two successive images enables to distinguish if a coalescence is followed, or not, by a jump. Using this automated treatment, statistics are made possible on a large number of coalescences (few thousands) over 30 minutes. To quantify the antifogging ability of a material, Mouterde examined different quantities [1]: the jumping rate (number of ejected drops over the number of coalescences), the jumping rate for symmetric coalescences as a function of the mean radius of the merging drops and the area covered by water. To compare our different substrates, we will again resort to these three metrics.

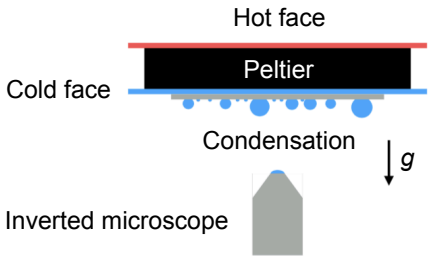

Figure 4.1: Schematic of the experiment: a sample is placed upside down on a Peltier. Subsequent cooling generates condensation, which is imaged by an optical microscope. Adapted from [1].

Because of the orientation of the sample (upside down), gravity prevents self-propelled drops from returning to the surface, which could hinder imaging. However, it may detach droplets (with radius r) and one should compare its magnitude to the one induced by adhesion [1]. We can introduce the Bond number Bo that compares the two effects:

$$Bo \sim \frac{\rho g r^2}{\gamma \sin\theta_a (\cos\theta_r - \cos\theta_a)} \ . \tag{4.1}$$

Bo is maximum for large droplets and the maximum radius is found around 100 μm. Our surfaces exhibiting advancing and receding angles of $\theta_a \approx 165°$ and $\theta_r \approx 150°$, respectively, one finds $Bo \approx 0.1$. Hence, gravity can be neglected.

4.3 Nanometric cones

4.3.1 Surface characterization

We first focus on nanometric cones (Family N). Their corresponding receding and advancing contact angles after a hydrophobic treatment (Chap. 2) are shown in Table 4.1. Almost all surfaces, except N3, exhibit high contact angles with low hysteresis ($\theta_a - \theta_r$), a manifestation of their superhydrophobicity. For surfaces with an equal pitch (N4-7), similar advancing angles are observed, while the receding angle varies. Cones on surface N7 have not a perfect tip (Figure 2.10), which may increase pinning and lower the receding angle. Conversely, surfaces N4-6 have an identical cone shape but different heights - the higher they are, the larger the receding angle. Increasing the height h decreases the area fraction of liquid on solid for a drop lying on the top of the cones (see Chap. 2). A lower contact tends to increase the receding angle, which explains why N6 has the largest observed θ_r.

Sample	Advancing contact angle θ_a (°)	Receding contact angle θ_r (°)
N1	167 ± 2	157 ± 2
N2	166 ± 2	154 ± 2
N3	132 ± 3	23 ± 5
N4	167.5 ± 2	153 ± 2
N5	168.5 ± 1	159 ± 1
N6	166.5 ± 1	160.5 ± 1
N7	164 ± 2	153 ± 2

Table 4.1: Contact angles of water on the N family.

Furthermore, the low advancing and receding angles of surface N3 indicate that water is in Wenzel state. Its cone angle ($\beta = 57.1°$) is very close to the critical angle given by Eq. (1.11), $\beta_c = 2\theta_0 - \pi = 60 \pm 2°$, which could explain this behaviour (see Chap. 1). In that case, the force exerted by the solid on the contact is oriented downwards, which pushes the liquid into the texture, that is, in a Wenzel morphology. To probe the influence of texture sizes on antifogging ability, two parameters can be examined: the influence of cones' height h and pitch p. We first focus on the influence of size keeping the aspect ratio h/p constant.

4

4.3.2 Homothetic structures

4.3.2.1 Materials used

Samples N1, N2 and N5 have a similar aperture angle $\beta = 25 \pm 1.5°$, *i.e* h/p is constant (Table 2.1), and their SEM images are shown in Figure 4.2. Their respective pitches are $p = 52$, 56 and 110 nm and they have comparable θ_a and θ_r (Table 4.1). The corresponding cone heights h are $h = 115$, 133 and 250 nm.

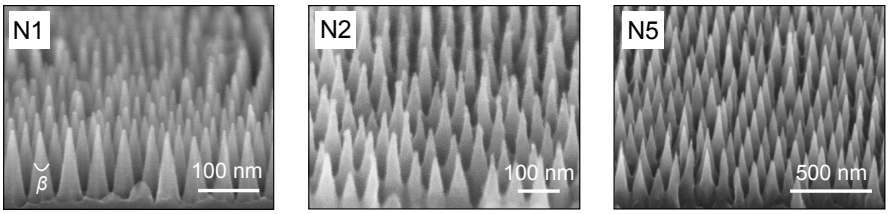

Figure 4.2: SEM images of the homothetic samples N1 (a), N2 (b) and N5 (c).

4.3.2.2 Evolution of the breath figures

Figure 4.3 shows the breath figures obtained at different times on the three samples. At short time ($t = 20$ s), all substrates are similarly covered by microdroplets (radius ~ 5 μm and nucleation density $n \approx 10^{-3}$ μm^{-2}), albeit N5 has a slightly larger n. They later behave identically: after 5 min, they show only a few of intermediate size ($r \sim 15$ μm) and new generation of microdroplets ($r \sim 5$ μm). For all structures, growing droplets coalescing with their neighbours can jump off the surface, which results in similar breath figures with time and area fraction covered by droplets ϕ: $\phi \approx 35 \pm 3\%$, a suprising and unexpected observation because of the differences in texture size between surfaces.

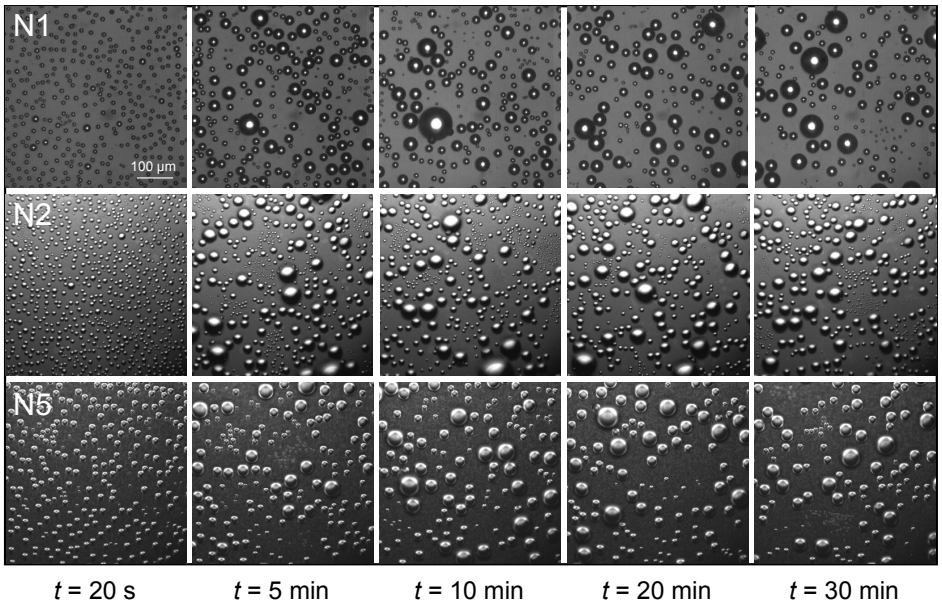

Figure 4.3: Breath figures on samples N1, N2 and N5 under an optical microscope after 20 s, 5 min, 10 min, 20 min and 30 min. The room temperature is $T = 21 \pm 1°C$, relative humidity $RH = 52 \pm 2\%$ and sample temperature is $T_s = 4 \pm 1°C$, which corresponds to a supersaturation $S = 1.6 \pm 0.2$. We recall that S is the ratio between vapour pressure at laboratory temperature T and saturated vapour pressure at surface temperature T_s.

4.3.2.3 Antifogging ability

Jumping rate

We quantify the antifogging efficiency of a substrate by measuring the proportion N of drops jumping after coalescence. N is defined as the number of jumps over the total number of coalescences. This analysis is performed over 30 minutes in an area of 700 μm $\times$ 700 μm for samples N2 and N5 and 760 μm $\times$ 760 μm for sample N1 (two different microscopes were used because N1 was first studied in [1]). N is plotted as a function of time t in Figure 4.4a for the three samples and each point is obtained after averaging the proportion of jumps over one minute. For all materials, N is high and found constant in time, which reveals a good stability of the antifogging properties, and nearly equal between the three homothetic surfaces. Yet, small differences can be noticed between the three samples: N have mean values of 90, 88 and 84 % for the corresponding samples N1, N2 and N5. N1 was the first ever reported antifogging material (with such a high N) [36] but homothetic samples (with larger dimensions) can also equal its performances. It is worth noting that the same experiment on surface A, that is on nanopillars with same pitch as N1, yields $N \approx 0.2\%$ (see Figure 1.13 in Chap. 1), which stresses the paramount importance of having conical structures.

Symmetric coalescences

To complement the comparison between surfaces, one can look at the symmetric coalescences between two drops. Denoting, as in Chap. 3, the radii of the two drops as r' and r ($r' < r$), we consider the case where $r'/r > 0.8$. Figure 4.4b displays the jumping rate N as a function of $<r>$, where $<r>$ is the common radius of the two drops ($<r> = (r' + r)/2$). Antifogging is found to keep its full efficiency ($N \approx 99\%$) in a very broad range of radii (from ~ 3 μm to 30 μm), which confirms that the 10-15 % probability of having no jump in Figure 4.4a is mostly due to the size contrast between merging drops. For the three samples,

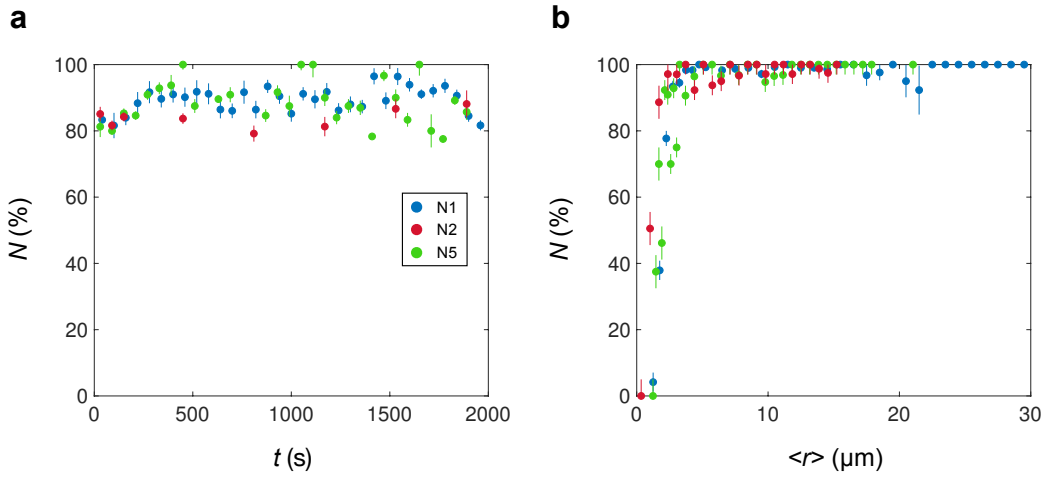

Figure 4.4: (a) Time evolution of the percentage N of coalescences resulting in droplet jumps for the homothetic family: samples N1 (blue data), N2 (red data) and N5 (green data). Each point is obtained after averaging the proportion of jumps over one minute. (b) Antifogging ability N as a function of $<r>$, the common radius ($r'/r > 0.8$) of coalescing drops. For the three samples, N reaches a constant value of 99% independent of $<r>$, down to a sharp cutoff value $r \approx 1$ μm that hardly varies between the samples.

N exhibits a sharp fall as $<r>$ decreases, reaching 0% for $<r> \approx 1.0 \pm 0.3$ μm, in accordance with the minimum jumping radius $r_m \approx 1$ μm measured on surface N1 (see Chap. 3). The three data sets remarkably collapse on the same curve, despite the texture differences. A sudden decrease of N at small r defines a threshold radius r_c for departing. Quantifying r_c as the radius at which $N = 50\%$, we measure $r_c = 1.8 \pm 0.2$ μm, 1.0 ± 0.3 μm and 1.6 ± 0.3 μm for the respective homothetic samples N1, N2 and N5. Again, this quantity varies little with texture size and no direct correlation can be found between r_c and p. The cutoff radius r_c can be used as a metric of water mobility on textures: the smaller r_c, the more fog-repellent the material. Besides, the three measured values of r_c are really small, which confirms the extreme mobility of droplets on nanocones, even at a microscale.

4.3.2.4 Macroscopic effects

One more parameter can be examined to probe the antifogging ability of a texture, that is the area fraction ϕ covered with water. It mainly defines the optical properties of a surface: the larger ϕ, the larger the area where light will be deviated by water [1]. For the three samples, we can measure ϕ as a function of time t (Figure 4.5). At small time, ϕ is the same for the homothetic family and it increases with time, albeit a bit higher for N2 because of its higher nucleation density. After growing, ϕ stabilizes around a constant value that hardly differs between the three surfaces: $\phi = 30$, 31 and 36 % for samples N1, N2 and N5, respectively. Again, the non-monotonic evolution of ϕ with the pitch p does not enable us to determine a possible influence of the texture size.

At the beginning of the experiment, drops have small radii and their individual growth is dictated by condensation, which leads to $r \approx at^{1/3}$ [87]. For surface N1, the parameter a was found to be equal to 3 μm.s$^{-1/3}$ [1]. This first phase ends when individual drops can contact each other, that is, when r becomes equal to the half of the mean distance l between nuclei, $l \sim 1/2\sqrt{n}$, where n is the nucleation density. At small time, ϕ is then given by [1]:

$$\phi \approx n\pi a^2 t^{2/3} \ . \tag{4.2}$$

This law is drawn in dotted line in Figure 4.5 until $r \approx l/2$. l being of order 20 μm, the duration of the first phase is on the order of 30 s, in good agreement with the data.

We can also model the steady value of ϕ. As jumping occurs for most droplets, we can estimate that, during this period, droplets have radii of order $l/2$ in average. Over time, there will be jumping and renucleation but we can approximate these phases by writing $r \approx l/2$. The corresponding steady state value reads:

$$\phi \approx n\pi l^2/4 \ . \tag{4.3}$$

As $l \approx 20$ μm, one obtains $\phi \approx 31\%$, in very good agreement with the experimental values (dashed line in Figure 4.5).

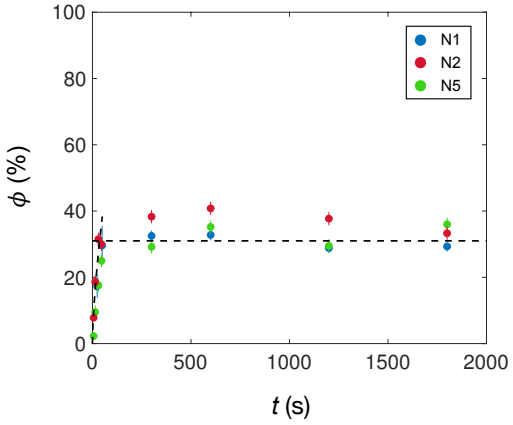

Figure 4.5: Area fraction ϕ covered by liquid as a function of time t for samples N1, N2 and N5. The dashed lines correspond to Eqs. (4.2) and (4.3).

The time evolution of the maximum drop radius $r_{\max}$ can also be examined since it governs the maximum light deviation. However, because of this non-statistical characteristic, we cannot choose this parameter as a metric for antifogging. After increasing at small time, the maximum radius is observed to plateau at a constant value, $r_{\max} \approx 35 \pm 5$ μm for the three surfaces. This value contrasts with the large one found on surface A where nearly no jumping is observed ($r_{\max} \approx 150$ μm after 30 min). Besides, $r_{\max}$ is found much larger than $l/2$, while one could think that the largest drop observed would originate from an individual growth. Despite a high jumping rate, drops' radii can be as high as ~ 35 μm due to asymmetric coalescences that decrease N and can generate bigger drops that do not jump.

In summary, through these three metrics, the three homothetic samples are found to be equally fog-repellent, despite their difference in texture size. We now look at a family with constant pitch and different cone heights.

4.3.3 Constant pitch family

4.3.3.1 Materials used

We now consider a family with a constant pitch $p = 110$ nm and different heights h, which includes four samples N4-7 (Table 2.1), with respective heights $h = 220$, 250, 284 and 420 nm (Figure 4.6). They have comparable θ_a and θ_r (Table 4.1) with contact angle hysteresis smaller than 15°, the especially low value of θ_r for N7 can be attributed to the roundness of its tip.

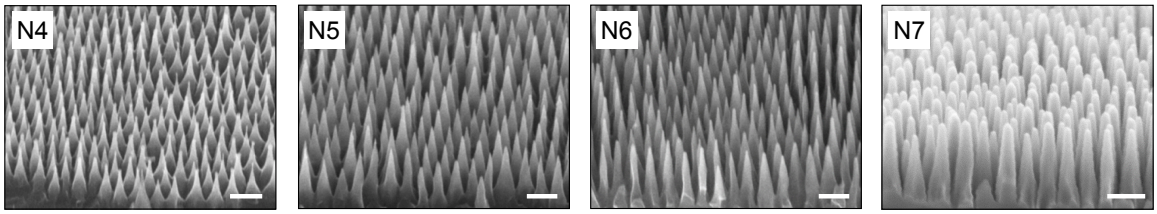

Figure 4.6: SEM images of samples of the constant pitch family, N4-7. For the four images, the scale bars indicate 200 nm. N7 has a rounder tip compared to the other surfaces.

4.3.3.2 Antifogging ability

Jumping rate

The time evolution of the jumping rate N is shown in Figure 4.7a for the four surfaces: the whole family has remarkable antifogging efficiencies with comparable mean ejection rate N of around 90% for all samples. It is again tricky to distinguish which is the most antifogging sample and cone height does not seem to impact the value of N.

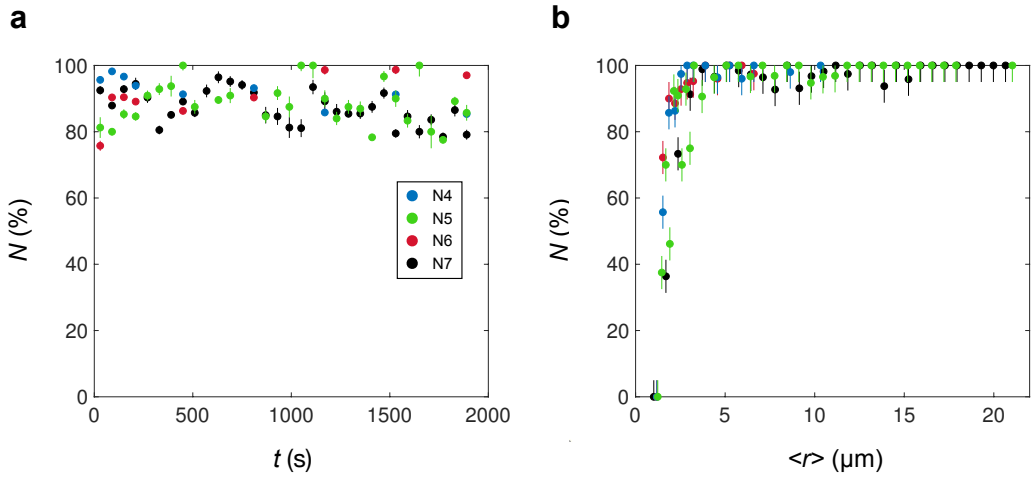

Figure 4.7: (a) Jumping rate N as a function of time t for samples N4 (blue data), N5 (green data), N6 (red data) and N7 (black data). Each point is obtained by averaging the proportion of jumps over one minute. (b) Antifogging ability N as a function of $<r>$, the common radius ($r'/r > 0.8$) of coalescing drops. For the four samples, N reaches a constant plateau value of 99%, after a sharp rise above $<r> \approx 1$ μm, a value independent of the surfaces.

Symmetric coalescences

For symmetric drops coalescing ($r'/r > 0.8$), we observe in Figure 4.7b that the jumping rate N with the mean radius $<r>$ follows the same evolution as in Figure 4.4b. N approaches 100% for $<r>$ spanning from 3 to 25 μm and suddenly decreases for smaller radii until reaching 0% for $<r> \approx 1$ μm. The cutoff radii r_c (when $N = 50\%$) are found of the same magnitude with $r_c = 1.5 \pm 0.3$ μm, 1.6 ± 0.3 μm, 1.3 ± 0.3 μm, and 1.9 ± 0.3 μm for the samples N4-7.

Conclusion

In summary, these results show that antifogging efficiency can be obtained in a broad range of texture size (between 50 and 420 nm), provided this texture is conical. In this whole range of texture size, the antifogging efficiency is found to be described by a unique curve

$N(r)$ as a function of the radius of ejected drops - a remarkably universal behaviour. Its evolution with r successively follows two regimes: a critical behaviour at small r, showing an onset of antifogging around $r = 1$ μm, followed by a plateau regime that saturates around $N \approx 99\%$, highlighting the unprecedented ability of hydrophobic nanocones to expel dew.

4.3.3.3 Macroscopic effects

For the constant pitch family, the area fraction covered by water ϕ is found similar for the four samples: $\phi = 34 \pm 4\%$, a value close to the ones measured on the homothetic family (Figure 4.8).

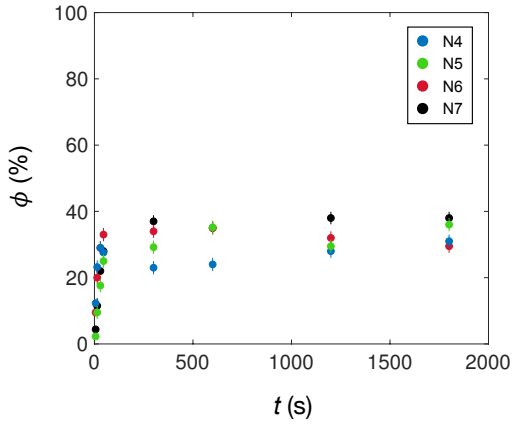

Figure 4.8: Area fraction ϕ covered by droplets as a function of time t for samples N4-7.

4.3.3.4 Jumping velocity

We have complemented our study by measuring the jumping velocity U of drops resulting after a two-bodies symmetric coalescence ($r'/r > 0.95$). We use the same apparatus as in Chap. 3: two synchronized high-speed videocameras film the coalescence from the side and from the top at respective rates of 1 and 40 kHz. Figure 4.9a reports the jumping velocity U as a function of droplet radius r for the four samples N4-7 and much information can be extracted from this plot:

(1) All four experimental data align on the same curve, despite the different texture sizes, which confirms the already observed similarities in the whole family. It is worth noting that the differences in receding angle θ_r between the 4 surfaces (7°) do not seem to influence the jumping velocity, except at low radius: the minimum jumping radius was observed for surface N6, for $r = 980 \pm 100$ nm, which has the highest receding angle ($\theta_r = 160.5°$).

(2) The takeoff velocities U follow the same evolutions as for surface N1 (see Figure 3.6 in Chap. 3): for $r > 5$ μm, all series of data collapse on a line with slope -0.5. The black dotted line corresponds to $U = (U^\star/4)\left[1 - 6\sin^2\theta_r(1 + \cos\theta_r)\right]$ (see Eq. (3.6) in Chap. 3), where we recall the inertio-capillary velocity $U^\star = (\gamma/\rho r)^{1/2}$. Because of the variability of θ_r between the four samples, we have chosen for the fit the mean value of θ_r, namely $\theta_r = 156°$. The upper limit of U represented by the dotted line tends to overestimate the jumping velocity. For smaller radii ($r < 5$ μm), and for the whole family, U exhibits a sharp decrease and equals 0 as r approaches 1 μm, in agreement with the curve $N = f(< r >)$ (Figure 4.7b), and the evolution found for N1 (Figure 3.6). Finally, taking into account viscous and adhesion effects, the jumping velocity U can be modelled by Eq. (3.8). This law is drawn with a red solid line with the same prefactor in front of the Ohnesorge number

as for N1 (4.9). A good agreement is observed between the data and the model, despite a slight underestimate of U around $r = 4 \pm 1$ μm.

Furthermore, we can confront our data with those of N1 reported in Chap. 3. The jumping velocities U measured on surfaces N1 and N7 are compared in Figure 4.9b and again data superimpose and are well described by the model given by Eq. (3.8). We now try to provide an explanation for this universal behaviour observed on the whole N family.

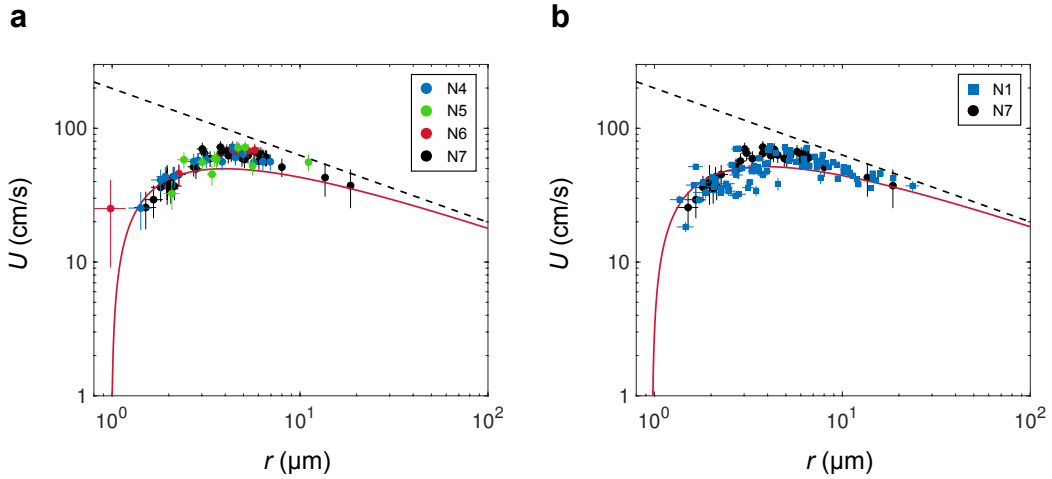

Figure 4.9: (a) Jumping velocity U for symmetric coalescence ($\varepsilon = r'/r > 0.95$) as a function of the radius r of the two merging drops. The data correspond to the four samples with same pitch $p = 110$ nm and various heights h, N4-7. Black dashes show $U = \alpha U^\star/4 \approx 0.22U^\star$, denoting $U^\star = \sqrt{\gamma/\rho r}$ and $\alpha = 1 - 6\sin^2\theta_r(1 + \cos\theta_r)$. The red solid line represents Eq. (3.8), $U = (U^\star/4)\ [\alpha - 4.9\,Oh]$, where $\alpha = 1 - 6\sin^2\theta_r(1 + \cos\theta_r)$ and $Oh = \eta/\sqrt{\rho\gamma r}$ is the Ohnesorge number with η the water viscosity. θ_r is taken as the mean value for the 4 samples ($\theta_r = 156°$) and the coefficient in front of Oh is 4.9, as for surface N1 (see Figure 3.6). (b) U as a function of r for samples N1 and N7. Despite their differences in texture size, the jumping velocities on both materials follow the same evolution. The red solid line is again $U = (U^\star/4)\ [\alpha - 4.9\,Oh]$.

4.4 Discussion

4.4.1 ESEM experiments on nanocones

ESEM images on samples N1 and N7 (see Chap. 2) suggest a robust Cassie state for droplets condensing on nanocones. In order to check if this morphology is observed for all sizes of nanocones, we have complemented our study with ESEM observations on samples N4 and N6. Images of water condensing on both samples (Figures 4.10a and b respectively) favour this hypothesis: micrometric droplets all exhibit large contact angles, as high as 170°, a manifestation of their non-wetting Cassie states. We now try to explain why nanocones do favour this morphology.

4.4.2 Effect of nanocones on condensation

4.4.2.1 Nucleation

We complement here the work of Mouterde presented in his PhD thesis [1]. During condensation of water on a substrate, classical nucleation theory stipulates that water nuclei

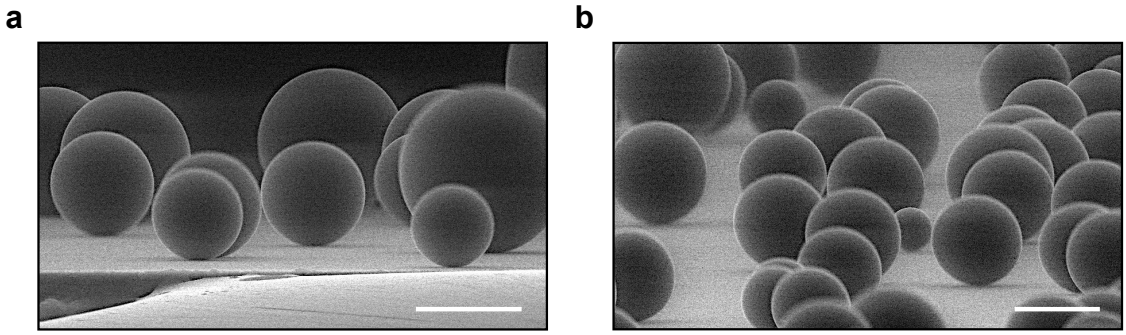

Figure 4.10: ESEM images of water condensing on surfaces N4 ($h = 220$ nm) (a) and N6 ($h = 284$ nm). (b) As for samples N1 and N7, drops are spherical, a manifestation of their Cassie state. Scale bars = 10 μm.

have sizes ranging from several nanometers to several hundred nanometers [24, 88], that is, on the order of the texture size for nanocones. In our experimental conditions, we expect a critical radius for nucleation $r^\star$ on the order of tens of nm (see Eq. (1.16) in Chap. 1). In a nanocone array, a nucleus preferentially forms on the inner walls (Figure 4.11a) and, more preferably, at the bottom, in the cavities, where it minimizes its surface energy [89] (Figure 4.11b).

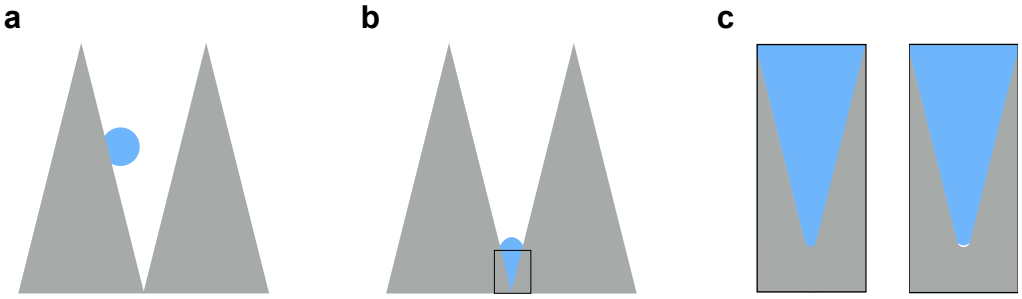

Figure 4.11: (a) Schematic of a nucleus growing on the inner walls of cones. (b) Nucleus developing at the bottom of the structures. (c) Closer look of the liquid-surface contact of case. Dewetting can occur and induce a liquid-vapour interface. Extracted from [1].

4.4.2.2 Nucleus growth

Molecular simulations of Xu *et al.* were performed on cones with different angles β [90]. Provided that β is small enough, so that cones are superhydrophobic ($\beta < 2\theta - \pi$, with θ the contact angle of water on the flat surface), simulations stress that a water nucleus at the bottom of the structures will grow, yet spontaneously dewets the most confined region, so that a vapour pocket appears at this place (Figure 4.12a where $\beta = 28°$). With time, the nucleus moves upwards until it reaches the top of the structures. In contrast, for large cone angles, *i.e.* $\beta = 53°$, that is, if relaxing the confinement, the growing nucleus remains stuck at the bottom of the features (Figure 4.12b). Based on these results, two spontaneous phenomena must be emphasized: firstly, the dewetting at the beginning of nucleation (for small β), and secondly, the upward motion of the growing nucleus.

At small radius, the nucleus is trapped and an energy barrier must be overcome to dewet the bottom of the cavity (Figure 4.11c). Recent theoretical works and simulations have suggested that water density fluctuations are enhanced on hydrophobic surfaces, which

can promote dewetting at the nanoscale [91, 92, 93]. They stipulate that hydration shells of hydrophobic solutes are soft, highly compressible, and characterized by strenghtened density fluctuations that can eventually lead to higher probabilities for cavity formation. In order to study Wenzel-to-Cassie transitions, Prakash *et al.* performed dynamic molecular simulations of water on a superhydrophobic surface made of pillars [94]. They estimated the free energy ΔF of water in several wetting configurations. This quantity is normalized by the thermal energy $k_B T$, where k_B is the Boltzmann constant and T the temperature, and its evolution with the water density ρ_n is studied. ρ_n defines the density of water molecules inside a cell delimited by four pillars: for instance, $\rho_n = 0$ defines the Cassie state, while $\rho_n = 1$ the Wenzel state (Figure 4.13a). The energy barrier between the two states must be overcome, as shown in Figure 4.13b. Because of the variability of ρ_n on hydrophobic surfaces, vapour pockets can form at the base of pillars (region IV in Figure 4.13c), which eventually leads to a complete dewetting. This observed mechanism is not predicted by macroscopic theory, which reinforces its non-classical nature.

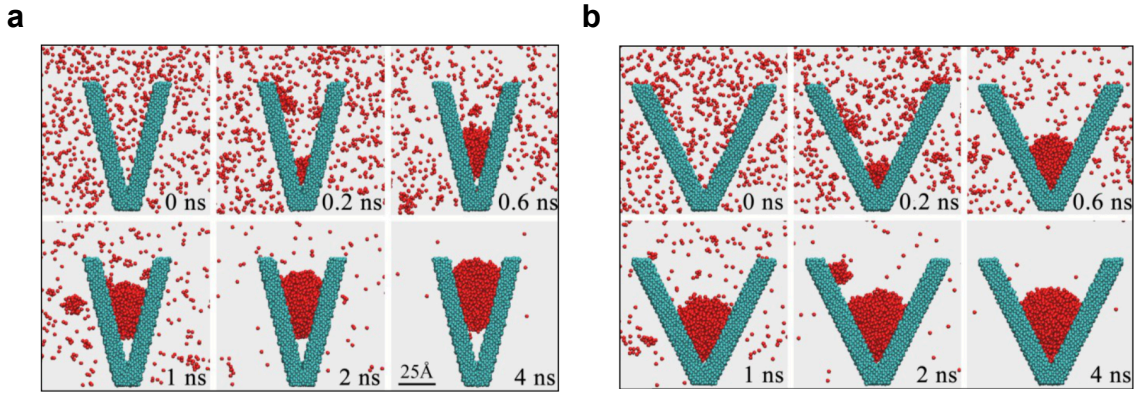

Figure 4.12: Images of molecular dynamics simulations showing the condensation of water in a V-shape, for two V-angles: (a) $\beta = 28°$ and (b) $\beta = 53°$. The red dots denote the water molecules. At low β, the nucleus grows and rises in the texture, after a vapour pocket has formed below it. At high β, it remains in the Wenzel state at the bottom of the structures. Extracted from [90].

Water density fluctuations causing dewetting can happen because of Van der Waals forces, at a scale smaller than 100 nm. Considering a thin film of water lying on a material, if the disjoining pressure due to Van der Waals interactions $\Pi(h) = A/6\pi h^3$ is negative, it can be instable and dewet [95, 96]. We here denote h as the film thickness and A as the Hamaker constant of water on the material. For water on silane, we have: $A = A_{ws} - A_{ww} < 0$, where $A_{ws} \approx 8$ zJ and $A_{ww} \approx 40$ zJ (1 zJ $= 10^{-21}$ J) are the respective Hamaker constant of water with silane and water with water [97, 98]. When a nucleus develops at the bottom of cones, its size is on the order of tens of nm. At this scale, spinodal dewetting can occur and generates an increase in density fluctuations. Nanocones can experience this phenomenon because cavities have sizes of tens of nm. We expect that cones with larger structures should not experience such transition, which we further discuss with microcones (see Sec. 4.6).

Since dewetting can also occur in nanopillars, a second mechanism must be invoked to explain the stable Cassie state for condensed droplets on nanocones only. In the latter situation, soon after a vapour pocket is formed and provided that β is small enough, the nucleus might move upwards (Figure 4.12a). Several experiments and simulations confirm this scenario [99, 90, 100, 101]. For instance, Checco *et al.* studied the liquid interfaces on nanocones using X-rays diffraction [99]. After increasing the liquid pressure, they managed to reach the Wenzel state. Yet, after a subsequent decrease in pressure, the interface was

observed to move and the Cassie state was recovered, unlike pillars in a same experiment.

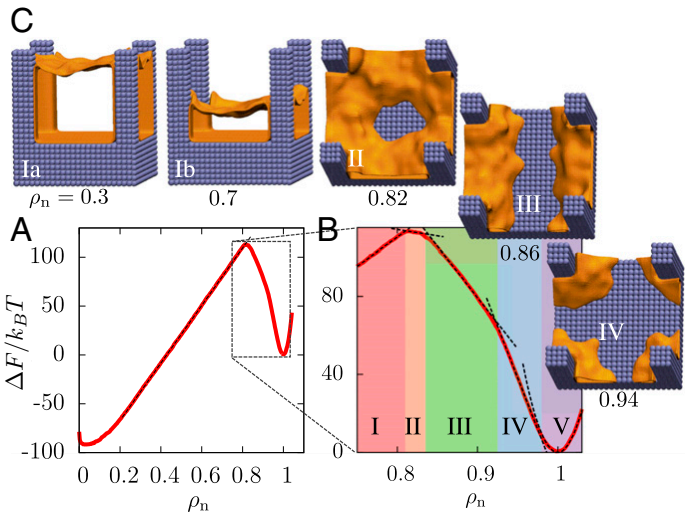

Figure 4.13: Results of molecular simulations for water in a cell delimited by four nanopillars. (a) Normalized free energy $\Delta F/k_BT$ as a function of the water density ρ_n. The two limits $\rho_n = 0$ and $\rho_n = 1$ correspond to Cassie and Wenzel states, respectively. (b) Closer look of the plot shown in (a) with the different scenarii in (c). Water density fluctuations can generate dewetting and a transition from Wenzel to Cassie. Orange colors represent vapour pockets. As ρ_n decreases, the size of the liquid-vapour interface increases. Extracted from [94].

The different nucleation stages are as followed: a nucleus forms at the bottom of the cones and can be further depinned, which leads to the formation of a vapour pocket developing below it (Figure 4.11c). With time, the nucleus grows in size, and confinement makes its upper radius increase, hence decreasing its upper curvature. To minimize its total energy and equilibrate the two pressures associated with the two curvatures (corresponding to the upper and lower radii), the nucleus must rise (Figure 4.14) until it reaches the top of the structures. This scenario is not achievable for pillars for which the nucleus curvature remains the same with height, without Laplace pressure to push up the water droplet. In the case of cones, the nucleus suspending height H can be estimated as a function of its radius r [90]:

$$H = r\frac{\sin(\theta - \pi/2)}{\sin(\beta/2)} \ . \tag{4.4}$$

The nucleus reaches the cone height when $H + r = h$. For the highest cones (sample N7, $h = 420$ nm), ones finds $r = 280$ nm, a value close to the minimum radius observed in ESEM images, $r = 330$ nm (see Figure 2.17b in Chap. 2).

4.4.3 Back to experimental observations

Condensation experiments on the N family have evidenced a similar antifogging behaviour for all samples, independently of the cones' heights and pitches: the jumping rate with time and with radius, as well as the jumping velocity, all follow the same evolutions, whatever the samples. Our ESEM observations suggest that condensed droplets lie in Cassie state, at the top of the cones, which has been further validated by recent experiments and simulations [99, 90] and by our antifogging experiments. For such wetting state, droplets are little influenced by texture sizes, except during merging with neighbours where the receding motion can be

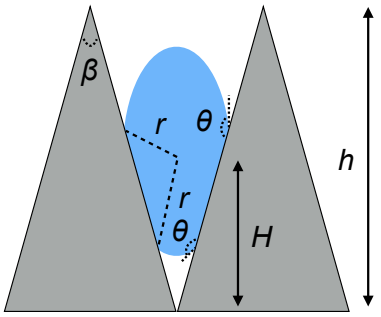

Figure 4.14: Sketch of a suspended nucleus with radius r between two cones with height h and angle β. The suspending nucleus height is denoted as H. To be at equilibrium, the nucleus must have equal curvature at the top and bottom. The water contact angle is denoted as θ.

impacted by the structures, as evidenced by the (low) variability of the receding angle θ_r (Table 4.1). For drops in Cassie state, adhesion remains marginal because they exhibit high contact angles and pinning is low. As suggested in Chap. 3 for the jumping velocity, viscous effects can be the main cause of the decrease in mobility for droplets' jumping, as it is not influenced by the structures' dimensions, which explains the universal behaviour reported up to now.

4.5 Asymmetric coalescences

The case of symmetric coalescences ($\varepsilon = r'/r > 0.8$) was only considered and smaller asymmetry ratios ε can be discussed. We plot in Figures 4.15a the jumping rate N as a function of the small drop radius r' for different levels of asymmetry and for droplets condensing on sample N7.

As noted by Mouterde, no matter the asymmetry ratio, N always reaches 100% for large drops [1]. Yet, asymmetry controls the evolution of N from 0 to 100%: the transition between these two extreme values is observed to be all the larger given ε is small: for $r'/r > 0.8$ (red data), N transitions from 0 to 100% from $r \approx 1$ μm and with a width of ~ 2 μm, while for $0.4 < r'/r < 0.6$ (blue data), it occurs for $r \approx 6$ μm and with a range of ~ 10 μm. This evolution can be understood using the results of Chap. 3: as asymmetry increases, the smaller drop cannot communicate enough momentum to generate takeoff.

The behaviours observed for N can now be investigated. First, for the 3 sets of data, the cutoff radius r_c when $N = 50\%$ must correspond to the radius where the jumping velocity U of the merging drop is found to be zero. Chap. 3 provides an estimation of U as a function of the asymmetry ratio ε and of the small drop radius r' (Eq. (3.11)). Setting $U = 0$ in Eq. (3.11) yields the critical jumping radius $r'_{c,\varepsilon}$ for the small drop:

$$r'_{c,\varepsilon} = \frac{\eta^2}{\rho\gamma} \frac{16\varepsilon^3}{\left[\varepsilon^{5/2} - 3\sin^2\theta_r(1+\cos\theta_r)(1+\varepsilon^{5/2})\right]^2} \,. \tag{4.5}$$

The critical jumping radii are estimated at the mean of ε for each range ($\varepsilon = 0.5$ and 0.7). For $0.6 < \varepsilon < 0.8$, the law gives $r'_{c,0.7} = 3.1$ μm, while for $0.4 < \varepsilon < 0.6$, $r'_{c,0.5} = 10.7$ μm, to be compared with the measured ones $r'_{c,0.7} = 3.3 \pm 0.5$ μm and $r'_{c,0.5} = 12 \pm 1$ μm. In the whole, Eq. (4.5) provides a good agreement with the experimental data (less than 15% error).

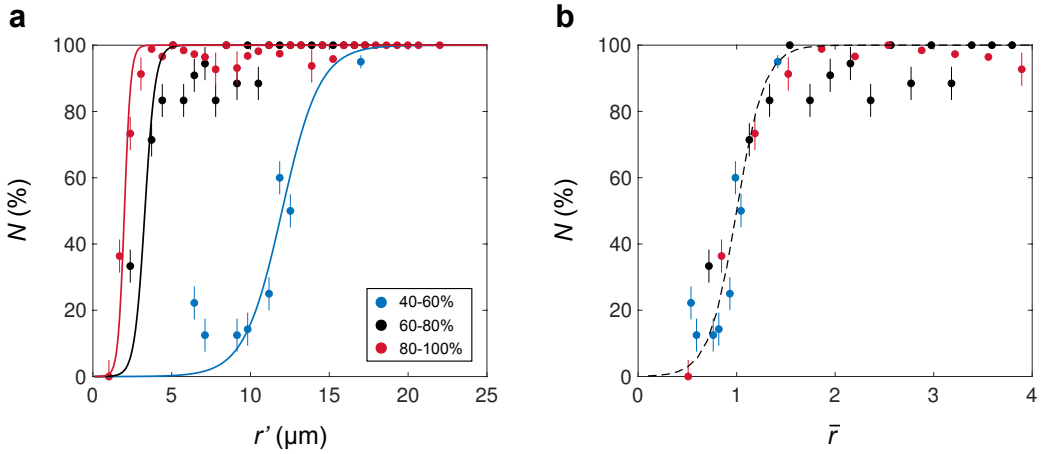

Figure 4.15: (a) Asymmetric coalescences on sample N7. N as a function of the small droplet radius r' for $\varepsilon = r'/r$ between 40-60% (blue data), 60-80% (black data) and 80-100% (red data). Solid lines are Eq. (4.7) plotted with the critical jumping radius r_c, that is the radius for which $N \approx 50\%$, and $\sigma = 0.2$, corresponding to the width of each range of ε. We measure $r_{c,\varepsilon} = 1.8 \pm 0.2$ μm, 3.3 ± 0.5 μm and 12 ± 1 μm for the 3 ranges of ε. (b) Jumping rate N as a function of the normalized radius $\bar{r} = r'/r_{c,\varepsilon}$. All data fairly collapse on the same curve and the dashed line is Eq. (4.6) with $\sigma = 0.2$.

We can now focus on the transitions observed for the 3 ranges of ε: as stated before, it is found to be all the softer given ε is small. To visualize this asymmetry effect, N is shown as a function of the normalized radius $\bar{r} = r'/r_{c,\varepsilon}$, that is the small droplet radius divided by the measured critical jumping radius (Figure 4.15b). Remarkably, all data collapse on the same curve centered in $\bar{r} = 1$. The evolution of N with $\bar{r}$ can be assimilated to a phase transition from the state non-jumping ($N = 0\%$) to total jumping ($N = 100\%$). The relative width of the curve (width during which N transitions from 0 to 100%) can be due to the heterogeneities of radius (here $\Delta r/r = 0.2$). Common functions for modelling soft phase transitions are sigmoid function or tanh, as observed in Curie's law and magnetization:

$$N(\bar{r}) = \frac{1}{2} + \frac{1}{2}\tanh\left(\frac{\bar{r}-1}{\sigma}\right) , \tag{4.6}$$

where the parameter σ is here introduced. For $\sigma = 0$, N becomes the step function (heaviside), where it jumps to 100% for $\bar{r} = 1$, *i.e.* $r = r_c$. We can understand σ as the standard deviation, hence we choose $\sigma = 0.2$ as the width of each range of ε is 0.2. Eq. (4.6) is drawn in dashed line in Figure 4.29b and matches quite well the data, except for high radii and $0.6 < \varepsilon < 0.8$. Furthermore, Eq. (4.6) provides us with an expression of N as a function of r_c:

$$N(r) = \frac{1}{2} + \frac{1}{2}\tanh\left(\frac{r-r_c}{\sigma r_c}\right) . \tag{4.7}$$

This law, drawn in solid lines in Figure 4.15a for the 3 ranges of ε, agrees well with data except for high radii and $0.6 < \varepsilon < 0.8$ where it slightly deviates and tends to sharpen the transition from 0 to 100%.

4.6 Micrometric cones

4.6.1 Introduction

Unlike nanocones where resistance to fog was reported [86, 35, 36], the behaviour of materials composed of microcones towards condensation remains little studied. For instance, Chen *et al.* used a surface with two-tier roughness of micrometric cones and nanograss [102]. Similarly, Rykaczewski *et al.* studied different materials composed of truncated microcones with a nano-roughness with a decent proportion of ejected drops of about 30% with a large uncertainty [37]. Although the superhydrophobic properties of micrometric spikes and their dependence on the cone angle are well documented [103, 104, 105], the influence of texture size on fog repellency is of practical importance. To that end, we have performed experiments on a family of samples covered with microcones of different sizes (family M), which we develop here. Our aim, in particular, is to determine whether the antifogging abilities reported on nanocones resist the magnification of the structures.

4.6.2 Surface characteristics

The M family is composed of materials covered with micrometric cones (Table 2.1). The three samples have respective pitch $p = 0.5$, 1.6 and 2.4 μm. Their corresponding advancing and receding angles are displayed in Table 4.2: all three surfaces have large advancing angles and low hysteresis. The experiment sketched in Figure 4.1 and presented in Sec. 4.2 is performed to observe condensation: the supersaturation is set at $S = 1.6 \pm 2$ and images are recorded every 2 seconds for 30 minutes.

Sample	**Advancing contact angle θ_a (°)**	**Receding contact angle θ_r (°)**
M1	169 ± 1	165 ± 2
M2	168 ± 1	163 ± 1
M3	171 ± 1	170 ± 1

Table 4.2: Contact angles of water on the M family.

4.6.3 Water configuration

Compared to the case of nanocones, the cones in the M family are roughly ten times larger. It then enables us to observe the shape adopted by droplets condensing on the samples, and we can even resort to optical tools. We first present the morphologies adopted by droplets condensing on the M family.

4.6.3.1 Droplet shape

If filming from the top and focusing through the droplets, one can access the water configuration inside the conical structures, as evidenced in the four images of Figure 4.16. Images of condensation on M1 (Figure 4.16a) reveals a dark square area inside each droplet, with a size of $\sim 2 \times 2$ μm^2. This dark zone evidences the presence of water inside the cones below the drop.

Working with larger structures (M2-3) allows us to be more precise. On M2 (Figure 4.16b), a cross pattern appears at the center of each droplet, delimited by five unit cells (each unit cell being composed of 4 cones), with a central one brighter than the 4 others. Surface M3 exhibits the same pattern at all droplet sizes (Figure 4.16c). Focusing even deeper inside the droplets reveals one dark square with a width of 2.4 μm, at the center

of each drop (Figure 4.16d). These black areas (pointed by red triangles) confirm that the drop grows above a single wetted cell. The black dots around each square in Figure 4.16d are the cones distorted by the drop, their size being large enough to be directly observed (in contrast with Figure 4.16a). Because of the small texture size of M1, it is tricky to know how much cells are filled, which we further discuss. Conversely, for both surfaces M2 and M3, all droplets tend to grow above only one central filled cell.

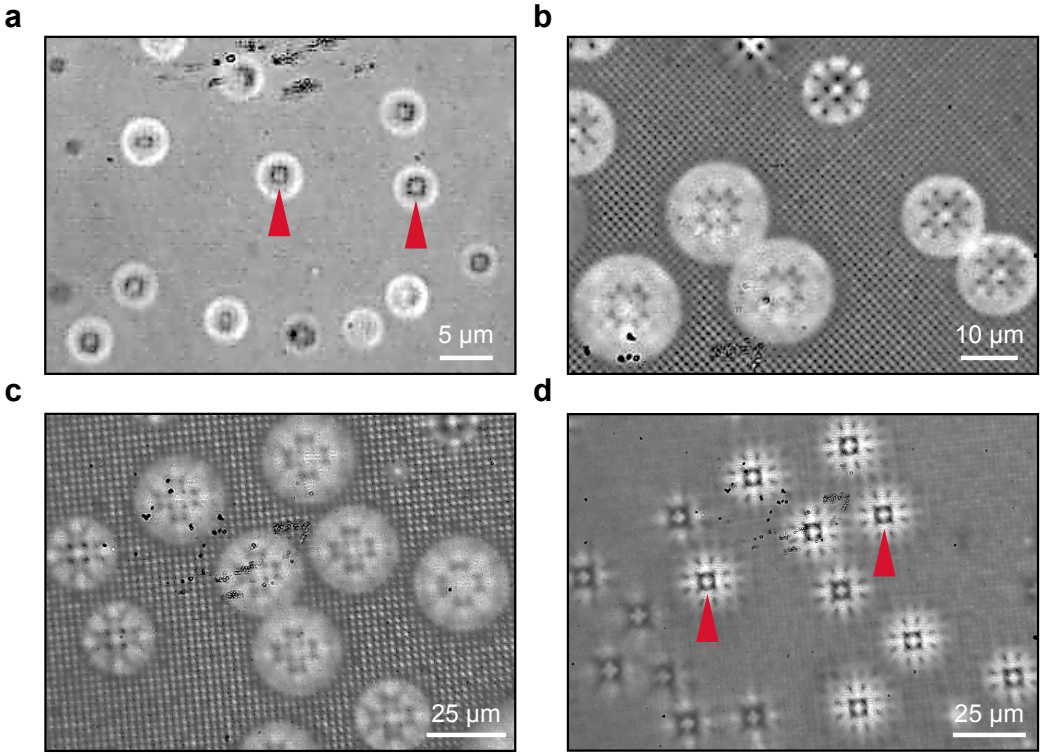

Figure 4.16: Top images of droplets condensing on surface M1 (a), M2 (b) and M3 (c and d). For the three samples, focusing through water reveals dark areas, a manifestation of wetted unit cells (red triangles). For samples M2 and M3, images show a cross pattern below each droplet with a dark area at the middle that corresponds to a unit filled cell.

Aiming at getting a better understanding of droplet shapes, we have performed ESEM experiments on the three substrates. Because of the similarities between M2 and M3, we only show results obtained for the latter sample. ESEM imaging on sample M3 confirms that condensed droplets are only locally pinned to the surface, which gives them the shape of a balloon (Figures 4.17a and b): every drop presents one wetted unit cell below it, while the two neighbours are partially filled with water, as sketched in Figure 4.17c. This shape is typical of droplets found in a partial Cassie state (see Chap. 1): upon condensation, water fills texture from the inside until it subsequently grows above the trapped nucleus of water. In this case, only one cell is filled and the pinned neck has a diameter of 2.4 μm, that is, M3's pitch. Furthermore, these images confirm the observations made with the optical microscope: the dark area is the wetted cell and the cross pattern is due to the four partially wetted cells around the filled one (4 because of the symmetry of the cone array). This wetting state has been discussed by Enright *et al.* who reported it on surfaces composed of nano or micropillars [29]. For Cassie stable surfaces, this state is the most favourable upon condensation, because pillars rarely favour a Cassie state, even at the nanoscale. In our case, microcones contrast with nanocones where it seems that all droplets end up at the top of cones with no pinned area.

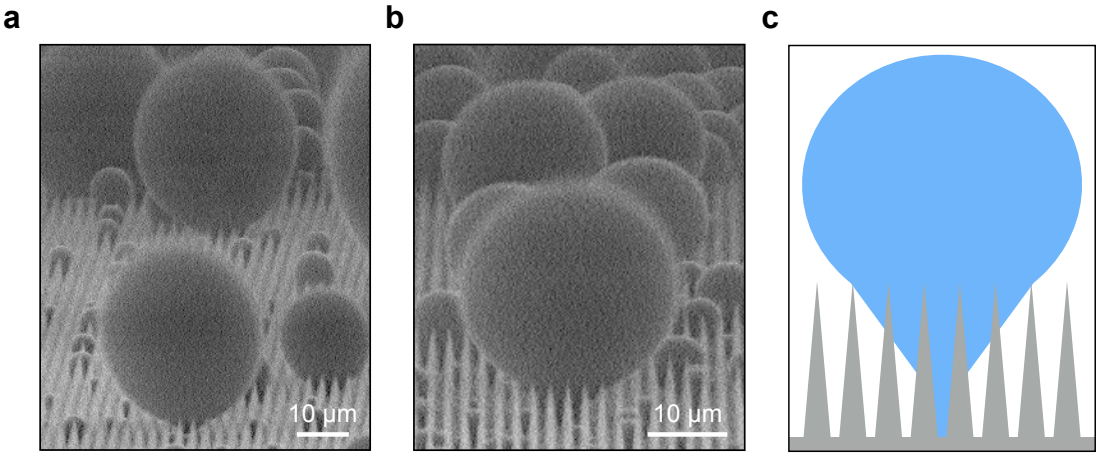

Figure 4.17: ESEM images of drops condensing on M3 (a and b). The high tilting angle reveals a single wetted cell and the drop adopts the shape of balloon with a pinned neck, whose width looks localized within one cell of pillars, as sketched in (c).

Experiments on sample M1 suggest the same scenario (Figure 4.18): droplets of all sizes adopt a quasi-spherical shape with a contact area of radius on the order of 2 μm, that is four times the texture pitch ($p = 500$ nm). Because of e-beam limitations, imaging the cones was rendered difficult and resulted most of the time in droplet evaporation. It is therefore tricky to distinguish how many cells are totally or partially filled below each droplet, which is why we resorted to top ESEM imaging (next subsection). Besides, for droplets much larger than p, contact angles can be as high as 170° before the onset of coalescence, a characteristic also evidenced in [29]. It is worth noting than the mean separation distance between nuclei ($l \approx 20$ μm) is found much larger than the cone pitch, which enables droplets to develop in Cassie/partial Cassie states (see Chap. 1). We now focus on the initial phase of droplet growth.

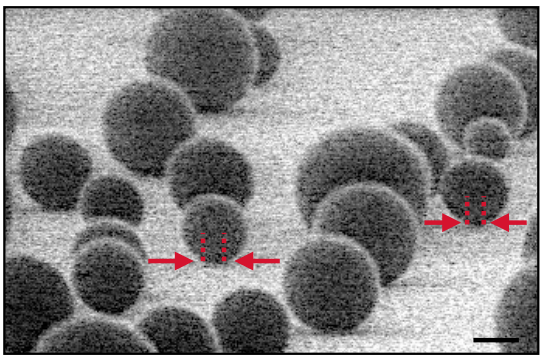

Figure 4.18: ESEM images of water condensing on sample M1. All drops are in partial Cassie state: small drops ($r < 5$ μm) exhibit a contact area with length ~ 2 μm and delimited by the red dotted lines, as shown on two examples. For bigger drops ($r > 5$ μm), the contact area increases. The scale bar indicates 5 μm.

4.6.4 Water filling

4.6.4.1 Large cones

We have investigated the individual growth of a nucleus inside the texture, using top view imaging under ESEM. Figure 4.19a presents a chronophotography of a droplet condensing on material M3 ($p = 2.4$ μm), together with the sketched droplet morphologies at the different times (Figure 4.19b).

At small time, the nucleus develops inside a unit cell, delimited by four cones, and grows until it reaches the top of the texture ($t = 5.8$ s). After this initial phase, the droplet expands out of the structures and adopts a different growth behaviour [29]. After a brief moment (between $t = 5.8$ s and 10.6 s), the different interfacial tensions cannot support the increasing droplet curvature, hence the contact line depins from one cone to the next row of cones. This pinning-depinning occurs all around the unit filled cell until reaching a final pinning barrier where the droplet is symmetric ($t = 16.4$ s). Finally, after this period, the droplet grows isotropically into a partial Cassie state ($16.4 \text{ s} < t < 19.3$ s). Besides, from the last image ($t = 19.3$ s), one can note that the droplet is no longer deformed by the cones and adopts a spherical shape, in constrast with the "octogonal" shape observed at $t = 16.4$ s. The pinning-depinning mechanism was observed and carefully investigated on pillar-textured surfaces, unlike cone-like ones [29]. For the latter case instead, the contact line cannot sink to the bottom of the texture because its sinking height is dictated by droplet radius, as noted in Chap. 2, hence less solid-liquid contact. Furthermore, the different snapshots confirm our previous observations: only one unit cell is wetted and its four neighbours are partially filled with water because of pinning-depinning mechanisms.

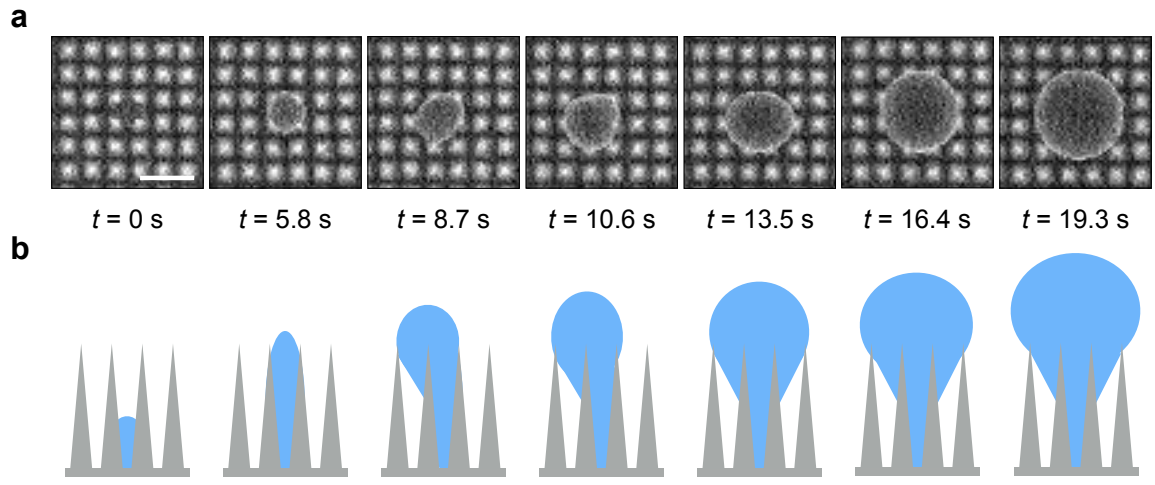

Figure 4.19: (a) Chronophotography of a water nucleus on sample M3 using ESEM from the top. The corresponding sketched droplet morphologies are shown below for clarification. The scale bar indicates 5 μm. (b). The nucleus first fills a unit cell until connecting the four neighbouring cells with pinning-depinning mechanisms. At large time, the drop expands isotropically around the wetted cell. This confirms the cross pattern observed in Figure 4.16c and explains the shape shown in Figure 4.17.

4.6.4.2 Small cones - M1

On small cones (sample M1 - $p = 500$ nm), the nucleus experiences the same expansion phases but the number of filled cells differs. As evidenced in Figure 4.20a, a nucleus emerges in a unit cell, reaches the top but subsequently wets three other unit cells ($t = 4.8$ s). At

this time, side view imaging shows a droplet with indeed a pinned neck of length ~ 1 μm, that is 2 unit cells length (Figure 4.20b). Once these four cells are totally filled with water, the droplet can grow out from the structures, in the same manner as on M3: the contact line pins and depins to the neighbour unit cell, as also illustrated in the bottom images that show an increase of the size of the liquid-solid area, from 1 μm ($t = 4.8$ s), to 1.5 μm ($t = 6.7$ s) and 2 μm ($t = 8.6$ s). Finally, the droplet occupies 16 unit cells with 4 totally filled with water ($t = 8.6$ s). After this period, the droplet enters a new expanding stage where the pinned area does not vary with time while its contact angle increases until reaching 165° for a radius $r \approx 5.3$ μm (last image of Figure 4.20b).

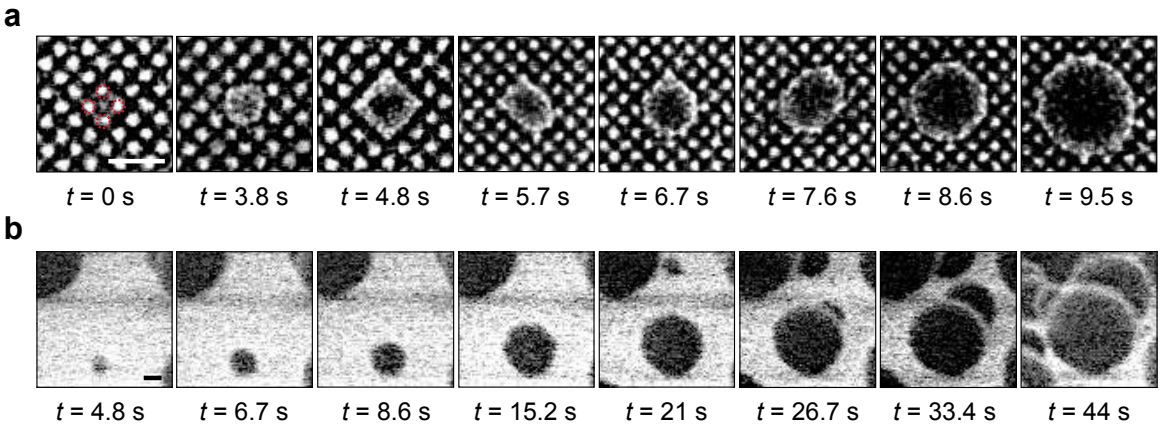

Figure 4.20: ESEM images of water condensing on sample M1. (a) Snapshots of a nucleus growth from the top. Water fills four unit cells until growing out from the structures and partially filling 12 unit cells. Scale bar = 1 μm. Images were transformed to enhance the contrast. (b) Snapshots of a water droplet growing from the side (tilting angle = 80°). At small time, the contact area is of length ~ 1 μm, that is the length of two wetted cells. Drop contact angle increases with time until reaching 165° for $r = 5.3$ μm ($t = 44$ s), indicating that the droplet is in a partial Cassie state. Scale bar = 1 μm.

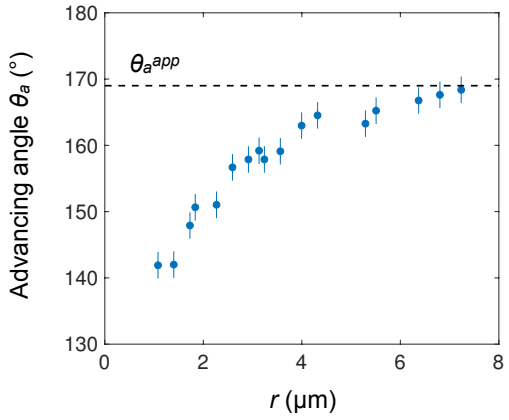

Figure 4.21: Advancing angle θ_a of a drop condensing on M1 with increasing radius r. θ_a increases with time because of the constant pinned area and increasing radius. The advancing angle converges towards the apparent advancing angle measured on millimetric drops $\theta_a^{app} = 169°$ (black dotted line).

The corresponding advancing angle θ_a of the droplet shown in Figure 4.20b is presented in Figure 4.21 as a function of its radius r. At low radii, θ_a plateaus around 142°: r is of

order 1 μm which corresponds to values where the droplet experiences pinning-depinning phenomena, hence θ_a does not evolve much. For larger r instead, θ_a increases with radius, as also observed in the ESEM images, until reaching the value measured on millimetric drops, $\theta_a^{app} = 169°$. This evolution differs from the one obtained on nanocones on surface N7 (Figure 2.17b) where θ_a already reaches 160° for $r > 1$ μm (compared to 4 μm for M1). This discrepancy originates in the pinned neck that tends to decrease the contact angle.

4.6.4.3 Model

The first growth phase of a nucleus developing in a unit cell can occur in two different directions: sideways where water invades the neighbouring cells, or upwards, where water expands vertically until filling the unit cell. As evidenced by Enright *et al.*, the magnitude of the dimensionless energy $E^\star$, that compares a liquid advancing in a Wenzel or Cassie state, determines which scenario is preferred [29]. As expressed in Chap. 1 (Eq. (1.17)), $E^\star = -1/r_f \cos\theta_0$, where r_f is the roughness factor and θ_0 the advancing angle of water on hydrophobic silicon ($\theta_0 \approx 120°$). For a surface covered with cones, the roughness factor r_f is :

$$r_f = 1 + \frac{\pi d}{4p^2}\left(\sqrt{d^2 + 4h^2} - d\right) \ , \tag{4.8}$$

where we recall that d, p and h are the corresponding cone diameter, pitch and height. For our three samples M1-3, one obtains respectively $r_f = 5.5$, 5.9 and 4.6, which yields $E^\star = 0.36$, 0.34 and $0.43 < 1$. Hence, upward growth is always favoured, as confirmed in Figures 4.19a ($0 < t < 5.8$ s) and 4.20a ($0 < t < 3.8$ s) where a unit cell is first filled before water reaches the top of texture. However, the influence of cone shape is not present in Enright's model. More than pillars, growing sideways for water in cones is energetically unfavourable as the solid-liquid contact is extended by a factor $1/\cos(\beta/2)$ due to the wetting of a diagonal compared to a line for pillars. This fact makes upward growth even more favourable.

After reaching the top of the structures, water can either grow above the structures or wets the neighbouring cells. We propose here an argument to estimate the two energy barriers [29, 32]. As evidenced in the top ESEM images, after reaching the top of the texture, the drop expands over the diagonal between two cones: for 5.8 s $< t <$ 8.7 s in Figure 4.19a. The same behaviour is observed on M1 where, after being confined in a unit cell (Figure 4.18a, $t = 3.8$ s), the nucleus later fills 3 more unit cells ($t = 4.8$ s) as the wetting is made in the diagonal direction. We represent in Figure 4.22a a droplet confined between four cones: it can expand upwards by a vertical distance $\mathrm{d}z$ or sideways by a distance $\mathrm{d}x$. From the top (Figure 4.22b), the droplet expands over two directions. For a nucleus filling 1 unit cell ($n_c = 1$), the energy barrier $E_t(n_c = 1)$ to expand upwards is:

$$E_t(n_c = 1) = 4\gamma p \, \mathrm{d}z \ , \tag{4.9}$$

while the one associated with sideways growth is E_s:

$$E_s(n_c = 1) = \gamma \left[4h/\cos(\beta/2) - 2(p-d)(1-\cos\theta_a) + 2p\right] \mathrm{d}x \ , \tag{4.10}$$

where the first right-hand term corresponds to the creation of four liquid-air interfaces over a diagonal $h/\cos(\beta/2)$, the second to the floor wetting and the final term to the creation of two liquid-air interfaces at the top.

Furthermore, equal volume constraint when expanding in either direction gives:

$$(2p - d)h \, \mathrm{d}x = p^2 \mathrm{d}z \ , \tag{4.11}$$

and the energy ratio $\Delta E^\star$ reads:

$$\Delta E^\star(n_c = 1) = \frac{E_t(n_c = 1)}{E_s(n_c = 1)} = \frac{4p}{4h/\cos(\beta/2) - 2(p-d)(1-\cos\theta_a) + 2p} \frac{(2p-d)h}{p^2} \ . \quad (4.12)$$

If we estimate $\Delta E^\star(n_c = 1)$, we find $\Delta E^\star(n_c = 1) = 1.05$, 0.93 and 0.95 for the corresponding materials M1, M2 and M3. The model predicts that upward growth is favourable for M2 and M3, as indeed observed experimentally. Conversely, growing sideways is energetically favourable for sample M1. However, our model is not able to predict the correct number of wetted cells for M1. Indeed, as for $n_c = 1$, doing the same reasoning for $n_c = 4$ yields exactly the same value for $\Delta E^\star(n_c = 4)$: $\Delta E^\star(n_c = 4) = 1.05$. Other effects may not be taken into account in our energy analysis, which could explain why sideways growth ends after 4 cells are filled with water. Yet, this simple reasoning enables us to rationalize our experimental observations and explains how the droplet morphology can depend on the material.

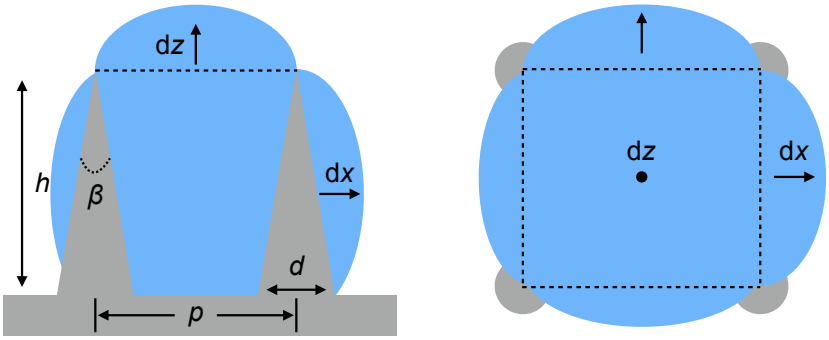

Figure 4.22: (a) Sketch of a nucleus confined in a unit cell delimited by four cones. It can either expand upwards by a distance dz or sideways by dx in two directions. (b) Top view of a condensation droplet in a unit cell. The wetting occurs over the diagonal when sideways growth is favoured. Hence, water expands over two directions, as stressed by the two arrows. Adapted from [29].

We have focused on individual droplets condensing on microcones, but one may now wonder whether they can take off the substrate after coalescing with their neighbours.

4.6.4.4 Water configuration after droplet jumping

Unlike nanocones where water lies on a cushion of air, condensed droplets are here pinned. A first question to raise is whether water can still jump despite pinning, and more generally, how pinning modifies the picture established with nanocones. To that end, we film at a high rate (4 kHz) the coalescence of droplets from the top. Figure 4.23a shows the jump of 5 droplets on M3, before (left) and after (right) coalescence and the two images are spaced of 0.75 ms, a time much smaller than the one required to fill a unit cell ($\sim$ 1 s). Hence drops can still take off but, as indicated by the 5 red triangles that point to wetted unit cells, some liquid remains trapped within the structures after the jump. The 5 unit cells correspond to the 5 filled cells that gave birth to the 5 droplets. Only liquid in these cells remains pinned, while the partially filled cells are emptied after the jump, which the sketch in Figure 4.23b illustrates. An energetic estimation of leaving liquid or depinning can explain this observation. The energy E_1 to depin water inside n_c filled unit cells is:

$$E_1 = \gamma n_c r_f p^2 (1 + \cos\theta) \ , \quad (4.13)$$

denoting r_f as the roughness factor. In contrast, the energy E_2 associated with leaving liquid at the top of the structures is:

$$E_2 = 2\gamma n_c p^2 \ . \tag{4.14}$$

For the latter case, in each unit cell, two water interfaces are created with area p^2 and we here denote θ as the receding angle for water on hydrophobic silicon ($\theta \approx 90°$). For M2 and M3, where one cell is wetted, it yields $E_1 > E_2$, as well as for M1 where four unit cells are filled with water ($n_c = 4$), and experimental observations have confirmed us that these cells do remain wet after droplet jump.

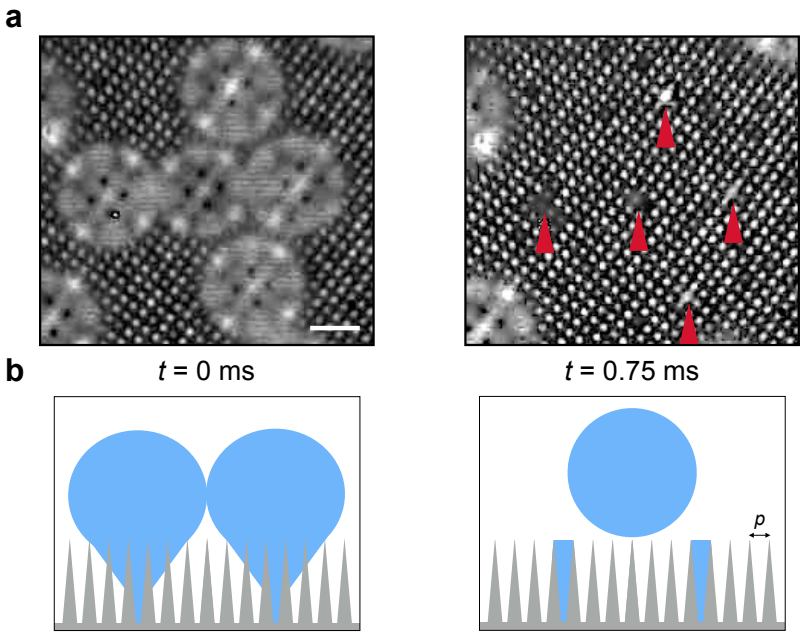

Figure 4.23: (a) Top images of five droplets coalescing and jumping on material M3 (p = 2.4 μm). Images are separated by 0.75 ms, a time much lower than the one required to fill a cell ($\sim$ 1 s). After the jump, liquid remains pinned in each unit cell where droplets had developed, as pointed by red triangles. Scale bar = 5 μm. (b) Sketch of the merging of two droplets followed by a jump. The two unit wet cells remain filled with water after the jump.

This experiment has definitely confirmed us the existence of wet cell(s) that pin(s) condensed droplets on samples M. However, we have only showed here one case of favourable droplet jumping. Let us now measure the antifogging efficiency of microcones in a statistical approach, as for nanocones.

4.6.5 Antifogging abitilies

4.6.5.1 Breath figures

We present in Figure 4.24 images of water condensation on the M family at different times. At short time, the three breath figures are comparable with a nucleation density $n = (1.0 \pm 0.2).10^{-3}$ μm^{-2} and droplets have radii $\sim$ 5 μm. Subsequently, images differ between the 3 samples: the area fraction covered by water increases with texture size and larger drops appear ($r > 100$ μm). Yet, at the end of the experiment, the surface covered by droplets does not exceed 50 %, unlike pillar-textured materials, that are usually covered with water after several tens of minutes with a fraction of more than 65%. A mechanism

involving spontaneous jumping-droplet must be at stake here again, although the breath figures dramatically differ from those obtained for nanometric cones where drops radii never exceed 40 μm.

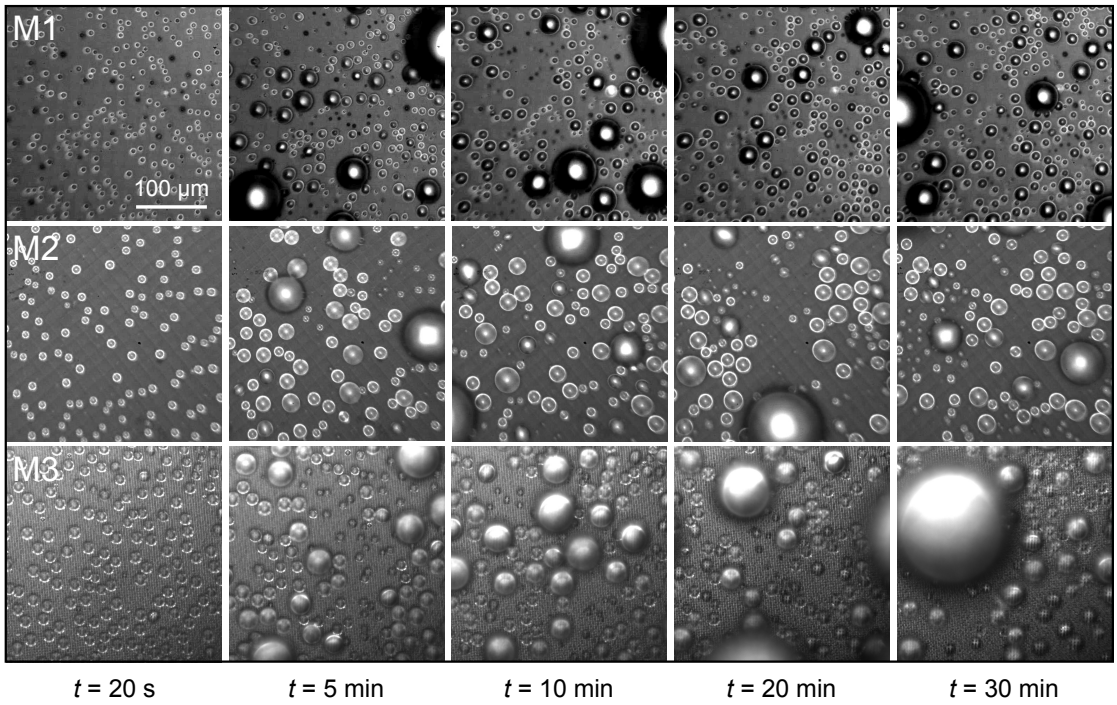

Figure 4.24: Breath figures on samples M1, M2 and M3 under an optical microscope after 20 s, 5 min, 10 min, 20 min and 30 min. The room temperature is $T = 21 \pm 1°C$, relative humidity $RH = 52 \pm 2\%$ and sample temperature is $T_s = 4 \pm 1°C$, which corresponds to a supersaturation $S = 1.6 \pm 0.2$ (ratio between vapour pressure at laboratory temperature T and saturated vapour pressure at surface temperature T_s). At large time, the surface covered by water increases with the cone size.

4.6.5.2 Antifogging efficiency

We present in Figure 4.25a the jumping rate N and its evolution with time. Interestingly, many differences can be noted between the three surfaces and with the case of nanocones:

(1) At short time, while N is essentially 0% for M2 and M3, it jumps up to 70% for M1. This increasing phase is later observed for the two largest pitches where N rises up to 60% and 25% respectively. The three maximum values of N evolve monotically with the texture size.

(2) After this rising phase, the jumping rate decreases for the three surfaces.

(3) Finally, for $t > 500$ s, N plateaus at a value that varies between the three surfaces, with $N = 45$, 35 and 15% for samples M1, M2 and M3. Again, the steady state values are ranked according to the texture size: it is maximum for the lowest pitch p (M1) and it decreases with p. These three values contrast with the large ones obtained on nanocones where N gravitates around 90%. Thus, droplet jumping may be partly inhibited on microcones with a magnitude that increases with their size.

Similarly, if we now examine the jumping rate N as a function of the common radius $< r >$ for symmetric coalescences (Figure 4.25b), experimental data present notable differences in comparison with those obtained on nanocones: small drops never jump for radii smaller

than a minimum radius r_m where N starts increasing until reaching $\sim 100\%$, and larger drops always jump despite thin anchoring in the texture (Figures 4.17 and 4.19). However, r_m varies with texture size and is found to be 4.0 ± 0.5 μm, 7.0 ± 0.5 μm and 9.6 ± 0.5 μm for the samples M1-3. After crossing this critical radius, N increases but with a different slope: the larger the texture size, the smaller the slope. Indeed, N varies from 0 to 100% in respectively 6, 7 and 10 μm. This scenario contrasts that obtained for nanocones where N increases swiftly in 2 μm from 0 to 100% for $r_m \approx 1$ μm. It is mainly due to scale effects as the influences of heterogeneities (drop radii, cone size) are reinforced at larger sizes. Hence, the cutoff radius r_c, *i.e.* the radius when $N = 50\%$ (as for nanocones), is a better quantity to examine and we measure $r_c = 6.3$, 9 and 15 μm. We shall come back to this point in Subsec. 4.6.6. For microcones, we can now rationalize the observations of Figure 4.25a: at short time, drops are small and do not jump after coalescence, and even more for the largest texture, which explains the low values of N. After drops have reached a sufficient size, jumping can occur but it is partly inhibited by the presence of small drops, leading to asymmetric coalesences, and thus to a lower steady state value of N.

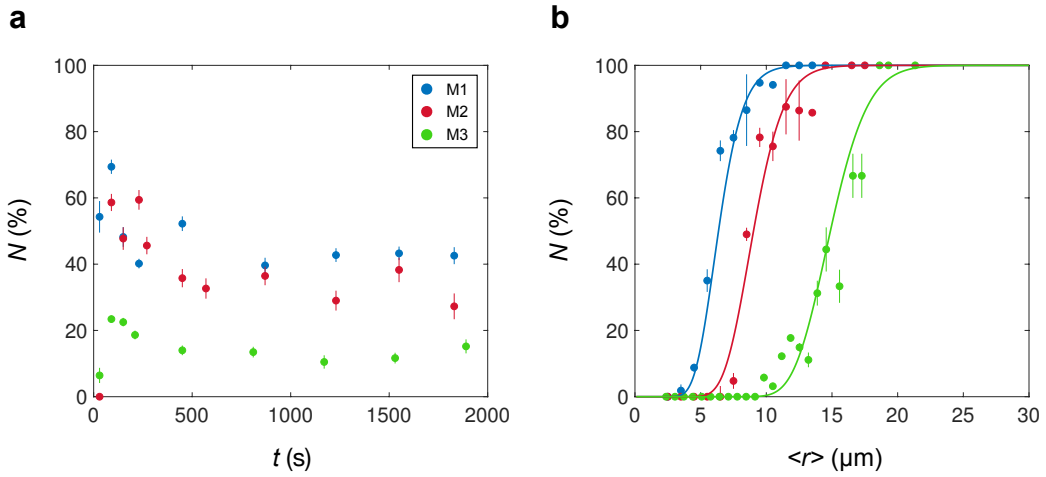

Figure 4.25: (a) Jumping rate N as a function of time t for samples M1 ($p = 500$ nm - blue data), M2 ($p = 1.6$ μm - red data) and M3 ($p = 2.4$ μm - green data). Each point is obtained after averaging the proportion of jumps over one minute. Differences in performance clearly appear between the three samples. (b) Antifogging ability N as a function of $< r >$, the common radius ($r'/r > 0.8$) of coalescing drops. Defining the cutoff radius r_c for $N = 50\%$, we find $r_c = 6.3$, 9 and 15 μm for the materials M1, M2 and M3, respectively. At large radii, N always reaches $\sim 100\%$. Solid lines are guides for the eyes.

In agreeement with the previous observations, the area fraction ϕ covered by water is found to be slightly larger than 35%, the average steady state value measured on nanocones (Figure 4.26): ϕ stabilizes around similar values between the three samples, $\phi = 40 \pm 3\%$. In order to elucidate these findings, we now focus on the water configuration inside texture during condensation.

4.6.5.3 Influence of height

Based on our observations, droplet jump seems only influenced by the number of wetted cells and their width, that is a function of the pitch p and not the height h. To verify this hypothesis, we have resorted to another sample named M3'. It has quite the same characteristics as M3 but a smaller cone height: its respective pitch, cone height and diameter are $p = 2.4$ μm, $h = 3.6$ μm and $d = 1.6$ μm. For this sample, one also has $E^\star < 1$ (favoured upward growth) and experiments do confirm that a unit cell remains filled after droplet jump,

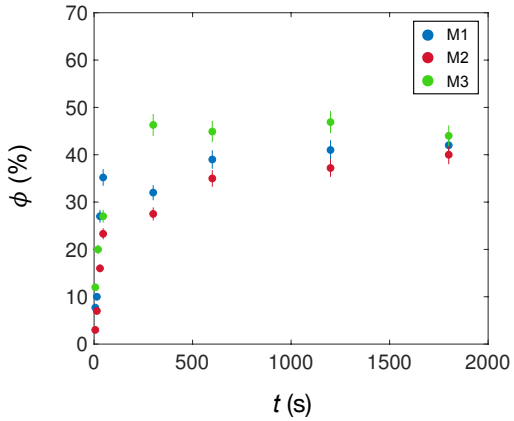

Figure 4.26: Time evolution of the area fraction ϕ covered by water for the M family. The differences at large time reflect the observations made earlier.

as for M3. We compare in Figure 4.27 the jumping rates N as a function of the common radius $< r >$ for symmetric coalescences on both surfaces. Remarkably, data collapse on the same curve, which shows that cones' height does not influence jumping, taking all other parameters constant.

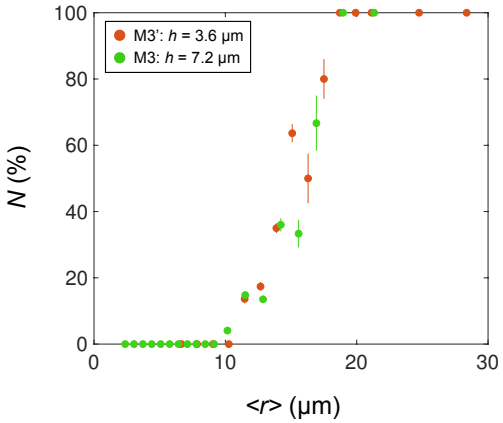

Figure 4.27: Comparison of the antifogging abilities of samples M3 and M3' that have same pitch $p = 2.4$ μm but different cone heights ($h = 7.2$ and 3.6 μm respectively). Jumping rate N as a function of the common radius $< r >$: both data collapse on the same curve, which shows the low influence of h on the jumping efficiency.

4.6.5.4 Critical jumping radius

Let us now develop a model to predict the critical jumping radius for symmetric coalescences. Compared to nanocones, condensed droplets are pinned on n_c unit cells in microcones. Based on our previous findings, we can estimate the adhesion E_{pinned} associated with the pinned regions. Because the cells remain filled after jump, the energy to separate the droplet from a unit cell is $2\gamma p^2$ (Eq. (4.14)). For n_c pinned cells, one obtains then $E_{\text{pinned}} = 2\gamma n_c p^2$. This energy can be seen as the work of the force F_{pinned} over the pinned neck length, that is $\sqrt{n_c}\, p$. It then reads:

$$F_{\text{pinned}} \approx 2\gamma\sqrt{n_c}\, p \ , \tag{4.15}$$

with the corresponding momentum $P_{\text{pinned}} = F_{\text{pinned}}\,\tau_r$, denoting τ_r as the droplet retraction time. The residual adhesion generated by the depinning of the contact line is also incorporated, as in Chap. 3: $E_{\text{a}} = \pi r^2 \gamma \sin^2\theta_r(1+\cos\theta_r)$, where θ_r is the receding angle. As for nanocones, we assume that $\tau_r = 2(\rho r^3/\gamma)^{1/2}$, a scaling already observed for partial Cassie droplets [65], and the retraction speed v is $v = r/\tau_r$. The momentum transfer is finally written as:

$$2mU = mv - (F_{\text{pinned}} + F_{\text{v}} + F_{\text{a}})\,\tau_r \ , \tag{4.16}$$

where F_{v} is the force associated with viscous dissipation, $F_{\text{v}} \approx (2\pi\eta/3)(\gamma r/\rho)^{1/2}$. The ratio $F_{\text{pinned}}\,\tau_r/mv$ scales as $\sqrt{n_c}\,p/r$, which suggests a critical radius r where $U = 0$ with a value on the order of the texture size. Setting $U = 0$ in Eq. (4.16) yields the following equation for the droplet radius r:

$$\alpha - \frac{4\eta}{\sqrt{\rho\gamma r}} - \frac{12}{\pi}\frac{\sqrt{n_c}\,p}{r} = 0 \ , \tag{4.17}$$

where we introduce again the parameter $\alpha = 1 - 6\sin^2\theta_r(1+\cos\theta_r)$ and we choose the value $\theta_r = 166°$ for our model, that is, the mean of the measured receding angles on the M family (Table 4.2). We name x the quantity $\sqrt{n_c}\,p$. For sufficient x and because viscosity is negligible at that micrometric scale, Eq. (4.17) can be solved as:

$$r \approx \frac{12x}{\pi\alpha} + \frac{4\eta}{\alpha\sqrt{\rho\gamma}}\left(\frac{12x}{\pi\alpha}\right)^{1/2} + \frac{8\eta^2}{\alpha^2\rho\gamma} \ . \tag{4.18}$$

Eq. (4.18) yields the threshold radius for jumping, after considering totally symmetric drops. Our experiments have provided us with two quantities, the minimum jumping radius r_m, that is when the jumping rate N starts becoming non-null, and the critical jumping radius r_c, when $N = 50\%$. It is tricky to distinguish which of the two quantities is most suitable. For nanocones or small microcones (M1 and M2), the two quantities are found almost equal. However, for M3, one has $r_m = 9.6$ μm, to be compared with $r_c = 15$ μm, hence a huge discrepancy. We show in the next subsection (see Subsec. 4.6.6) that the slope of N is directly influenced by the relative asymmetry between drops (here $r'/r > 0.8$). Consequently, one expects that the shape of N resembles that of a step (or heaviside function) centered on r_c ($N = 50\%$), when drops are totally symmetric ($r'/r = 1$). Thus, the quantity r_c is the most suitable for comparison with the solution given Eq. (4.18).

Eq. (4.18) is drawn in black solid line in Figure 4.28 as a function of $x = \sqrt{n_c}\,p$, the wetted cells length, together with the experimental data (red dots). We choose the coefficient 4.9 instead of 4 in front of $\eta/(\rho\gamma r_c)^{1/2}$ (Eq. (4.17)), as in Chap. 3, which modifies a little Eq. (4.18). Let us remind that our experiments yield respective $r_c = 6.3$, 9 and 15 μm for M1, M2 and M3 and a good agreement is observed between the model and the data. Despite the simplicity of our model, Eq. (4.18) manages to describe correctly the evolution of r_c with texture size and it explains why larger cones induce high jumping radii, a consequence of adhesion generated by wetted cells.

4.6.6 Discussion

The jumping rate N plotted as a function of the common radius $<r>$ (Figure 4.25b) for the three materials covered with microcones has evidenced differences in behaviour as the slope of N decreases with texture size. Similarly, the same quantity plotted for nanocones exhibit an even sharper transition from 0 to 100 %, in only 2 μm. As in Sec. 4.5, to visualize this scale effect, N is shown as a function of the normalized radius $\bar{r} = <r>/r_c$ (Figure 4.29a), that is the common radius divided by the critical jumping radius r_c, and

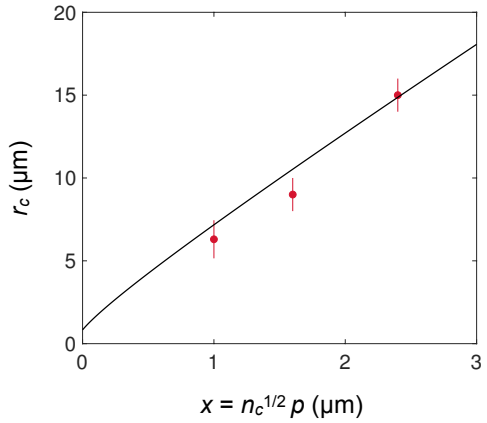

Figure 4.28: Critical jumping radius r_c as a function of the pinned neck length $x = \sqrt{n_c}\,p$. For M1, one has $x = \sqrt{n_c}\,p = 1$ μm and for M2 and M3, it is equal to p. Eq. (4.18), drawn in solid line, matches well the experimental data (red dots).

for the four materials N1, M1, M2 and M3, with pitch varying from 50 nm to 2.4 μm. Remarkably, all data collapse on the same curve and are centered in $\bar{r} = 1$. The evolution of N with $\bar{r}$ can again be assimilated to a phase transition from the state non-jumping ($N = 0\%$) to total jumping ($N = 100\%$). The relative width of the curve (width during which N transitions from 0 to 100%) can be due to several factors such as heterogeneities of radius (here $\Delta r/r = 0.2$) or cones' size which induces differences in adhesion.

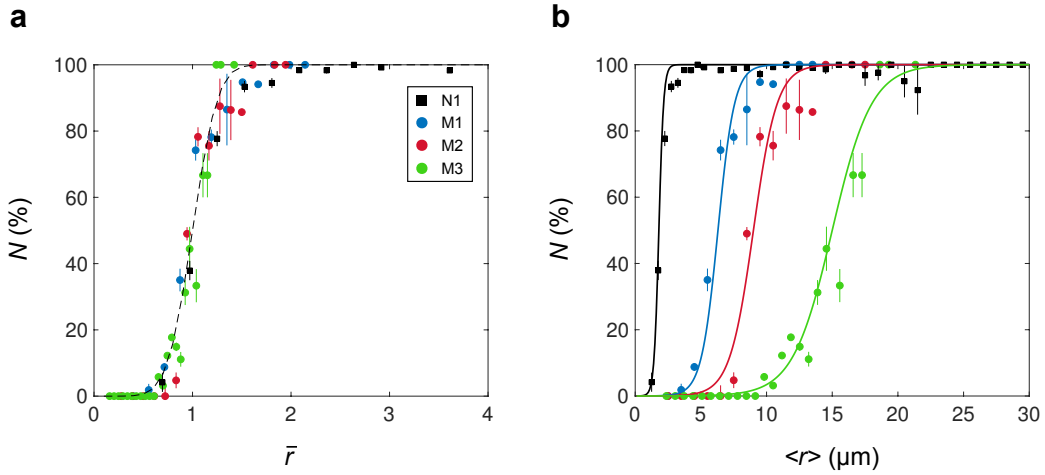

Figure 4.29: (a) Jumping rate N as a function of the normalized radius $\bar{r} = < r > /r_c$ for the four materials N1 ($p = 52$ nm - black squares), M1 ($p = 500$ nm - blue dots), M2 ($p = 1.6$ μm - red dots) and M3 ($p = 2.4$ μm - green dots) and their respective critical jumping radii $r_c = 1.8$, 6.3, 9 and 15 μm. All data collapse on the same curve and are nicely fitted by Eq. (4.6) with $\sigma = 0.2$, the width of the asymmetry ratio: $N(\bar{r}) = 50 + 50 \tanh[(\bar{r} - 1)/\sigma]$. (b) N as a function of the common radius $< r >$ for the 4 surfaces. Solid lines show Eq. (4.7) and describe well the evolutions of N: $N(r) = 0.5 + 0.5 \tanh[(r - r_c)/\sigma r_c]$.

We resort to Eq. (4.6) to model the phase transition and choose as before $\sigma = 0.2$, as the standard deviation of radii is $\Delta r/r = 0.2$: $N(\bar{r}) = 0.5 + 0.5 \tanh[(\bar{r} - 1)/\sigma]$. Thus, Eq. (4.6) is drawn in dashed line in Figure 4.29a and matches very well the data. Similarly, modelling N as a function of r_c yields Eq. (4.7), shown in solid line in Figure 4.29b for the four

materials N1, M1, M2 and M3 and it is found to describe the whole ensemble of data. This study shows that a finite size scaling is possible for that type of systems, like in statistical physics.

4.6.7 Conclusion

Antifogging abilities are influenced by both the texture size and the texture shape. Before our experiments on microcones, there was not a clear hierarchy between which of the two effects is the most important for repelling dew. Our study has shown that micrometric cones can expel condensed droplets unlike pillars at the same scale - the first ever seen case of drop departure on micrometric features. Hence, we can conclude that the texture shape is the most significant aspect for repelling condensation. Compared to nanocones, microcones expel only larger drops, yet with the maximum possible rate (around 100%): this property remains of high practical interest since larger drops carry most of the mass of water, showing that the content expelled out of the surface is comparable in both cases.

4.7 Truncated cones

We have presented the antifogging efficiencies of surfaces covered with sharp nano and microcones. Because of the scale, filled cells cannot develop in nanocones and condensed droplets lie in a non-wetting state, hence promoting spontaneous jumping after coalescence. Cones present two advantages compared to pillars: they favour the Cassie morphology and lower contact angle hysteresis because of their sharp tips that prevent pinning. To estimate the latter effect, we wonder here how truncated nanocones behave under fog conditions.

4.7.1 Surfaces

As presented in Chap. 2, three surfaces named NT1-3 and composed of truncated cones are tested (Table 2.2). Their pitch p is respectively 93, 105 and 115 nm, close to 110 nm, the pitch of samples N3-N7. The cones are truncated at a different height, which yields top diameters t of respectively $t = 42$, 53 and 60 nm. We can estimate the solid fraction $\phi_s = \pi t^2/2\sqrt{3}p^2$, that represents the fraction of water in contact with the tops for a drop in a Cassie state for a hexagonal array. We report its three values along with the advancing and receding angles in Table 4.3.

Sample	**Advancing angle θ_a (°)**	**Receding angle θ_r (°)**	**Solid fraction ϕ_s (%)**
NT1	164 ± 1	138 ± 1	18.5
NT2	163.5 ± 2	130 ± 1	22.2
NT3	160.5 ± 1	131 ± 2	24.7

Table 4.3: Contact angles and solid fractions of the NT family.

Similar to cones, the NT family exhibits high advancing contact angles (ϕ_s is still small), but the receding angles have much lower values. This difference originates in the pinning of the contact line at the top edge of the truncated cone. This is in agreement with Patankar's remark, that in the case of flat posts, the contact line leaves behind a thin layer of liquid during the receding motion [106]. In the Cassie-Baxter equation, the receding angle θ_r would then be given by $\cos\theta_r = \phi_s \cos 0 + (1 - \phi_s)\cos\pi$, as the drop lies on solid with a fraction ϕ_s and on air with $1 - \phi_s$. The expression of the receding angle can then be rewritten as [106]:

$$\cos\theta_r = 2\phi_s - 1 \ . \tag{4.19}$$

For our samples, Eq. (4.19) predicts $\theta_r = 129°$, 124° and 120.5° for the samples NT1-3, that is 10% smaller than the measured angles (Table 4.3), yet in agreement with their dependence on ϕ_s and it explains why θ_r decreases on truncated cones.

4.7.2 Antifogging abilility

Images of water condensation on the three NT samples at different times are shown in Figure 4.30. At small time, breath figures are similar and droplets have radii as large as 15 μm, slightly bigger than on nanocones ($\sim$ 10 μm). However, with time, drops larger than 100 μm are observed and the area fraction covered by water increases. This phenomenon is seen for all the surfaces and we now present their antifogging abilities to rationalize these observations.

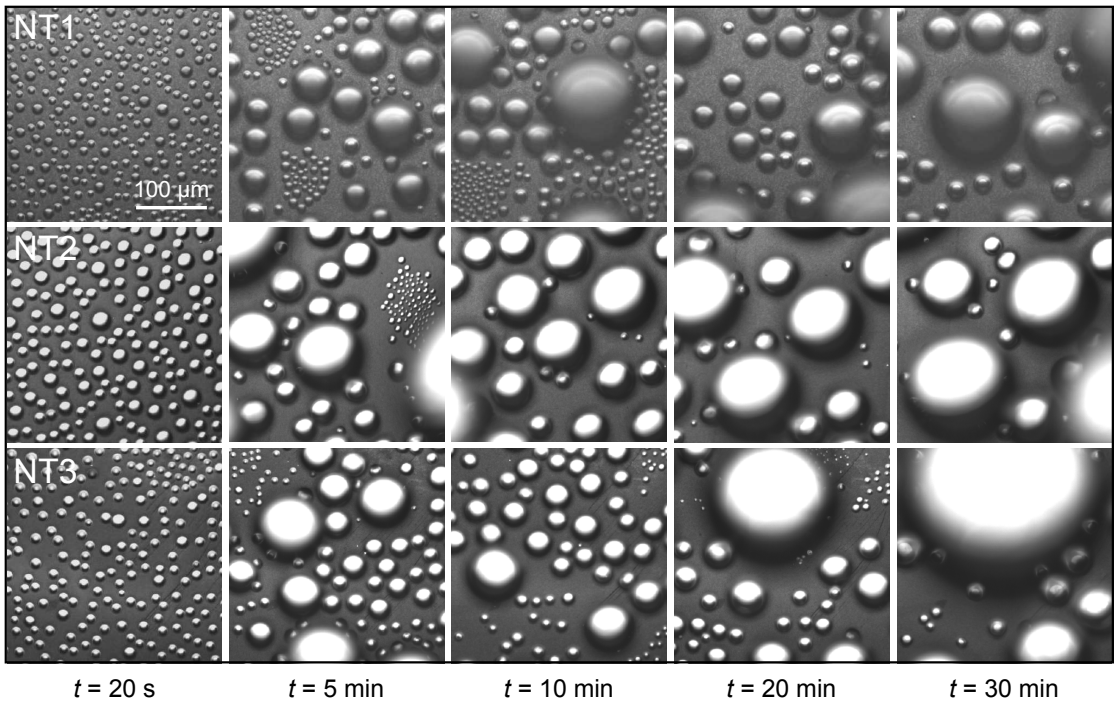

Figure 4.30: Breath figures on the NT family under optical microscope after 20 s, 5 min, 10 min, 20 min and 30 min. The room temperature is $T = 21 \pm 1°$C, relative humidity $RH = 52 \pm 2\%$ and sample temperature is $T_s = 4 \pm 1°$C, which corresponds to $S = 1.6 \pm 0.2$. At large time, all samples are covered by a large fraction of water.

We compare in Figure 4.31a the time evolution of the jumping rates N of the NT family and superimpose data obtained for sample N5 (p = 110 nm and h = 250 nm) because of its similar cone angle and pitch. On truncated cones, data are markedly different than that with nanocones: N drops to an average value of $\sim$ 2% with tiny variations between samples: N is maximum for sample NT1 with 2% and goes to 1.5% for NT3. These values contrast with the high antifogging efficiency of nanocones ($N \approx 90\%$), yet truncated nanocones perform much better than a surface covered with nanopillars of same size (surface A) where $N \approx 0.2\%$. Furthermore, on all samples, none of the two-droplet coalescences lead to jump and all jumps come from coalescences of four or more droplets where at least one of them has a radius larger than 30 μm. The area fraction covered by water reflects this decrease in antifogging ability (Figure 4.31b): ϕ stabilizes around 60%, in contrast with the 35% measured on nanocones but with comparable value, yet slightly lower, to that obtained on nanopillars or Glaco (hydrophobic silica nanobeads) where $\phi \approx 70\%$ [1].

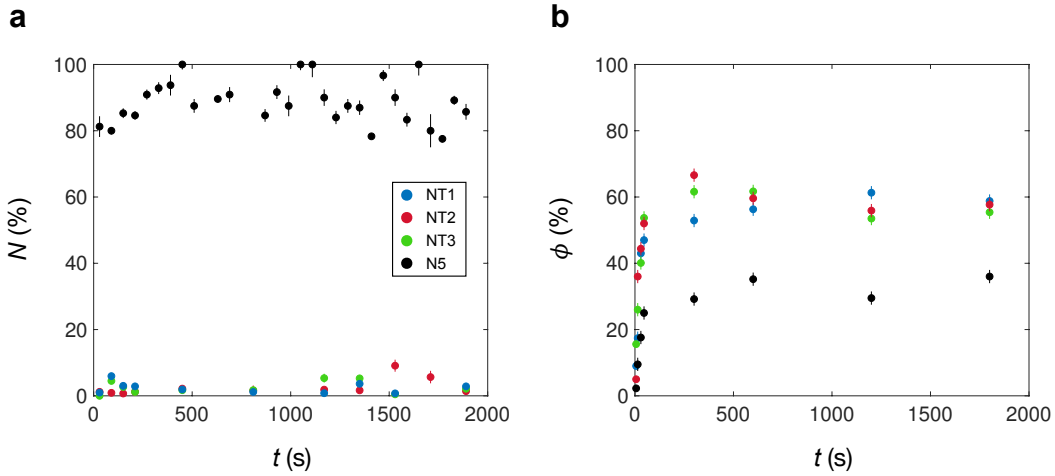

Figure 4.31: (a) Time evolution of the jumping rate N for the NT family and surface N5. For truncated cones, $N \approx 1.5\%$ compared to nanocones where $N \approx 90\%$ (b) Time evolution of the area fraction ϕ for the NT family. At large time, ϕ converges towards $\sim 60\%$ for all surfaces, that is, much higher than the value measured on nanocones ($\phi \approx 35\%$).

The critical jumping radius r_c for two-droplet symmetric coalescences can now be estimated. Drops condensing on truncated nanocones should lie on the top of the structures with no pinned cell owing to the cone shape. ESEM experiments confirm this hypothesis, as illustrated in Figure 4.32 that shows images of water condensation on NT1 (a) and NT3 (b). On both materials, droplets of all sizes exhibit large contact angles and their quasi-spherical shape indicates they are in Cassie state. This is further confirmed by plotting the advancing contact angle θ_a as a function of the droplet radius r for the two samples (Figure 4.33): similar to N7 (see Chap. 2), for both samples, θ_a increases for $r < 2$ μm and reaches already 160° for radii as small as 2 μm and increases up to θ_a^{app} (dashed lines), the contact angle of millimetric drops (Table 4.3), and even sometimes with higher values (as also noted in Chap. 2).

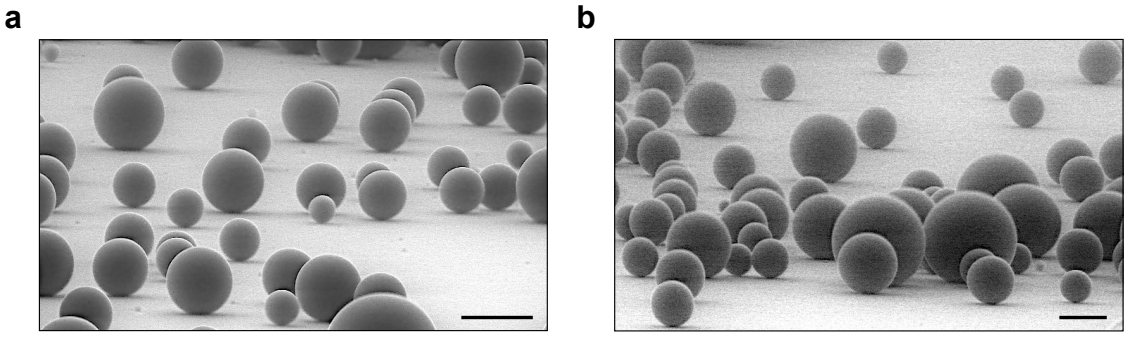

Figure 4.32: ESEM images of water condensation on NT1 (top diameter $t = 42$ nm) (a) and NT3 ($t = 60$ nm) (b). All droplets exhibit a quasi-spherical shape and their contact angles approach $\sim 160°$. Their low contact area with the solid suggests a Cassie state. Both scale bars indicate 10 μm.

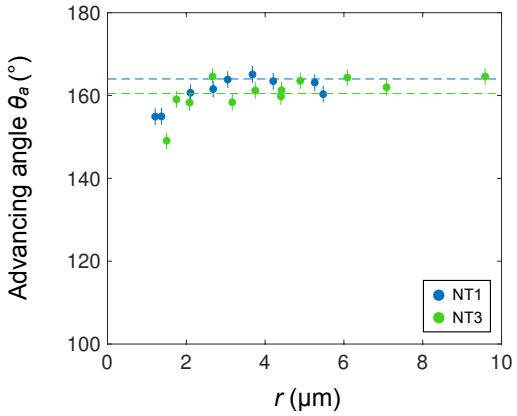

Figure 4.33: Advancing contact angle θ_a as a function of the drop radius r for samples NT1 and NT3. θ_a increases towards the value measured on millimetric drops (dashed lines): $\theta_a^{app} = 164 \pm 1°$ and $160.5 \pm 1°$ for NT1 and NT3, respectively.

4

Consequently, our model for the jumping velocity (see Chap. 3) can be used. In order to predict the threshold radius of jumping r_c, we set the jumping velocity $U = U^\star[\alpha - 4Oh]$ equal to 0 in Eq. (3.8), which yields:

$$r_c = \frac{\eta^2}{\rho\gamma\left[1 - 6\sin^2\theta_r(1+\cos\theta_r)\right]} \ . \tag{4.20}$$

This equation defines a critical Ohnesorge number $Oh_c = \eta/(\rho\gamma r_c)^{1/2}$ as a function of the receding angle θ_r: $Oh_c^2 = 1 - 6\sin^2\theta_r(1+\cos\theta_r)$. Eq. (4.20) yields $r_c = 9$ μm for NT1 and $r_c < 0$ for NT2 and NT3 meaning that no jumping should occur. Eq. (4.20) predicts a correct behaviour for the latter surfaces but not for NT1 where jumping is expected. The origin of this discrepancy may lie in an additional adhesion that exists during coalescence: when two droplets coalesce, a bridge form and later impacts the surface before the resulting drop takes off or not. This additional liquid-solid contact generates a dissipation proportional to the hysteresis $\Delta\theta = \theta_r - \theta_a$. Indeed, the bridge expands on the surface with an angle θ_a and will retract with an angle $\theta_r < \theta_a$. This adhesion was neglected for sharp cones because of the low hysteresis ($\Delta\theta < 10°$). However, for pillars or truncated cones, $\Delta\theta$ can be as important as 40°. We assume a liquid-solid contact with radius $\sim r\sin\theta_a$ for two coalescing droplets with radii r. The additional adhesion E_b then scales as $E_b \sim \pi r^2\gamma\sin^2\theta_a(\cos\theta_r - \cos\theta_a)$. If we add this term in our model, we find a modified expression for r_c:

$$r_c \approx \frac{\eta^2}{\rho\gamma\left[1 - 6\sin^2\theta_r(1+\cos\theta_r) - 6\sin^2\theta_a(\cos\theta_r - \cos\theta_a)\right]} \ . \tag{4.21}$$

This law predicts $r_c \approx 20$ μm for NT1, more than twice larger than predicted by Eq. (4.20). However, two-droplet coalescences with radii larger than r_c are never observed. First, the mean separation distance l between nuclei is found around 20 μm, that is much smaller than the distance between two drops with radii $r > r_c$ (distance > 40 μm). Secondly, as stated by Patankar, when droplets coalesce, they can leave a thin layer of water at the top of the cones [106]. This phenomenon is evidenced in Figure 4.34: after the jump of several droplets, tiny droplets are left (2^{nd} image). The presence of such droplets favours asymmetric coalescences and increases the number of droplets, hence making impossible the symmetric coalescences between droplets with radii as large as 20 μm.

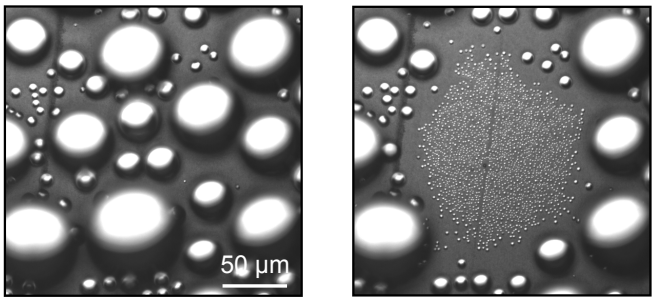

Figure 4.34: Top images of the coalescence of several droplets condensing on sample NT2 (p = 105 nm and t = 53 nm) before and after their jump. The right image (t = 4 s) highlights the presence of multiple microdroplets after the jump, a consequence of the water left behind on the top of posts during the receding motion of droplets.

4.7.3 Conclusion

We described in this section the case of truncated nanocones, an intermediate situation between nanopillars and nanocones. Because of the flat tops of the structures, a significant contact angle hysteresis is observed, which inhibits the antifogging efficiency that yet, slightly outperforms that of nanopillars. A further step would be to study less truncated nanocones, which should increase the receding angle and fill the gap between truncated cones and cones. Indeed, truncated cones can be promising because they present the advantage of a better resistance to compression compared to sharp cones, hence a great potential for industrialization.

4.8 Discussion

This systematic study on surfaces covered with cones of size ranging from 50 nm to 2.4 μm has enabled us to understand the influence of texture scale and shape on the antifogging ability. Nanocones promote non-wetting states for condensed droplets because their shape and size push nuclei to grow up the texture and lie on their top, namely in a Cassie state. In addition, for cones with sizes smaller than 100 nm, Van der Waals forces are significant and may induce liquid dewetting in the cavities. It results in remarkable antifogging abilities with more than 90% of drops ejected and a minimum jumping radius of 1 μm, independently of the cone size. In contrast, spinodal dewetting cannot be statisfied for microcones so that nuclei that form within unit cells fill them, and drops then develop beyond the structures and exhibit partial Cassie wetting state. Because of liquid pinned in cells, antifogging efficiency decreases because the critical radius of jumping r_c increases with the microcones size. However, the jumping rate remains extremely high above r_c, a consequence of the state of water in such partial Cassie states - showing that the shape effect (conical structure) is a key feature at any scale for repelling water at a small scale. Finally, jumping-droplet condensation is marginal on samples composed of pillars owing to the wetting states adopted by condensed drops on such texture and to the shape of posts that favours pinning, hence decreasing the receding angle. To that end, truncated nanocones were used to examine the latter phenomenon. Our experiments show the importance of having sharp tips to enhance antifogging as the jumping rate drops to few percents on materials covered with conical pillars.

Take home message of Chapter 4

1. Nanocones. Hydrophobic materials covered with nanocones exhibit high antifogging abilities with more than 90% of ejected droplets. This quantity, as well as the minimum jumping radius ($\sim$ 1 μm), is little influenced by the texture characteristics (pitch, height and cone angle).

2. Spontaneous dewetting. A water nucleus developing at the bottom of nanocones may spontaneously depin from the surface because of disjoining pressure that generates spinodal dewetting for sizes smaller than 100 nm. The creation of a liquid-vapour interface followed by condensation growth pushes the nucleus upwards owing to the cone shape. The water droplet eventually lies at the tops of the cones in a Cassie state. In this morphology, the influence of texture size is negligible, which explains why behaviours are similar on different textures.

3. Microcones. Surfaces composed of microcones favour partial Cassie morphologies, where a few unit cells are filled with water. This wetting state decreases the antifogging efficiency of micro-textured surfaces (droplets remain stuck), but preserves the possibilities of massive drop ejection above a threshold in drop size.

4. Truncated cones. When cut at their top, nanocones cannot repel efficiently dew as their flat tips induce high contact angle hysteresis. Despite exhibiting Cassie states, droplets rarely depart the surface.

5

Repelling hot water

How to repel hot water is an issue that has been poorly addressed despite its importance in industrial processes such as clothing, coating, painting or windshield design. This class of questions also includes the early stages of ice formation and accretion, potentially leading to serious damages to aircrafts, power lines, dams or wind turbines. We wonder here how just the texture size may control the behaviour of hot water at impact. We first introduce our experimental set-up. Then, the results of our experiments on four materials and their different behaviours towards hot water impacting them are shown. Finally, a model for the adhesion induced by condensation is developed and compared with the experiments.

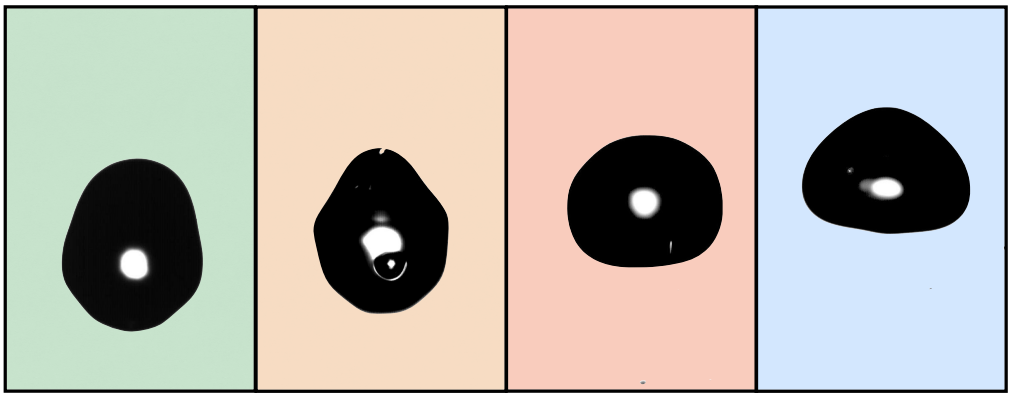

Drops bouncing on non-wetting surfaces.

Contents

This work was a collaboration with Timothée Mouterde as we were both PhD students and it was a pleasure for me to work together. It was first initiated by him and this study has been published in *Nature Communications* (see Appendix B).

5.1 Introduction

While most rough, hydrophobic materials repel rain in a dry atmosphere, humid conditions or dew repellency are much more challenging, as water nuclei condensing in the texture are then at the scale of the cavities, which fills the lubricating air layer and thus destroys superhydrophobicity [26, 28]. In this context, it is not surprising that hydrophobic microtextures most often lose their superhydrophobicity when impacted by hot drops [107, 108], except if the solid itself is hot [109]. The contact, even short, of hot water with a colder substrate promotes condensation within the microcavities at the solid surface, so as to bridge the incoming water to the solid that it hits. This modification of properties occur when the phase change (from vapour to liquid or liquid to ice) typical time becomes shorter than the contact time of the impinging water. A first idea to shorten the contact between the drop and the substrate was achieved by tailoring large surface "defects" [110, 111, 112]. By introducing macrotextures on superhydrophobic surfaces, the authors were able to drastically reduce the drop contact time. Gauthier *et al.* [112], and more recently Chantelot *et al.* [113], managed to link the shape of the defect with the decrease in contact time. Furthermore, Shiri *et al.* recently evidenced that only 1% of the heat carried by a bouncing hot drop is transferred to the solid surface through conductive heat exchange [114]. In our study, we wonder how just the texture size may control the behaviour of hot water at impact.

5.2 Experimental set-up

5.2.1 Principal of the experiment

Our goal is to determine how water repellency is affected by condensation at impact, which we control through the temperature of impinging drops (Figure 5.1).

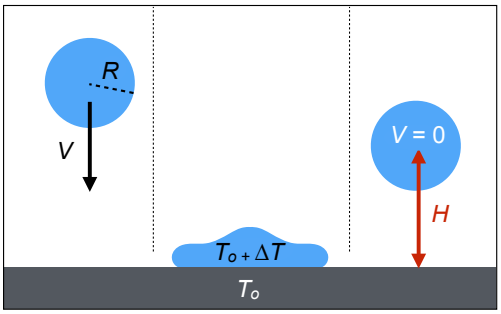

Figure 5.1: Schematic of the experiment: a water drop with radius R and temperature $T_0 + \Delta T$ impacts at velocity V a superhydrophobic substrate kept at T_0. We measure the maximum height H reached after impact (when the speed is null).

Water is brought to a temperature $T_0 + \Delta T$ and dispensed from a syringe kept at the same temperature. To achieve so, the syringe and the connecting tube are immersed in a thermostated liquid that controls the drop temperature. The thermostated water is contained in a cylindrical copper pipe closed with a brass plate where the needle is attached. We control the temperature via the voltage applied to a silicon heater mat. The syringe dispenses drops with a radius $R = 1.40 \pm 0.05$ mm and is held at a dispensing height $L \approx 1$ cm. After detaching from the needle, water drops impact the substrate and then rebound and we measure the height H reached. Substrates kept at $T_0 = 24 \pm 1°C$ and in a hygrometry of $32 \pm 2\%$ are impacted by drops at a velocity $V = 40 \pm 5$ cm/s. The corresponding Weber number $We = \rho V^2 R/\gamma$, that measures the importance of inertia over surface tension, is

around 3 and where ρ and γ are respectively the density and surface tension of water. In our experiment, We is larger than 1 which implies that the drop deforms significantly at impact and low enough to ensure that there is no splashing: one has $We\sqrt{Re} \approx 60 \ll 3000$, the threshold observed for splashing [115] and where Re is the Reynolds number, $Re = \rho VR/\eta$, with η the viscosity of water. Besides, images are captured from side-view using a high-speed videocamera (Photron FastCam Mini UX100) at a rate of 8 kHz. Using image processing, the relative position of the drop center of mass is obtained with time as well as the maximum elevation height H after rebound.

5.2.2 Surfaces used

Geometrical properties

Experiments are performed with model texture with size ranging from 100 nm to 10 μm. We use silica or silicon sculpted with cylindrical pillars (radius a, height h) which are disposed on a square lattice with pitch p (Figure 5.2). Surface A is fabricated by combining block-copolymer self-assembly with anisotropic plasma etching in silicon and has a roughness factor $r_{\mathrm{A}} \approx 4.5$ (see Chap. 2). Let us remind that the roughness factor is defined as $r = 1 + 2\pi ah/p^2$. Surfaces A' and B are fabricated by electron-beam lithography and anisotropic plasma etching in silica and have respective roughness factors $r_{\mathrm{A'}} \approx 3.4$ and $r_{\mathrm{B}} \approx 2.2$. Finally, suface C is obtained by photolithography and has a roughness factor $r_{\mathrm{C}} \approx 1.8$. All texture having a comparable geometry ($a \sim 0.1h$ and $p \sim h$), our materials are characterized by their pillar height h, of respectively ~ 100 nm, ~ 200 nm, ~ 1 μm and ~ 10 μm.

a

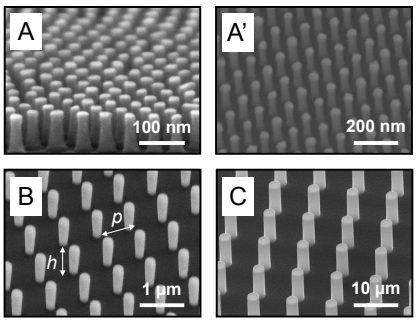

b

	p (nm)	a (nm)	h (nm)	r
A	52	15	88	4.5
A'	140	35	210	3.4
B	840	150	900	2.2
C	10^4	1500	10^4	1.8

Figure 5.2: (a) Scanning-electron viewgraph of the four substrates. (b) Dimensions of the four surfaces. All texture having a comparable geometry ($a \sim 0.1h$ and $p \sim h$), our materials are characterized by their pillar height h, of respectively ~ 100 nm, ~ 200 nm, ~ 1 μm and ~ 10 μm.

Wetting properties

Texture is finally rendered hydrophobic by vapour deposition of a hydrophobic molecule: 1H,1H,2H,2H-perfluorodecyltrichlorosilane and such treatment on flat silicon provides an advancing angle θ_a for water of 120° ± 2°. For the four surfaces, the resulting advancing angles are shown in Figure 5.3 and are respectively $\theta_a = 167°$, 155°, 168° and 169° (± 2°) on the rough materials A, A' B and C. The corresponding receding angles are $\theta_r = \theta_a$ - $\Delta\theta = 140°$, 132°, 143° and 152° (± 3°), providing contact angle hysteresis $\Delta\theta_{\mathrm{A}} = 27°$, $\Delta\theta_{\mathrm{A'}} = 23°$, $\Delta\theta_{\mathrm{B}} = 25°$ and $\Delta\theta_{\mathrm{C}} = 17°$. The four surfaces exhibit low contact angle hysteresis, typical for a superhydrophobic surface; and surface A has the highest one, a value that may be due to the relatively high solid fraction ϕ_s ($\phi_s = 2\pi a^2/\sqrt{3}p^2 \approx 26\%$), in comparison with that of the other materials.

	θ_a (°)	θ_r (°)	$\Delta\theta$ (°)
A	167	140	27
A'	155	132	23
B	168	143	25
C	169	152	17

Figure 5.3: Advancing and receding angles θ_a and θ_r of samples A, A', B and C along with their contact angle hysteresis $\Delta\theta = \theta_a - \theta_r$.

Control of the temperature

Water does not cool down during its fall, the dispensing height L being such that the falling time $(2L/g)^{1/2} \approx 40$ ms is negligible compared to the thermalizing time $\rho C_p R/H_T \approx 40$ s, where $\rho = 1000$ kg/m^3 and $Cp = 4180$ J.kg^{-1}.K^{-1} are the density and thermal capacity of water, and $H_T \approx 100$ W.m^{-2}.K^{-1} the heat transfer coefficient.

5

5.3 Experimental results

5.3.1 Qualitative results

Figure 5.4 displays high-speed snapshots (separated by 6.9 ms) of drop impacts on surface B ($h = 900$ nm) for two values of water/substrate temperature difference: $\Delta T = 0$°C (top) and 21°C (bottom). Without temperature difference ($\Delta T = 0$°C), water bounces off the solid, as also observed for all of our samples. This regular superhydrophobic behaviour can be understood by introducing a local Weber number [116, 117]: it compares the water dynamics pressure ρV^2 and the Laplace pressure γ/p opposing the penetration in pillars. In our case, $\rho V^2 p/\gamma$ is smaller than 0.01, hence the liquid never penetrates in the pillars and remains at their top, which makes rebounds possible. The last snapshot shows the maximum elevation H ($H \approx 3.2$ mm) of the drop and a strong deformation is notable at impact (maximum spreading radius of around 1.9 mm). However, when the drop temperature is elevated (bottom images), an impinging drop spreads identically as before but sticks to the sample B and the surface fails at repelling water. In that case, the elevation H remains very modest, on the order of R.

5.3.2 Quantitative results

Figure 5.5a shows impacting drops at their maximum bouncing height H for three values of drop temperature. As previously observed for substrate B, for $\Delta T = 0$°C, drops are reflected by the three other substrates. Nevertheless, contrary to surface B (Figure 5.4 bottom), for $\Delta T = 21$°C, drops rebound on surfaces A, A' and C. Finally, for $\Delta T = 40$°C, drops only bounce on surfaces A and C. These first observations indicate that repellency depends in a non-trivial way on the texture scale and water temperature.

Let us now introduce the restitution coefficient ε of the impacting drops to quantify the ability of a solid to repel hot water. Before impact, the kinetic energy of a drop with mass $M = (4\pi/3)\rho R^3$ is $E_b = (1/2)MV^2$. When a drop bounces to its maximum height H, the potential energy after take-off is $E_a = Mg(H - R)$. ε can be defined as $\varepsilon = E_a/E_b$, that is $2g(H - R)/V^2$. Besides, ε is taken null when drops stick to the surface ($H \approx R$). Our

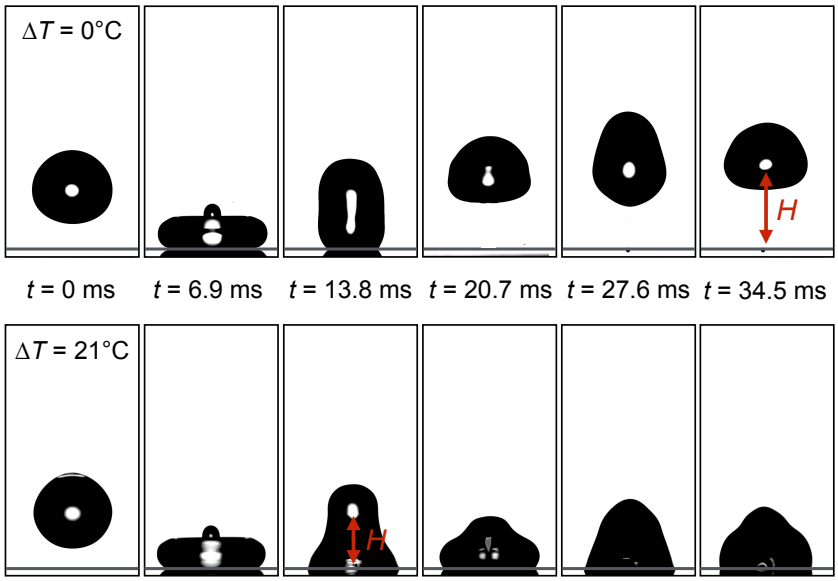

Figure 5.4: Snapshots of water drops ($R = 1.4$ mm) impacting the substrate B at $V = 40$ cm/s. Images are separated by 6.9 ms and the temperature difference ΔT between the drop and the substrate is either 0°C (top) or 21°C (bottom). Water bounces in the first case, but it gets stuck in the second one.

definition of ε allows us to distinguish bouncing ($H > R$, $\varepsilon > 0$) from sticking ($H \approx R$, $\varepsilon = 0$). For $\Delta T = 0$°C, this quantity, that we name ε_0, is known to depend on the impact speed and contact angle hysteresis.

Richard *et al.* [19] measured the quantity $|V'/V|$ on a superhydrophobic surface, where V' is the speed of the drop center of mass when it takes off the substrate. The quantity $|V'/V|$ is proportional to $\sqrt{\varepsilon}$. The authors observed that for low impact speeds ($V \approx 0.1$ m/s), ε increases with V, due to a minimal speed of rebound fixed by adhesion. Then, the restitution coefficient reaches a maximal value of around 0.8 for V between 0.1 and 0.3 m/s. Finally, for larger impact speeds, ε is observed to decrease with speed V and scale as $We^{-1/4}$ [118]. As reported by Biance *et al.*, this behaviour was attributed to viscous dissipation during impact and partition of the energy between drop oscillations and translation at take-off [118]. The higher the velocity, the larger the amplitude of oscillations, and thus the less elastic the shock. Furthermore, contact angle hysteresis generates dissipation at the contact line, hence a loss of energy [119]: a higher contact angle hysteresis leads to less efficient rebound. It is worth adding that the surface energy of a drop is modified at impact, owing to its oscillations at takeoff. This effect together with the contact angle hysteresis fixes the value of ε_0. Our goal is to see how we deviate from this value when water becomes hot ($\Delta T > 0$°C), that is, when condensation at impact is added to the process.

We report the variation of ε with ΔT in Figure 5.5b for the surfaces A, A', B and C. We split the data in two graphs, in order to distinguish the behaviour on nano and micro features, which highlights the different nature of repellency in these two cases. Much information can be extracted from these plots:

(1) At $\Delta T = 0$°C (where condensation effects are marginal), the coefficient of restitution slightly varies with the texture (of slightly different contact angle hysteresis), with a typical value $\varepsilon_0 \approx 0.2$ characteristic of superhydrophobic rebounds at such impact velocity [118]. ε_0 is the lowest for surface A ($\varepsilon_0 = 0.12$), in agreement with its high contact angle hysteresis ($\Delta\theta = 27°$); on the contrary, drops rebound the highest on surface C ($\varepsilon_0 = 0.29$), owing to the low contact angle hysteresis ($\Delta\theta = 17°$).

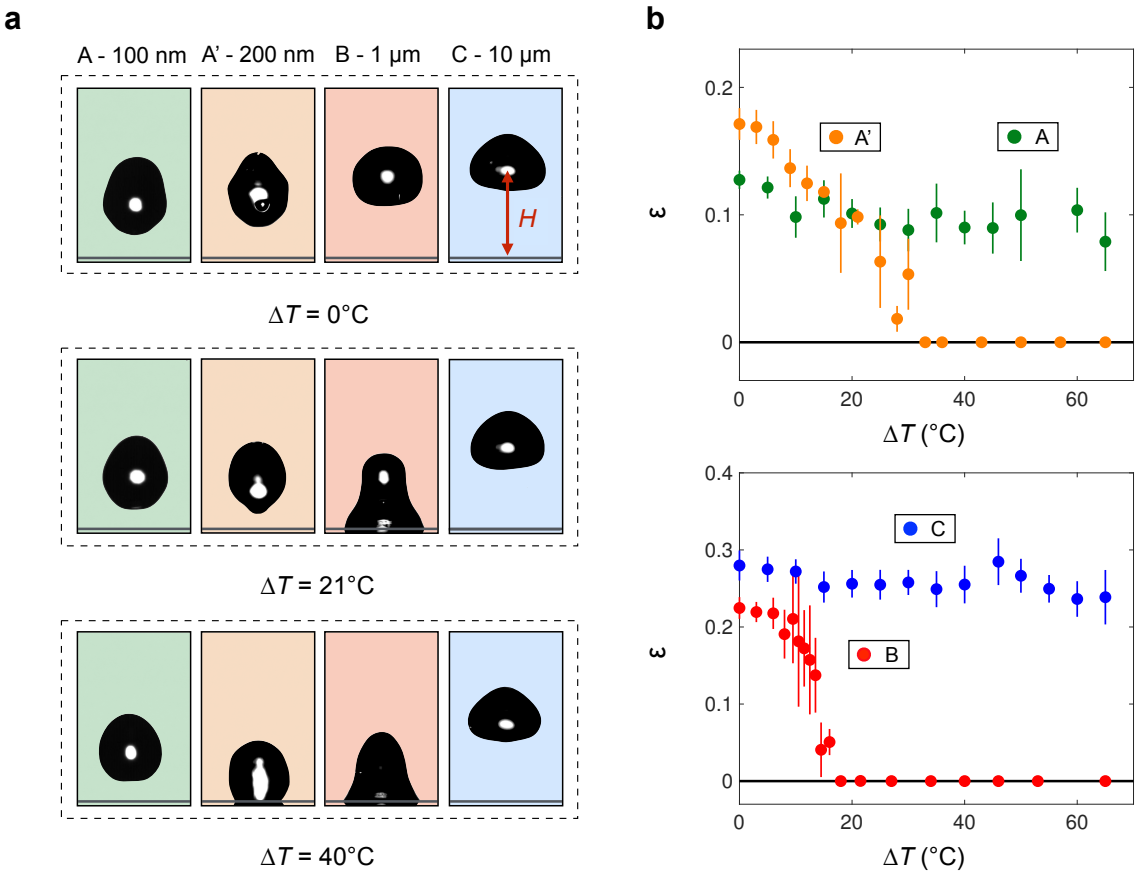

Figure 5.5: (a) Impacting drops ($R = 1.4$ mm and $V = 40$ cm/s) at their maximum bouncing height H for $\Delta T = 0$°C (top row), $\Delta T = 21$°C (middle row), $\Delta T = 40$°C (bottom row) on materials A, A', B and C with respective pillar heights of about 100 nm, 200 nm, 1 μm and 10 μm. (b) Coefficient of restitution ε of the rebound as a function of the temperature difference ΔT between water and the solid surface. For the sake of clarity, we separate data on nanometric features (top graph) from data on micrometric features (bottom graph). Water bounces on samples A and C at all drop temperatures, while it gets trapped on A' and B ($\varepsilon = 0$) when ΔT exceeds ~ 40°C and ~ 15°C, respectively.

(2) On the smallest features (green data, $h \approx 100$ nm), drops systematically bounce. However, we observe that ε slowly decreases with ΔT, showing a small, continuous loss of kinetic energy at take-off as water gets warmer. This effect is amplified when using larger features (orange data, $h \approx 200$ nm), for which the decrease of ε with ΔT becomes strong enough to intercept the abscissa axis in the range of explored temperature: drops hotter than 60°C do not bounce on the substrate A'.

(3) Observations are quite different with a micrometric texture. On the largest one (blue data, $h \approx 10$ μm), ε is quasi-independent of ΔT ($\varepsilon = 0.27 \pm 0.04$) in the whole range of explored temperatures, 0°C$< \Delta T <$ 65°C. This is a surprising result since we expect condensation to stick water all the more efficiently since ΔT increases [36]. At smaller scale (red data, $h \approx 1$ μm), the behaviour is markedly different: after a small plateau, ε tumbles around $\Delta T_c \approx 15$°C and water sticks to the surface above this value, as already seen in Figure 5.4.

5.4 Theoretical model

We now try to understand these observations by developing a model.

5.4.1 Condensation time

When hot water contacts a colder superhydrophobic material, water nuclei form and grow within the texture (Figure 5.6a). If they fill the elementary cells enclosed by neighbouring pillars (*i.e.* a square with size p), the resulting water bridges connect and stick the drop to its substrate (Figure 5.6b). The formation of a bridge requires a time τ that can be evaluated.

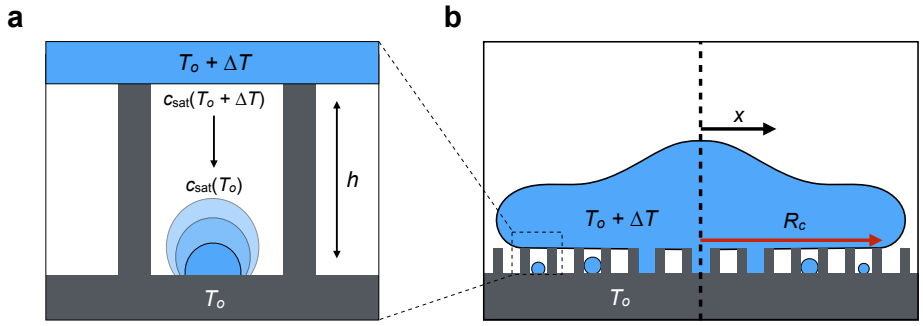

Figure 5.6: (a) Schematic of the growing nucleus under the hot drop in an elementary cell delimited by four pillars. Water vapour condenses on the nucleus creating a diffusing flow (indicated by the arrow) and makes it grow until it fills the cell with a time τ. (b) Sketch of the spreading drop. x is the radial distance from the impact point and R_c the contact radius.

We assume that condensation is driven by a diffusive flux of water from the evaporating interface to the growing nucleus, whose respective vapour mass concentrations are $c_{\text{sat}}(T_0)$ and $c_{\text{sat}}(T_0 + \Delta T)$. We assume that under the hot drop, which is at temperature $T_0 + \Delta T$, liquid is at equilibrium with its vapour (the time to saturate the air being much lower than the contact time of the drop): it imposes that the vapour partial pressure in water is equal to the saturated vapour pressure $P_{\text{sat}}(T_0 + \Delta T)$. This same condition is also assumed to be verified at the vicinity of the nucleus. Using Dalton Law, it yields:

$$c_{\text{sat}}(T) = \rho_a \frac{M_{H20}}{M_{\text{air}}} \frac{P_{\text{sat}(T)}}{P_0} \ , \tag{5.1}$$

where ρ_a is the density of air, M_{H20} and M_{air} the respective molar masses of water and air, $P_{\text{sat}}(T)$ the saturated vapour pressure of water at temperature T and P_0 the atmospheric pressure. $P_{\text{sat}}(T)$ can be obtained using Rankine formula: $P_{\text{sat}}(T) = P_0 \exp(13.7 - 5120/T)$. Finally, denoting $\Delta c_{\text{sat}}(\Delta T) = c_{\text{sat}}(T_0 + \Delta T) - c_{\text{sat}}(T_0)$, the diffusive flow rate can be described by a Fick law and scales as $D\Delta c_{\text{sat}}(\Delta T)/h$, where $D \approx 20$ mm^2/s is the diffusion coefficient of vapour in air. If we integrate this rate over the cell surface area p^2 and time τ, one obtains the mass of the filled cell, that is $\rho h p^2$. Because one has $h \sim p$ for our surfaces, τ finally reads:

$$\tau \sim \frac{\rho h^2}{D\Delta c_{\text{sat}}} \ . \tag{5.2}$$

In usual conditions ($T_0 \approx 24°$C) and for $\Delta T \approx 10°$C, one has $\Delta c_{\text{sat}} \approx 10$ g/m^3, which leads to $\tau \sim 1$ ms for $h \approx 1$ μm. τ increases by four orders of magnitude as h rises from 100 nm to 10 μm, and it can be compared to the contact time τ_r of bouncing drops. τ_r being the

response time of a spring with mass ρR^3 and stiffness γ, by analogy with the frequency of a harmonic oscillator, we have [68]: $\tau_r \sim (\rho R^3/\gamma)^{1/2}$. The two quantities ρ and γ vary little with temperature (respectively 3 and 10 % over the whole range of temperature) so one can neglect the variation of τ_r with temperature. The time τ_r is on the order of 10 ms for millimetric drops and thus possibly comparable to τ: as τ depends directly on the texture height h (increasing function of h), there is a texture (in the range of a few micrometres) for which we expect the two times to be equal, which allows us to model the different impacts. One must note that the different bouncing times τ_r are relatively similar between the four surfaces, varying from 15.5 to 17.4 ms. Based on this comparison, one expects that the different texture heights (two orders of magnitude between surfaces A and C) will induce different scenarii. Three cases must be distinguished: $\tau \ll \tau_r$, $\tau \sim \tau_r$ and $\tau \ll \tau_r$. Let us first consider the case when the condensation time τ is significant.

5.4.2 Large condensation time

When the condensation time τ is larger than the bouncing time τ_r, water nuclei are smaller than the roughness height h, as sketched in Figure 5.7a. As a result, they do not connect the impacting drop and condensation has no effect on the bouncing dynamics. As a consequence, the coefficient of restitution ε is equal to ε_0, its value at $\Delta T = 0°\text{C}$:

$$\varepsilon = \varepsilon_0 \ . \tag{5.3}$$

This mechanism explains the observations for the material C in Figure 5.5b: its large pillars' height ($h = 10$ μm) explains that $\tau > \tau_r$. Eq. (5.3) is plotted for surface C with a blue solid line in Figure 5.7b and captures very well the behaviour of ε with ΔT. Furthermore, Eq. (5.3) implies that a material with a tall texture can dynamically repel hot water, in stark contrast with the static case when the smaller, the better for repelling hot water [36]. In that case, the exposure time is on the order of the tens of seconds much larger than τ, which ensures that the water nuclei have filled their hosting cell. One must note however that if exposed longer to humidity, these texture will lose their superhydrophobicity.

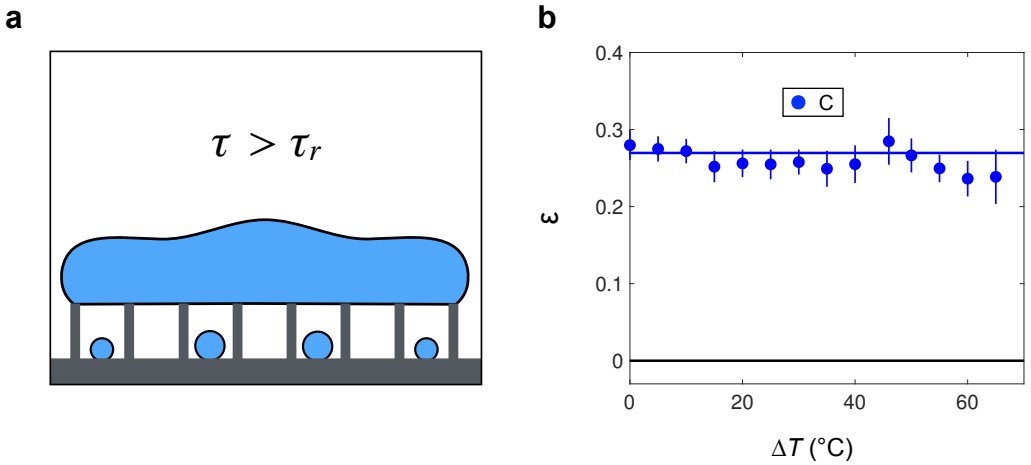

Figure 5.7: (a) The condensation time τ being larger than the bouncing time τ_r, no water bridge exists between the substrate and the drop as water nuclei are smaller than the height h. (b) Coefficient of restitution ε as a function of the temperature difference ΔT for surface C together with its fit (blue solid line) deduced from Eq. (5.3). In that case, $\varepsilon = \varepsilon_0$ and condensation has no impact on ε.

5.4.3 Small condensation time

The opposite limit ($\tau < \tau_r$) then concerns short pillars as $\tau \propto h^2$. In this scenario, cavities enclosing a condensation droplet instantaneously fill at drop impact (Figure 5.8a). As sketched in Figure 5.8b, two quantities must be compared: the nucleation density n (number of water nuclei per unit square) and the total area of a cell rp^2 (r being the roughness and p the pitch). We use the same modeling as in the static case [36].

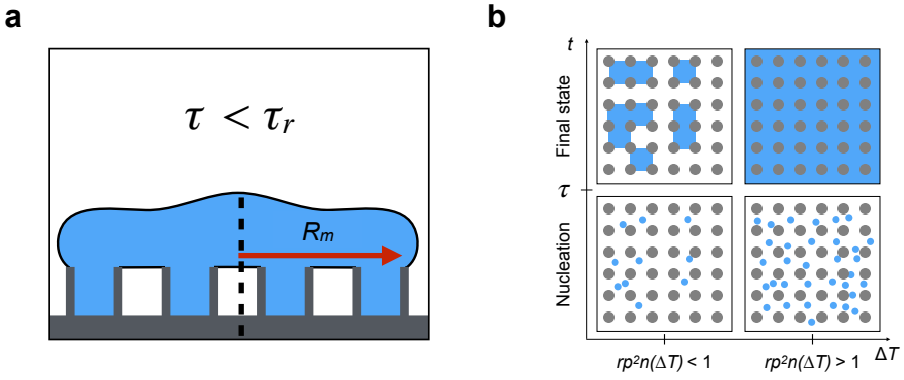

Figure 5.8: (a) The condensation time τ being smaller than the bouncing time τ_r, bridges form with a probability N below the drop and connect the drop. It eventually generates dissipation when the drop recoils from its maximum contact radius R_m. In our case, one finds $R_m = 1.55$ mm $\pm$ 0.05 mm. (b) Schematic of the condensation steps in a cold texture beneath a hot drop as a function of ΔT (horizontal axis) and time t (vertical axis). Blue dots show the water nuclei (of density n) condensing on the substrate. At small ΔT, there is on average less than one nucleus per cell, which generates disconnected patches when cells are filled ($t > \tau$). At large ΔT, there is at least one nucleus per cell, so that water later invades all the structures. Extracted from [36].

Let us define N the probability of having a water nucleus in a cell. As n is the number of water nuclei per unit area, N is written as:

$$N = \min(1, nrp^2) \ . \tag{5.4}$$

The two scenarii are shown in Figure 5.8b: for large n, there is more than one nucleus in a cell, hence $N = 1$ and all the cells under the drop are filled by water. The opposite case is then $N = nrp^2$ where wet cells remain disconnected. After a time larger than the condensation time τ, each cell enclosing a water nucleus is filled. Each filled cell will then connect the drop and induce adhesion as the drop recoils. The nucleation density n increases with ΔT, so are N and the condensation-induced adhesion. This adhesion occurs as the drop recoils from its maximum contact radius R_m (Figure 5.8a) to 0. We introduce the force $F(R)$ induced by adhesion during the drop recoiling from a radius R to $R - \mathrm{d}R$. The breaking of a water bridge between an elementary filled cell and the drop during recoiling costs an energy $2\gamma p^2$ because two water interfaces are created. The elementary force f per cell is then:

$$f = 2\gamma p \ , \tag{5.5}$$

as it is on a length of p. Finally, multiplying this force f over the number of filled cells in the trailing edge (that is the perimeter of the drop $2\pi R$), one obtains the total force $F(R)$:

$$F(R) \approx 4\pi R\gamma N \ . \tag{5.6}$$

Besides, the energy E_{adh} induced by condensation is given by the work of F on the radius R_m:

$$E_{\text{adh}} = \int_0^{R_m} F(R)\mathrm{d}R = 2\pi\gamma R_m^2 \min(nrp^2, 1) \ , \tag{5.7}$$

where n can be determined using static measurements and found to be roughly equal to 0.06 $\Delta T/\mu\text{m}^2$ [36]. Finally, the coefficient of restitution ε is $\varepsilon = \varepsilon_0 - E_{\text{adh}}/E_b$ (E_b being the kinetic energy at impact), since E_{adh} is seen as a dissipation energy, and reads:

$$\varepsilon = \varepsilon_0 - 4\pi\gamma R_m^2 \min(nrp^2, 1)/MV^2 \ . \tag{5.8}$$

For Eq. (5.8), at small nucleus density ($n(\Delta T) < 1/rp^2$), n varies linearly with ΔT, hence the model predicts a linear decrease of ε with temperature. For small texture, one has $nrp^2 < 1$, which yields $\varepsilon = \varepsilon_0 - 4\pi\gamma R_m^2 rp^2 n/MV^2$. Eq. (5.8) is drawn in Figure 5.9 with solid lines (green and orange), for the experimental value $R_m = 1.55$ mm and taking $p \sim h$, and found to quantitatively fit the data for both samples A and A'. It explains the persistence of bouncing at any water temperature for surface A (green data and $h \sim 100$ nm) and the slight decay of ε with ΔT (slope of $7.5.10^{-4}$ K^{-2}). One must note that the variations of ρ and γ with temperature are incorporated in the model but their weak variations make negligible their influence for the fit. The model also explains the behaviour observed with sample A' (orange data) which texture is twice larger than that of A ($h \sim 200$ nm): we expect a stronger decrease of the function $\varepsilon(\Delta T)$ (absolute slope 4 times higher than for A), which intercepts the axis $\varepsilon = 0$ for $\Delta T = 40°\text{C}$, close to the experimental value of 35°C. Furthermore, Eq. (5.8) enables us to find what is the feature size limit for repelling hot water with a nanotexture (see Sec. 5.5).

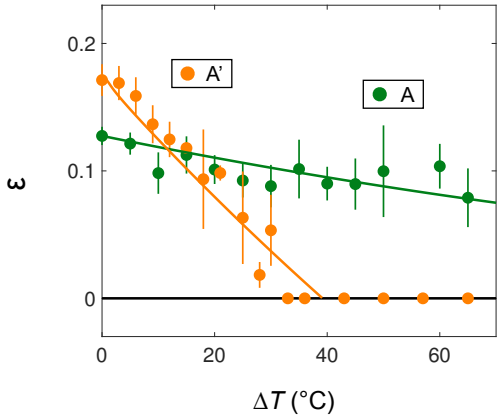

Figure 5.9: Coefficient of restitution ε as a function of the temperature difference ΔT for samples A (green data) and A' (orange data) together with their fit (solid lines) deduced from Eq. (5.8). It predicts a slow decrease of ε for surface A and a stronger one for A' owing to the larger pillars height. Both predictions match fairly well the data for the whole range of explored temperature.

5.4.4 Intermediate condensation time

Let us now consider the last case, that is when the two timescales are of same magnitude ($\tau \approx \tau_r$). In that situation, some parts of the substrate "under" the spreading drop are in contact long enough with the drop to have their elementary cells filled with water. On the opposite, the other parts do not have sufficient time to enable the water nuclei enclosed to be high enough to develop water bridges with the drop. As sketched in Figure 5.10a and

b, water spends more time at the impact point ($x = 0$ denoting x as the distance from the drop centre) than at the drop periphery ($x = R_m$), hence condensation will be favoured at small x and will delimit two areas for the condensation-induced adhesion. We can introduce a local contact time $\tau_L(x)$ that depends on the distance x. Thus, at the impact point, τ_L is the drop contact time $\tau_L(0) = \tau_r$ and at the maximal contact radius R_m, $\tau_L(R_m) = 0$. One can thus expect that τ_L is a decreasing function of x. For some distance x that we denote as $R^\star$ and name the adhesion radius (Figure 5.10a), the local contact time is equal to the condensation time τ: $\tau_L(R^\star) = \tau$, which enables us to define two areas: for $x > R^\star$, τ_L is larger than τ, hence no adhesion occurs, while for $x < R^\star$, $\tau_L < \tau$, implying that adhesion occurs on a disk with radius $R^\star$. Finally, the adhesion energy E_{adh} can be calculated in the same manner as for the previous case but by replacing R_m by $R^\star$ (Eq. (5.7)).

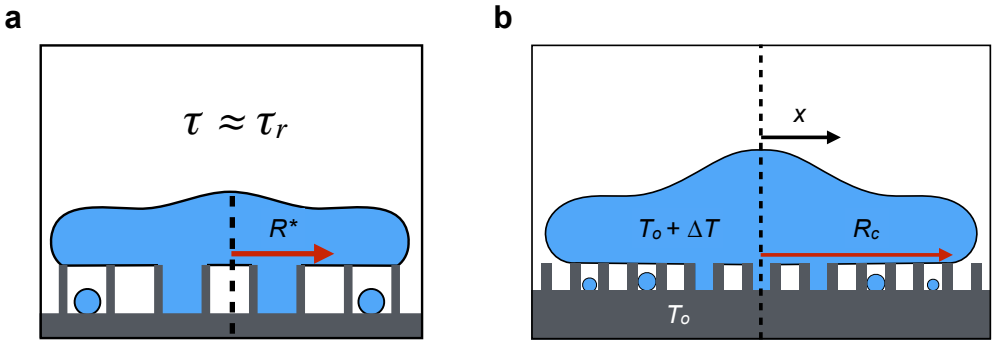

Figure 5.10: (a) Bridges only connect the drop on a radius $R^\star < R_m$ and $R^\star$ is given by Eq. (5.15). (b) Sketch of the spreading drop: x is the radial distance from the impact point and R_c the contact radius. Water nuclei at small x are larger than at the periphery because water spends more time.

Nevertheless, at this point, $R^\star$ remains to be determined. To achieve so, one needs to understand the time evolution of the contact radius R_c. As shown in Figure 5.11a, this dynamics can be divided into two phases: the first phase is the spreading phase while the following concerns the drop retraction.

Spreading phase

At small time, the drop shape can be assimilated to that of a truncated sphere sinking at a velocity V (Figure 5.11b): by a geometric reasoning, one finds a Hertzian scaling for R_c:

$$R_c(t) \sim \sqrt{RVt}\ , \tag{5.9}$$

after using $\delta = Vt$. This scaling law was verified experimentally and theoretically [121, 122, 123, 124, 125] and it leads either to $R_c \approx 2\sqrt{RVt}$ or to $\sqrt{3RVt}$. We use in our model the first expression as it fits the best our data. This scaling is valid for $t < R/V$: our impact speed being small, this relationship remains valid all along the spreading.

Retraction phase

Bartolo *et al.* studied the retraction phase of drops on superhydrophobic materials [119] and they distinguished two regimes: the capillary-inertial regime and the viscous-capillary regime. The limit between these two regimes is set by the Ohnesorgue number, $Oh = \eta/\sqrt{\rho\gamma R}$. Our situation is characterized by a Reynolds number larger than 1 and $Oh \sim 10^{-3} < 0.05$, the threshold observed in [119]. It implies that our case lies in the

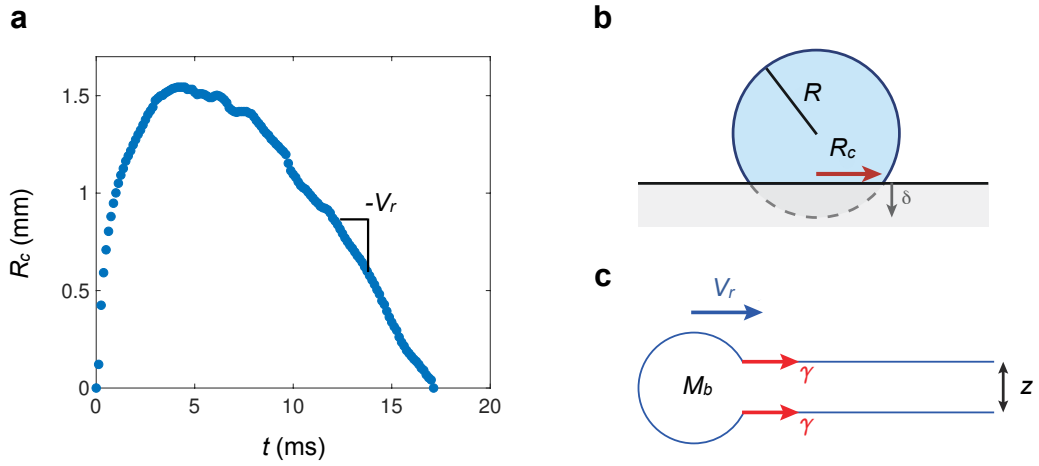

Figure 5.11: **Contact radius.** (a) Contact radius R_c as a function of time t for a drop impacting sample B with $R = 1.4$ mm and $V = 0.4$ m/s. The maximum contact radius is $R_m = 1.55$ mm and the bouncing time $\tau_r = 17.4$ ms. During the retraction phase, the speed of retraction is observed to be roughly constant and denoted as V_r. (b) Beginning of impact when the drop has a shape of a truncated sphere and $R_c(t) \sim \sqrt{RVt}$. Adapted from [120]. (c) Retraction phase: The bulge retracts at a constant Taylor-Culick velocity V_r in a thin film with thickness z, the drop height during the retraction phase. One finds $V_r = (2\gamma/\rho z)^{1/2}$. Adapted from [120].

capillary-inertial regime where the retraction speed V_r can be modeled and found to be constant (Figures 5.11a and c). The inertial dewetting leads to a Taylor-Culick velocity: the drop has a bulge of mass M_b and radius R_m that collects the liquid forming a thin film of thickness z. Using Newton's second law, one finds $V_r = \sqrt{2\gamma/\rho z}$ [119] where z is the height of the recoiling drop (Figure 5.11c). Using volume conservation, z can be rewritten as $z \approx (4R^3/3R_m^2)$. By considering a balance between inertia and surface tension, Clanet *et al.* found that $R_m \sim RWe^{1/4}$ [126]. Combining the two expressions, the height z is given by $z \approx (4R/3)We^{1/2}$. As observed in Figure 5.11a, R_c is found to be linear with t for nearly the whole retraction phase and reads:

$$R_c(t) \approx -(3\gamma/2\rho R)^{1/2}\, We^{1/4} t \ , \tag{5.10}$$

using $R_c(t) = -V_r t$. We finally assume that the two contributions of R_c are additive, which yields:

$$R_c(t) \approx 2\sqrt{RVt} - (3\gamma/2\rho R)^{1/2}\, We^{1/4} t \ . \tag{5.11}$$

This function is drawn with a solid line in Figure 5.12a and found to nicely fit the data for the whole range of time. This description is valid at modest Weber number, during which no rim forms. Otherwise, the intermediate phase ($t > R/V$) was modelled in [127, 128] and it is much trickier to get a simple law for R_c.

Local contact time

Coming back to the local contact time τ_L, one must recall it is the time spent at a distance x by the liquid. R_c is found to be non-monotonic with time (Figure 5.11a) which implies that for $0 < x < R_m$, $R_c(t) = x$ has two solutions in time, which we denote as t_1 and t_2 ($t_1 < t_2$). The local contact time τ_L is then simply $\tau_L(x) = t_2 - t_1$ (Figure 5.12a): it is observed to be a decreasing function of x with a maximum at $x = 0$ where $\tau_L(0) = \tau_r$. The local contact time is plotted in Figure 5.12b as a function of distance x and indeed

found to be a decreasing function of x. For $\tau \leq \tau_r$, the adhesion radius $R^\star$ is graphically obtained using the expression $\tau_L(R^\star) = \tau$, while for $\tau > \tau_r$, $R^\star$ is set to 0. As indicated in the figure (red arrow), an increase in temperature $\Delta T+$ decreases the condensation time τ (Eq. (5.2)), which induces a larger adhesion radius $R^\star$ and one expects more dissipation.

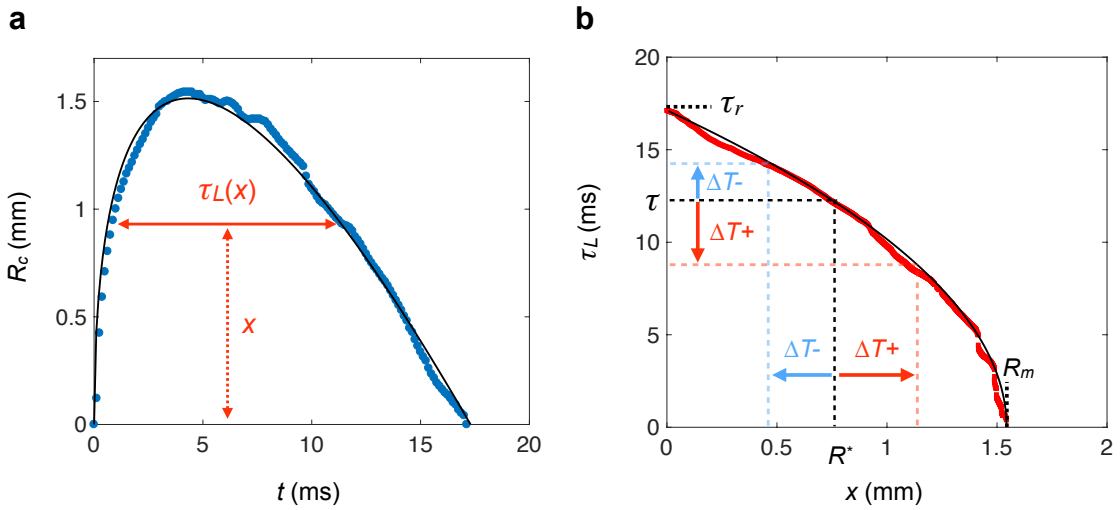

Figure 5.12: (a) Contact radius R_c as a function of time t for a drop bouncing on sample B with $R = 1.4$ mm and $V = 0.4$ m/s. The solid line $R_c(t) \approx 2\sqrt{RVt} - (3\gamma/2\rho R)^{1/2} We^{1/4} t$ fits well the data (Eq. (5.11)). (b) Local contact time τ_L as a function of the distance x. The solid line shows Eq. (5.14), with $\tau_r = 17.4$ ms and $R_m = 1.55$ mm. For $\tau_L(x) > \tau$, adhesion occurs on a disk with radius $x = R^\star(\tau)$.

The analytical expression of $\tau_L(x)$ is obtained using the expression of $R_c(t)$ deduced in Eq. (5.11). Solving $R_c(t) = \beta\sqrt{t} - \mu t = x$, where $\beta = 2(RV)^{1/2}$ and $\mu = (3\gamma/2\rho R)^{1/2} We^{1/4}$, one gets:

$$t_{1,2} = \left(\frac{\beta \pm \sqrt{\beta^2 - 4x\mu}}{2\mu} \right)^2 , \tag{5.12}$$

and using $\tau_L(x) = t_2 - t_1$, it finally yields:

$$\tau_L(x) = \frac{\beta^2}{\mu^2} \sqrt{1 - \frac{4x\mu}{\beta^2}} , \tag{5.13}$$

which can be written as:

$$\tau_L(x) = a\sqrt{1 - \frac{x}{b}} . \tag{5.14}$$

We here denote $a = (8/3)(\rho R^3/\gamma)^{3/2} \approx \tau_r$ and $b = RWe^{1/4} \approx R_m$. Surprinsingly, the prefactor in front of the inertio-capillary time $(\rho R^3/\gamma)^{1/2}$ in a ($8/3 \approx 2.7$) is found really close to the one obtained in the experimental data and in the first experimental study of τ_r by Richard *et al.*, where $\tau_r \approx 2.6\,(\rho R^3/\gamma)^{3/2}$ [129]. Eq. (5.14) is drawn in Figure 5.12b and observed to fit the data for $a \approx 17.4$ ms and $b \approx 1.6$ mm, that is, the experimental values of τ_r and R_m (sample B) that themselves are close to the expected ones, $a \approx 15.9$ ms and $b \approx 1.8$ mm. From the analytical expression of $\tau_L(x)$, one can finally deduce the expression

of the adhesion radius $R^\star$:

$$R^\star = \begin{cases} R_m \left[1 - \left(\frac{\tau}{\tau_r}\right)^2\right] & \text{for } \tau \leq \tau_r \\ 0 & \text{for } \tau > \tau_r \ , \end{cases} \tag{5.15}$$

and combining Eq. (5.15) with the expression of ε for small condensation time $\varepsilon = \varepsilon_0$ - $4\pi\gamma R_m^2 \min(nrp^2, 1)/MV^2$ (Eq. (5.8)), we can obtain a general expression for the restitution coefficient:

$$\varepsilon = \varepsilon_0 - 4\pi\gamma R_m^2 \max^2([1 - (\tau/\tau_r)^2], 0) \min(nrp^2, 1)/MV^2 \ . \tag{5.16}$$

This equation remains valid for the three regimes. For $\tau < \tau_r$, when condensation is instantaneous (samples A and A'), one has $R^\star = R_m$ and we recover Eq. (5.8). On the opposite, when $\tau > \tau_r$ and where condensation does not affect bouncing (sample C), one has $\max([1 - (\tau/\tau_r)^2], 0) = 0$, hence one gets Eq. (5.3). The only adjustable parameter in Eq. (5.16) is the numerical factor α in the condensation time (Eq. (5.2)), $\tau = \alpha\rho h^2/D\Delta c_{\text{sat}}$. Drawn with a solid line in Figure 5.13 with $\alpha = 8$, Eq. (5.16) matches fairly well the data. It manages to predict the failure of repellency at intermediate pillar height (sample B) and the transition from bouncing to sticking is found to be abrupt and to occur for $\tau(\Delta T_c) = \tau_r$ ($\Delta T_c \approx 15°\text{C}$). For $\Delta T > \Delta T_c$, drops cease to bounce, which we indicate by the line $\varepsilon = 0$. We have varied some parameters (radius, impact speed, hygrometry), as presented in Sec. 5.6, and found that the model remains robust.

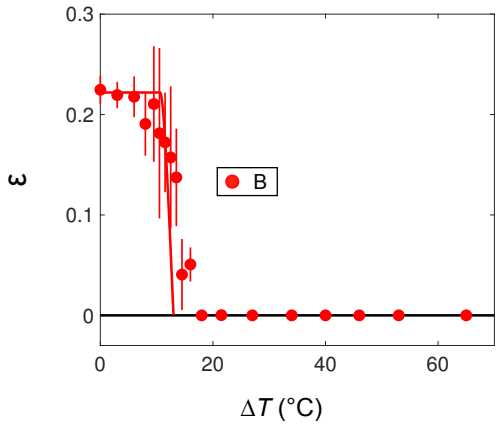

Figure 5.13: Coefficient of restitution ε as a function of the temperature difference ΔT for sample B together with its fit (solid line) deduced from Eq. (5.16). Water gets trapped when ΔT exceeds $\sim 15°\text{C}$.

5.5 Phase diagram

The model (Eq. (5.16)) allows us to construct a theoretical phase diagram for predicting the behaviour of hot drops impacting texture with different heights. We choose as control parameters the water temperature (defined by the quantity ΔT, difference of temperature between water and its substrate) and the pillar height h, keeping all other parameters fixed by the choice of the height (homothetic samples with $p = h$ and $a = h/6$, which yields $r \approx 2$). In addition, we fix the value of the contact angle hysteresis so as to have a constant ε_0 ($\varepsilon_0 = 0.2$, a value comparable to that in our experiments), the restitution coefficient for $\Delta T = 0°\text{C}$. We also fix the drop radius and impact velocity, $R = 1.4$ mm and $V = 0.4$ m/s,

respectively. In the resulting phase diagram (Figure 5.14), green and red colours distinguish bouncing from sticking. Two limits h_1 and h_2 for the height h must be considered to compute the phase diagram. For "short" pillars, rebound is observed in the whole range of ΔT and one can calculate the lower bound h_1 of h at which sticking becomes possible. The substrate temperature being at $T_0 = 24 \pm 1°C$, the maximum ΔT is 75°C (very close to the water boiling point).

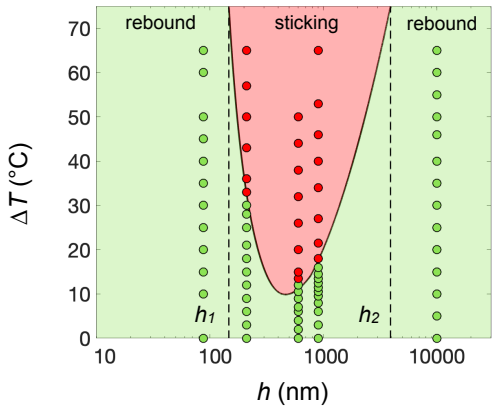

Figure 5.14: **Phase diagram for hot water impacting hydrophobic texture**. The two control parameters are the water/substrate temperature difference ΔT and the pillar height h. The critical temperature ΔT_c defining the frontier between bouncing (green region) and sticking (red region) is calculated by solving the equation $\varepsilon = 0$ in Eq. (5.16), with $p = h$, $a = h/6$, $r \approx 2$, $\varepsilon_0 = 0.2$, $R = 1.4$ mm and $V = 40$ cm/s, all values comparable to that in our experiments. The lower and upper bounds h_1 and h_2 for which bouncing is observed whatever the drop temperature are stressed with vertical dashes and given by Eqs. (5.18) and (5.20). Observations (green and red symbols for bouncing and sticking, respectively) are made for the five tested samples (A, $h = 88$ nm; A', $h = 210$ nm; B', $h = 600$ nm; B, $h = 900$ nm; C, $h = 10$ μm) and found to be in good agreement with the model.

The nucleus density being small for small pillars ($n(\Delta T) < 1/rp^2$), h_1 is obtained by writing $\varepsilon = 0$ in Eq. (5.8) for $\Delta T_m = 75°C$. It reads:

$$\varepsilon_0 = 4\pi\gamma R_m^2 n(\Delta T_m) r h_1^2 / MV^2 \ , \tag{5.17}$$

after taking $h_1 = p_1$ and one obtains the expression for h_1:

$$h_1 = [\varepsilon_0 MV^2 / 4\pi\gamma R_m^2 r n(\Delta T_m)]^{1/2} \ . \tag{5.18}$$

For typical values of the different parameters, h_1 is expected to be on the order of 100 nm. Similarly, the upper bound h_2 of h is obtained after writing $\varepsilon = 0$ in Eq. (5.16) for $\Delta T_m = 75°C$. For tall pillars, we have $n(\Delta T_m) > 1/rp^2$ and assume that $\tau < \tau_r$. Eq. (5.16) then rewrites as:

$$\varepsilon_0 = 4\pi\gamma R_m^2 [1 - (\tau/\tau_r)^2]^2 / MV^2 \ , \tag{5.19}$$

and using the expression of τ given by Eq. (5.2), one can relate h_2 to the other parameters and deduce:

$$h_2 = [\tau_r D \Delta c_{\mathrm{sat}}(\Delta T_m)/\alpha\rho]^{1/2} [1 - (\varepsilon_0 MV^2 / 4\pi\gamma R_m^2)^{1/2}]^{1/2} \ . \tag{5.20}$$

For typical values of the parameters, h_2 is found ~ 4 μm. Note that we can further simplify the model by noticing that the correction to 1 in the bracket in Eq. (5.18) is ~ 0.25 - so

that the first term only in the equation can be used for roughly estimating the value of h_2. The two limits given by Eqs. (5.18) and (5.20) (dashed lines in Figure 5.14) depend on the coefficient of restitution ε_0 at $\Delta T = 0°C$, respectively as $\varepsilon_0^{1/2}$ and $\varepsilon_0^{1/4}$. These variations are weak (Figure 5.15), which explains that taking a unique, average value $\varepsilon_0 = 0.2$ in the model allows us to draw a phase diagram valid for samples having slightly different values for this parameter. Besides, h_1 and h_2 are found to be increasing functions of the drop radius R. Finally, at intermediate pillar height, that is for $h_1 < h < h_2$, one expects sticking for $\Delta T > \Delta T_c$, where ΔT_c is given by $\varepsilon(\Delta T_c) = 0$ in Eq. (5.16) and this quantity is plotted in solid line in the figure. The minimum is found for $h_m \approx 460$ nm and $\Delta T_c \approx 10°C$.

Comparison with experiments can be refined by marking the observed behaviour (bouncing or sticking) using green or red symbols. Experiments are performed with the samples A, A', B and C, to which we add data obtained with a fifth material B' where pillars characteristics are $a = 100$ nm, $h = 600$ nm (a height close to h_m) and $p = 560$ nm ($r \approx 2.2$). For samples A and C only (extreme values of h, $h = 88$ nm and $h = 10$ μm), we remain in the bouncing regime whatever the water temperature, while bouncing/sticking transitions are observed at intermediate texture size (samples A', B' and B). The location of the transition is in good agreement with the prediction for ΔT_c, confirming for instance the non-monotonic character of ΔT_c with the pillar height.

5

Finally, one can examine the influence of ε_0 on ΔT_c, as indicated in Figure 5.15 where ΔT_c is plotted for three typical values of ε_0 ($\varepsilon_0 = 0.1$, 0.2 and 0.3): as noted earlier, the influence of ε_0 on the two limits h_1 and h_2 is relatively negligible, especially on h_2: h_1 varies from 104 to 180 nm from $\varepsilon_0 = 0.1$ to 0.3 and from 3.7 to 4.1 μm for h_2 for the same range of ε_0. Concerning ΔT_c, the curve is shifted rightwards with an increase of ε_0: for instance, the minimum of ΔT_c varies from 7.3 to 11.8°C. A higher ε_0 implies a better repellency to hot water and particularly for the smallest texture ($\tau < \tau_r$): $\varepsilon = 0$ will occur at a higher ΔT all the more since ε_0 is large (Eq. (5.8)). For intermediate texture ($\tau \approx \tau_r$), the influence of ε_0 is negligible since the transition from bouncing to sticking is abrupt (Figure 5.13). As a consequence, the second term of the expression of ε (Eq. (5.16)) becomes much larger than ε_0, which explains its low influence on ΔT_c.

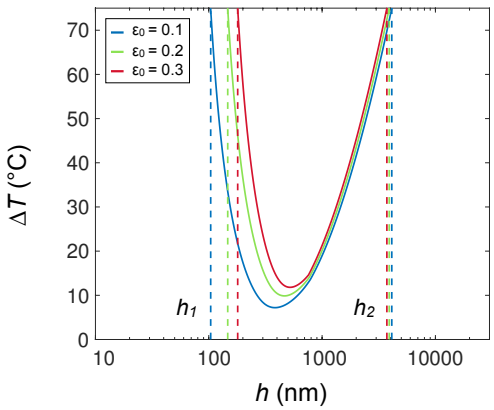

Figure 5.15: Infuence of ε_0 on the critical temperature ΔT_c as a function of pillar height h, ΔT_c defining the frontier between bouncing and sticking. We take three values of ε_0 with the same parameters used in Figure 5.14: $p = h$, $a = h/6$, $r \approx 2$, $R = 1.4$ mm and $V = 40$ cm/s, all values comparable to that in our experiments. An increase in ε_0 shifts the curve $\Delta T_c = f(h)$ rightwards and has a low influence on h_1 and h_2 (Eqs. (5.18) and (5.20)).

5.6 Limitations of the model

5.6.1 Influence of drop radius

To measure the robustness of our model, we have performed the same experiment on samples A, B and C with a drop of radius $R = 1.10 \pm 0.05$ mm, at an impact velocity $V = 40 \pm 5$ cm/s. For this new value of radius, the Weber number is not changed much ($We = 2.4$ compared to 3 before), as well as the Reynolds number. Hence, one expects similar behaviours for this new radius. The characteristics of the impact are close to that reported in Figure 5.16: the restitution coefficient ε of the shock is quite insensitive to water temperature for sample C, it slightly decreases with sample A, and evidences a sharp transition to sticking with sample B for $\Delta T \approx 15$°C. The local contact time is also found to be nicely fitted by Eq. (5.14). There again, data are convincingly fitted by Eq. (5.16) drawn with solid lines. The adjustable parameter for the condensation time τ (in Eq. (5.2)) is the same as for the larger radius, *i.e.* $\alpha = 8$.

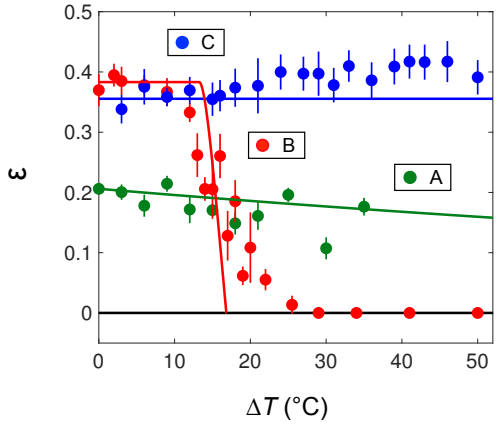

Figure 5.16: Bouncing efficiency ε as a function of the temperature difference ΔT for substrates A, B and C and impacting drops with radius $R = 1.1$ mm and velocity $V = 40 \pm 5$ cm/s. The coloured lines show the model (Eq. (5.16)) for the three regimes: $\tau > \tau_r$ where no condensation adhesion occurs (sample C), $\tau < \tau_r$ in quasi-static regime, where adhesion is fully developed (sample A), and the transition regime, where $\tau \approx \tau_r$, observed on sample B for ΔT around 15°C.

5.6.2 Influence of impact speed

Our experiment was performed at one impact velocity and to measure its influence, we have done two series of experiments on samples A, B and C at $V = 59 \pm 5$ cm/s and $V = 86 \pm 5$ cm/s. The two experiments are carried out with the two radii $R = 1.10 \pm 0.05$ mm and $R = 1.40 \pm 0.05$ mm. Slower speeds than 40 cm/s are intricate to implement as, for slower impacts, the contact time increases with decreasing V [130], which complicates the analysis. Besides, V is fixed by an upper limit, that is the threshold for splashing. As indicated by Josserand *et al.*, one can expect splashing for $K = We\sqrt{Re} \approx 3000$. For our two radii, it yields $V = 2$ m/s and 1.76 m/s for $R = 1.10$ mm and 1.40 mm, two quantities larger than our largest impact velocity.

Figure 5.17 presents the local contact time τ_L as a function of distance x, together with its fit (Eq. (5.14)), for the two impact velocities and for $R = 1.4$ mm. As V increases, the model still captures well the experimental data for the lower and upper bounds of x. Yet, for intermediate x (0.5 mm $< x <$ 1.5 mm), the model seems to overestimate $\tau_L(x)$.

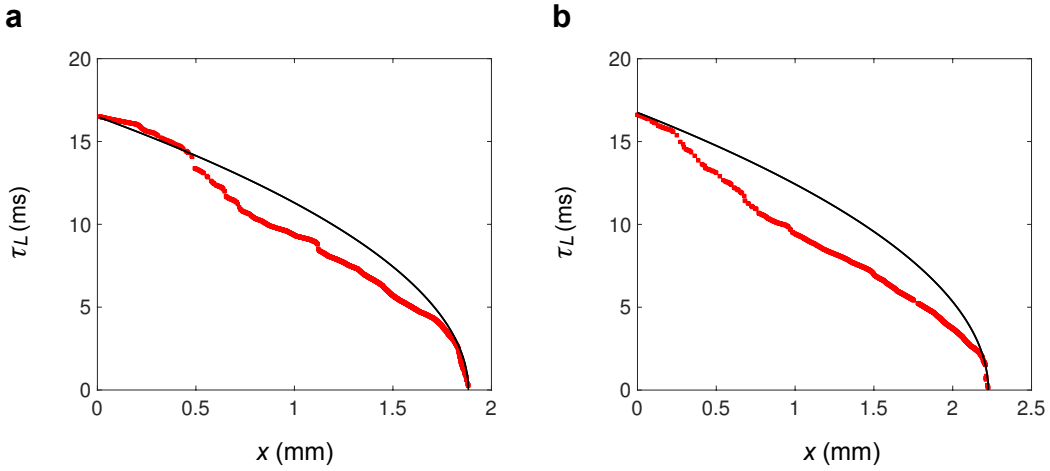

Figure 5.17: Local contact time τ_L as a function of distance x to the impact point for impact velocities $V = 59$ cm/s (a) and 86 cm/s (b). Sample B is impacted by a drop with radius $R = 1.4$ mm. Eq. (5.14) is drawn in solid line in the two figures: differences appear between the model and the experimental data for 0.5 mm $< x <$ 1.5 mm.

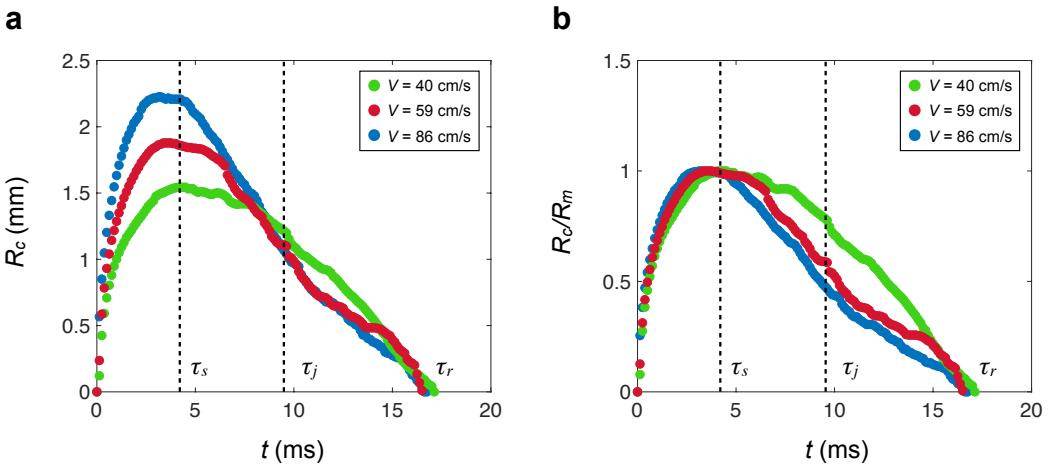

Figure 5.18: (a) Contact radius R_c as a function of time t for three impact velocities V, $V = 40$ cm/s (green data), $V = 59$ cm/s (red data), $V = 86$ cm/s (blue data) and $R = 1.4$ mm. The phase $\tau_s < t < \tau_j$ is marked by a retraction speed given by the Taylor-Culick velocity whereas it is constant for the 3 velocities for $\tau_j < t < \tau_r$. (b) Normalized contact radius by its maximum R_c/R_m as a function of t. The retraction speed V_r is indeed found to be proportional to R_m for $\tau_s < t < \tau_j$ [119].

Let us now look at the contact radius R_c for the three impact velocities to rationalize this observation. Figure 5.18a presents the contact radius $R_c(t)$ for the three impact velocities and for a drop with $R = 1.4$ mm impacting sample B. One defines τ_s the time where R_c is maximum and τ_j where a vertical jet is created. For $\tau_s < t < \tau_j$ and $\tau_j < t < \tau_r$, the temporal evolutions of R_c are different [120]. Indeed from $t = \tau_j$, the contact radius R_c seems to follow the same evolution with a constant retraction speed. It is in contrast with the first phase of retraction ($\tau_s < t < \tau_j$) where the retraction speed depends on V. After normalizing R_c by the maximum contact radius R_m (Figure 5.18b), the normalized retraction speeds $-\dot{R}_c/R_m$ are equal during this phase, as evidenced by the same slopes of R_c/R_m in the figure, in agreeement with the Taylor-Culick velocity where $V_r \propto R_m$ [119] (Eq. (5.10)). The phase $\tau_j < t < \tau_r$, where the retraction speeds are equal, is not predicted in our model,

which explains the inconsistency between our model and the data in Figure 5.17. Despite this fact, we have chosen to keep our analytical expression of τ_L to fit the data for the two larger impact velocities.

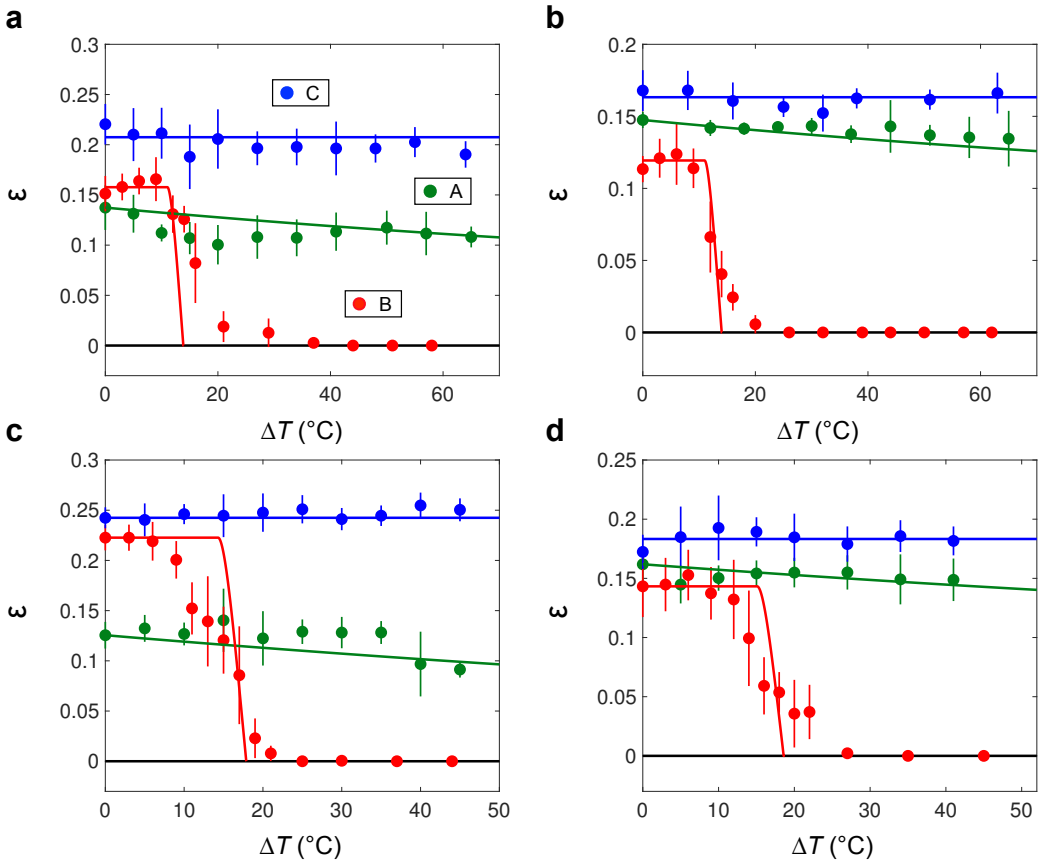

Figure 5.19: Water coefficient of restitution ε as a function of the water/substrate temperature difference ΔT, on samples A, B and C, for two radii R and two impact velocities V. Top figures: $R = 1.4$ mm and $V = 59 \pm 5$ cm/s (a) or $V = 86 \pm 5$ cm/s (b). Bottom figures: $R = 1.1$ mm and $V = 59 \pm 5$ cm/s (c) or $V = 86 \pm 5$ cm/s (d). Solid lines show Eq. (5.16).

As shown in Figure 5.19, the model (Eq. (5.16), solid lines) resists the variation of impact velocity V by a factor 2: it convincingly fits the data at all explored values of V and R. One can note the decrease of ε_0 with increasing V as predicted ($\varepsilon_0 \sim We^{-1/4}$) [118]. Besides, suprisingly, the hierarchy of ε_0 between samples A and B is changed at the highest impact velocity (Figure 5.19b and d) where $\varepsilon_0(A)$ becomes larger than $\varepsilon_0(B)$, despite the highest contact angle hysteresis for material A (Figure 5.3). Furthermore, for higher V, the transition from bouncing to sticking for material B is found to be less abrupt than for $V = 40$ cm/s (Figure 5.13): an explanation could be the difference observed between the local contact time τ_L and the model. This discrepancy induces a lower adhesion radius $R^\star$ than predicted for a given τ, hence a smaller slope for $\mid \mathrm{d}\varepsilon/\mathrm{d}\Delta T \mid$. Finally, it is worth noting that even with the highest V, the local Weber number ($\rho V^2 p/\gamma$) remains smaller than 0.01 and the dynamic pressure of water drops is typically 1% of the atmospheric pressure, which could explain the low influence of V on our model.

5.6.3 Influence of humidity

Humidity could have an impact on the condensation time. To check the influence of hygrometry, we performed an experiment where we doubled the hygrometry of ambient air

($RH = 60\%$). We tested sample A, that is, the surface with the smallest features and thus the most likely to be filled by condensed water. We report our results in Figure 5.20, where we do not observe any significant effect between hygrometries of 30 % and 60%, a range that covers the typical range of commonly observed humidity. The negligible influence of hygrometry can be attributed to the fact that the air enclosed in the cells becomes saturated in a time much smaller than the condensation time (around 5 μs for sample C against a condensation time of around 100 ms) [108]. For the upper limit of hygrometry, *i.e.* an atmosphere with a humidity of 100%, we expect microfeatures to be filled with water, so that superhydrophobicity is destroyed even in "static" conditions - that is, without considering neither dynamical phenomena nor drop temperature effects.

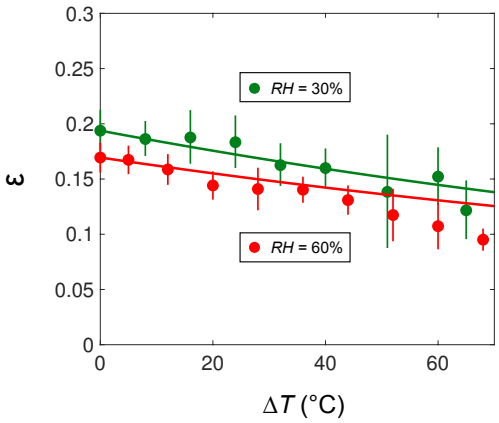

Figure 5.20: **Influence of hygrometry**. Water drop coefficient of restitution ε as a function of the water/substrate temperature difference ΔT for two hygrometries, on sample A for $R = 1.4$ mm: $RH = 30\%$ and $V = 36 \pm 4$ cm/s (green symbols); $RH = 60\%$ and $V = 40 \pm 4$ cm/s (red symbols).

5.6.4 Condensation time

5.6.4.1 Convective flow

The present model for the condensation time τ ignores vapour/air flow: as it hits the solid, the impacting drop generates an aerodynamic flow inside the pillars. This adds a convective term to the diffusive growth of the nucleus, as sketched in Figure 5.21. The typical velocity U of this lateral air flow can be estimated thanks to the balance of viscous stresses at the liquid/vapour interface below the drop. Using the fact that the Reynolds number is very large ($Re \approx 600$), the dissipation is inertial and mainly in the air. Indeed, the stress in the drop would occur on a distance of $R/\sqrt{Re}$ that is negligible. We can then write the balance: $\eta V/R \sim \eta_v U/h$, denoting η_v as the vapour viscosity, and find:

$$U \sim \frac{\eta h}{\eta_v R} V \ . \tag{5.21}$$

The expression is obtained after neglecting the friction around pillars. The speed U is maximum for the tallest pillars ($h = 10$ μm) and reaches 10 cm/s. In that case, one can calculate the Péclet number Pe that compares convective to diffusive flow. The diffusive flow has a timescale $\tau \sim h^2/D$ while for the convective flow $\tau' \sim h/U$. Comparing these two times yields the Péclet number $\mathrm{Pe} = Uh/D$. It is found to be at most 0.1 for sample C, and smaller for shorter features, which justifies our assumption of a diffusive dynamics for the nucleus condensation. Even for the experiments at larger impact velocities where it should be enhanced, the influence of air/vapour flow is found negligible.

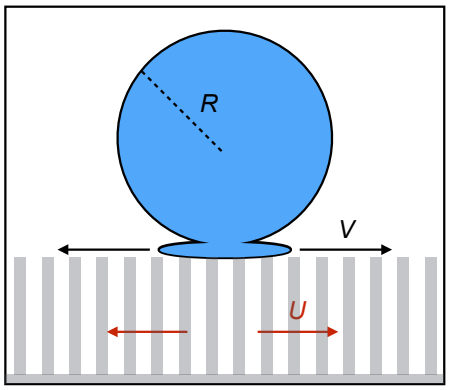

Figure 5.21: Sketch of the convective flow generated by an impacting drop with radius R and velocity V. The vapour flow has a typical speed U given by Eq. (5.21).

5.6.4.2 Large texture size

In our model of diffusive growth of nucleus, we have only considered one nucleus in each elementary cell which grows with time until eventually reaching the height h. Yet, for large texture (such as sample C) and sufficient water/substrate temperature difference, the nucleation density n (number of water nuclei per unit square) can become sufficiently large so that a cell delimited by four pillars can contain more than one nucleus. After time, water nuclei can coalesce and generate a bigger drop, hence a smaller condensation time τ.

The mean separation distance l between nuclei can be approximated as $l \approx 1/2\sqrt{n}$ and is drawn as a function of ΔT in Figure 5.22. It decreases with ΔT as n is linear with ΔT, $n = 0.06\ \Delta T/\mu\text{m}^{-2}$. The coalescence of water nuclei becomes critical for surfaces where $\tau \approx \tau_r$, that is for features with $h \gtrsim 1\ \mu$m: for instance $l \approx 1\ \mu$m for $\Delta T = 5°$C. For features larger than 1 μm, the condensation time is then expected to be smaller than the one given by Eq. (5.2). As a consequence, the increasing part of ΔT_c ($h_m < h < h_2$) should then have a smaller slope (Figure 5.14), hence a smaller value for h_2 (Eq. (5.20)).

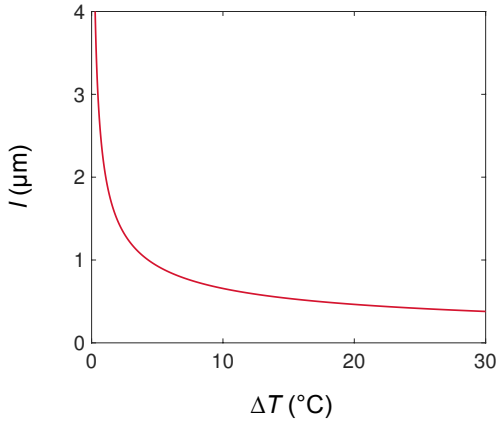

Figure 5.22: Typical distance of nucleation l as a function of water/substrate temperature difference ΔT. l is given by $l = 1/2\sqrt{n}$, where $n \approx 0.06\ \Delta T/\mu\text{m}^2$ is the nucleation density.

Take home message of Chapter 5

1. Repelling hot water. As it contacts a substrate, hot water generates condensation within the cavities at the solid surface through a diffusive flow, which eventually builds bridges between the substrate and the water and thus could destroy repellency.

2. Condensation-induced adhesion. While hot water sticks to the 1 μm features owing to condensation, drops always rebound on 100 nm and 10 μm features. The comparison between the condensation time and the drop contact time enables one to develop a theoretical model, relying on the dissipation due to condensation, to understand the three behaviours observed for three ranges of texture size.

3. First recipe. A first recipe for repelling hot water on a superhydrophobic material consists in resorting to "large features" ($\sim$ 10 μm) which prevent the texture filling and the formation of water bridges between impacting drops and the solid material.

4. Second recipe. The second recipe consists in using nanometric features ($\sim$ 100 nm) which limit the size of water bridges and thus their sticking abilities.

PART II

GRANULAR MATTER

6

Dust capture on a fiber

Dust produced by glass wool deterioration is a serious concern in industry. It has been adressed by resorting, during the fabrication process, to the addition of oil in the binder that makes glass wool stable. Here, the issue of the capture efficiency of beads by a fiber coated with oil is addressed. We first present our experiment and the results obtained on the mass of captured grains of different sizes on a fiber coated with a varying quantity of oil. We then develop a model to understand the dependence between the captured mass of particles and the mass of oil. We also study the growth dynamics of wet aggregates (oil-grains) in different oil configurations. Finally, a model is proposed to understand the different growth behaviours and is confronted with the experimental data.

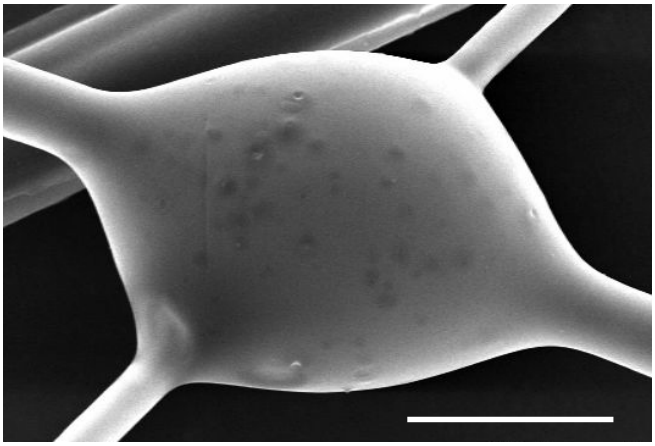

Picture of glass wools wetted by a binder. The scale bar indicates 10 µm. Photo credits: Pierre-Brice Bintein [131].

Contents

This work is the result of our collaboration with Saint-Gobain Recherche. It involved Joël Azevedo, Hélène Parant, Laure Cossalter, Marie Lamblet, Romain Labbé and Aditya Jha. I sincerely thank them for this joint work.

6.1 Introduction

The capture of micro or nanoparticles is a challenge in many industrial processes such as car industry because of the particles emitted by the exhaust pipes or construction because of the released dust. One commonly used means to tackle this issue is the use of particle filters. Another proposed solution for capturing these dusts is the use of liquid mixtures such as oil: the great stability of wet aggregates, consisting of liquids and grains, owing to the existence of capillary bridges between particles, confers this method a great advantage [132, 133]. This solution, for instance, was adopted by Saint-Gobain for the production of glass wool, which is achieved by assembling glass fibers. These, with a size of 1 to 20 micrometers, bind to each other thanks to the addition of a binder. With time and because of the handling, the fibers can break and form dust, making the installation unpleasant and uncomfortable for the craftsman. The solution considered for tackling this issue is the incorporation of oil in the binder as an emulsion. This addition enables to capture dust and prevents their release into the air. However, little is known about the capture efficiency of oil on dust. Although the properties of wet granular materials are well described and especially the influence of the proportion of the liquid, the coupling between liquid and moving particles has been poorly examined. Pacheco *et al.* studied the formation of sand castle towers built by accretion of dry grains on a wet substrate [134]. Recently, Saingier *et al.* developed a similar experiment but oriented horizontally [135]: the authors have managed to describe thoroughly the accretion process by measuring the growth dynamics of the aggregate.

Despite these two complete works on accretion dynamics on a flat substrate, the effect of using a liquid-coated fiber has been little studied. Mainly used for filters or meshes, the coating of fibers with oil can prevent the rebound of impacting grains [136], similar to what is observed on flat surfaces. Besides, the spreading of liquid on fibers can lead to complex geometries, promoted by the Plateau-Rayleigh instability of a cylindrical thin film. The growth of an aggregate resulting from a flow of grains impacting a wetted fiber increases the fiber diameter which may influence the collection efficiency. Several studies discuss this aspect, mainly because of the importance of oil-treated filters, as used in the car industry [137, 138]. However, a systematic study on the influence of particles' size and oil properties on capture efficiency is lacking. Similarly, compared to flat substrates where growth dynamics is well documented, the aggregate growth on a fiber coated with oil remains to be understood. Here, we build a reference experiment with one fiber coated with a certain quantity of oil and impacted by grains with a well controlled size. Glass wool is a much more complex system since fibers are distributed in meshes and where the liquid distribution is non-uniform, because liquid tends to aggregate at fiber intersections [131]. Nevertheless, the effect of using instead one fiber is a first path towards the design of more efficient systems where dust could be captured inside glass wool.

6.2 Dust capture on a fiber

6.2.1 Principle of the experiment

6.2.1.1 Parameters used

To study the influence of oil-coated fibers on dust capture, spherical glass beads with defined size (diameter d_g and density ρ_g) are used (Table 6.1) and impacted on a nylon fiber coated with silicon oil (viscosity η and density ρ). Oil wets totally the beads [139] and two silicon oils are used with viscosity equal to 100 and 1000 mPa.s. The surface tension γ of oil at ambient temperature is on the order of 20 mN/m.

To coat the fibers with oil, the dip-coating method [140] is not used here. Indeed, as the fiber needs to be manipulated after the coating, the newly created oil film could be

Material	Parameters	
Glass beads	$d_g = 55 \pm 15$ μm and 90 ± 20 μm	$\rho_g = 2.5$ g/cm^3
Silicon oil	$\eta = 100, 1000$ mPa.s, $\rho = 0.965$ g/cm^3	Film thickness $\sim$ 1 to 100 μm
Fiber	Radius $r = 102.5$ μm	Nylon fiber

Table 6.1: Experimental parameters

destabilized. As a matter of fact, the fiber is instead delicately coated with a brush soaked with oil. Besides, a force sensor connected to the fiber gives information about the mass of oil deposited and a side-view recording indicates the uniformity of the oil film over the whole fiber. After coating the fiber, the film happens to rapidly destabilize into beads (Figure 6.1). The fiber diameter ($d = 205$ μm) being much lower than the capillary length $\kappa^{-1} = (\gamma/\rho g)^{1/2}$ (~ 1.5 mm), denoting g as gravity, the Bond number $Bo = \kappa^2 d^2$, that measures the influence of gravity over surface tension, is much smaller than 1. It implies that this instability is driven by surface tension and is known as the Plateau-Rayleigh instability: an ondulated shape exhibits a lower surface than a cylinder with same volume provided the wavelength is large enough. In that limit, considering the fiber curvature, the Laplace pressure will be more important in the troughs than in the peaks. This difference of pressure is at the origin of this instability.

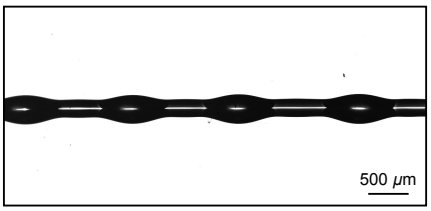

Figure 6.1: Beads of droplets resulting from the Plateau-Rayleigh instability of a cylindrical oil film deposited on a nylon fiber.

6.2.1.2 Experimental device

To bomb an oil-coated string with beads, we have designed the experiment sketched in Figure 6.2: spherical glass beads are deposited into a 8 cm-diameter cylinder closed in one end by a circular plate drilled with holes with diameter of 600 μm and spaced with 1 mm. It enables to decrease the flow and make it spatially uniform. After they flow through the plate, the beads impact a sieve excited by a motor so as to spatially distribute them. Finally, the beads fall along a 50 cm long canal, a length large enough to ensure they attain their sedimenting velocity u. At impact on the fiber, u is on the order of 10 cm/s, using Stokes formula $u = (2/9)\rho_g g r_g^2/\eta_a$, denoting η_a as the viscosity of air and r_g the bead radius. The mass flow of particles Q is found to be ~ 900 g/m^2/s for the 55 μm beads and ~ 640 g/m^2/s for the 90 μm ones. At the bottom of the canal stands the wetted fiber tied to a rod that is connected to a force sensor (*Futek LSB200*), the precision of which is 0.01 mg. The force sensor enables us to measure the mass of oil deposited as well as the mass of captured grains. The strings are 8 cm long and the mass of oil ranges from 0 to 10 mg.

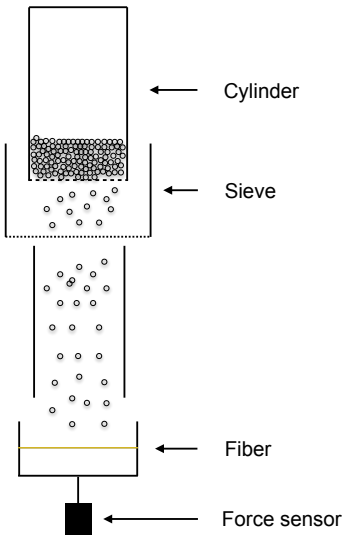

Figure 6.2: Sketch of the experiment: glass beads are deposited in a cylinder before being uniformly distributed over the horizontal. They eventually impact a fiber wetted with oil with speed u. The evolution of the fiber surface is recorded with a side-view imaging and a force sensor connected to the fiber yields the time evolution of the mass captured.

6.3 Experimental results

6.3.1 Growth evolution

The beads capture is recorded using a high-speed videocamera (Photron Fastcam Mini UX 100) at a rate of 50 Hz. The typical evolution of the capture with time is presented in Figure 6.3.

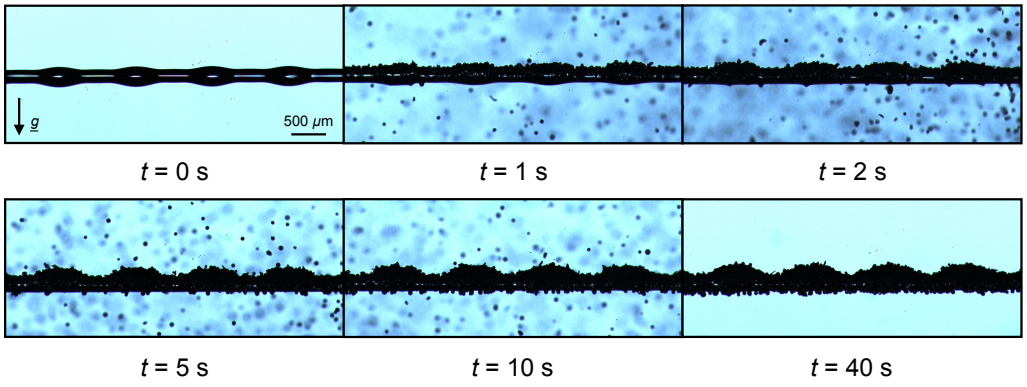

Figure 6.3: Snapshots of a wetted fiber impacted by glass beads with diameter $d_g = 55$ μm. The oil mass is $m_h = 0.9$ mg and viscosity $\eta = 1000$ mPa.s. At short time, the liquid at the bottom of the fiber rises up owing to the capillary pump. After $t = 5$ s, the aggregate does not evolve much, which indicates that it is fully saturated.

At short time (less than 5 seconds), we observe the emergence of an asymmetry between the top and the bottom of the fiber, a result of the rising liquid. Indeed, the top of the fiber is depleted in oil because of the impacting particles, which eventually generates a depression that pulls the liquid up. This region has thus the role of a capillary pump as the accumulation in grains at the surface induces a depression. The capillary rise remains possible because oil wets completely the grains and because their size is much smaller than the capillary length

($\kappa^{-1} \sim 1.5$ mm). Besides, the geometry of the Plateau-Rayleigh instability is observed to be conserved over time. Finally, the capture seems to saturate from $t = 5$ s. Indeed, between the last three images (spaced of 35 s), the aggregate height does not seem to change much, while, at short time, it varies significantly, hence suggesting that capture is more efficient at its beginning. Furthermore, the final particles' height on the fiber is much larger that the initial wetted radius, a result of an efficient capture (400 μm over 175 μm before impact).

Let us consider the effect of particle size on the capture efficiency. Figure 6.4 shows the initial and final states of two fibers coated with the same amount of oil and impacted by two different sizes of beads (top figures $d_g = 55$ μm and bottom $d_g = 90$ μm). After the saturation, the aggregates have almost the same shape (height of the aggregate particles-oil), which suggests that the bead size does not impact the efficiency of capture. These observations are addressed in the next subsection, as well as the influence of viscosity.

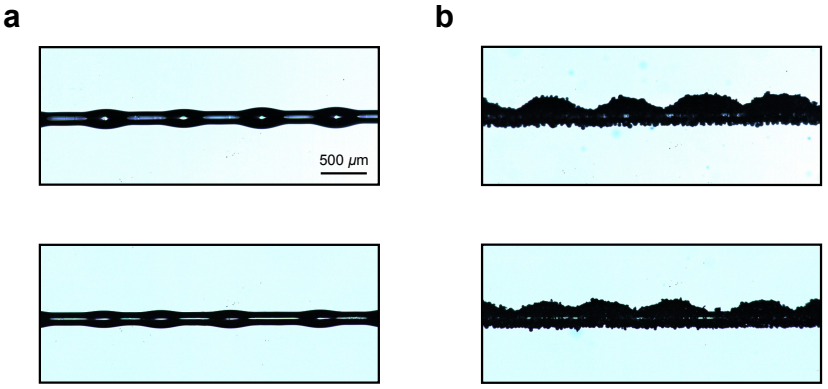

Figure 6.4: Initial (a) and final (b) states of two fibers coated with the same amount of oil ($m_h = 0.9$ mg) and impacted by beads with different sizes: $d_g = 55$ μm (top) and $d_g = 90$ μm (bottom). After saturation, the two aggregates have almost the same shape.

6.3.2 Force sensor

6.3.2.1 Typical signal

As mentioned in the previous paragraph, the force sensor connected to the fiber provides the oil mass and the quantity of captured particles. A typical signal is shown in Figure 6.5, that displays the force sensor signal in mass S_m over time t; the beads having a diameter $d_g = 55$ μm and impacting a fiber coated with 0.9 mg of oil. The total mass of captured beads is defined as m_c ($m_c = S_m(t \to \infty)$). As shown in the figure, m_c is observed to be much significantly higher than the oil mass m_h: $m_c = 5.7$ mg over $m_h = 0.9$ mg. Besides, the signal appears to be very noisy over the whole phase of impact. It originates in the fact that the majority of particles impacting the fiber do not stick to it but rather rebound, hence exerting a force on the sensor. This results in a "felt" mass much higher than the final mass m_c during the experience and the plateau reached at the end of the signal corresponds to the interruption of the particles flow. The existing noise prevents us from knowing the captured mass m with time. To avoid this issue, the mass evolution can be obtained by performing stops: at regular time intervals, the flow of particles is interrupted, which enables the force sensor signal to stabilize and to give access to the captured mass. By repeating this operation several times, the mass of captured particles over time is obtained.

6.3.2.2 Influence of bead size

To complete the observations of Figure 6.4, Figure 6.6 shows two force sensor signals of fibers coated with the same quantity of oil ($m_h = 0.9$ mg) but impacted by two sizes of

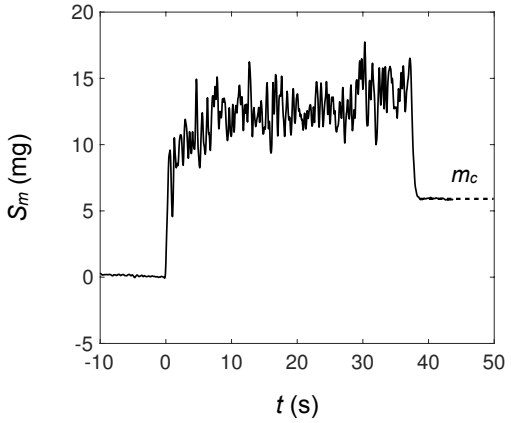

Figure 6.5: Force sensor signal in mass S_m over time t for beads impacting a wetted fiber. The total mass captured is denoted as m_c and is found to be around 5.7 mg, a value much higher than the mass of oil $m_h = 0.9$ mg. Due to impacting beads, the signal is very noisy and prevents us from obtaining the exact captured mass over time. Parameters used: $\eta = 1000$ mPa.s and $d = 55$ μm.

particles. The total captured mass m_c is observed to be quite insensitive to the grain size, in agreement with snapshots of Figure 6.4: $m_c = 6.1$ mg for $d_g = 55$ μm (Figure 6.6a) and $m_c = 6.9$ mg for $d = 90$ μm (Figure 6.6b). Yet, the number N of total captured particles over time, defined as $S_N(t \to \infty)$ is different, as a result of their difference in size.

6.3.2.3 Dry thread

6

As evidenced in Figure 6.7, even without oil, the fiber captures particles, which shows the initial and final states of a dry fiber impacted by a flow of glass beads. Some of them manage to stick to the fiber and the force sensor indicates a captured mass of 0.6 mg, a value much lower than that measured when the fiber is coated with oil. The origin of capture may be the electrostatic interactions between the beads and the thread.

6.3.2.4 Different oil configurations

Our fibers are uniformly coated with oil in a film that undergoes a Plateau-Rayleigh instability. Yet, different oil configurations can be investigated such as a drop of oil deposited on the fiber instead of a film. To test the influence of oil configurations on m_c, a fiber is coated with a drop of oil (Figure 6.8) and impacted by a flow of glass beads. Before impact, the drop is held on the fiber, provided its radius R is smaller that the critical radius R_c of capture: $R_c = (3\gamma d/\rho g)^{1/3} \approx 1.1$ mm [141]. At very short time ($t = 0.6$ s), the grains impacting the fiber sediment in the drop and they have still not reached the bottom. Then, after few seconds ($t = 9.5$ s), the capillary suction begins, caused by the depletion of liquid at the top of the drop. The liquid rises up, because of the capillary depression at the top of the aggregate, in the same manner as on the liquid film (Figure 6.3). In addition to stretching upwards, the aggregate spreads horizontally on the fiber. Finally, after a while ($t = 79.5$ s), the liquid rise ends while the aggregate goes on growing vertically until saturation ($t = 148$ s).

The efficiency of the two oil configurations (film and drop) on the capture is finally compared in Figure 6.9 where the two corresponding force sensor signals in mass S_m are plotted with time (with similar $m_h = 3.1 \pm 0.1$ mg). The first observation to make is the difference of timescale observed for the phenomenon between the two cases and knowing that the flow of particles was interrupted at saturation: for the drop, the capture is much

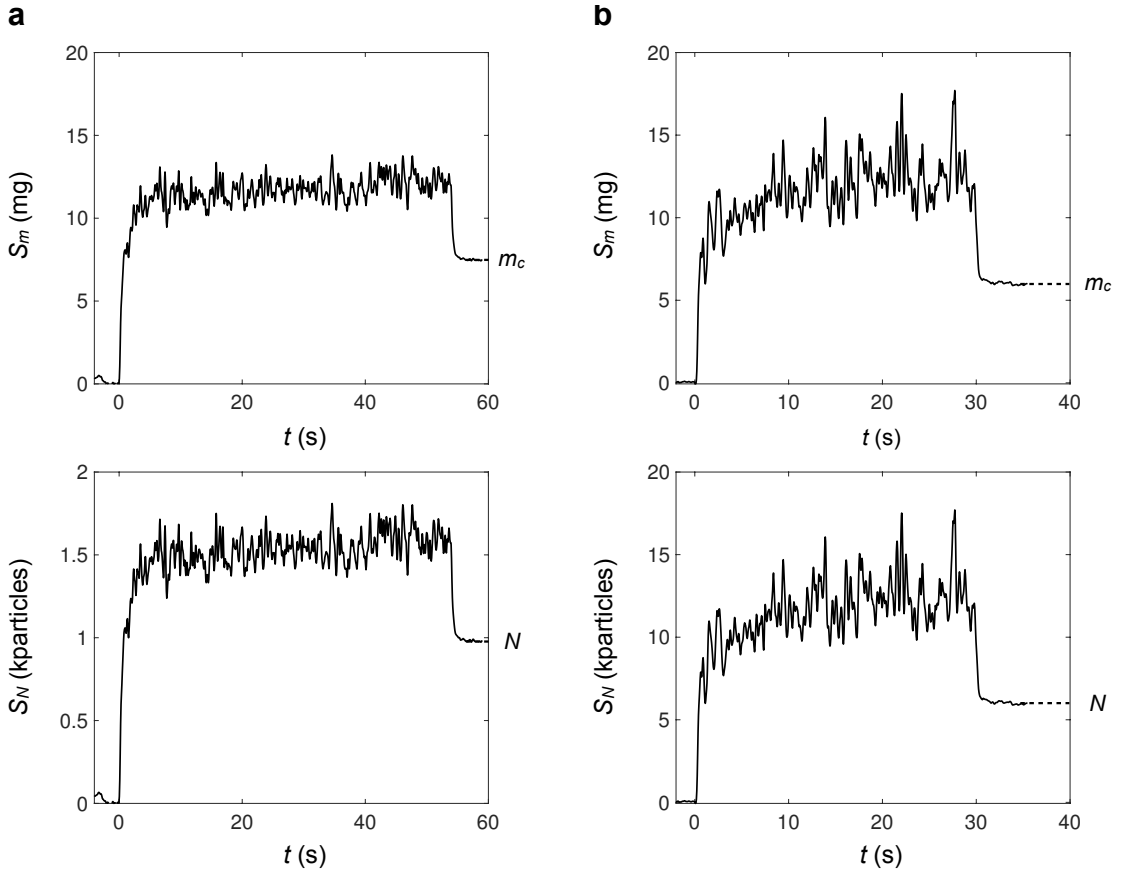

Figure 6.6: Force sensor signal in mass S_m and number of particles captured S_N over time t for two different sizes and identical mass of oil. $m_h = 0.81 \pm 0.03$ mg and $\eta = 1000$ mPa.s. (a) $d_g = 55$ μm and $m_c = 6.1$ mg. (b) $d_g = 90$ μm and $m_c = 6.9$ mg. The captured mass m_c appears to be relatively independent of the beads size d_g.

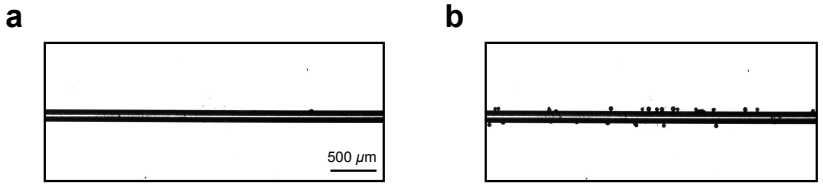

Figure 6.7: Initial (a) and final (b) states of a dry fiber impacted by glass beads. The captured mass m_c is not null and equal to 0.6 mg, which may originate in electrostatic interactions between the beads and the fiber.

longer and lasts 110 seconds while 35 seconds for the film. This variation in time duration originates in the effective capture surface that is much more significant for the film, hence its faster saturation. Furthermore, m_c is observed to be independent of the oil configuration ($m_c = 14.6 \pm 0.4$ mg), whichs shows that m_c is only controlled by the oil volume.

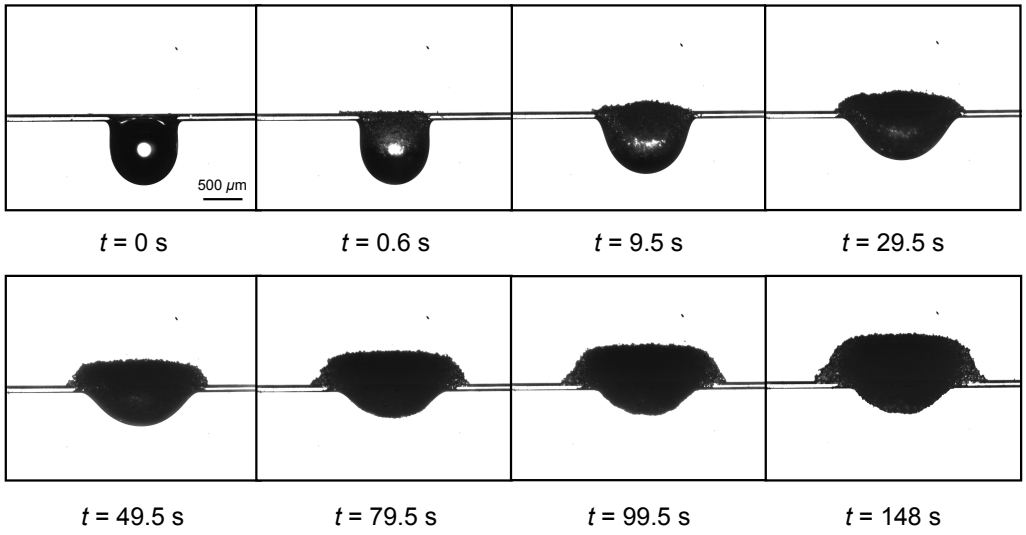

Figure 6.8: Snapshots of beads capture ($d_g = 55$ μm) over time on a fiber coated with a drop of oil with mass $m_h = 1.1$ mg.

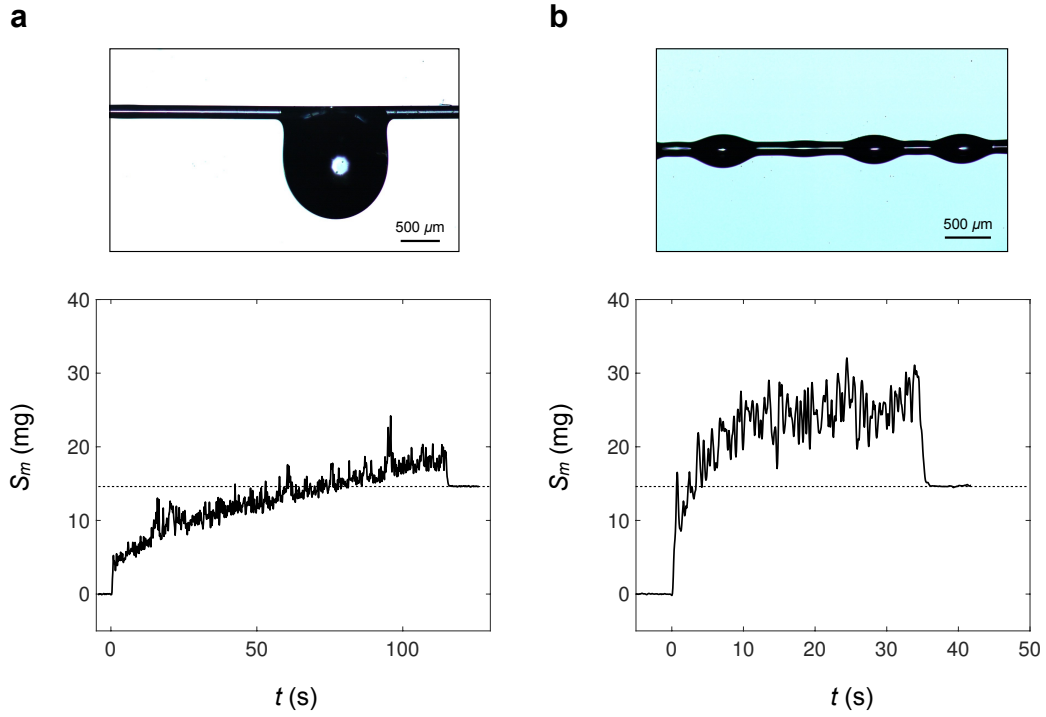

Figure 6.9: Force sensor signal in mass S_m as a function of time t for the capture on a fiber coated with a drop (a) or with a film (b) of oil. m_h is the same for the two experiments, $m_h = 3.1 \pm 0.1$ mg and $m_c = 14.6 \pm 0.4$ mg. The two evolutions are different and the aggregate saturation takes much longer for the drop.

6.3.3 Total captured mass

6.3.3.1 Quantitative results

We report in Figure 6.10 the total mass of captured particles m_c as a function of the mass of deposited oil m_h. As mentioned earlier, two particle sizes and two viscosities were used and the cases corresponding to the two oil configurations are also reported. We denote

as V100 the viscosity of oil η when it is equal to 100 mPa.s and V1000 when equal to 1000 mPa.s. Three features are remarkable on this plot: (1) m_c increases with m_h and seems to align on a line ($m_c \approx 4\ m_h$). (2) Viscosity, bead size and oil configuration do not seem to influence m_c, as previously observed (Figures 6.7 and 6.10). These two points lead us to validate our hypothesis: m_c is only influenced by m_h. (3) A dispersion of points is noticed. It is first due to our measurements errors (force sensor). Another explanation may be the final effective capture surface: indeed, at saturation, all the liquid is distributed between the beads and the only "available" liquid is at the aggregate surface. This surface depends on the oil configuration (smaller for a drop) and also on the length of the coated fiber (which slightly varies between experiments). This last layer of liquid, more or less significant, captures the last particles, hence explaining the dispersion of points for a given mass of oil. We now try to build a model to understand all these observations.

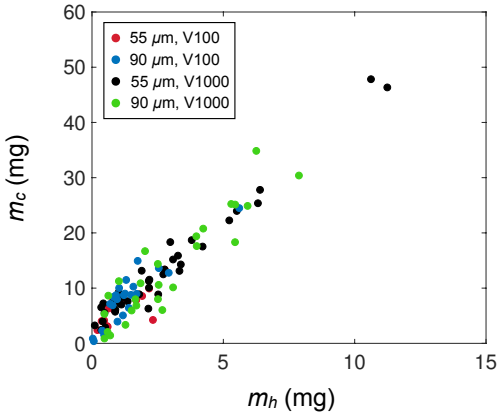

Figure 6.10: Total mass of captured particles m_c as a function of the mass of deposited oil m_h for two bead sizes ($d_g = 55\ \mu$m and 90 μm) and two viscosities V100 and V1000. m_c seems to be independent of the bead size and viscosity and all data align on a line.

6.3.3.2 Model of capture

Following the results of Figure 6.10, it is legitimate to assume that only m_h influences m_c. In order to model the mass of captured particles, one needs to investigate the stucture of the aggregate formed by air, oil and glass beads. A wet aggregate composed of liquid and grains can have air bubbles trapped. To verify this point, X-ray tomography experiments have been performed on our samples after the saturation of the aggregate. This method consists in reconstructing cut by cut the analyzed object thanks to radiographs obtained at different angles. It enables then to reconstruct in three dimensions the internal structure of the aggregate. Figure 6.11 thus shows a 2D cut of an aggregate where we distinguish the grains, the oil and the fiber. The tomogram indicates that the aggregates are always saturated without any air bubble and are thus in a capillary state [142]. It implies that the liquid fills all the pores and cohesion is ensured through a capillary depression induced by the liquid-air menisci. Besides, the mean compacity of the aggregate ϕ (defined as the ratio of the volume occupied by grains over the total volume) is determined and found equal to 0.63 ± 0.02, a value identical to that obtained by Saingier *et al.* [135]. This value is very close to the one obtained when hard perfect spheres are packed randomly in the most compact way, and for which $\phi = 0.64$. It is also found less that the maximum compacity, that is close-packing where $\phi = \pi/3\sqrt{2} \approx 0.74$. This analysis was only carried out for aggregates composed of grains with diameter 55 μm. Nonetheless, Figure 6.10 suggests that ϕ little varies with the grain size.

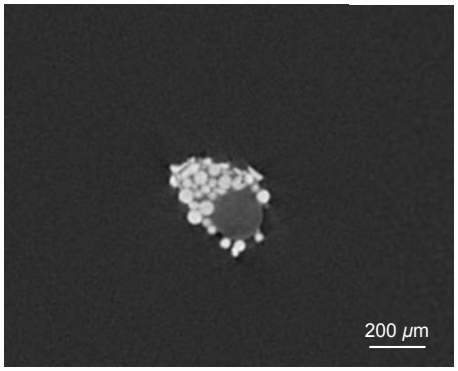

Figure 6.11: 2D cut of the beads-oil aggregate on the fiber. Images are performed using a tomogram. The tomography experiments show that the aggregate is in capillary state, *i.e.* no air bubbles are trapped. As a result, the compacity ϕ is high and found equal to 0.63.

Since the aggregate is free of air, the compacity ϕ is assumed to be spatially uniform, the total volume of oil and particles V_{tot} is the sum of the volume of oil V_h and the volume of particles V_c. As $V_c = \phi V_{\text{tot}}$, one can rewrite $V_c = \phi/(1-\phi)V_h$. In terms of mass, this relation becomes simply:

$$m_c = \frac{\rho_g}{\rho}\frac{\phi}{1-\phi} m_h \ . \tag{6.1}$$

This equation predicts a linear relation between m_c and m_h, in agreement with our experimental observations. Besides, m_c only depends on the compacity and on the quotient of the two densities (oil and particles) and not on the oil viscosity, nor on its configuration on the fiber (film/drop). Tomography experiments provide us with a compacity equal to 0.63. A fit of Eq. (6.1) on our experimental points (Figure 6.10) yields a value for ϕ of 0.63, the same obtained during compacity experiments.

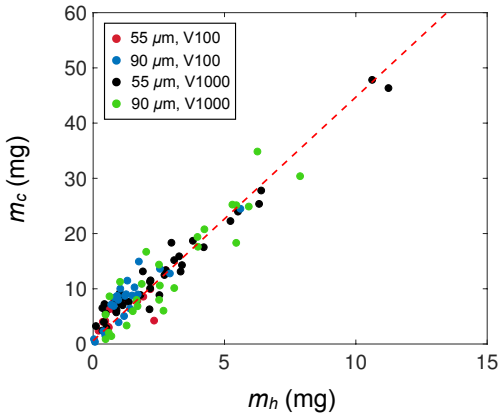

Figure 6.12: Total mass of captured particles m_c as a function of the mass of deposited oil m_h. The red dotted line is Eq. (6.1) plotted with an intercept of 0.6 mg and $\phi = 0.63$, and found to agree well with the experimental data.

Finally, Figure 6.12 shows Eq. (6.1) plotted with $\phi = 0.63$ in red dashed line with an intercept of 0.6 mg that corresponds to the mass captured on a dry thread. From the figure, the model captures well the behaviour of m_c with m_h. The total number of captured particles N is also displayed as a function of m_h in Figure 6.13. Smaller particles ($d_g = 55$ μm) have a larger N because of the independence of m_c on d_g (Figure 6.12). N can be predicted using

Eq. (6.1) and reads:

$$N = \frac{6}{\pi d_g^3} \frac{\phi}{1-\phi} \frac{m_h}{\rho} \ . \tag{6.2}$$

Eq. (6.2) is plotted in Figure 6.13 for the two bead sizes. As for Figure 6.12, the model is found to quantitatively fit the data, especially for the large oil masses ($m_h \geq 4$ mg). However, for smaller m_h, Eq. (6.2) underestimates the number of trapped particles: a higher compacity could explain this discrepancy. Indeed, at lower oil volume, captured particles that accumulate in the aggregate can reorganize themselves to make a more compact ensemble. On the contrary, at larger oil volume, particles impacting fall in a large quantity of liquid and the liquid is not depleted at the beginning of the capture. Beads may then arrange in a more random way, hence inducing a lower ϕ. Moreover, one notices the existence of a liquid layer at the surface that is not taken into account in our model, and which could explain the discrepancy between our model and the data at low m_h.

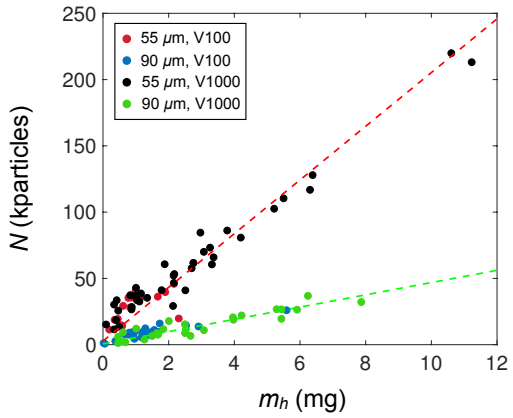

Figure 6.13: Total number of captured particles N as a function of the mass of deposited oil m_h for two bead sizes and two viscosities V100 and V1000. Eq. (6.2) is drawn with dotted lines for $d_g = 55$ μm (red line) and 90 μm (green line).

6.4 Capture kinetics

6.4.1 Oil film

6.4.1.1 Experimental results

The capture efficiency of a wetted fiber varies over time. At short time, Figure 6.3 shows that the oil film grows very rapidly, a manifestation of the high capture efficiency. On the contrary, at larger time ($t \geq 5$ s), the aggregate height seems to saturate. Qualitatively, at short time, particles impacting the fiber encounter a liquid bath. The surface layer depletes in oil with time because of the grains. It results in a less and less efficient capture which explains the stabilization of the aggregate size at long times. Figure 6.14 presents the captured mass m over time t and it validates these observations: in 20 seconds, m grows from 0 to 20 mg, while it increases by 5 mg in 60 secondes before saturating at $m = m_c = 25.2$ mg at $t = 90$ s.

6.4.1.2 Influence of viscosity

Viscosity was previously shown to have no influence on m_c. Nonetheless, it must play a role in the growth dynamics. Indeed, as observed in Figure 6.3, at short time, because

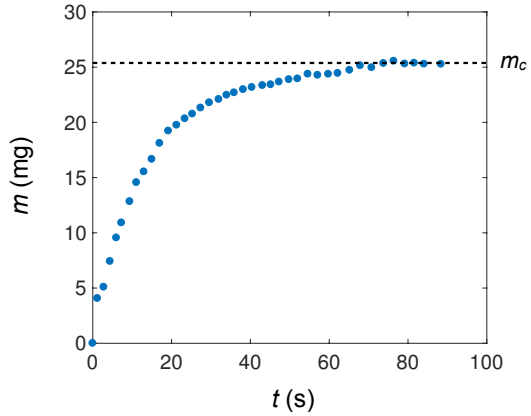

Figure 6.14: Time evolution of the mass of captured particles m on a wet fiber coated with an oil film. Parameters used: $d_g = 90$ μm, $\eta = 1000$ mPa.s, $m_h = 5.3$ mg. m is a concave function of time and saturates at long time at $m = m_c$.

of impacting beads, the liquid "under the fiber" rises due to capillary suction. Capture is thus limited by the viscous displacement of oil in a granular medium, hence the influence of viscosity. As such, the evolution of m with time t is plotted in Figure 6.15 for two viscosities and where m_h is the same. At short time, ($t \leq 20$ s), m is higher for the lowest viscosity (by 75%). However, the two captured masses rapidly become equal: at larger time, the growth dynamics is only limited by the capture efficiency and not by viscosity and the two curves converge towards the same total captured mass m_c, independently of viscosity.

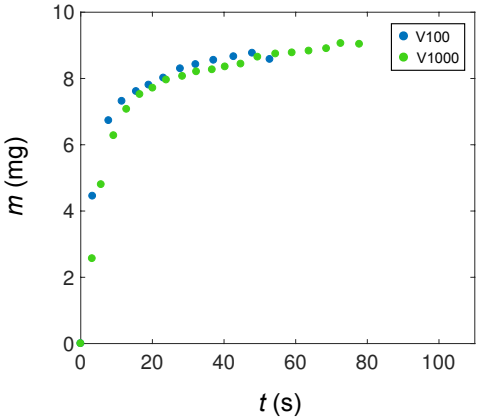

Figure 6.15: Influence of viscosity on the mass of captured particles m as a function of time t on a wetted fiber: $\eta = 100$ mPa.s (blue data) and 1000 mPa.s (green data). The beads have a diameter $d_g = 55$ μm and the mass of oil is $m_h = 1.8$ mg.

6.4.2 Drop of oil

6.4.2.1 Experimental results

For a drop of oil, the kinetics of capture differs from the one obtained with an oil film. The captured mass m in a drop of oil is plotted with time in Figure 6.16 and compared to the oil film, taking an identical mass of oil. The catch for the drop is slightly slower than for a film with an initial mass growth ($\mathrm{d}m/\mathrm{d}t(t = 0)$) 3 times larger for the film. The difference in the efficient surface of capture S explains this discrepancy: the drop has a radius on the order of a millimeter which yields S on the order of 3 mm^2. For the film instead, the wet

length is on the order of 10 cm for an oil thickness of around 100 μm, which yields S on the order of 10 mm^2, that is around 3 times larger than for the drop, a value comparable the difference of initial mass growth between the two configurations. Moreover, we observe a different evolution with time of m for the drop and for the film: contrasting with the film for which m increases strongly in a short time and rapidly saturates, the capture on a drop exhibits a quasi-linear behavior over time, lasting about 20 s compared to the $\sim$ 3 s for the film. In the case of the drop, the dynamics seems to be divided into two regimes, as first observed in Figure 6.8: the 1$^{\text{st}}$ regime occurs when the liquid rises up. During this period ($0\text{ s} \leq t \leq 20\text{ s}$), the captured mass evolves linearly in time. The second regime arises when the liquid has finished to rise up and the dynamics is limited by the efficiency of capture. In this period, m follows the same dynamics as for the film: the growth speed decreases with time and m saturates at $m = m_c$. For the following, we only consider the smallest bead size, that is $d_g = 55$ μm.

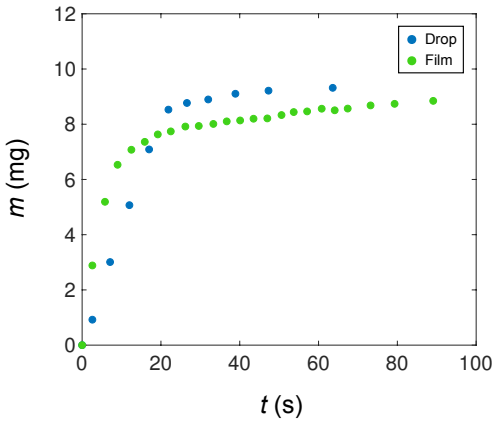

Figure 6.16: Influence of the oil configuration on the time evolution of the captured mass of particles m: film (green data) and drops (blue data). The two dynamics are different: for the drop, m follows a linear evolution in time during more than 20 s. The oil mass is identical: $m_h = 2.1 \pm 0.2$ mg with $\eta = 100$ mPa.s. The particles have a diameter $d_g = 55$ μm.

6.4.3 Model

6.4.3.1 Capture efficiency

The geometry of our system is complex since the thickness of oil is not constant horizontally owing to the Plateau-Rayleigh instability. The radius of the wetted fiber r_w and the height h of the aggregate must then depend on the horizontal position (Figure 6.17).

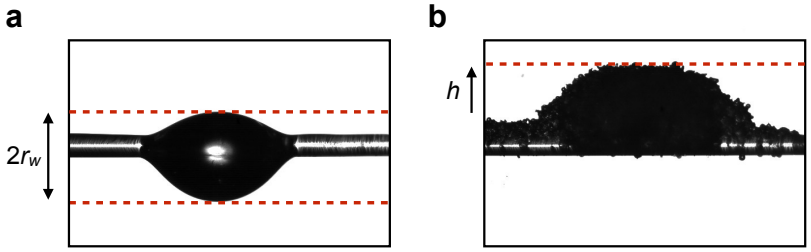

Figure 6.17: Scheme of the radius of the wetted fiber r_w and height of the aggregate h.

Two regimes coexist during the growth of the aggregate [135] and two timescales must be introduced: τ_{visc}, the transport time of liquid in the porous medium and τ_{capt}, the capture

time of a bead (Figure 6.18a). A first regime occurs when $\tau_{\text{visc}} \gg \tau_{\text{capt}}$: the capture is then limited by the upward viscous displacement of liquid that is driven by the capillary suction. The second regime occurs when the capture time is very long and is thus limited by the capture efficiency at the aggregate surface. First, the viscous regime is modeled as the flow of a liquid into a porous medium and is described by the Lucas-Washburn dynamics [143, 144]: the driving force of the capillary suction is the capillary pressure in the pores. The pressure p_d in the aggregate can be obtained using Darcy's law:

$$p_d = \frac{\eta(1-\phi)}{k} h v \ , \tag{6.3}$$

where k is the permeability of the packing and $v = \mathrm{d}h/\mathrm{d}t$ the speed of growth. Besides, the pressure is also given by Laplace's law: the Laplace pressure p_l is associated with the bead diameter d_g: $p_l = \gamma c/d_g$, where c is a coefficient of order unity [139].

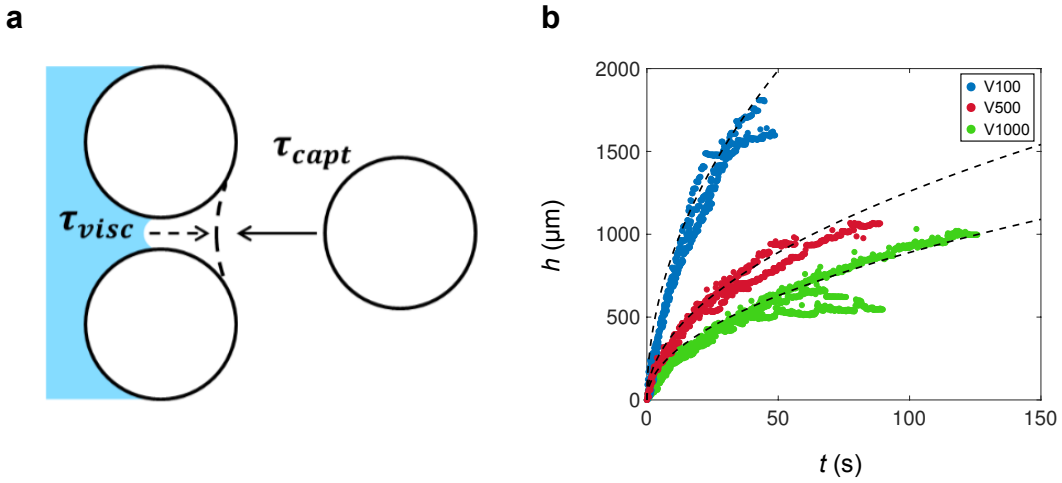

Figure 6.18: (a) Sketch of the two capture processes associated with the two timescales: viscous displacement in a time τ_{visc} followed by grain capture in a time τ_{capt}. Extracted from [135]. (b) Height of the aggregate h as a function of time t for different drop radii and viscosities: $\eta = 100$ mPa.s (blue data), $\eta = 500$ mPa.s (red data) and $\eta = 1000$ mPa.s (green data). The grains have diameter 55 μm. For each viscosity, data collapse on one single curve, independently of the drop radius. The higher the viscosity, the lowest the final height of the aggregate. Eq. (6.4) is drawn in black dashed line for the three viscosities, taking the adjustable parameter $c = 2$, and matches well the data.

Equalizing the two pressures p_d and p_l yields the height h after integration:

$$h(t) \approx \sqrt{\frac{2c\gamma\, k\, t}{\eta\,(1-\phi)\, d_g}} \ . \tag{6.4}$$

The permeability k is obtained using Carman-Kozeny formula [145]: $k = d_g^2(1-\phi)^3/180\phi^2$. The only adjustable parameter in Eq. (6.4) is c which governs the curvature radius of the meniscus. To get an insight into the growth dynamics, the height h is plotted with time t in Figure 6.18b in the drop configuration and for three viscosities ($\eta = 100$, 500 and 1000 mPa.s) and different drop radii (ranging from 500 μm to 1.5 mm). The height increases up to a saturation where it stabilizes and which value depends on the drop radius.

Before saturation, the dynamics exhibits a $t^{1/2}$ dependence, as predicted by Eq. (6.4). This equation is drawn in dotted line for the three viscosities and describes well the data before saturation. We choose here $c = 2$, *i.e.* $p_l = 2\gamma/d_g$, which indicates that the pore radius is two times the bead radius r_g. This value is larger than the one expected: the

meniscus has usually a radius of curvature that varies between $r_g/10$ and r_g [146]. However, Saingier *et al.* also noted that the capillary pressure p_l, connected to the bead dimension r_g, can overestimate the depression in the aggregate [135]. Another possible explanation for the value of c is the uncertainty on ϕ at the beginning of the capture: grains may be packed in a less compact way ($\phi < \phi_{\max} = 0.63$) because of the large volume, which decreases the typical dimension between the beads. Furthermore, at the onset of saturation, the slope of h decreases and the dynamics enters a new regime governed by the capture probability of beads. Besides, h is not impacted by the initial drop radius at the beginning of capture, as evidenced by the collapse of the experimental data on one curve for each viscosity (Figure 6.18b). Finally, the aggregates are observed to grow higher at lower viscosity. Indeed, at higher viscosity, the aggregate tends to be more rigid and impacting grains have difficulty in incorporating into the aggregate, hence inducing a lower height and slower evolution. Based on the expression of h, one deduces the viscous timescale τ_{visc}:

$$\tau_{\text{visc}} \approx \frac{h^2(1-\phi)\,\eta\, d_g}{2c\gamma\cos\theta\, k} \ . \tag{6.5}$$

For the Plateau-Rayleigh configuration, the average aggregate height h is on the order of 100 μm, hence $\tau_{\text{visc}} \approx 0.1$ and 1 s for $\eta = 100$ and 1000 mPa.s, respectively. In the case of the drop of oil, h is found to be around 1 mm and we obtain $\tau_{\text{visc}} \approx 10$ and 100 s for $\eta = 100$ and 1000 mPa.s, slightly slower than the one observed for $\eta = 100$ mPa.s in Figure 6.18b where $\tau_{\text{visc}} \approx 50$ s. For the Rayleigh-Plateau configuration, τ_{visc} is very small compared to the total time of the experiment (on the order of 100 s), hence the viscous regime will not be observable, which explains the results of Figure 6.16.

The second regime occurs when $\tau_{\text{capt}} \gg \tau_{\text{visc}}$. The growth dynamics is then limited by the capture efficiency [135]. As observed in Figure 6.14, the mass captured at each moment decreases over time, which shows that the capture is less and less efficient as the grains accumulate. We introduce a capture probability P_{capt}, that is the fraction of grains captured, and the growth rate of the aggregate $v = \mathrm{d}h/\mathrm{d}t$ is thus given by [134, 135]:

$$v = \frac{Q}{\rho_g \phi} P_{\text{capt}} \ , \tag{6.6}$$

Pacheco-Vazquez *et al.* and Saingier *et al.* [134, 135] studied identical systems, namely the accretion dynamics on wet granular media. In both studies, the authors showed theoretically and experimentally that the capture probability P_{capt} decreases exponentially with the height h, as well as the growth velocity v (Eq. (6.6)): ones finds $v(h) = v_0 \exp(-h/h^*)$, where v_0 is the growth rate of the aggregate at the initial time and h^* a typical length that characterizes the velocity decrease. One has $v_0 = QP_0/\rho_g\phi$, where $P_0 = P_{\text{capt}}(h = 0)$ is the capture probability at initial time. This exponential dependence means that as the capture progresses, less and less liquid is available on the surface. Saingier *et al* theoretically demonstrated that the surface liquid fraction does decrease exponentially with h [135].

Figure 6.19 illustrates this explanation: as the aggregate grows, less liquid is available at the surface, which retracts the liquid meniscus, hence inducing a decrease of the surface liquid area [135]. The capture probability is directly related to this fraction of liquid available on the surface: the more oil on the surface, the greater the probability that the grains impacting the fiber will be captured.

In both experiments [134, 135], the grains impact a porous medium under which there is liquid. Our case is different as grains directly impact the liquid and we assume that this model can be applied here. To confirm this hypothesis, the height of grains h is measured

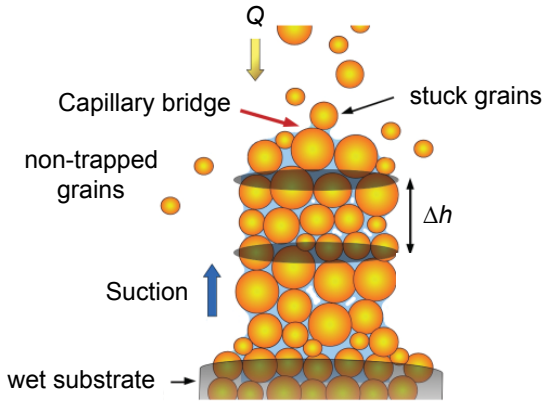

Figure 6.19: Sketch of the aggregate for increasing h. Extracted from [134].

over time. Assuming that v decreases exponentially with h, one finds:

$$h(t) = h^* \ln(1 + \frac{v_0 t}{h^*}) \ . \tag{6.7}$$

As shown earlier, the viscous regime is predominant in the drop configuration while negligible in the film configuration because of the low thickness in liquid. Figure 6.20 shows different aggregate heights h as a function of time for different oil masses in a film configuration. At small time, all data relatively collapse on the same curve with an initial growth speed $v_0 \approx 35 \pm 20$ μm/s. Besides, the aggregate height increases until saturating at large t (as for m). The maximum reached height differs between the four data and increases with the oil mass and can reach up to 200 μm, that is around the diameter of the fiber. Eq. (6.7) considers an "infinite" volume of liquid and does not predict a saturation of h at large time.

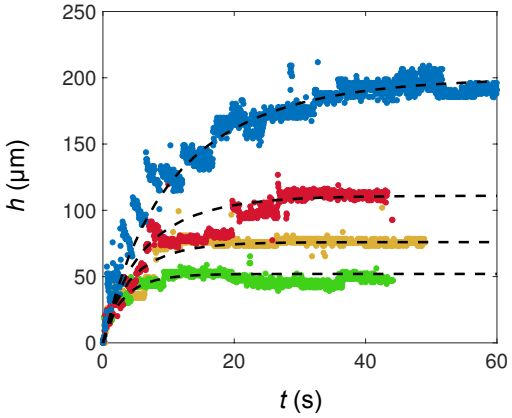

Figure 6.20: Height h of four aggregates as a function of time t for beads with diameter $d_g = 55$ μm impacting a film of oil. The four colours correspond to four different oil thicknesses. The solutions of Eq. (6.9) are plotted in black dashed lines for $v_0 = 35$ μm/s and $h_c = h^\star$ and found in good agreement with the experimental data. The parameter $h^\star$ depends on the oil thickness and corresponds to the maximum height reached by the aggregate: $h^\star = 52$ μm (green data), $h^\star = 76$ μm (yellow data), $h^\star = 111$ μm (red data) and $h^\star = 200$ μm (blue data).

To account for the limited volume of oil, Saingier *et al.* resorted to a additional parameter h_c, that is the critical height for which the capture probability becomes null [135]: it is coherent in our model as, after some time, all the liquid will rest between the grains and no more oil will be available at the aggregate surface, hence no capture. In that case, the

capture probability P_{capt} reads [135]:

$$P_{\text{capt}} = \begin{cases} P_0 \left(e^{-z/h^\star} - e^{-h_c/h^\star} \right) & \text{for } z < h_c \\ 0 & \text{for } z > h_c \ , \end{cases} \tag{6.8}$$

where P_{capt} is taken null at $h = h_c$ and the general expression of h with time can be deduced after solving the equation:

$$t = \frac{h^\star}{v_0} e^{h_c/h^\star} \left[-\frac{z}{h^\star} - \ln \left(\frac{e^{-z/h^\star} - e^{-h_c/h^\star}}{1 - e^{-h_c/h^\star}} \right) \right] \ . \tag{6.9}$$

The solutions of Eq. (6.9) are plotted in black dashed lines in Figure 6.20 and observed to agree well with the data. We choose an initial growth speed v_0 equal to 35 μm/s for all data: indeed, at the beginning of the capture regime, the growth process is not impacted by the film thickness but only by the liquid configuration, hence an independence of v_0 on r. Besides, we choose $h_c = h^\star$ and $h^\star$ is taken at the saturation height for each film thickness. The saturation height is dictated by the initial oil volume per unit length of fiber, which we now discuss.

6.4.3.2 Captured mass

6.4.3.3 Low oil volume

For low oil volumes, the film is uniform horizontally and does not destabilize (Figure 6.1): the mass of the aggregate is deduced from its height. The growth only occurs vertically, meaning that the thickness of the fiber-aggregate (plane perpendicular) is approximately constant and equal to $2r_w$, r_w being the mean radius of the wetted fiber. The volume of the aggregate is then $2r_w(r_w + h - r_w)L$, using the fact that capture only occurs in the upper part of the fiber and reminding that L is the length of the wetted fiber. Assuming that the compacity is relatively homogeneous with time, one obtains:

$$m(t) \approx 2\phi\rho_g L r_w h(t) \ , \tag{6.10}$$

and this equation must be combined with the solution of Eq. (6.9) to get the expression of m with time. In our analysis, we use the same value of v_0 as before, that is 35 μm/s. This value can be obtained using the equality $v_0 = QP_0/\rho_g\phi$. Besides, one has:

$$\frac{\mathrm{d}m}{\mathrm{d}t}(t = 0) = 2r_w L Q P_0 \ . \tag{6.11}$$

Our experimental data yield $P_0 = 0.07 \pm 0.05$, found very close to the values obtained in [134, 135]. We find $v_0 = 40 \pm 20$ μm/s, in very good agreement with the fitted value of 35 μm/s. We plot in Figure 6.21 the time evolution of the captured mass m for four data sets and at large time, m saturates at the value m_c. The experimental data are fitted using Eqs. (6.9) and (6.10) and the solutions are drawn in black dotted lines. A good agreement is observed, except at short time where it tends to underestimate the growth. Similarly to Figure 6.20, the critical height h_c is set to $h^\star$ and the computed parameters $h^\star$ are very close to the final height measured, hence showing the robustness of the model. $h^\star$ is observed to increase with the thickness of oil $r_h = r_w - r$. The dynamics of m can thus be predicted knowing only the total mass captured m_c and the initial growth velocity v_0.

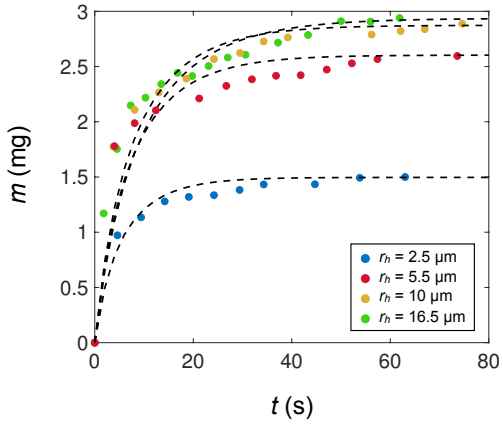

Figure 6.21: **Captured mass for low oil volume**. Captured mass m plotted as a function of time t for four data sets. We denote as the oil thickness $r_h = r_w - r$, where r and r_w are respectively the radius of the dry and wetted fiber. Dashed lines correspond to the solutions of Eq. (6.9), taking as before $v_0 = 35$ μm/s and $h_c = h^\star$, and match well the data. We take $h^\star = 90$ μm (blue dots), 130 μm (red dots), 140 μm (yellow dots) and 170 μm (green dots). Despite different r_h, yellow and green data are relatively similar because of the slight difference in wetted length L, the key parameter in the captured mass being Lr_w. The particles have here a diameter of 55 μm.

6.4.3.4 Normal oil volume

For a larger oil volume, *i.e.* when the Rayleigh-Plateau instability occurs, the geometry of the wetted fiber becomes more complex. Because of the combination of droplets and oil film, the aggregate height depends on the horizontal position. Different horizontal positions x on a wetted fiber yield different evolution of the aggregate height with time (Figure 6.22).

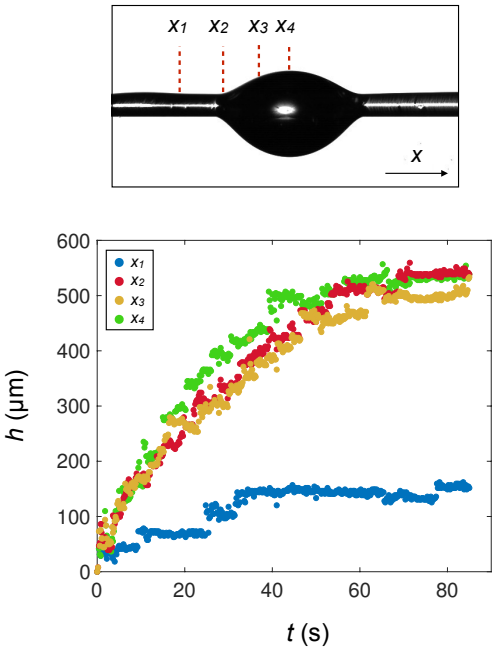

Figure 6.22: Dynamics of the aggregate height h with time t for four horizontal positions x in an oil film in Plateau-Rayleigh configuration impacted by beads with diameter 55 μm. In the "drop", the three heights follow the same dynamics while in the film, the height is much smaller and reaches a maximal value of 150 μm ($\approx$ 500 μm in the drop).

Firstly, for $x = x_1$ (film), the final height is observed to be much smaller than the three other heights, a consequence of the low oil thickness at this position. Secondly, in the "drop", the heights are observed to follow the same evolution despite the different local oil thickness. For sake of simplicity, h is then assumed to be horizontally constant: this assumption is far from reality but drops occupy much more space than the film in the Plateau-Rayleigh configuration, hence it is not so illegitimate. The consequence of this assumption will be an overestimation of the captured mass.

Finally, using the same reasoning as for low oil volumes, the captured mass m reads:

$$m(t) \approx 2\phi\rho_g L r_w h(t) \ . \tag{6.12}$$

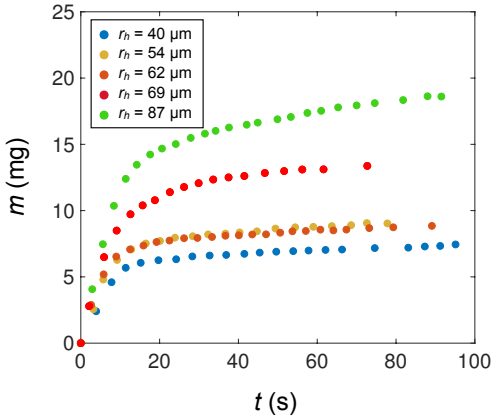

Figure 6.23: Captured mass m over time t for normal oil volumes and five different volumes of oil. At short time ($t < 10$ s), the data collapse on a line and it may originate in the liquid reconfiguration during the flow interruption processes. After this period, m increases until saturation at $m = m_c$, a quantity that depends on the oil mass.

However, one discrepancy exists between the two cases (normal and low oil volumes). For the low oil volumes, as soon as the capture starts, the capture probability diminishes and Eq. (6.9) describes well the dynamics for the whole capture process (Figure 6.21). As evidenced in Figure 6.23, in the case of the normal oil volume, the captured masses seem to follow a linear behavior with time during a first phase that lasts up to 10 s. This first period of capture was shown to be in the viscous regime (duration ~ 10 s) so one would have expected a $t^{1/2}$ evolution for m. This difference may originate in our experimental set-up: to extract the mass m at different times, the flow is interrupted for few seconds so that the force sensor can stabilize. During this period, the liquid has enough time to rise up and the growth dynamics enters the capture regime where h is instead linear with time (Eq. (6.6)).

To complement this observation, Figure 6.24a displays the computed aggregate height $h = m/2\phi\rho_g L r_w$ as a function of time t. The initial slopes are found to be the same and equal to 35 ± 5 μm/s, a value equal to v_0, the one found earlier. Consequently, because of the liquid reorganization during the flow interruption, the viscous regime is not observed. The capture regime is then first characterized with a constant capture probability because beads only impact a liquid bath: the growth velocity v is therefore constant and found equal to v_0 (Eq. (6.6)). Later on, after the liquid has risen up, a second phase emerges where the capture probability decreases with h (Eq. (6.9)). The solutions of Eq. (6.9) are plotted in dashed lines in Figure 6.24a and b from a time when the linear behaviour ends, which is on the order of r^2 according to Eq. (6.5) (between 5 and 10 s for our experimental r). The model matches fairly well the data for the normalized mass and captured mass. The only uncertainty in our modelling is the transition time when the capture probability is not constant anymore.

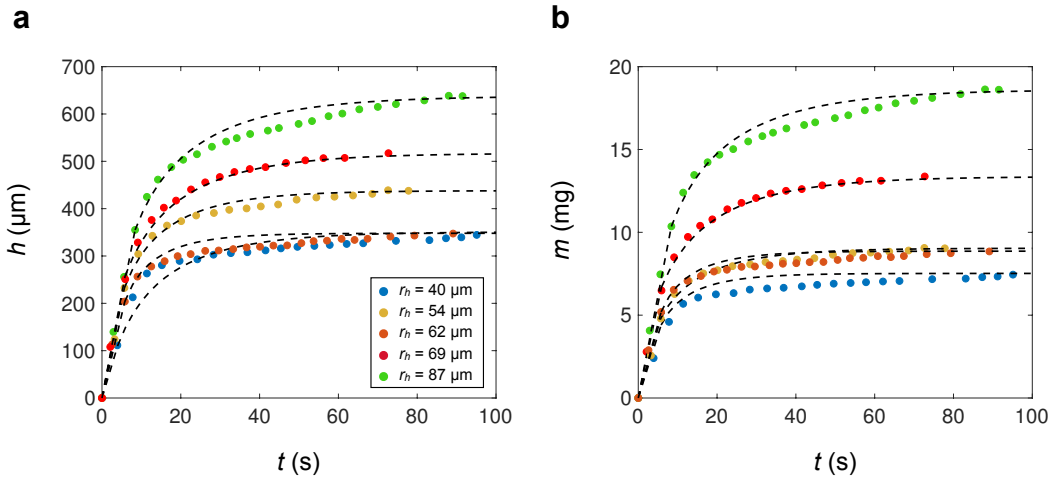

Figure 6.24: **Captured mass for normal oil volume**. (a) Computed height $h = m/2\phi\rho_g L r_w$ as a function of time t of five wetted fibers with oil thickness $r_h = r_w - r$. The data are fitted with the solutions of Eq. (6.9) at the end of the linear behaviour ($t \approx 5-10$ s), taking as before $v_0 = 35$ μm/s and $h_c = h^\star$, and the model matches well the data except for the lowest oil volume (blue data). (b) Captured mass m plotted with time t, together with Eq. (6.10), taking $h(t)$ the solution of Eq. (6.9) (dashed lines). We take $h^\star = 305$ μm (blue dots), 420 μm (yellow dots), 310 μm (orange dots), 520 μm (red dots) and 630 μm (green dots).

We have not thoroughly studied the growth dynamics for the drop configuration as the geometry of the aggregate is too complex (Figure 6.8). Nonetheless, the captured mass m seems to follow two regimes (Figure 6.16): a first regime where m is linear with time and is the capture regime. In that case, when the viscosity is low ($\eta = 100$ mPa.s), the viscous time τ_{visc} (Eq. (6.5)) is low and the dynamics is governed by the capture efficiency: the capture probability is first constant with time because particles only impact liquid and captured particles can sink fastly in the aggregate (speed in the liquid of around 25 μm/s using Stokes formula). After some time ($t \sim 20$ s), the capture efficiency decreases with height and one recovers the dynamics predicted by Eq. (6.9). For higher viscosity, τ_{visc} becomes large enough so that the viscous regime cannot be neglected and one expects a Lucas-Washburn evolution for m during a first phase, $m \sim t^{1/2}$ (Eq. (6.4)).

Take home message of Chapter 6

1. A cohesive aggregate. Particles impacting wetted fibers can be captured. Their trapping generates a liquid reorganization inside the aggregate and an upward motion of liquid. The capture ends when the aggregate is saturated. Oil and particles form a cohesive aggregate where no air bubbles are trapped (capillary state) and which compacity ϕ is found constant and equal to 0.63.

2. Total captured mass. The maximum mass of captured particles is only limited by the quantity of deposited liquid. It varies linearly with the mass of oil and is not influenced by particles size, liquid configuration on the fiber and liquid viscosity.

3. Growth dynamics. The aggregate growth results from the competition between the motion of liquid in the porous medium (viscous regime) and the capture efficiency of particles at the aggregate surface (capture regime). For the film configuration, the kinetics is only limited by capture efficiency which is found to decrease with increasing aggregate height. The growth of the aggregate generates a depletion of surface liquid fraction at the interface with air, hence a decreasing capture probability of particles.

PART III

COMPLEX ECONOMICS

7

Slutsky equations and beyond

The Slutsky equation is central in consumer choice theory in microeconomics. We first introduce the concept and the expression of the Slutsky matrix. We then present a framework where agents are no longer rational and study its impact on the substitution matrix. Finally, we look at the influence of different forms of interactions (products, agents) on the Slutsky equation and how they can reveal features that are not predicted within the classical economics framework.

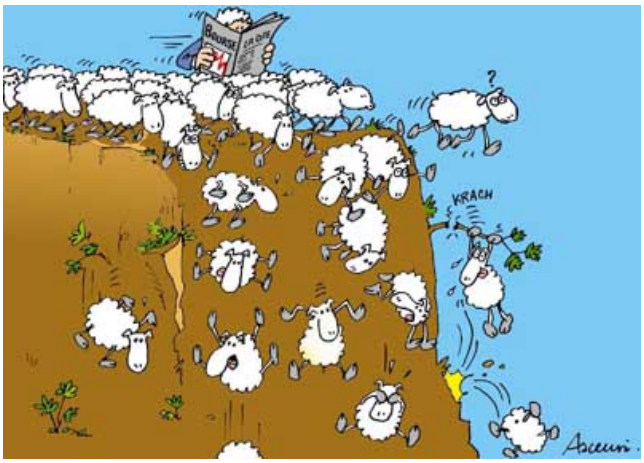

Panurge sheeps jumping into a ravine. Photo credits: [147].

Contents

This work was undertaken under the supervision of my colleague Michael Benzaquen that introduced me to the field of econophysics. It was a great pleasure to work with him and I warmly thank him. I also thank people from *Capital Fund Management* and *LadHyX* that helped me and with whom I learned at lot: Jean-Philippe Bouchaud, Antoine Fosset, José Morán, Pierre-Philippe Crépin and Davide Luzzati.

7.1 Introduction

Classical economics theory appears to be wedded to the *Homo economicus* hypothesis: in most models, the economic agents are assumed to be fully rational, independent, homogeneous and able to solve their utility maximization instantaneously, in contradiction with what behavioural economics (and common sense) indicates [148, 149]. For instance, interactions between individuals are hardly negligible as they can be mainly responsible for trends, mass panic and avalanches of opinion changes, to name a few. Studying the effect of relaxing some of the unrealistic hypotheses, especially in financial markets, gave birth to the field of econophysics. Several crises were indeed found to be endogeneous, self-generated without the influence of any external event. Challenging the standard representative agent approach has enabled one to identify some of their causes.

One may then wonder what features can emerge when introducing some irrationality, heterogeneities or interactions in the decision rules. It can lead to aggregate behaviours completely different from the classical theoretical predictions and which exhibit strong non-linearities, phase transitions and out-of-equilibrium dynamics, as indeed observed in many complex systems [150, 151].

The aim of the present study is to illustrate how the effects of non-equilibrium (arising from heterogeneity and interactions) can modify results predicted by classical economics. Here we focus on the very classical case of the *Slutsky equation* [152]. We shall challenge the *Homo economicus* hypothesis by investigating the effects of finite temperature, heterogeneities and further, of interactions.

7.2 Consumer choice theory

7.2.1 Optimization problem

In the theory of consumer choice, for a given bundle of goods with prices $\boldsymbol{p}$,[1] classical agents maximize their utility u subject to a budget constraint. Their utility function shall depend on the quantities $\boldsymbol{x}$ of goods and one defines w as their budget: $w = \boldsymbol{p} \cdot \boldsymbol{x}$. The optimization problem can then be written as:

$$\boldsymbol{x}^\star = \text{argmax}\left[u(\boldsymbol{x}) | \boldsymbol{p} \cdot \boldsymbol{x} = w\right] \ . \tag{7.1}$$

The utility function u is usually a concave function of $\boldsymbol{x}$ and can exhibit maxima $\boldsymbol{x}^\star$.

7.2.2 Effect of a price change

Let us consider two goods 1 and 2 with their respective quantities x_1 and x_2 and prices p_1 and p_2. Fixing these two prices, at equilibrium, a classical agent has a certain utility u' associated with the budget constraint $p_1 x_1 + p_2 x_2 = w$. Figure 7.1 presents the effect of an increase in price p_1 on the equilibrium. Eq. (7.1) is verified when an iso-utility of u becomes tangent to the budget constraint (blue solid line): it is the case for u' (black solid line) and the equilibrium is marked by a black dot. Let us now assume that p_1 increases. In that case, the slope of the budget constraint decreases, as $x_2 = -(p_1/p_2)x_1 + w/p_1$, and is now marked by a red solid line. The new equilibrium (red dot) is situated at the intersect between the iso-utility u'' (black solid line) and the new budget constraint.

The effect of the price change can be separated into two effects, namely the substitution effect (SE) and the income effect (IE). The first effect is illustrated in Figure 7.1 with the green arrow from the blue to the black dots: the utility is kept constant but the equilibrium

[1] Bold symbols refer to vectors while normal ones to scalars.

is modified towards the new budget constraint (red dashed line). The substitution effect is only due to the relative price variation: the good 2 becomes cheaper so the agent will substitute some quantity of good 1 into good 2. Conversely, the income effect is only due to the variation of real income and shown with the green arrow from the black to the red dots. The purchasing power of the consumer decreases as p_1 increases, which induces a decrease of utility.

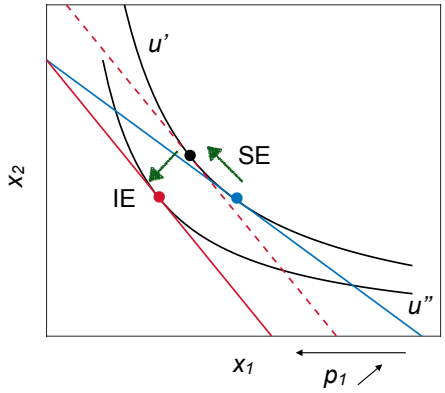

Figure 7.1: Change of equilibrium in response to a change of price p_1 for two goods associated with quantity x_1 and x_2. The effect of the price change can be decomposed into two effects, the substitution effect (SE) and the income effect (IE). The blue and red solid lines represent the budget constraint. The black solid lines represent the iso-utilities u' and u'' and dots show the different steps: blue and red dots correspond to the two equilibria while the black dot denotes the separation between the two effects.

7.2.3 Slutsky equation

The Slutsky equation is non other than the mathematical transcription of Subsec. 7.2.2. More precisely, in microeconomics, two consumer demand functions can be found: the *Marshallian* and the *Hicksian* demand functions. The first one is $\boldsymbol{x}(\boldsymbol{p}, w)$ and specifies what a consumer would buy if solving the utility maximization problem (Eq. (7.1)). The *Hicksian demand* $\boldsymbol{h}(\boldsymbol{p}, u)$ is the demand that minimizes the expenditure given a certain utility level u. For a given bundle of goods with price $\boldsymbol{p}$, the Slutsky equation [152] relates changes in *Marshallian demand* $\boldsymbol{x}(\boldsymbol{p}, w)$ to changes in *Hicksian demand* $\boldsymbol{h}(\boldsymbol{p}, u)$. Assuming they are equal, one can write for the good i: $h_i(\boldsymbol{p}, u) = x_i(\boldsymbol{p}, e(\boldsymbol{p}, u))$, where $e(\boldsymbol{p}, u)$ is the expenditure function. If we now differentiate h_i to a change of price p_j, it yields:

$$\frac{\partial h_i(\boldsymbol{p}, u)}{\partial p_j} = \frac{\partial x_i(\boldsymbol{p}, e(\boldsymbol{p}, u))}{\partial p_j} + \frac{\partial x_i(\boldsymbol{p}, e(\boldsymbol{p}, u))}{\partial e(\boldsymbol{p}, u)} \frac{\partial e(\boldsymbol{p}, u)}{\partial p_j} \ , \tag{7.2}$$

and using $\partial e(\boldsymbol{p}, u)/\partial p_j = h_j(\boldsymbol{p}, u)$ (Shepard's lemma), one obtains the Slutsky equation:

$$\frac{\partial x_i}{\partial p_j} = S_{ij} - x_j \frac{\partial x_i}{\partial w} \quad \text{with} \quad S_{ij} := \frac{\partial h_i}{\partial p_j} \ . \tag{7.3}$$

The term S_{ij}, coined the Slutsky matrix, denotes the substitution effect, while the second term on the right hand side denotes the income effect. Provided that the utility function is sufficiently regular, one has:

$$S_{ij} = \frac{\partial h_i}{\partial p_j} = \frac{\partial}{\partial p_j}\left(\frac{\partial e(\boldsymbol{p}, u)}{\partial p_i}\right) = \frac{\partial}{\partial p_i}\left(\frac{\partial e(\boldsymbol{p}, u)}{\partial p_j}\right) = S_{ji} \ . \tag{7.4}$$

Eq. (7.4) shows that $\boldsymbol{S}$ is symmetric. Besides, being the Hessian of the expenditure function, which is a concave function according to classical economics' hypotheses, $\boldsymbol{S}$ is then negative semidefinite.

The very definition of the deterministic quantities above assumes fully rational agents that maximize their utility, a questionable premise. Furthermore, the finding that the empirical Slutsky matrix is indeed quite symmetric (see [153]) is often raised as proof of agents' rationality.

7.3 Irrational agents and statistical ensembles

More reasonable is the idea that agents are irrational, at least partially, and do not maximize their utility function. We introduce instead a probability to choose a certain quantity $\boldsymbol{x}$ as a function of the associated level of utility $u(\boldsymbol{x})$. We resort to two thermodynamical ensembles found in statistical physics: the canonical ensemble where the system is in thermal equilibrium with a "heat bath" at a fixed temperature. The other one is the grand canonical ensemble where the system exchanges "particles", which here is instead budget.

7.3.1 Canonical approach

In this subsection, we introduce the canonical ensemble and study the expression of the Slutsky matrix in that framework.

7.3.1.1 Finite temperature

Agents are assumed to choose their bundle $\boldsymbol{x}$ according to a Gibbs-Boltzmann measure - also coined *logit rule* and chosen for its analytical convenience:

$$P(\boldsymbol{x}) = \frac{1}{Z} e^{\beta u(\boldsymbol{x})} \quad \text{with} \quad Z(w) = \int \mathrm{d}\boldsymbol{x} e^{\beta u(\boldsymbol{x})} \delta(\boldsymbol{p}\cdot\boldsymbol{x} - w) \ . \tag{7.5}$$

We introduce here the parameter β that specifies the amount of noise (or "irrationality") in the decision process. The system is in equilibrium with a "heat bath" that fixes β. This canonical approach defines a partition function that is the sum of probabilities of each microstate. The additional term $\delta(\boldsymbol{p}\cdot\boldsymbol{x} - w)$ refers to the budget constraint that limits the space of integration. Note that the framework of Sec. 7.2 is recovered in the limit of zero temperature $\beta \to \infty$ (full rationality). With finite temperature the Slutsky matrix may be defined as:

$$\boldsymbol{S}_{ij} = \frac{\partial \langle x_i \rangle}{\partial p_j} + \langle x_j \rangle \frac{\partial \langle x_i \rangle}{\partial w} \ , \tag{7.6}$$

where $\langle O \rangle = Z^{-1} \int \mathrm{d}\boldsymbol{x} O(\boldsymbol{x}) e^{\beta u(\boldsymbol{x})} \delta(\boldsymbol{p}\cdot\boldsymbol{x} - w)$.

7.3.1.2 Correlations

The Slutsky equation (Eq. (7.6)) can be rewritten using correlations between x_i and x_j. Integrating the RHS of Eq. (7.6) (integration by parts) yields:

$$\boldsymbol{S}_{ij} = -\Gamma \langle x_i x_j \rangle_c - \frac{\partial}{\partial w} \langle x_i x_j \rangle_c \ . \tag{7.7}$$

We here define $\Gamma = \partial_w \log Z$ (≥ 0 for reasonable u) and $\langle AB \rangle_c = \langle AB \rangle - \langle A \rangle \langle B \rangle$. The detailed calculus is shown in App. A. Eq. (7.7) shows that S_{ij} is symmetric for all β, including $\beta \to 0$ (full indifference or full irrationality), such that this argument cannot be used to demonstrate agents' rationality.

7.3.1.3 Low temperatures

At high β (quasi-rationality), one can rewrite the Slutsky equation (Eq. (7.7)). We here consider N goods. Let $(\boldsymbol{e}_i)_{1\leq i\leq N}$ be the canonical orthogonal basis of $\mathbb{R}^N$, and $\boldsymbol{O}$ the matrix of rotation that is such that the image of $\boldsymbol{e}_N$ by the rotation is aligned with $\boldsymbol{p}$. This will make things much easier as $\boldsymbol{p}\cdot\boldsymbol{x} = p\,\tilde{x}_N$ with $p = ||\boldsymbol{p}||$ and $\tilde{\boldsymbol{x}} = \boldsymbol{O}^T\boldsymbol{x}$, hence $\tilde{u}(\tilde{x}_1,..,\tilde{x}_{N-1}) = u(\tilde{x}_1,..,\tilde{x}_{N-1},w/p)$. We assume that the utility function $\tilde{u}$ has a maximum for $\tilde{\boldsymbol{x}} = \tilde{\boldsymbol{x}}^\star$ in the hyperplane and that its Hessian matrix evaluated at $\tilde{\boldsymbol{x}} = \tilde{\boldsymbol{x}}^\star$, $\tilde{\boldsymbol{H}} = [\tilde{u}''(\tilde{\boldsymbol{x}}^\star)]$ is definite negative. Similarly, the hessian of u is denoted as $\boldsymbol{H} = [u''(\boldsymbol{x}^\star)]$. In that case, it reads $\tilde{\boldsymbol{H}} = [(\boldsymbol{O}^T\boldsymbol{H}\boldsymbol{O})_{(N-1)\times(N-1)}]$.

The expression of Γ can be first simplified to (see App. A):

$$\Gamma = \beta\partial_w u(\boldsymbol{x}^\star) - \frac{1}{2}\partial_w \log\det(-\tilde{\boldsymbol{H}})\ , \tag{7.8}$$

and after some calculus, one can obtain the substitution matrix $\boldsymbol{S}$:

$$\boldsymbol{O}^T\boldsymbol{S}\boldsymbol{O} = \partial_w u(\boldsymbol{x}^\star)\left[\begin{array}{c|c}\tilde{\boldsymbol{H}}^{-1} & \boldsymbol{0}\\ \hline \boldsymbol{0} & 0\end{array}\right] + \beta^{-1}\left(\left[\begin{array}{c|c}\partial_w\tilde{\boldsymbol{H}}^{-1} & \boldsymbol{0}\\ \hline \boldsymbol{0} & 0\end{array}\right] - \frac{1}{2}\partial_w\log\det(-\tilde{\boldsymbol{H}})\left[\begin{array}{c|c}\tilde{\boldsymbol{H}}^{-1} & \boldsymbol{0}\\ \hline \boldsymbol{0} & 0\end{array}\right]\right)\ . \tag{7.9}$$

We refer to App. A for the details of the procedures that have led to the expression of $\boldsymbol{S}$. Let us now comment on Eq. (7.9). First, one is tempted to say that for $\beta\to\infty$, the second term on the RHS is negligible and thus one recovers the classical result $S_{ij}\propto -[u'']^{-1}_{ij}$. More precisely, the first term on the RHS alone would indicate that the substitution effect (i) is negative, (ii) is proportional to the variations of the peak utility with income (a priori >0), and (iii) increases in amplitude with increasing flatness of the utility peak (equiv. decreasing width of the energy well) consistent with the idea that substituting a good to another is easier when such a transaction has little effect on the utility.

However, the second term can have arbitrary sign and may remain large if $\boldsymbol{x}^\star$ displays jumps as function of w. In particular this could contradict microeconomics textbooks that always insist on the fact that, while the income effect can be both positive (for inferior goods) or negative (for normal goods), the substitution effect should always be negative. More precisely, if we focus on the first term of the β^{-1} contribution on the RHS, provided $\partial_w[u'']^{-1}_{ij}$ is positive semidefinite (that is the utility peak flattens with increasing budget, $\boldsymbol{S}$ might become semidefinite positive for $\beta^{-1} > T_\mathrm{c}$ with T_c a critical temperature beyond which the second term on the RHS overrules the first. On the other hand, if $\partial_w[u'']^{-1}_{ij}$ has the opposite sign (that is the utility peak sharpens with increasing budget, strange as it would mean that one is somehow less tolerant on substitution when richer but why not can we find such a utility function?), the temperature has just the effect of increasing in amplitude the substitution effect, consistent with larger excursions in the energy wells.

7.3.2 Grand canonical ensemble

The analytical difficulties arising from the dirac function $\delta(\boldsymbol{p}\cdot\boldsymbol{x}-w)$ led us to also consider the grand canonical approach. Similar to the former section, the ensemble is first introduced followed by the expression of the Slutsky matrix. The limit case of infinite β is also considered.

7.3.2.1 Slutsky matrix

In this ensemble, the budget is assumed to be not constant but only in average equal to w and a new variable, the chemical potential μ, is introduced. The budget is not a strong

constraint and enabling it to vary makes sense as agents can borrow or set money aside, which explains the advantage of this statistical ensemble. Within this framework, agents choose their bundle $\boldsymbol{x}$ according to:

$$P(\boldsymbol{x}) = \frac{1}{\mathcal{Z}} e^{\beta\{u(\boldsymbol{x}) - \mu \boldsymbol{p}\cdot\boldsymbol{x}\}} \quad \text{with} \quad \mathcal{Z}(\mu) = \int \mathrm{d}\boldsymbol{x} e^{\beta\{u(\boldsymbol{x}) - \mu \boldsymbol{p}\cdot\boldsymbol{x}\}} \ , \tag{7.10}$$

and $\langle \boldsymbol{p}\cdot\boldsymbol{x}\rangle = w$. Using the identity $w = -\beta^{-1}\partial \log \mathcal{Z}/\partial\mu$, the Slutsky matrix is given by:

$$\boldsymbol{S}_{ij} = -2\mu\beta\langle x_i x_j\rangle_c + \mu\beta \frac{\boldsymbol{p}\cdot\langle \boldsymbol{x} x_i\rangle_c \, \boldsymbol{p}\cdot\langle \boldsymbol{x} x_j\rangle_c}{\boldsymbol{p}^T\left[\langle x_k x_l\rangle_c\right]\boldsymbol{p}} \ . \tag{7.11}$$

$\boldsymbol{S}$ remains symmetric for all β, as also observed in the canonical ensemble. We observe a factor 2 in front of $\langle x_i x_j\rangle_c$, in contrast with the expression obtained in the canonical ensemble (Eq. (7.7)). Between two statistical ensembles, the fluctuations, such as the Slutsky matrix, can be indeed different unlike means. Furthermore, a small step using existing equalities enables us to find an equation relating w and μ:

$$w = -\frac{1}{\beta\mu}(\boldsymbol{p}\cdot\nabla_{\boldsymbol{p}}) \log \mathcal{Z} \ , \tag{7.12}$$

where $\boldsymbol{p}\cdot\nabla_{\boldsymbol{p}} = \sum_i p_i \partial/\partial p_i$. Hence, Eq. (7.11) can be written as:

$$\boldsymbol{S} = -2\mu\beta\langle \boldsymbol{x}\otimes\boldsymbol{x}\rangle_c + \mu\beta \frac{\boldsymbol{p}\cdot\left(\langle \boldsymbol{x}\otimes\boldsymbol{x}\rangle_c^T \otimes \langle \boldsymbol{x}\otimes\boldsymbol{x}\rangle_c\right)\cdot\boldsymbol{p}}{\boldsymbol{p}^T\langle \boldsymbol{x}\otimes\boldsymbol{x}\rangle_c\boldsymbol{p}} \ . \tag{7.13}$$

We introduce here the Kronecker product $\langle \boldsymbol{x}\otimes\boldsymbol{x}\rangle = [\langle x_i x_j\rangle]$. The Slutsky matrix $\boldsymbol{S}$ can be decomposed into the sum of a negative-symmetric matrix and a rank-one matrix, in line with the empirical results of Browning and Chiappori [153] on a database of household expenditures in Canada. The first term of $\boldsymbol{S}$ is a negative matrix as $[\langle x_i x_j\rangle]$ is a correlation matrix, hence with positive eigenvalues.

7

7.3.3 Low temperature

Γ and $\boldsymbol{S}$ can also be simplified in the limit of low temperature. Let us use the method of steepest descent and consider $\boldsymbol{x}^\star$ the maximum of the function $u(\boldsymbol{x}) - \mu\boldsymbol{p}\cdot\boldsymbol{x}$. The constant μ is not fixed and chosen such as $\langle \boldsymbol{p}\cdot\boldsymbol{x}\rangle = w$. At the vicinity of $\boldsymbol{x}^\star$, we have $u(\boldsymbol{x}) - \mu\boldsymbol{p}\cdot\boldsymbol{x} = u(\boldsymbol{x}^\star) - \mu\boldsymbol{p}\cdot\boldsymbol{x}^\star + \frac{1}{2}(\boldsymbol{x}-\boldsymbol{x}^\star)^T\boldsymbol{H}(\boldsymbol{x}-\boldsymbol{x}^\star) + \mathcal{O}(||\boldsymbol{x}-\boldsymbol{x}^\star||^2)$, where $\boldsymbol{H} = [u''(\boldsymbol{x}^\star)]$. Consequently, one has:

$$\mathcal{Z} = \int \mathrm{d}\boldsymbol{x} e^{\beta\{u(\boldsymbol{x}) - \mu\boldsymbol{p}\cdot\boldsymbol{x}\}} \approx e^{\beta\{u(\boldsymbol{x}^\star) - \mu\boldsymbol{p}\cdot\boldsymbol{x}^\star\}} \sqrt{\frac{(2\pi)^N}{\det(-\beta\boldsymbol{H})}} \ , \tag{7.14}$$

which yields:

$$\Gamma = -2\beta w^{-1}(\boldsymbol{p}\cdot\nabla_{\boldsymbol{p}})\left\{u(\boldsymbol{x}^\star) - \mu\boldsymbol{p}\cdot\boldsymbol{x}^\star\right\} + w^{-1}(\boldsymbol{p}\cdot\nabla_{\boldsymbol{p}}) \log\det(-\boldsymbol{H}) \ . \tag{7.15}$$

Similarly, $\langle x_i x_j\rangle_c = -\beta^{-1}\left[\boldsymbol{H}^{-1}\right]_{ij}$ at large β and the Slutsky matrix $\boldsymbol{S}$ reads:

$$\boldsymbol{S}_{ij} = -2w^{-1}(\boldsymbol{p}\cdot\nabla_{\boldsymbol{p}})\left\{u(\boldsymbol{x}^\star) - \mu\boldsymbol{p}\cdot\boldsymbol{x}^\star\right\}\left[\boldsymbol{H}^{-1}\right]_{ij} - \frac{\mu}{\boldsymbol{p}^T\boldsymbol{H}^{-1}\boldsymbol{p}} \sum_k p_k \left[\boldsymbol{H}^{-1}\right]_{ik} \sum_k p_k \left[\boldsymbol{H}^{-1}\right]_{jk} \ . \tag{7.16}$$

7.4 Multiple goods

Products can interact with each other, which can influence the level of satisfaction of an agent: for instance, if I already have a motorbike, I shall be less keen to buy a car. One can thus expect some modifications in the Slutsky equation after introducing interactions between goods, in contrast with the classical case where all goods are independent between each other. We resort to specific utility functions to simplify the calculus and get a clearer idea. The canonical approach is here adopted. Let us choose a vector of goods $\boldsymbol{x}$ and constrain the variable x_N. The tilde utility function is here introduced:

$$\tilde{u}(x_1, ..., x_{N-1}) = u\big(x_1, ..., x_{N-1}, (w - \textstyle\sum_{i\neq N} p_i x_i)/p_N\big) \ , \tag{7.17}$$

and one can then link the partial derivatives of $\tilde{u}$ and u with respect to $x_i x_j$. Denoting $u_{i,j} = \partial^2_{x_i x_j} u$ yields:

$$\tilde{u}_{i,j} = u_{i,j} - \frac{p_i}{p_N} u_{i,N} - \frac{p_j}{p_N} u_{j,N} + \frac{p_i p_j}{p_N^2} u_{N,N} \ . \tag{7.18}$$

7.4.1 Log utility

A utility function of the form $u(\boldsymbol{x}) = \sum_i a_i \log x_i$ is in line with economists habits, its natural generalization with interactions could be:

$$u(\boldsymbol{x}) = \sum_i \left(a_i + \sum_j J_{ij} \log x_j \right) \log x_i \ . \tag{7.19}$$

Using Eq. (7.18), in our case, one obtains:

$$\tilde{u}_{i,j} = -\frac{a_i}{x_i^2}\delta_{ij} + \frac{J_{ij}}{x_i} + \frac{J_{ji}}{x_j} - \delta_{ij} \sum_k x_k \frac{J_{ik}}{x_i^2} + \frac{u_{N,N}}{p_N^2} p_i p_j \ . \tag{7.20}$$

Let us now focus on different particular cases for $\boldsymbol{J}$.

7.4.1.1 No interactions

The first case considers no interaction, *i.e.* $\boldsymbol{J} = \boldsymbol{0}$. Solving the Lagrangian for this problem – $\mathcal{L} = \sum_i a_i \log x_i + \lambda \left(\sum_i p_i x_i - w \right)$ – we find: $\forall i \in [\![1; N]\!]$, $\lambda = -a_i/(p_i x_i^\star)$ and:

$$x_i^\star = \frac{a_i w}{p_i \sum_k a_k} \ . \tag{7.21}$$

Computing the Hessian matrix $\tilde{\boldsymbol{H}}$ of $\tilde{u}$ at $\boldsymbol{x}^\star$ (see Eq. (7.21)) yields:

$$\tilde{\boldsymbol{H}}_{ij} = \tilde{u}_{ij}(\boldsymbol{x}^\star) = -\delta_{ij} \frac{A^2 p_i^2}{a_i w^2} - \frac{A^2}{a_N w^2} p_i p_j \ , \tag{7.22}$$

where we have defined $A = \sum_k a_k$. The matrix $\tilde{\boldsymbol{H}}$ is found to be the sum of a diagonal matrix and a dyadic product. In order to obtain the Slutsky matrix, we compute Γ and $\langle x_i x_j \rangle_c$. Eq. (7.8) reads:

$$\Gamma = \beta \frac{A}{w} + \frac{N-1}{w} \ , \tag{7.23}$$

and using $\langle x_i x_j \rangle_c = -\beta^{-1}[\tilde{\boldsymbol{H}}^{-1}]_{ij}$ and Sherman-Morrisson formula[2] the Slutsky matrix finally reads:

$$\boldsymbol{S}_{ij} = [A + \beta^{-1}(N+1)]\frac{a_i w}{A^2 p_i}\left[-\frac{\delta_{ij}}{p_i} + \frac{a_j}{A p_j}\right] . \tag{7.24}$$

Note that at the first order in β, the finite "temperature" has just the effect of linearly increasing the substitution effect. Let us now study the eigenvalues of $\boldsymbol{S}$ for different distributions of $\{a_i\}$ and $\{p_i\}$.

I. a **and** p **constant** We first study the simple case where all the $\{a_i\}$ and $\{p_i\}$ are constant. In this case, $\forall i$, $x_i^\star = w/Np$ where $p_i = p$ and $a_i = a$. The Slutsky matrix $\boldsymbol{S}$ then becomes:

$$\boldsymbol{S}_{ij} = [Na + \beta^{-1}(N+1)]\frac{w}{N^2 ap}\left[-\frac{\delta_{ij}}{p} + \frac{1}{Np}\right] , \tag{7.25}$$

and $\boldsymbol{S}$ has then two eigenvalues, λ_1 which is nondegenerate and λ_2 which is degenerate with a multiplicity $N-2$. Their respective expression is:

$$\begin{cases} \lambda_1 = -[Na + \beta^{-1}(N+1)]\dfrac{w}{N^3 a p^2} \\ \lambda_2 = -[Na + \beta^{-1}(N+1)]\dfrac{w}{N^2 a p^2} . \end{cases} \tag{7.26}$$

At large N, λ_1 converges to 0 much faster than λ_2. At large β and N, one has $\lambda_1 \approx -w/(N^2 p^2)$ and $\lambda_2 \approx -w/(Np^2)$. The eigenvector $\boldsymbol{v}_1$ associated to λ_1 is given by: $\forall i$, $v_{1,i} = 1/\sqrt{N-1}$. It is called the "market mode" (no diversification) [154]. λ_1 is very small for large N and then, if choosing a basket of goods in the basis of $\boldsymbol{v}_1$, the substitution effect is roughly zero after an increase in price. The eigenvectors associated to λ_2 have the shape $(0, 0, ..., \sqrt{2}/2, 0, ..., -\sqrt{2}/2, 0..., 0)$ and this situation corresponds to baskets that are only sensitive to events corresponding to the 2 goods: if one price increases, then a substitution wil occur between the 2 goods.

II. a **random and** p **constant** Let us now assume that the $\{a_i\}$ are drawn from a given distribution $p(a)$. In this case, $\boldsymbol{S}$ becomes:

$$\boldsymbol{S}_{ij} = [A + \beta^{-1}(N+1)]\frac{a_i w}{A^2 p^2}\left[-\delta_{ij} + \frac{a_j}{A}\right] . \tag{7.27}$$

We then study the distribution of eigenvalues $\{\lambda_i\}$ for different distributions of $\{a_i\}$. Two distributions are then considered: one uniform between 0.4 and 0.6 and one gaussian with mean 0.5 and standard deviation 0.1. They are both shown for $N = 1000$ in the top panels of Figure 7.2ab. We have computed the eigenvalues for these two distributions and the spectrum of $\boldsymbol{S}$ is represented in Figure 7.2ab (bottom panels) with parameters $w = 1$, $p = 1$ and $\beta = 10000$. One can observe that for the two distributions, the eigenvalues have mean of order -10^{-3} and one negative eigenvalue roughly equal to 0. As observed in the previous case, this eigenvalue λ_1 is associated to an eigenvector $\boldsymbol{v}_1$ with equal coefficients, *i.e.* $\forall i$, $v_{1,i} = 1/\sqrt{N-1}$. The eigenvectors are orthogonal to one another and can thus be seen as uncorrelated baskets of goods x_i. In the case of $\boldsymbol{v}_1$, there is full diversification in this mode

[2] Sherman-Morrisson states that if $\boldsymbol{B} \in \mathbb{R}^{N\times N}$ is invertible, $\boldsymbol{u}, \boldsymbol{v} \in \mathbb{R}^N$, then if $1 + \boldsymbol{v}^T\boldsymbol{B}^{-1}\boldsymbol{u} \neq 0$ then $\boldsymbol{B} + \boldsymbol{u}\boldsymbol{v}^T$ is invertible and:

$$(\boldsymbol{B} + \boldsymbol{u}\boldsymbol{v}^T)^{-1} = \boldsymbol{B}^{-1} - \frac{\boldsymbol{B}^{-1}\boldsymbol{u}\boldsymbol{v}^T\boldsymbol{B}^{-1}}{1 + \boldsymbol{v}^T\boldsymbol{B}^{-1}\boldsymbol{u}}$$

between the goods and because $\lambda_1 \approx 0$, the curvature of u is really high at this point, which means that the substitution effect is null.

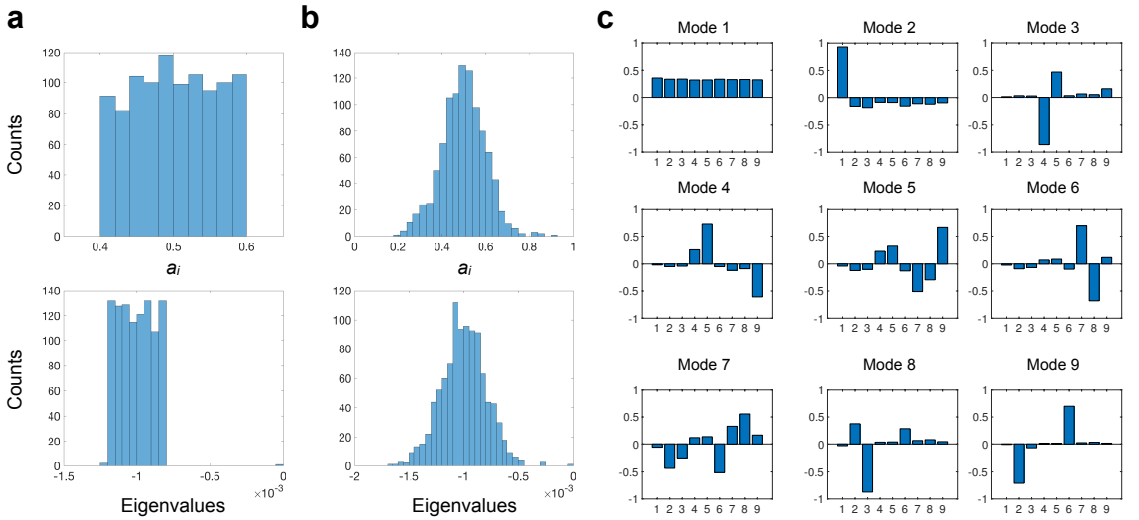

Figure 7.2: Distribution of the eigenvalues $\{\lambda_i\}$ of $\boldsymbol{S}$ for two distributions of $\{a_i\}$. We choose $p = 1$, $w = 1$, $\beta = 10000$ and $N = 1000$. (a) The $\{a_i\}$ follow an uniform distribution between 0.4 and 0.6 and shown in the top. The $\{\lambda_i\}$ are shown in the bottom. They are centered around -10^{-3} that corresponds to $-w/Np^2$ and one eigenvalue λ_1 is found very close to 0. (b) The $\{a_i\}$ follow a gaussian distribution with mean 0.5 and standard deviation 0.1 and shown in the top. The $\{\lambda_i\}$ are shown in the bottom. They are centered around -10^{-3} that corresponds to $-w/Np^2$ and one eigenvalue λ_1 is very close to 0. (c) Composition of the eigenvectors of $\boldsymbol{S}$ for a gaussian distribution of $\{a_i\}$ between 0 and 1. The chosen parameters are $N = 10$, $w = 1$, $p = 1$ and $\beta = 10000$. The first eigenvector $\boldsymbol{v}_1$ has equal components in the canonical basis and it corresponds to the "market mode".

To get some intuition on the eigenmodes, we have computed the eigenvectors for $N = 10$ and shown their compositions in Figure 7.2c for a gaussian distribution for $\{a_i\}$ ($\mu = 0.5$, $\sigma = 0.1$, $w = 1$ and $p = 1$). The first eigenvalue λ_1, that is close to 0, is associated with $\boldsymbol{v}_1$ with equal components (marked mode). For the other eigenvectors, there are two modes (modes 3 and 9) with two components much higher (in magnitude) compared to the others. These modes, also found in correlation matrices in the finance market [154], are associated to baskets with two goods that are only sensitive to price changes on such two goods. Consequently, with such a basket, an increase of the price of a good different that the two associated with the mode shall yield no substitution effect.

7.4.1.2 Log interactions

We now consider the case of interactions between products, *i.e.* $\boldsymbol{J} \neq \boldsymbol{0}$. The utility defined in Eq. (7.19) is modified by introducing a log-log interaction between products to keep the concavity. Associated to a budget constraint $\boldsymbol{p} \cdot \boldsymbol{x} = w$, the Lagrangian $\mathcal{L}$ reads:

$$\mathcal{L} = \sum_i \left(a_i + \sum_j J_{ij} \log x_j \right) \log x_i + \lambda \left(\sum_i p_i x_i - w \right) , \tag{7.28}$$

where we have defined $\forall i \in [\![1; N]\!]$, $y_i = \log x_i$. Differentiating $\mathcal{L}$ by y_k and assuming that $\boldsymbol{J}$ is symmetric, one obtains:

$$a_k + 2\sum_i J_{ik} y_i + \lambda p_k e^{y_k} = 0 \ . \tag{7.29}$$

We apply a perturbative method in J_{ij} at the first order, *i.e.* we replace J_{ij} by ηJ_{ij}, where $\eta \ll 1$. We also have $\forall i, y_i = y_i^{(0)} + \epsilon y_i^{(1)} + o(\epsilon)$. $x_i^{(0)} = \exp\left(y_i^{(0)}\right)$ is the solution given by Eq. (7.21). Finally, at the first order, $\boldsymbol{x}^\star$ reads:

$$x_k^\star = \frac{a_k w}{A p_k}\left[1 + 2\eta\left[\sum_i \log(a_i w / A p_i)\left(\frac{J_{ik}}{a_k} - \sum_j \frac{J_{ij}}{A}\right)\right]\right] + o(\eta) \ , \tag{7.30}$$

which leads to the matrix $\boldsymbol{H}$:

$$\boldsymbol{H}_{ij} = -\frac{A^2 p_i^2}{a_i^2 w^2}\left[a_i + 2\eta\sum_k\left(-J_{ik} + 2\frac{a_i}{A}\sum_j J_{jk}\right)\log B_k\right]\delta_{ij} + 2\eta\frac{A^2 p_i p_j J_{ij}}{a_i a_j w^2} + o(\eta) \ . \tag{7.31}$$

We here introduce $B_k = a_k w / A p_k$. Using Eq. (7.18), $\tilde{\boldsymbol{H}}$ can be written as $\tilde{\boldsymbol{H}} = \boldsymbol{B} + \eta \boldsymbol{C}$, where both expressions can be found in App. A. At the first order in η, one has $\tilde{\boldsymbol{H}}^{-1} = \boldsymbol{B}^{-1} - \eta \boldsymbol{B}^{-1}\boldsymbol{C}\boldsymbol{B}^{-1}$ and the Slutsky matrix is then $\boldsymbol{S} = \left[A + \beta^{-1}(N+1)\right]\tilde{\boldsymbol{H}}^{-1}$.

We first consider a common interaction matrix $\boldsymbol{J}_1$: $\boldsymbol{J}_1 = \begin{pmatrix} 1 & \rho & \dots & \rho \\ \rho & \ddots & \ddots & \vdots \\ \vdots & \ddots & \ddots & \rho \\ \rho & \dots & \rho & 1 \end{pmatrix}$. Figure 7.3a shows the histogram of the eigenvalues of the perturbed $\boldsymbol{S}$ for two values of ρ: orange bars ($\rho = 1$) and blue bars ($\rho = -1$). We consider here $N = 1000$, $\eta = 0.1$, $\beta = 10000$, $w = 1$, an uniform distribution of $\{a_i\}$ between 0.4 and 0.6 and constant $\{p_i\}$. For positive ρ, all eigenvalues are negative, as already observed in the non-perturbed case (Figures 7.2a and b). Conversely, when $\rho = -1$, all eigenvalues become positive. Interactions can be negative when it is not optimal to have two goods: this is the case for example when they are quite similar such as a motorbike and a car! In classical nconomics, the Slutsky matrix is shown to be always negative, which we contradict here after introducing some irrationality and interactions between products.

From the figure, a threshold ρ_c seems to exist and for which $\forall \rho < \rho_c$, at least one eigenvalue is positive. The eigenvalues of the perturbed Slutsky matrix $\boldsymbol{S}_\eta$ depend on η. However, defining the matrix $\boldsymbol{T} = \eta^{-1}(\boldsymbol{S}_\eta - \boldsymbol{S}_{\eta=0})$ enables us to remove this dependence on η. For a given number of goods N, we have computed the maximum eigenvalue of $\boldsymbol{S}_\eta$ and the critical value of ρ, ρ_c. Another interaction matrix $\boldsymbol{J}_2$, that has instead 0 in the diagonal, is also considered: $\boldsymbol{J}_2 = \begin{pmatrix} 0 & \rho & \dots & \rho \\ \rho & \ddots & \ddots & \vdots \\ \vdots & \ddots & \ddots & \rho \\ \rho & \dots & \rho & 0 \end{pmatrix}$. As such, Figure 7.3b presents the critical value ρ_c as a function of N for the interaction matrices. Behaviours dramatically differ between $\boldsymbol{J}_1$ and $\boldsymbol{J}_2$: for $\boldsymbol{J}_1$, ρ_c increases with N and converges towards 0. Conversely, for $\boldsymbol{J}_2$, ρ_c is found constant equal to 0, independently of the number of goods N. In that case, $\boldsymbol{C}_{i,j}$ is proportional to ρ (see App. A), which leads at the first order of η to $\lambda(\boldsymbol{T}) = \lambda\left[\eta^{-1}(\boldsymbol{S}_\eta - \boldsymbol{S}_{\eta=0}))\right] \propto -\rho$. Hence, for a fixed value of N, the value of ρ such as

$\forall \rho < \rho_c$, $\lambda(\boldsymbol{T}) \geq 0$ is equal to 0, hence $\forall N$, $\rho_c(N) = 0$. Interactions between products can then lead to positive Slutsky matrices, in contradiction with classical economics' predictions, but in line with observed habits.

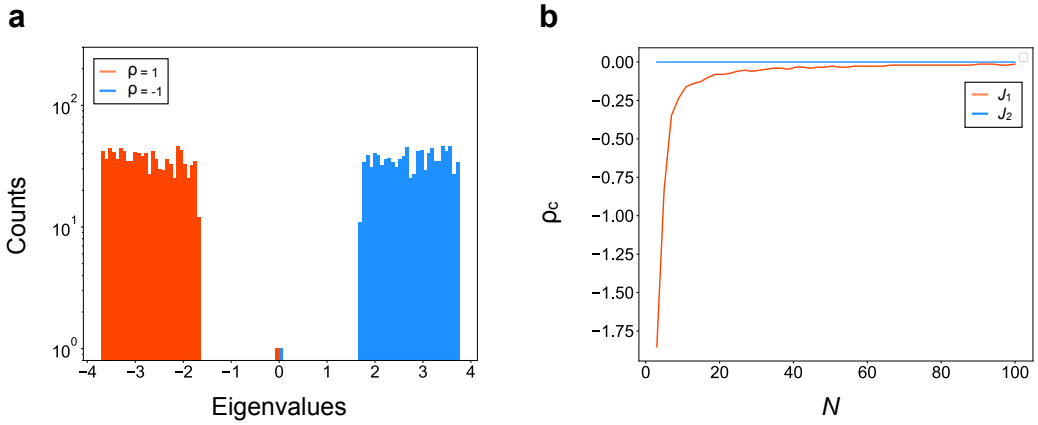

Figure 7.3: (a) Distribution of the eigenvalues of $\boldsymbol{S}$ for two values of ρ ($\rho = -1$ and 1) and considering the interaction matrix $\boldsymbol{J}_1$. For negative ρ (blue bars), all eigenvalues are positive in contrast with the predictions of classical economics. We consider $N = 1000$, $\eta = 0.1$, $\beta = 10000$, $w = 1$, uniform distribution of $\{a_i\}$ between 0.4 and 0.6 and constant $\{p_i\} = 1$. (b) Critical ρ_c as a function of the number of products N and plotted for the two interaction matrices $\boldsymbol{J}_1$ (orange line) and $\boldsymbol{J}_2$ (blue line). $\forall \rho < \rho_c$, $\boldsymbol{S}$ has one positive eigenvalue.

7.5 Heterogeneous agents

After having shown the influence of irrationality on the Slutsky matrix, one can wonder what happens when classical agents are not considered homogenenous but instead differ from one another.

We allow some degree of heterogeneities between agents. We can reason on more than one agent and assume that they each have a different budget w^α, where α refers to the agent α. We assume that the $\{w^\alpha\}$ are distributed with a density $\rho(w)$. If resorting to the grand canonical approach, Eq. (7.12) connects w with μ, hence our ability to compute an average Slutsky matrix in the context of budget heterogeneity. For the agent α, one has:

$$\boldsymbol{S}_{ij}^{\alpha} = \frac{\partial \langle x_i \rangle^\alpha}{\partial p_j} + \langle x_j \rangle^\alpha \frac{\partial \langle x_i \rangle^\alpha}{\partial w^\alpha} \ . \tag{7.32}$$

The mean of the Slutsky coefficient i, j over all the agents is denoted $[\boldsymbol{S}_{ij}]$. However, when considering data, the individual quantities are often non-measurable. Besides, $[\langle x_j \rangle^\alpha \partial \langle x_i \rangle^\alpha / \partial w^\alpha]$ cannot be measured based on the data, and it is instead $[\langle x_j \rangle^\alpha]\,[\partial \langle x_i \rangle^\alpha / \partial w^\alpha]$ that is more likely measurable on aggregated data. Consequently, can we estimate the difference? Knowing the distribution of wealth, our grand canonical approach may enable us to deduce the distribution of the Slutsky matrix.

We again consider a particular case, that is the log utility function $u(\boldsymbol{x}) = \sum_{i=1}^{N} a_i \log x_i$. In the grand canonical ensemble, we find for an agent α the chemical potential μ^α:

$$\mu^\alpha = \frac{\beta A + N}{\beta w^\alpha} \ , \tag{7.33}$$

which yields the Slutsky matrix:

$$\boldsymbol{S}_{ij}^{\alpha} = \frac{\beta a_i + 1}{\beta \mu^{\alpha} p_i} \left[-2\frac{\delta_{ij}}{p_i} + \frac{\beta a_j + 1}{p_j(\beta A + N)} \right] . \tag{7.34}$$

We again denote A as $A = \sum_{i=1}^{N} a_i$, where N is the number of goods.

The distribution of wealth $\rho(w)$ has been extensively studied and first by Pareto who suggested that wealth distributions obey universal laws [155]. He introduced the Pareto distribution $\rho(w) \propto w^{-(1+\theta)}$. Later, Mandelbrot proposed that the Pareto law only applied for high incomes [156]. To satisfy the condition $\rho(w = 0) = 0$, we resort to the inverse Gamma distribution for the wealth distribution:

$$\rho(w) = \frac{\bar{w}^{\theta}}{\Gamma(\theta) w^{\theta+1}} \exp(-\bar{w}/w) , \tag{7.35}$$

with $\theta > 1$. This distribution was found to describe well current data (taking $\theta = 1.9$) [157]. The distribution $h(\mu)$ of the chemical potential can be deduced using Eq. (7.33) and[3]:

$$h(\mu) = \left[\frac{\beta \bar{w}}{(\beta A + N)} \right]^{\theta} \frac{\mu^{\theta-1}}{\Gamma(\theta)} \exp\left[-\frac{\beta \bar{w} \mu}{(\beta A + N)} \right] , \tag{7.36}$$

and h follows a Gamma distribution. Going back to the Slutsky matrix, one has $\boldsymbol{S}_{ij} = \boldsymbol{K}_{ij}/\mu = g_{ij}(\mu)$ where $\boldsymbol{K}_{ij}$ is given by Eq. (7.34). Finally, S_{ij} has a distribution $f_{ij}(s)$ that reads:

$$f_{ij}(s) = \left[\frac{\beta \bar{w} \boldsymbol{K}_{ij}}{(\beta A + N)} \right]^{\theta} \frac{1}{\Gamma(\theta) s^{\theta+1}} \exp\left[-\frac{\beta \bar{w} \boldsymbol{K}_{ij}}{(\beta A + N) s} \right] . \tag{7.37}$$

The distributions $\rho(w)$ and $f_{ij}(s)$ are drawn in Figure 7.4a with $\theta = 2$, $\bar{w} = 1$ and $\beta \bar{w} \boldsymbol{K}_{ij}/(\beta A + N) = 2$. The complementary cumulative distribution functions $\mathbb{P}(X > x)$ are also shown (Figure 7.4b) and converge towards $x^{-\theta}$ at large x.

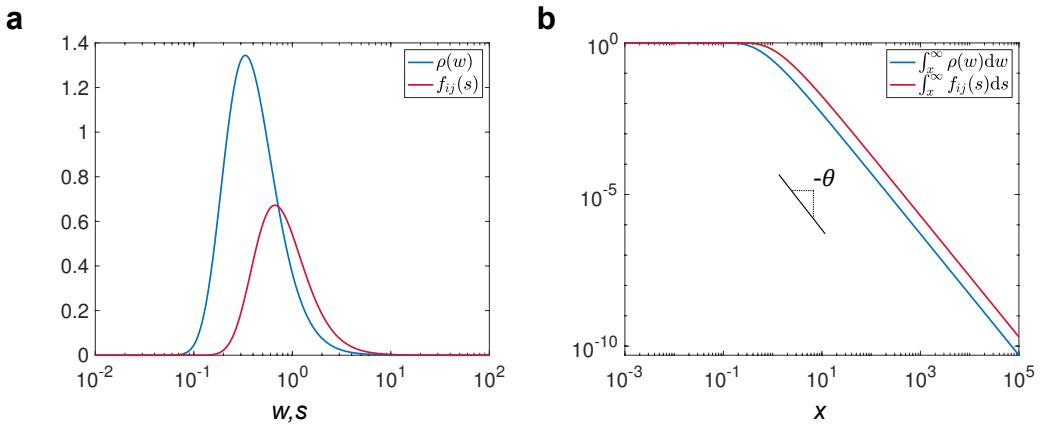

Figure 7.4: (a) Distribution $\rho(w)$ and $f_{ij}(s)$ for $\bar{\mu} = 1$, $\theta = 2$ and $\beta \bar{w} \boldsymbol{K}_{ij}/(\beta A + N) = 2$. (b) Complementary cumulative distribution function $\mathbb{P}(X > x)$ for $\rho(w)$ and $f_{ij}(s)$. At large x, both functions converge towards $x^{-\theta}$.

The important parameter to estimate is the difference $\boldsymbol{\Delta}_{ij} = [\langle x_j \rangle^{\alpha} \partial \langle x_i \rangle^{\alpha} / \partial w^{\alpha}] - [\langle x_j \rangle^{\alpha}] [\partial \langle x_i \rangle^{\alpha} / \partial w^{\alpha}]$. For a log utility, one finds $\Delta_{ij} = 0$.

[3] If a random variable X has a density f_X and there exists $Y = g(X)$ with g monotonous and differentiable whose derivative does not cancel, the distribution $f_Y(y)$ is given by: $f_Y(y) = \left| \frac{1}{g'(g^{-1}(y))} \right| f_X(g^{-1}(y))$.

Our grand canonical approach enables us to deduce the distribution of the Slutsky matrix given a certain wealth distribution for heteregeneous agents.

7.6 Interactions and crowding effect

This part was mainly carried out by Pierre-Philippe Crépin, a new postdoc in the EconophysiX group, and currently ongoing.

Agents are seldom independent and should influence one another in their decision making. Hence our idea here to introduce interactions between them through the utility function. We model herding and crowding, arising from mimicry: *"I want this good because everyone has it"* and this could be achieved by building a utility for an agent and a good i that would be increased if other agents also desire that particular good. One can then imagine a utility for agent α with the shape:

$$u_i^\alpha = [1 + c\left(\langle x_i^\alpha \rangle'\right)^2] u_i(x_i) \quad \text{with} \quad \langle x_i^\alpha \rangle' = \frac{1}{M-1} \sum_{\nu \neq \alpha} x_i^\nu \ , \tag{7.38}$$

where the term $[1 + c\left(\langle x_i^\alpha \rangle'\right)^2]$ is assumed constant and then determined in a self-consistent way, and where M denotes the number of agents. We expect that for high interaction strength c, a crowding phase transition should occur in which the equilibrium quantity of a given good i explodes and that of the others $j \neq i$ vanish.

We take a linear utility between goods; *i.e.* $u^\alpha(\boldsymbol{x}) = \sum_i u_i^\alpha = \sum_i [1 + c\left(\langle x_i^\alpha \rangle'\right)^2] u_i(x_i)$. The idea is to find a self-consistent equation and $\langle x_i \rangle = (1/M) \sum_\alpha \langle x_i^\alpha \rangle$ is a good variable for that. For this study, we resort to the grand canonical approach. Using Eq. (7.38) for the utility shape, one then has for N goods:

$$\langle x_i^\alpha \rangle = \frac{1}{\mathcal{Z}^\alpha} \int_{\mathbb{R}^N} \mathrm{d}\boldsymbol{x} x_i e^{\beta\{u^\alpha(\boldsymbol{x}) - \mu \boldsymbol{p}\cdot\boldsymbol{x}\}} \quad \text{with} \quad \mathcal{Z}^\alpha = \int_{\mathbb{R}^N} \mathrm{d}\boldsymbol{x} e^{\beta\{u^\alpha(\boldsymbol{x}) - \mu \boldsymbol{p}\cdot\boldsymbol{x}\}} \ , \tag{7.39}$$

and the average quantity $\langle x_i^\alpha \rangle$ for a good i and agent α reads:

$$\langle x_i^\alpha \rangle = \frac{\int_{\mathbb{R}} \mathrm{d}x_i x_i e^{\beta\left\{\left(1 + c\left(\langle x_i^\alpha \rangle'\right)^2\right) u_i(x_i) - \mu p_i x_i\right\}}}{\int_{\mathbb{R}} \mathrm{d}x_i e^{\beta\left\{\left(1 + c\left(\langle x_i^\alpha \rangle'\right)^2\right) u_i(x_i) - \mu p_i x_i\right\}}} \ . \tag{7.40}$$

7.6.0.1 Strong interaction

At large c, Eq. (7.40) can be easily solved using the theorem of steepest descent. One finds $\forall i \in [\![1; N]\!]$, $\langle x_i^\alpha \rangle = x_i^\star$ where $x_i^\star = \mathrm{argmax}[u_i(x_i)]$, *i.e.* $x_i^\star = w/p_i$. Another trivial solution is $\langle x_i^\alpha \rangle = x_i^\star = 0$. Because of $\langle \boldsymbol{p}\cdot\boldsymbol{x} \rangle = w$, only one good can have a non-null quantity while the others are zero. Hence, one should expect phase transitions in the quantities where one good is favoured over the others.

7.6.0.2 Particular case

Let us consider the particular case of a log utility function, $u(\boldsymbol{x}) = \sum_{i=1}^N a_i \log x_i$, and $\mathcal{Z}^\alpha$ reads:

$$\mathcal{Z}^\alpha = \prod_{k=1}^N \frac{\beta(1 + c\left(\langle x_k^\alpha \rangle'\right)^2) a_k \Gamma(\beta(1 + c\left(\langle x_k^\alpha \rangle'\right)^2) a_k)}{(\beta \mu p_k)^{\beta(1 + c\left(\langle x_k^\alpha \rangle'\right)^2) a_k}} \ , \tag{7.41}$$

where we have defined the function $\Gamma(z) = \int_0^\infty x^{z-1}e^{-x}\mathrm{d}x$ and used $\Gamma(z+1) = z\Gamma(z)$. Using the equality $(M-1)\langle x_i^\alpha\rangle' = M\langle x_i\rangle - \langle x_i^\alpha\rangle$, the average quantity for the good i writes simply:

$$\langle x_i\rangle = \frac{\beta a_i + 1}{\beta(\mu p_i - c\langle x_i\rangle a_i)} \ . \tag{7.42}$$

This self-consistent equation has two solutions:

$$\langle x_i\rangle^\pm = \frac{\mu p_i \pm \sqrt{(\mu p_i)^2 - 4ca_i\,(a_i + 1/\beta)}}{2ca_i} \ . \tag{7.43}$$

We also deal with 2^N degenerated equilibria combinations. By adding the budget constraint $\langle \boldsymbol{p}\cdot\boldsymbol{x}\rangle = w$, for each combination ($s_i \in \{-,+\}$), we obtain an equation on μ:

$$\sum_{1\le i\le N} p_i\langle x_i\rangle^{s_i} = w \ . \tag{7.44}$$

The four combinations for a specific set of parameters and $N = 2$ are plotted in Figure 7.5.

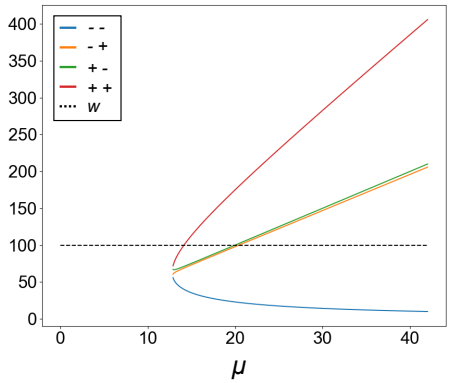

Figure 7.5: $\sum_{1\le i\le N} p_i\langle x_i\rangle^{s_i}$ for $N = 2$, $\beta = 0.005$, $c = 0.2$, $\boldsymbol{p} = [1, 1.4]$ and $\boldsymbol{a} = [1, 2]$. Each line corresponds to a different combination of s_i. The black dashed line represents the budget $w = 100$.

Notice that up to 2^N equilibria can coexist when reinjecting μ in Eq. (7.43). Figure 7.6 shows the different equilibria depending on the interaction parameter c. It demonstrates that for a given c, multiple equilibria can coexist.

7.6.0.3 Langevin dynamics

Our previous results have concerned the quantities taken at equilibrium for a given interaction strength c. One might instead be interested in the dynamics with time of each quantity for each agent. To that end, we consider a Langevin dynamics for each good i and agent α. The Langevin equation is thus given by:

$$\frac{\partial x_i^\alpha}{\partial t} = \nabla_{x_i}\left(u_i^\alpha(x) - \lambda\left[\boldsymbol{p}\cdot\boldsymbol{x} - w\right]^2\right) + \chi_i(t) \ , \tag{7.45}$$

where the utility $u_i^\alpha(x)$ is defined in Eq. (7.38). χ_i is a white noise with variance $2/\beta$ and reads:

$$\begin{cases} \langle\chi_i(t)\rangle = 0 \\ \langle\chi_i(t)\chi_i(t')\rangle = \dfrac{2}{\beta}\,\delta(t-t') \ . \end{cases} \tag{7.46}$$

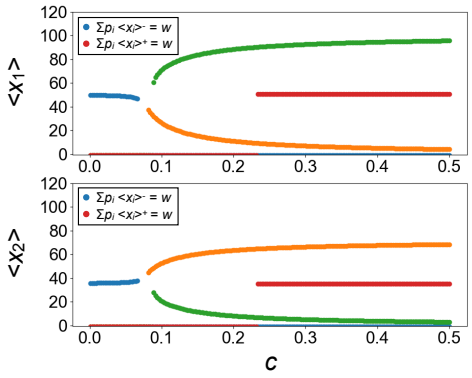

Figure 7.6: Average quantities $\langle x_i \rangle$ $(i = \{1, 2\})$ as a function of c. The parameters are $N = 2$, $\beta = 0.005$, $\boldsymbol{p} = [1, 1.4]$ and $\boldsymbol{a} = [1, 2]$. Colors are mapped to the combination colors of Figure 7.5.

Eq. (7.45) can be seen as a stochastic gradient descent equation. Besides, a penalty term $\lambda \nabla_{x_i} [\boldsymbol{p} \cdot \boldsymbol{x} - w]^2$ is added to account for the budget constraint. The white noise corresponds to the agents' irrationnality which magnitude decreases with β. Taking M agents and N goods, our system consists in solving $M \times N$ coupled equations.

We run a discreet scheme of $M \times N$ coupled equations for solving the Langevin equation with M sufficiently large in order to be consistent with the mean field approach. To avoid negative x_i^α values, we keep the scheme constant if the noise would put one of the x_i^α under 0. Two single trajectories x_1^1 and x_2^1 are plotted in Figure 7.7 for $\beta = 0.005$ and $c = 0.2$. One can note that during the dynamics, the quantities oscillate between the different equilibria, as predicted in Figure 7.6.

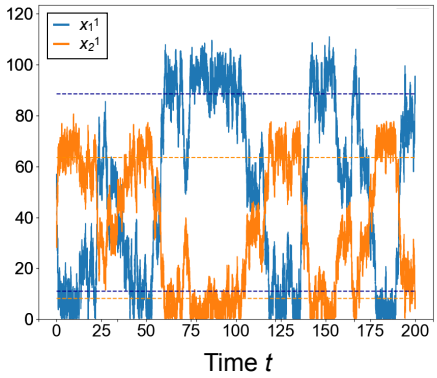

Figure 7.7: **Langevin dynamics.** $\langle x_i^1 \rangle$ $(i = \{1, 2\})$ as a function of time t and taking $c = 0.2$. Jumps between the different equilibria are clearly observable. The parameters are $N = 2$, $\beta = 0.005$, $\boldsymbol{p} = [1, 1.4]$ and $\boldsymbol{a} = [1, 2]$. Colors are mapped to the combination colors of Figure 7.5.

This study is only preliminary and a lot of work remains to be done. One can think of studying the effect of the parameters on the escape time between two equilibria and we refer to the work of Pierre-Philippe Crépin for such study.

Take home message of Chapter 7

1. Finite temperature. In the framework of agents irrationality and canonical or grand canonical approach, the Slutsky matrix, or *substitution effect*, remains symmetric, such that this argument cannot be used to demonstrate agents rationality.

2. Interactions between products. Products can interact with each other which can lead to positive eigenvalues for the Slutsky matrix, in contrast with the classical results.

3. Interactions between agents. Agents are not independent and rather heterogeneous. Introducing herding and crowding reveals *phase transitions* and *out of equilibrium* dynamics, generally absent from classical economics theory.

Conclusion and future research

In this thesis, we mainly studied the question of condensation on superhydrophobic surfaces and how to repel efficiently fog. We also focused on two unrelated problems: the first one addressed the issue of the ability of oily fibers to capture dust. The second work focused on the Slutsky equation in economics and how the challenge of some assumptions underlying classical economics can reveal surprising features.

Repelling water is a challenging subject. Although the design of superhydrophobic materials has enabled one to repel water at a centimeter or millimeter scale, micrometric droplets are much harder to expel. Typically encountered during condensation, they can fill the texture voids of surfaces and thus destroy superhydrophobicity. This scenario is all the more plausible since texture sizes are on the order of micrometer, that is at the scale of condensed droplets. However, this limitation was recently circumvented by using nanotexture that can promote non-wetting morphologies, even for droplets formed by condensation, namely the partial-Cassie and Cassie states. Furthermore, a nanocone texture proved the most efficient in antifogging with more than 90% ejected droplets. However, the influence of nanocones on fog-repellency still had unanswered questions.

In Chap. 2, we resorted to Environmental Scanning Electron Microscopy (ESEM) to image condensation on hydrophobic materials covered with nanostructures. This work was motivated by the huge differences observed between pillars and cones when subject to fog. Despite some limitations due to e-beam exposure, this tool enabled us to observe micrometric droplets condensing on nanotexture. The behaviour of such droplets on these surfaces largely depends on the texture shape. On nanopillars, drops are observed to be in a partial Cassie state with contact angles no larger than 140° and a significant contact area with the solid. Conversely, we highlighted that all drops on nanocones exhibit a quasi-spherical shape with a low contact area and contact angles as high as 170°, a hallmark of a Cassie state. For both texture shapes, contact angles are lower for radii smaller than 1 μm, which for nanocones, is due to a partial penetration of water inside the texture. These observations managed us to rationalize the difference in antifogging abilities between nanopillars and nanocones. For future work, the use of ESEM could enable one to study the mechanisms of condensation nucleation. Whether the nuclei develop in the cavities or at the top of the structures should be a subject of interest. Furthermore, our parameters as well as the size of structures prevented us from imaging water inside the texture. Although challenging, it would be of key importance to be able to image the droplet shape inside the structures, especially for nanocones.

It was recently evidenced that microdrops condensing on a highly nonadhesive substrate can benefit from coalescence to jump off the material. Our study specifically takes advantage of such novel materials for which droplet departure was observed at unprecedented rates (up to 99%) and scales (down to 1 μm), which allows us to discuss quantitatively the jump characteristics in Chap. 3. Using simultaneous side and top high-speed views, we understood how the departure velocity U varies as a function of the drop size r. We reported that the jumping velocity of droplets condensing on nanocones obeys the classical inertiocapillary scaling down to 5 μm, below which strong deviations are observed and interpreted as mainly a consequence of viscous dissipation. Jumping droplets condensing on our material can have radii as small as 1 μm, which enables us to provide measurements for radii ranging from 1 μm to 1 mm. The asymmetry of merging was also studied for all droplets' radii and shown to be another cause of reduced jumping efficiency. We provided a model to account for the influence of radius on the jumping velocity. We then characterized the flight (maximum height, descent kinetics and landing) of jumping microdroplets. Their trajectory

is always found to be a "Tartaglia trajectory" with maximum height as high as 1 mm, an important parameter if wind is present, so that it can sweep the droplets. Air viscosity rapidly stops ejected drops that later fall so slowly that they cannot bounce after impact. We complemented this study by measuring the jumping velocity of drops composed of water-glycerol mixtures in order to vary the viscosity. This work should be pursued to further understand the infuence of viscosity. For future work, the coupling of spontaneous droplet departure with a lateral wind would be interesting to study, as well as the case where drops take off with solid particles (contamination or ballistospore) [158, 159, 160, 161]. Another natural development would be to understand how more than two drops merging on the surface are ejected.

Only one sample covered with nanocones was reported up to now in the literature. We developed in Chap. 4 a systematic study on the antifogging abilities of families of surfaces composed of cones. Using three antifogging metrics, we showed that the cone size (height and pitch) has no influence on fog-repellency when it is at the size of tens of nm. On these materials, the proportion of ejected drops gravitates around 90% and the cutoff radius approaches 1 μm. We attributed these similar behaviours to the texture shape and size. At a scale of 100 nm, the water nuclei might depin from the cavities ends. The cone shape subsequently pushes the nuclei upwards, to the top of the structures, hence guaranteeing a Cassie morphology. Besides, the influence of asymmetry was also addressed and how it can modify the antifogging performance. The case of nanocones contrasts with that of microcones. In the latter, we observed that the jumping rate drastically decreases at small drop radii. Using ESEM, we showed that drops condensing on microcones are in a partial Cassie state where some unit cells below the drop are filled with water. We provided a quantitative study to model the cutoff radius and the number of filled cells as a function of texture size. We also found that the evolution of the jumping rate with radius can be understood for cones with sizes ranging from 50 nm to 2 μm. We finally studied the influence of truncated cones on fog-repellency. Despite a Cassie state, truncated nanocones do not perform well in fog conditions, which we attributed to the pinning at the top of the structures that generates low receding angles, impeding droplet jumping.

For future work, many aspects could be addressed. More surfaces are needed in the case of microcones to understand the influence of texture size on the antifogging properties. It would be wishable to have cones with a same pitch but different heights, in the same manner as for nanocones. Besides, the intermediate case of cones at the size of few hundreds of nanometers is worth examining, in order to determine the threshold at which Cassie morphology is no longer observed for condensed drops. We indeed expect partial Cassie state when the cavity size approaches $\sim$ 100 nm. More practically, playing with the nucleation conditions could be a way to optimize the antifogging abilities of nanocones. The creation of preferential nuclei locations could enable one to control the maximum droplet radius on these surfaces, a key parameter for optical properties. Focusing an ion beam on defined spots creates hydrophilic points where nuclei can develop and later jump after coalescence. Finally, the mechanical properties of nanocones should be examined in order to check how they resist compression, for instance, which is of paramount importance for future industrialization. To that end, truncated cones are known to perform better during mechanical tests and the testing of little truncation on antifogging efficiency should be investigated. One could also think of designing soft nanocones, made of PDMS for example, which could resist fog and at the same time mechanical sollicitations.

Furthermore, in another phase change phenomenon between vapour and liquid, namely boiling, materials covered with nanocones could be tested. Nucleate boiling is a serious concern in a broad range of industries and enhancing the critical heat flux is of paramount importance. Beyond this value, a vapour layer develops between the liquid and the solid and decreases drastically the heat transfer [162, 88]. One could imagine using superhydrophilic,

hence superaerophobic nanocones to increase the critical heat flux. Similar to condensed droplets, nanocones may promote spontaneous jumping of vapour bubbles during boiling. This phenomenon would decrease the amount of vapour in contact with the solid, hence increasing the heat transfer and the critical heat flux.

In Chap. 5, we discussed a related situation where fog also appears, that is, the case of hot water drops contacting repellent materials. We reported how the texture scale can be used to repel impacting hot water. By varying the texture size by two orders of magnitude (from 100 nm to 10 μm), we obtained two main results: (1) Surprisingly, the ability to repel hot water non-monotonically varies with the texture size: while for the 1 μm features condensation annihilates hot water repellency, drops always rebound on smaller and larger features. (2) Antifogging at submicrometric and supermicrometric scales differs by nature: a small texture is intrinsically antifogging, while this property is kinetically achieved on a large texture. Our study proved the existence of two structural recipes for repelling hot water: (1) Tall features dynamically prevent the texture filling and the formation of water bridges between impacting drops and the solid material. (2) Small features miniaturize the bridges and thus their sticking abilities. In both cases, repellency is robust, as it is observed in the whole range of explored impact velocity and water temperature. The existence of two scenarii of repellency is reflected by differences in the repellency itself: although rebounds are found to be nearly unsensitive to water temperature in case 1, warmer drops are repelled slightly slower in case 2, due to the multiplication of water bridges when the impacting water is hotter. These findings were completed by a quantitative model based on the bouncing and condensation timescales, which predicts the liquid behaviour on a given texture design.

For future work, it would be interesting to mix the two kinds of texture to see what is the dominant scenario in such a case. However, the scale is not the only geometrical parameter: for instance, modifying (at constant height) the distance between the features or their order (square, hexagonal, etc.) should be alternative ways to design materials that repel hot water. It would finally be worth exploring what happens when water impacts repellent materials at room temperature in a rarefied atmosphere. Both the evaporation rate [163] and impact characteristics [164] are dramatically affected in a low-pressure environment, which might modify water repellency [15]. Non-condensable gases in air act as a neutral medium in our experiment. Replacing them by pure vapour should favour water condensation, whereas an increased rate of evaporation can conversely induce self-taking off (trampolining) of water, *i.e.* an increase of repellency [163]. On the whole, the interplay of impact at low pressure with the texture geometry and scale should be a subject of interest for the future.

Another (short) facet of this thesis focused instead on **granular matter**. Inspired by an industrial application, we studied the ability of oily fibers to capture dust. We first showed that the quantities of captured particles is directly influenced by the quantity of oil deposited on the fiber. Tomography experiments showed that the aggregate, formed by oil and the grains, is in capillary state with a defined compacity, which we used to model the total mass of captured grains. Besides, oil configurations (film or drop) were found to have no impact on the total captured mass. However, growth kinetics dramatically differs between the two configurations. In the context of a drop resting on a fiber, the aggregate height was shown to depend on the oil viscosity and the capture is linear with time until it evolves in the same manner as the film. In that case instead, the kinetics was demonstrated to be only limited by capture efficiency, which is found to decrease with the aggregate height. For future research, it would be interesting to focus on the shape adopted by the aggregate in the drop configuration, since the aggregate grows upwards and also horizontally. Examining the influence of drop radius and viscosity could be a further step. It would be useful to study the impact of the waiting time on the growth kinetics during the flow interruptions: leaving more time between steps enables liquid to reorganize and perhaps improves the capture efficiency. Furthermore, many parameters could have been investigated such as the

influence of flow rate, surface tension or particle polydispersity.

The final part of the thesis dealt with **complex economics**. We studied how the Slutsky equation is modified when challenging classical economics assumptions. To account for agents' irrationality, we resorted to two statistical ensembles, the canonical and the grand canonical ones. The Slutsky matrix was demonstrated to be symmetric, even in the context of partially irrational agents, by that disproving classical economics statement that this property is the signature of agents' rationality. We then found that introducing interactions between goods can lead to positive eigenvalues in the Slutsky matrix, in contrast with the predictions of consumer choice theory that stipulates that the matrix is always negative. We also addressed the issue of heterogeneity between agents. We first showed that for a budget heterogeneity, the grand canonical ensemble enables one to deduce the distribution of the Slutsky matrix, for a given wealth distribution. We then focused on the interactions between agents, which can lead to crowding phase transitions where one good can be artificially preferred over others. Herding can then reveal out-of-equilibrium dynamics which are not predicted by classical economics. We then showed our preliminary results on the crowding dynamics using a Langevin equation with a noise referring to the agents' irrationality. For future work, it would be interesting to study the influence of the parameters on the equilibria chosen during the dynamics. Furthermore, our theoretical results remain to be confronted to available data such as the ones provided by the French national institute for statistical and economic studies.

APPENDICES

A

Technical details of Chapter 7

We detail here some calculation procedures to provide clarification for the results of Chap. 7.

Contents

A.1 Expression of the Slutsky matrix

The first term on the RHS of Eq. (7.6) can be computed using integration by parts as:

$$\begin{aligned}\frac{\partial\langle x_i\rangle}{\partial p_j} &= -\frac{\langle x_i\rangle}{Z}\int \mathrm{d}\boldsymbol{x} e^{\beta u(\boldsymbol{x})} x_j \delta^{(1)}(\boldsymbol{p}\cdot\boldsymbol{x}-w) \;+\; Z^{-1}\int \mathrm{d}\boldsymbol{x} e^{\beta u(\boldsymbol{x})} x_i x_j \delta^{(1)}(\boldsymbol{p}\cdot\boldsymbol{x}-w)\\ &= \langle x_i\rangle\left[\partial_w\langle x_j\rangle - \partial_w Z^{-1}\int \mathrm{d}\boldsymbol{x} e^{\beta u(\boldsymbol{x})} x_j \delta(\boldsymbol{p}\cdot\boldsymbol{x}-w)\right]\\ &- \partial_w\langle x_i x_j\rangle + \partial_w Z^{-1}\int \mathrm{d}\boldsymbol{x} e^{\beta u(\boldsymbol{x})} x_i x_j \delta(\boldsymbol{p}\cdot\boldsymbol{x}-w)\\ &= \langle x_i\rangle\partial_w\langle x_j\rangle + \langle x_i\rangle\langle x_j\rangle\partial_w \log Z \;-\; \partial_w\langle x_i x_j\rangle \;-\; \partial_w \log Z\langle x_i x_j\rangle \;, \end{aligned} \tag{A.1}$$

which yields:

$$\begin{aligned}\boldsymbol{S}_{ij} &= \frac{\partial\langle x_i\rangle}{\partial p_j} + \langle x_j\rangle\frac{\partial\langle x_i\rangle}{\partial w}\\ &= \langle x_i\rangle\partial_w\langle x_j\rangle + \langle x_i\rangle\langle x_j\rangle\partial_w \log Z \;-\; \partial_w\langle x_i x_j\rangle \;-\; \partial_w \log Z\langle x_i x_j\rangle + \langle x_j\rangle\partial_w\langle x_i\rangle \;, \end{aligned} \tag{A.2}$$

and defining $\Gamma = \partial_w \log Z$ (≥ 0 for reasonable u) and $\langle AB\rangle_c = \langle AB\rangle - \langle A\rangle\langle B\rangle$, one finally obtains:

$$\boldsymbol{S}_{ij} = -\Gamma\langle x_i x_j\rangle_c - \frac{\partial}{\partial w}\langle x_i x_j\rangle_c \;. \tag{A.3}$$

A.2 Low temperature

We detail here the steps that led to Eq. (7.9) in the canonical ensemble. Let $(\boldsymbol{e}_i)_{1\leq i\leq N}$ be the canonical orthogonal basis of $\mathbb{R}^N$, and $\boldsymbol{O}$ the matrix of rotation that is such that the image of $\boldsymbol{e}_N$ by the rotation is aligned with $\boldsymbol{p}$. This will make things much easier as $\boldsymbol{p}\cdot\boldsymbol{x} = p\tilde{x}_N$ with $p = ||\boldsymbol{p}||$ and $\tilde{\boldsymbol{x}} = \boldsymbol{O}^T\boldsymbol{x}$. Consequently, one can write:

$$Z = \int_{\mathbb{R}^N} \mathrm{d}\boldsymbol{x} e^{\beta u(\boldsymbol{x})}\delta(\boldsymbol{p}\cdot\boldsymbol{x}-w) = \int_{\mathbb{R}^{N-1}} \mathrm{d}\tilde{\boldsymbol{x}} e^{\beta\tilde{u}(\tilde{\boldsymbol{x}})} \;, \tag{A.4}$$

where we have defined $\tilde{u}(\tilde{x}_1,..,\tilde{x}_{N-1}) = u(\tilde{x}_1,..,\tilde{x}_{N-1},w/p)$ (and the Jacobian of $\boldsymbol{O}$ is equal to 1). We assume that the utility function $\tilde{u}$ has a maximum for $\tilde{\boldsymbol{x}} = \tilde{\boldsymbol{x}}^\star$ in the hyperplane and that its Hessian matrix $\tilde{\boldsymbol{H}}$ evaluated at $\tilde{\boldsymbol{x}} = \tilde{\boldsymbol{x}}^\star$, $\tilde{\boldsymbol{H}} = [\tilde{u}''(\tilde{\boldsymbol{x}}^\star)]$ is definite negative. Using the theorem of steepest descent ($\beta\to\infty$), one has $\tilde{u}(\tilde{\boldsymbol{x}}) = \tilde{u}(\tilde{\boldsymbol{x}}^\star) + \frac{1}{2}(\tilde{\boldsymbol{x}}-\tilde{\boldsymbol{x}}^\star)^T\tilde{\boldsymbol{H}}(\tilde{\boldsymbol{x}}-\tilde{\boldsymbol{x}}^\star) + \mathcal{O}(||\tilde{\boldsymbol{x}}-\tilde{\boldsymbol{x}}^\star||^2)$, which yields:

$$Z \approx e^{\beta\tilde{u}(\tilde{\boldsymbol{x}}^\star)}\int_{\mathbb{R}^{N-1}} \mathrm{d}\tilde{\boldsymbol{x}} e^{\frac{\beta}{2}(\tilde{\boldsymbol{x}}-\tilde{\boldsymbol{x}}^\star)^T\tilde{\boldsymbol{H}}(\tilde{\boldsymbol{x}}-\tilde{\boldsymbol{x}}^\star)} \;, \tag{A.5}$$

and changing variables through $\tilde{\boldsymbol{z}} = \tilde{\boldsymbol{x}} - \tilde{\boldsymbol{x}}^\star$, one obtains:[1]

$$Z = e^{\beta\tilde{u}(\tilde{\boldsymbol{x}}^\star)}\sqrt{\frac{(2\pi)^{N-1}}{\det(-\beta\tilde{\boldsymbol{H}})}} \;, \tag{A.6}$$

and finally using Eq. (A.6) together with $\tilde{u}(\tilde{\boldsymbol{x}}^\star) = u(\boldsymbol{x}^\star)$ we find:

$$\Gamma = \beta\partial_w u(\boldsymbol{x}^\star) - \frac{1}{2}\partial_w \log\det(-\tilde{\boldsymbol{H}}) \;. \tag{A.7}$$

[1] For $\boldsymbol{A}\in\mathbb{R}^{N\times N}$ a symmetric positive-definite matrix and $\boldsymbol{s}\in\mathbb{C}^N$, one has: $\int_{\mathbb{R}^N}\mathrm{d}\boldsymbol{x}\exp\left(-\frac{1}{2}\boldsymbol{x}^T\boldsymbol{A}\boldsymbol{x}+\boldsymbol{s}^T\boldsymbol{x}\right) = \sqrt{\frac{(2\pi)^N}{\det\boldsymbol{A}}}\exp\left(\frac{1}{2}\boldsymbol{s}^T\boldsymbol{A}^{-1}\boldsymbol{s}\right)$.

For $\beta \to \infty$ one has $\Gamma = \beta \partial_w u(\boldsymbol{x}^\star)$.

We can also find an expression for $\langle x_i x_j \rangle_c$. Let us consider the joint distribution of $\tilde{x}_i - \tilde{x}_i^\star$ for $1 \leq i \leq N-1$ and compute the covariance between $\tilde{x}_i - \tilde{x}_i^\star$ and $\tilde{x}_j - \tilde{x}_j^\star$ $(1 \leq i, j \leq N-1)$:

$$\langle (\tilde{x}_i - \tilde{x}_i^\star)(\tilde{x}_j - \tilde{x}_j^\star) \rangle = Z^{-1} e^{\beta \tilde{u}(\tilde{\boldsymbol{x}}^\star)} \int_{\mathbb{R}^{N-1}} \mathrm{d}\tilde{\boldsymbol{z}} \tilde{z}_i \tilde{z}_j e^{\frac{\beta}{2} \tilde{\boldsymbol{z}}^T \tilde{\boldsymbol{H}} \tilde{\boldsymbol{z}}} \ , \tag{A.8}$$

where we have changed variables through $\tilde{\boldsymbol{z}} = \tilde{\boldsymbol{x}} - \tilde{\boldsymbol{x}}^\star$. Using [2] with $\boldsymbol{A} = -\beta \tilde{\boldsymbol{H}}$ symmetric positive definite, $\boldsymbol{s} = \boldsymbol{0}$ and $\boldsymbol{Q} = 2\boldsymbol{E}_{ij}$ where $\boldsymbol{E}_{ij}$ is the matrix of the canonical basis of $\mathbb{R}^{(N-1)\times(N-1)}$ (*i.e.* $\boldsymbol{E}_{ij}$'s coefficients are zeros everywhere and 1 at line i and column j), one has $\mathrm{Tr}(\boldsymbol{Q}\boldsymbol{A}^{-1}) = -2\beta^{-1}\mathrm{Tr}(\boldsymbol{E}_{ij}\tilde{\boldsymbol{H}}^{-1}) = -2\beta^{-1}[\tilde{\boldsymbol{H}}^{-1}]_{ij}$ and finally:

$$\langle (\tilde{x}_i - \tilde{x}_i^\star)(\tilde{x}_j - \tilde{x}_j^\star) \rangle = -\beta^{-1}[\tilde{\boldsymbol{H}}^{-1}]_{ij} \ , \tag{A.9}$$

Besides, using $\langle \tilde{x}_i - \tilde{x}_i^\star \rangle \langle \tilde{x}_j - \tilde{x}_j^\star \rangle = 0$ (because we integrate over $\mathbb{R}^{N-1}$), it is easy to show that $\langle \tilde{x}_i \tilde{x}_j \rangle_c = \langle (\tilde{x}_i - \tilde{x}_i^\star)(\tilde{x}_j - \tilde{x}_j^\star) \rangle$. Consequently, for $1 \leq i, j \leq N-1$, $\langle \tilde{x}_i \tilde{x}_j \rangle_c = -\beta^{-1}[\tilde{\boldsymbol{H}}^{-1}]_{ij}$.

Let us consider now the case where i or j is equal to N. One has $\langle \tilde{x}_N \rangle = w/p$, that is a constant, hence $\forall i \in [\![1; N]\!]$, $\langle \tilde{x}_i \tilde{x}_N \rangle_c = 0$. The covariance matrix $\tilde{\boldsymbol{C}}$ of $(\tilde{x}_i)_{1 \leq i \leq N}$ thus reads:

$$\tilde{\boldsymbol{C}} = (\langle \tilde{x}_i \tilde{x}_j \rangle_c)_{1 \leq i,j \leq N} = -\beta^{-1} \left[\begin{array}{c|c} \tilde{\boldsymbol{H}}^{-1} & \boldsymbol{0} \\ \hline \boldsymbol{0} & 0 \end{array} \right] \ . \tag{A.10}$$

It is now worth expliciting the matrix $\tilde{\boldsymbol{H}}$. From equalities between change of basis, we can derive equalities between the hessians in the two bases. Recall that if one has $\boldsymbol{x}' = \boldsymbol{P}^T \boldsymbol{x}$, then $\boldsymbol{H}' = \boldsymbol{P}^T \boldsymbol{H} \boldsymbol{P}$. In our case we need to restrict to $N-1$. Consequently, $\tilde{\boldsymbol{H}} = [(\boldsymbol{O}^T \boldsymbol{H} \boldsymbol{O})_{(N-1)\times(N-1)}]$ because $\boldsymbol{H}$ is a $N \times N$ matrix and $\tilde{\boldsymbol{H}}$ a $(N-1) \times (N-1)$ matrix.

Finally, to come back to $\langle x_i x_j \rangle_c$, we need to make a change of basis and we have $\langle x_i x_j \rangle_c = \boldsymbol{O} \langle \tilde{x}_i \tilde{x}_j \rangle_c \boldsymbol{O}^T$, which yields the covariance matrix $\boldsymbol{C}$ for $\beta \to \infty$ [3] :

$$\boldsymbol{C} = (\langle x_i x_j \rangle_c)_{1 \leq i,j \leq N} = -\beta^{-1} \boldsymbol{O} \left[\begin{array}{c|c} \tilde{\boldsymbol{H}} & \boldsymbol{0} \\ \hline \boldsymbol{0} & 0 \end{array} \right] \boldsymbol{O}^T \ , \tag{A.11}$$

and finally combining Eq. (A.3) with the expressions found for Γ and $\langle x_i x_j \rangle_c$ (Eqs. (A.7) and (A.11)), we obtain the corrected substitution matrix $\boldsymbol{S}$:

$$\boldsymbol{O}^T \boldsymbol{S} \boldsymbol{O} = \partial_w u(\boldsymbol{x}^\star) \left[\begin{array}{c|c} \tilde{\boldsymbol{H}}^{-1} & \boldsymbol{0} \\ \hline \boldsymbol{0} & 0 \end{array} \right] + \beta^{-1} \left(\left[\begin{array}{c|c} \partial_w \tilde{\boldsymbol{H}}^{-1} & \boldsymbol{0} \\ \hline \boldsymbol{0} & 0 \end{array} \right] - \frac{1}{2} \partial_w \log\det(-\tilde{\boldsymbol{H}}) \left[\begin{array}{c|c} \tilde{\boldsymbol{H}}^{-1} & \boldsymbol{0} \\ \hline \boldsymbol{0} & 0 \end{array} \right] \right) \ . \tag{A.12}$$

[2] For $\boldsymbol{Q} \in \mathbb{R}^{N \times N}$ one has: $\int_{\mathbb{R}^N} \mathrm{d}\boldsymbol{x} \frac{1}{2} \boldsymbol{x}^T \boldsymbol{Q} \boldsymbol{x} \exp\left(-\frac{1}{2} \boldsymbol{x}^T \boldsymbol{A} \boldsymbol{x} + \boldsymbol{s}^T \boldsymbol{x}\right) = \sqrt{\frac{(2\pi)^N}{\det \boldsymbol{A}}} \exp\left(\frac{1}{2} \boldsymbol{s}^T \boldsymbol{A}^{-1} \boldsymbol{s}\right) [\frac{1}{2} \mathrm{Tr}(\boldsymbol{Q}\boldsymbol{A}^{-1}) + \frac{1}{2} (\boldsymbol{A}^{-1}\boldsymbol{s})^T \boldsymbol{Q} (\boldsymbol{A}^{-1}\boldsymbol{s})]$.

[3] Note that when $\boldsymbol{x} \in \mathbb{R}^{N+}$, we can extend our previous results and find the same as before. Indeed $\boldsymbol{x}^\star$ is assumed to be positive. When we apply the method of steepest descent, the maximal contribution of the integral is around $\boldsymbol{x}^\star$ and then integrating over $\mathbb{R}^{N+}$ or $\mathbb{R}^N$ will lead approximately to the same result.

A.3 Multiple goods

We give here the expression of $\tilde{\boldsymbol{H}}$ for the log utility function with interactions. $\tilde{\boldsymbol{H}}$ can be written as $\boldsymbol{B} + \eta \boldsymbol{C}$ where:

$$\begin{cases} \boldsymbol{B}_{i,j} = -\delta_{ij} \dfrac{A^2 p_i^2}{a_i w^2} - \dfrac{A^2}{a_N w^2} p_i p_j \\ \boldsymbol{C}_{i,j} = 2\dfrac{A^2 p_i^2}{a_i^2 w^2} (\sum\limits_k \left(J_{ik} - 2\dfrac{a_i}{A} \sum\limits_j J_{jk} \right) \log B_k) \delta_{ij} + 2\dfrac{A^2 p_i p_j J_{ij}}{a_i a_j w^2} - 2\dfrac{A^2 p_i^2 J_{iN}}{a_i a_N w^2} - \\ 2\dfrac{A^2 p_j^2 J_{jN}}{a_j a_N w^2} + 2\dfrac{A^2 p_i p_j}{a_N^2 w^2} (\sum\limits_k \left(J_{Nk} - 2\dfrac{a_N}{A} \sum\limits_j J_{jk} \right) \log B_k) + 2\dfrac{A^2 p_i p_j J_{NN}}{a_N^2 w^2} \ . \end{cases} \tag{A.13}$$

At the first order in η, one has: $\tilde{\boldsymbol{H}}^{-1} = \boldsymbol{B}^{-1} - \eta \boldsymbol{B}^{-1} \boldsymbol{C} \boldsymbol{B}^{-1}$ and the Slutsky matrix can be deduced: $\boldsymbol{S} = \left[A + \beta^{-1}(N+1) \right] \tilde{\boldsymbol{H}}^{-1}$.

B

Articles

The articles published during my thesis can be found below. The first one is about the ballistics of jumping droplets and corresponds to Chap. 3. It was published in the journal Physical Review Fluids *in January 2019. The second one deals with the subject of repelling hot water and corresponds to Chap. 5. It was published in the journal* Nature Communications *in March 2019.*

Contents

Ballistics of self-jumping microdroplets

Pierre Lecointre,[1,2] Timothée Mouterde,[1,2] Antonio Checco,[3] Charles T. Black,[4] Atikur Rahman,[5] Christophe Clanet,[1,2] and David Quéré[1,2,*]

[1]*Physique et Mécanique des Milieux Hétérogènes, UMR 7636 du CNRS, ESPCI, 75005 Paris, France*
[2]*Laboratoire d'Hydrodynamique de l'X, UMR 7646 du CNRS, École polytechnique, 91128 Palaiseau, France*
[3]*Mechanical Engineering Department, Stony Brook University, Stony Brook, New York 11794, USA*
[4]*Center for Functional Nanomaterials, Brookhaven National Laboratory, Upton, New York 11973, USA*
[5]*Department of Physics, Indian Institute of Science Education and Research (IISER)-Pune, Maharashtra 411008, India*

(Received 5 September 2018; published 7 January 2019)

Water-repellent materials ideally operate at very different liquid scales: from centimeter-size for bugs living on ponds through millimeter-size for antirain functions to micrometer-size for antifogging solids. In the last situation, it was recently evidenced that microdrops condensing on a highly nonadhesive substrate can take advantage from coalescence to jump off the material, even if the dynamical characteristics of the jump were not established at such microscales. We demonstrate in this paper that the jumping speed of drops is nonmonotonic with the drop size, showing a maximum around 5 μm (a size commonly observed in dew), below and above which viscous and inertial effects, respectively, impede the takeoff. We quantitatively describe this optimum in antifogging. We also studied the ballistics of the jumping microdrops, from the height they reached to their behavior at landing; a situation where retakeoff is surprisingly found to be nearly unachievable despite the extreme nonwettability of the material.

DOI: 10.1103/PhysRevFluids.4.013601

I. INTRODUCTION

Water-repellent materials provide a wide variety of functions, which makes them ubiquitous in the natural world. Such materials allow creatures to live at the surface of water [1–3] and they repel water in dynamic conditions (rain) by reflecting impacting millimetric drops [4–6]. These surfaces are also superaerophilic when immersed in water [7], a property that provides oxygen ressources for underwater animals, thermal insulation [8–10], antibiofouling, and slip properties [11–14]. Among these properties, one of the most challenging ones is the ability to repel water at a micrometric scale, that is, at the scale of the texture responsible for superhydrophobicity. However, it was recently shown that nanotextured surfaces may self-remove condensing water [15,16]: growing droplets coalesce and the excess of surface energy can lead to the departure of the resulting drop. Considering that surface energy is converted into kinetic energy, the jumping velocity U of the merged drop scales as $\sqrt{\gamma/\rho r}$, denoting γ as the liquid surface tension, ρ as its density, and r as the radius of the coalescing droplets [15,17,18]. It was first reported that only droplets with radius greater than 10 μm can depart from the substrate [15]. Below this critical radius ($\approx$10 μm), internal viscous dissipation during coalescence was proposed to impede the motion [17,19].

However, recent experimental and numerical studies proved that jumping can occur at a much smaller scale, for $r \approx 5\,\mu$m [20,21], $r \approx 1\,\mu$m [22,23], and even $r \leqslant 500$ nm [18,24–26]. Both this threshold and the jumping velocity are material-dependent [17,19,23,26], and modeling them

*Corresponding author: david.quere@espci.fr

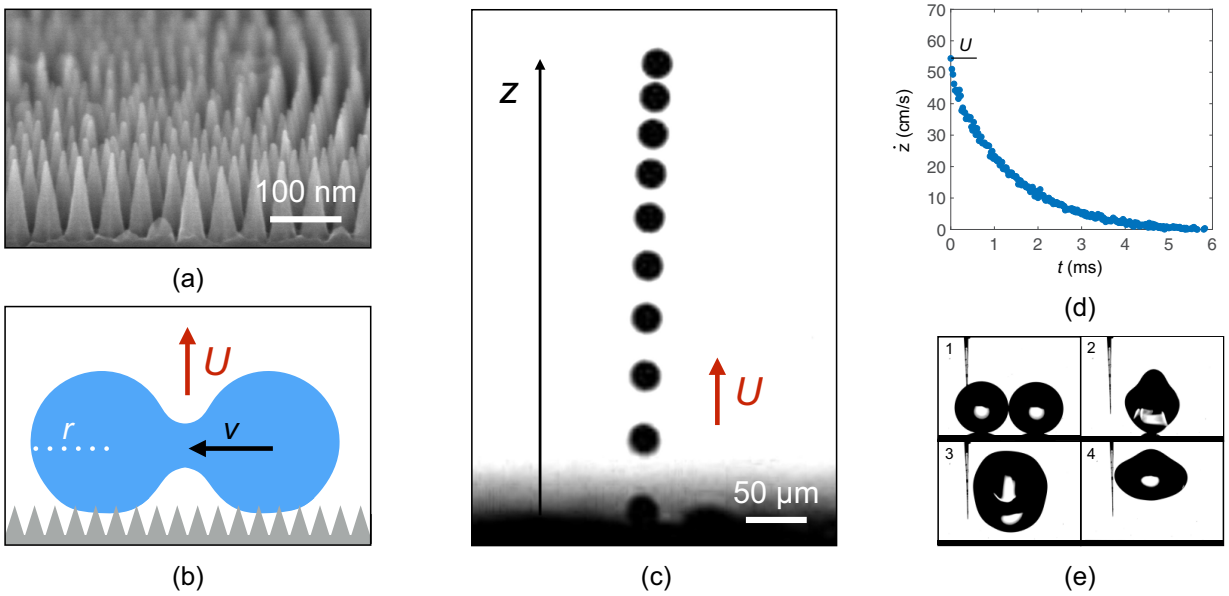

FIG. 1. (a) Scanning electron micrograph of the nanocones used in this study. The scale indicates 100 nm. (b) Sketch of two nonwetting droplets with radius r merging at a velocity v on hydrophobic nanocones; the jumping velocity of the resulting drop is denoted as U. (c) Side-view chronophotography of a jumping drop with radius $R = 11.3 \pm 0.1\,\mu$m resulting from the coalescence of a pair of droplets with $r = 8.9 \pm 0.1\,\mu$m. Images are separated by 0.125 ms. The drop takes off with a vertical jumping velocity $U = 55 \pm 5$ cm/s. (d) Plotting the drop velocity $\dot{z}$ as a function of time t for the experiment of Fig. 1(c) provides our definition of the jumping velocity U: it is taken as the maximum of $\dot{z}$. (e) High-speed photography of a symmetric coalescence of two drops with $r = 580 \pm 5\,\mu$m. Images are separated by 3.7 ms, except the last one which is at 15.5 ms, when the drop reaches its maximum height. The first snapshot (at the top left) shows the beginning of the coalescence while the second one corresponds to takeoff; the measured jumping velocity is $U = 7 \pm 1$ cm/s.

requires to consider both viscous and adhesive effects at such microscales. Our first aim in this paper is to shed light on this issue, based on experiments performed on special textures on which coalescing microdrops systematically take off [22]. We then describe the flight of the expelled drops, from merging and departure to return to the material. In our investigations, we measure the maximum height reached by the jumping water, which in natural cases must be large enough to leave the air boundary layer and to allow the drop to go with the wind, a condition for achieving a genuine antifogging material [16,27–30].

We consider water condensation on a silicon surface covered with nanocones inspired by the textures found on cicada wings [16] [Fig. 1(a)]. These surfaces are fabricated by combining block-copolymer self-assembly with anisotropic plasma etching [31]. The resulting cones have a base diameter of 52 nm and a height of 115 nm, and they are arranged in a dense hexagonal array. Chemical vapor deposition of 1H,1H,2H,2H-perfluorodecyltrichlorosilane makes the surface hydrophobic. This treatment on flat silicon gives an advancing water contact angle $\theta_0 = 120 \pm 2°$, a value that jumps to $\theta_a = 167 \pm 2°$ on the nanocones. The corresponding receding angle is $\theta_r = 157 \pm 2°$, which entails a modest hysteresis $\Delta\theta = \theta_a - \theta_r = 10 \pm 4°$. Condensation of water from the atmosphere is triggered by affixing the substrate on a Peltier module, and setting the temperature at $T_s = 3 \pm 1°$C, a value below the dew point in the laboratory conditions (temperature $T = 25 \pm 1°$C, relative humidity $RH = 39 \pm 1\%$ and supersaturation $S = 1.63 \pm 0.26$).

II. SYMMETRICAL MERGING

Our experiment, sketched in Fig. 1(b), consists of filming the coalescence of pairs of neighboring condensed droplets, simultaneously from above and from aside. Images are captured using

synchronized high-speed videocameras (Photron Fastcam Mini UX100) at a respective rate of 1 and 40 kHz for top and side views, and connected to a microscope (Infinitube In-line and Nikon ELWD 20x). The top view allows us to measure the radii of merging droplets, respectively denoted as r and r' ($r' < r$), and to check that only two-droplet coalescences are considered. We first focus on symmetric merging for which the radii ratio $\varepsilon = r'/r$ is larger than 0.95.

A typical experiment is shown in the chronophotography of Fig. 1(c), where we observe the takeoff of a water drop with radius $R = 11.3 \pm 0.1\,\mu$m resulting from the symmetric coalescence of a pair of droplets with $r = 8.9 \pm 0.1\,\mu$m. Computing the drop position $z(t)$ provides the drop velocity $\dot{z}$ as a function of time [Fig. 1(d)]. The jumping (or departure) velocity U is taken as the maximum of $\dot{z}(t)$. A layer of microdroplets sometimes hides the beginning of the jump, which generates an uncertainty on U on the order of 10%. For the particular case of Figs. 1(c) and 1(d), we measure a jumping velocity $U = 55 \pm 5$ cm/s. We also notice in these figures that the initial acceleration of the drop is extremely strong (with a value on the order of $100g$) and that the small size of the drop makes it highly sensitive to air (quick deceleration, slight deviation from the vertical).

The antifogging ability of our substrate allows us to observe the departure of droplets with radii r spanning from 1.3 to 24 μm [22]. We complemented this interval by also measuring the coalescence of needle-dispensed drops with radii ranging from 150 to 1100 μm. For this second series of experiments, we make our glass needles superhydrophobic by coating them with a Glaco solution (Mirror Coat Zero, Soft99) and drying the solution at 250 °C for half an hour. A first droplet is dispensed from a microneedle and a second one is made the same way until merging occurs, which is recorded from the side at a rate of 4 kHz. The resulting jumping velocity U is obtained as previously, but with larger time steps to filter the interface oscillations. Figure 1(e) shows the takeoff after merging of two drops with radius $r = 580 \pm 5\,\mu$m. The departure velocity is $U = 7 \pm 1$ cm/s, much smaller than observed for smaller drops [Fig. 1(c)]. In addition, we notice strong persistent droplet deformations after coalescence, another consequence of the much larger scale.

The evolution of the jumping velocity U after symmetric coalescence between two drops with radius r is reported in Fig. 2(a). We distinguish two families of data that respectively correspond to condensation ($r \leqslant 24\,\mu$m) and deposition ($r \geqslant 150\,\mu$m). For $r > 5\,\mu$m, U decreases as r increases and the data are well described by the dotted line with slope (0.5 in the log-log plot). "Large" drops depart with the inertiocapillary velocity $U \sim \sqrt{\gamma/\rho r}$, as reported by several authors [15,18,24], a law extended here down to 5 μm. However, drops smaller than 5 μm take off slower than predicted by this scaling and U tends to 0 as r approaches 1 μm, in agreement with the cutoff radius of jumping measured on the same substrate in [22].

The inertiocapillary velocity is generally derived by considering that surface energy is transferred into kinetic energy, an argument that yields $U = (3[2 - 2^{2/3}])^{1/2}\,U^* \approx 1.11U^*$, denoting $U^* = \sqrt{\gamma/\rho r}$. While we observe U scaling as $r^{-1/2}$, this relation overestimates the observed speed by a factor of order 5, as seen in Fig. 2(a), where the law $U = 1.11U^*$ is drawn as a black solid line. Mouterde *et al.* [32] showed that this discrepancy can be removed by expressing the balance of forces during merging. Each droplet retracts at a velocity $v \approx r/\tau$, where $\tau \approx 2\sqrt{\rho r^3/\gamma}$ is the inertiocapillary duration of coalescence. The transfer of momentum can be written $2mU = mv$ [denoting $m = (4\pi/3)\rho r^3$, the mass of each merging droplet], which yields $U = U^*/4$. This velocity has the same scaling form as U^*, but its numerical coefficient is 1/4 instead of 1.11. The best fit coefficient for the data in Fig. 2(a) is 0.22, 10% smaller than 1/4. A possible origin for this slight discrepancy arises from the typical energy $E_a = \pi r^2\gamma \sin^2\theta_r(1 + \cos\theta_r)$ needed to detach each droplet from the substrate. The corresponding momentum can be written $P_a \approx E_a\tau/r$, which modifies the takeoff velocity in $U = (U^*/4)[1 - 6\sin^2\theta_r(1 + \cos\theta_r)]$. A numerical coefficient of 0.22 corresponds to a receding angle of 154°, a value comparable to the measured angle $\theta_r = 157 \pm 2°$. This small correction in coefficient suggests that water adhesion remains marginal in our system.

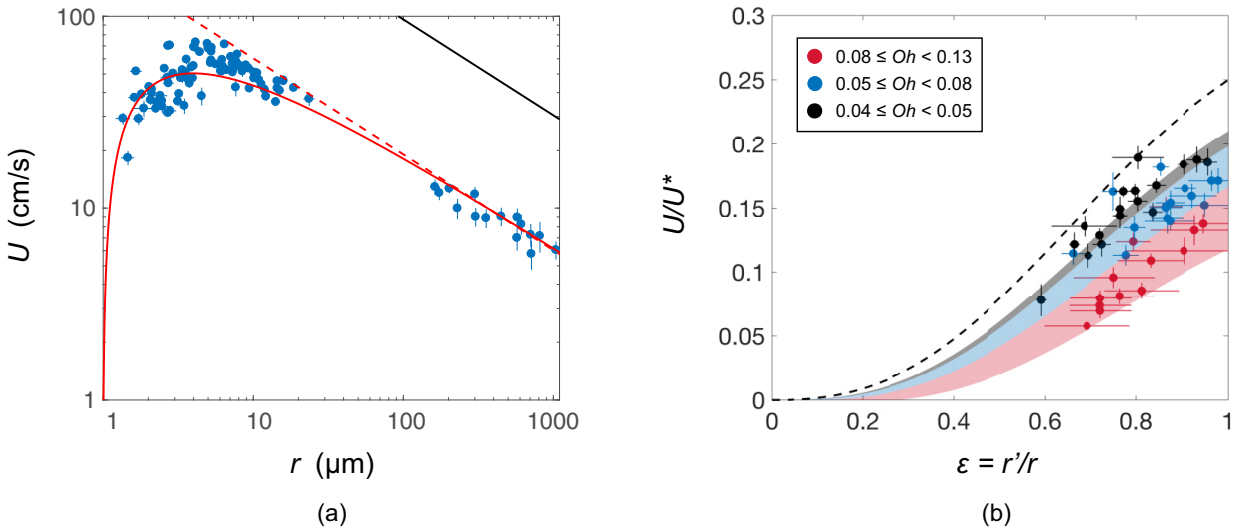

FIG. 2. Jumping velocity resulting from the coalescence of two droplets. (a) Velocity U for symmetric coalescence ($\varepsilon > 0.95$) as a function of the radius r of the two merging drops. Black line shows the speed resulting from energy conservation ($U = 1.11U^*$) and red dashes correspond to $U = 0.22U^*$, denoting $U^* = \sqrt{\gamma/\rho r}$. The red line shows the velocity $U = (U^*/4)\,[\alpha - 4.9\,Oh]$ where $\alpha = 1 - 6\sin^2\theta_r(1 + \cos\theta_r)$ and $Oh = \eta/\sqrt{\rho\gamma r}$ is the Ohnesorge number with η the water viscosity. The coefficient 4.9 is close to 4, the one predicted in Eq. (1). (b) Jumping velocity of droplets after an asymmetric coalescence; U is normalized by $U^* = \sqrt{\gamma/\rho r}$ and plotted as a function of the degree of symmetry $\varepsilon = r'/r$. The three sets of data correspond to three ranges for the larger radius: 2 μm $< r \leqslant 5$ μm (red) corresponding to $0.08 \leqslant Oh < 0.13$, 5 μm $< r \leqslant 13$ μm (blue) corresponding to $0.05 \leqslant Oh < 0.08$, and 13 μm $< r \leqslant 22$ μm (black) corresponding to $0.04 \leqslant Oh < 0.05$. The dashed line shows $U/U^* = \varepsilon^{5/2}/2(1 + \varepsilon^3)$ a function given by momentum conservation and neglecting adhesion and viscous dissipation [32], which provides an asymptotical behavior for the data. Red, blue, and black areas show Eq. (2) drawn with the corresponding colors for each range of Ohnesorge numbers.

The dashes in Fig. 2(a) fairly match the data obtained at "large" radius ($r > 5$ μm), which first suggests that water remains in the Cassie state despite condensation even at microscales [22,33]. Water nuclei growing within conical textures can be brought to the top of the surface by Laplace pressure. A few nanodroplets might remain pinned within the forest of cones, which could explain that the dotted line in Fig. 2(a) slightly overestimates some data in this region. However, adhesion remains marginal at both large and small scales, which explains that about 99% of merging microdroplets take off from nanocones arrays [22].

Conversely, the takeoff velocity U of droplets smaller than 5 μm strongly deviates from the dashes in Fig. 2(a). In the absence of significant adhesion, we interpret this decrease in mobility by the effect of viscosity. The flow during coalescence generates a dissipative force per droplet $F_v \approx \eta\Delta v\Omega$, where η is the viscosity of water and Ω the droplet volume. Since Δv scales as v/r^2, we deduce $F_v \approx (2\pi\eta/3)(\gamma r/\rho)^{1/2}$, an expression that depends on both viscosity and radius. The resulting loss of momentum $P_v \approx F_v\tau$ is found to be $(4\pi/3)\eta r^2$. For $r \approx 5$ μm and $U \approx 50$ cm/s, the ratio P_v/mU is of order unity and it decreases as $1/\sqrt{r}$, which suggests viscous dissipation as the main cause of loss at microscales. This result qualitatively agrees with numerical simulations that showed that water should be fully immobilized at a scale smaller than 300 nm [18,24].

Taking losses into account, the momentum balance becomes $2mU = mv - 2P_v - 2P_a$, where the factor 2 refers to the number of merging droplets. Hence we get a modified expression for the jumping velocity U:

$$U \approx \frac{U^*}{4}[\alpha - 4Oh], \tag{1}$$

where we introduced the Ohnesorge number $Oh = \eta/(\rho\gamma r)^{1/2}$ and where $\alpha = 1 - 6\sin^2\theta_r(1 + \cos\theta_r)$ is a numerical coefficient close to unity at large θ_r. It is interesting to note that an energy conservation argument leads to a normalized velocity U/U^* scaling as $\sqrt{1 - Oh}$ [17,19,34], a power law different from the one obtained with momentum transfer [Eq. (1)]. Equation (1) is drawn in Fig. 2(a) (red solid line), where $\alpha \approx 0.93$ is not adjusted since it corresponds to the measured value $\theta_r = 157°$; yet we use to best fit the data a coefficient 4.9 instead of 4 in front of the Ohnesorge number, which corrects the coefficient calculated with a scaling argument. We used $\eta = 1.62$ mPa.s, $\rho = 1000\,\mathrm{kg/m^3}$, and $\gamma = 75.3$ mN/m, all quantities considered for water at 3 °C. Equation (1) nicely captures the decrease of the departing velocity for $r \lesssim 5\,\mu$m, i.e., for $Oh \gtrsim 0.1$, showing how viscosity affects the inertiocapillary kinetics. In addition, this expression predicts a critical jumping radius of 1 μm and a maximum jumping velocity U for $r \approx 4\,\mu$m, in good agreement with the experiments. For $r \geqslant 150\,\mu$m, the predicted velocity approaches $U = 0.22U^*$, the asymptotic behavior drawn with a dotted line.

III. ASYMMETRICAL MERGING

Condensing droplets are often asymmetric when they merge due to the randomness of the condensation process. In Fig. 2(b), we plot the reduced takeoff velocity U/U^* as a function of the degree of symmetry $\varepsilon = r'/r$, for different radii r varying between 2 and 22 μm, which makes the Ohnesorge number vary between 0.13 and 0.04. We observe that U/U^* is sensitive both to the Ohnesorge number Oh [as expressed by Eq. (1)], and to the parameter ε: the larger the asymmetry (that is, the smaller ε), the slower the takeoff. A change in ε by typically 25% modifies the jumping velocity by a factor of 2. Hence asymmetry impacts the dynamics of jumping much more than adhesion [found in Eq. (1) to decrease U by only 7%]. For simplicity here, we analyze asymmetry effects by taking $\alpha = 1$ (negligible adhesion). In addition, if we also neglect viscosity, we can write the transfer of momentum as $(m + m')U = m'v'$, denoting $v' \approx r'/\tau'$ and $\tau' \approx 2\sqrt{\rho r'^3/\gamma}$ as the merging velocity and time of the smaller droplet. This yields $U = U^*\varepsilon^{5/2}/2(1 + \varepsilon^3)$ [32], a prediction drawn with a dashed line in Fig. 2(b). This behavior is found to capture asymptotically the data at large r (black symbols). Smaller droplets are slower, which we understand mostly as a consequence of the viscous dissipation described above. We generalize Eq. (1) to the case of asymmetric merging by rewriting the momentum balance as $(m + m')U = m'v' - P'_\mathrm{v} - P_\mathrm{v}$, using the same notations as previously. On the one hand, we have $P'_\mathrm{v} \approx F'_\mathrm{v}\tau'$, where the viscous force $F'_\mathrm{v} \approx \eta\Delta v'\Omega'$ is integrated over the merging time τ'. On the other hand, we assume $P_\mathrm{v} = P'_\mathrm{v}$ because the small drop induces fluid motion in the large one at its own scale, as shown in simulations by Eiswirth *et al.* [35]. Hence, we get an analytical expression for the jumping velocity U in an asymmetric configuration:

$$U \approx U^*\left[\frac{\varepsilon^{5/2}}{2(1+\varepsilon^3)} - 2Oh\frac{\varepsilon^2}{1+\varepsilon^3}\right]. \tag{2}$$

Despite the small size of the droplets, the Ohnesorge number $Oh = \eta/(\rho\gamma r)^{1/2}$ remains small (<0.2), so that U/U^* simply increases with ε at fixed r, and with r at fixed ε, as observed in Fig. 2(b). As asymmetry vanishes ($\varepsilon \to 1$), Eq. (2) reduces to Eq. (1) (with $\alpha = 1$ since we neglected adhesion). Drawn in Fig. 2(b) for three ranges of increasing radii, that is, three ranges of Oh (red, blue, and black areas), Eq. (2) is observed to show a fair agreement with the data. More generally, it describes how the conjunction of asymmetry and microscale affects drop departure, a key feature for understanding and tailoring the efficiency of antifogging materials.

IV. DROPLET FLIGHT AND LANDING

After takeoff, drops follow quasivertical paths [Fig. 1(c)] until falling back to the substrate. We discuss here the flight of microdrops ($r \leqslant 17\,\mu$m) formed after coalescence. We denote their radius

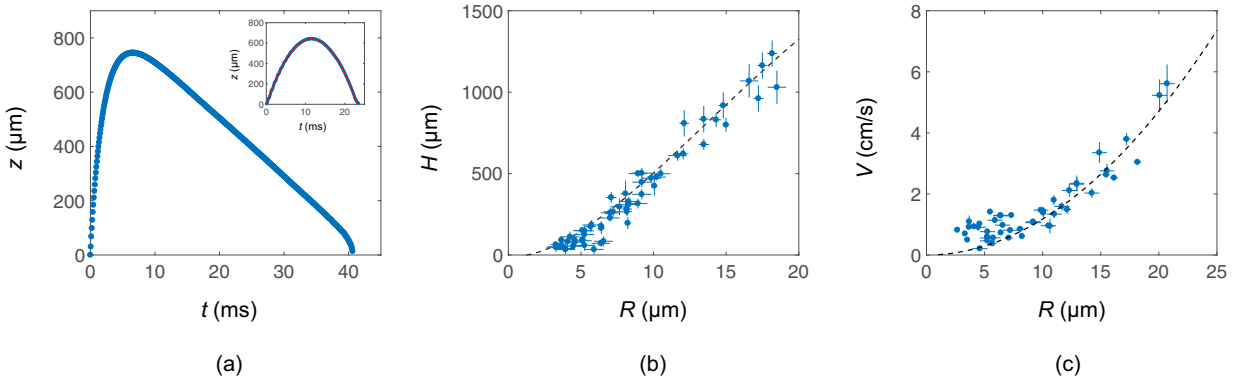

FIG. 3. Flight of departing drops after takeoff. (a) Vertical trajectory $z(t)$ of a drop with radius $R = 12.9 \pm 0.7$ μm after its ejection at a velocity $U = 29 \pm 2$ cm/s. Inset: Same plot for a drop with radius $R = 287 \pm 3$ μm departing at $U = 11 \pm 2$ cm/s. The function $z(t)$ is nicely fitted by a parabola (red solid line). (b) Maximum measured height H reached during flight as a function of radius R. The dashed line represents the theoretical height $H = U\tau_a - g\tau_a^2 \ln(1 + U/g\tau_a)$. (c) Absolute terminal velocity V as a function of radius R. The dashed line corresponds to the velocity given by the equilibrium between gravity and Stokes drag $V = (2/9)\rho g R^2/\eta_a$.

as $R = (r^3 + r'^3)^{1/3}$ (volume conservation), and we report in Fig. 3(a) the temporal evolution $z(t)$ for a drop with radius $R = 12.9 \pm 0.7$ μm departing at $U = 29 \pm 2$ cm/s. The function $z(t)$ is observed to be highly asymmetric. While the ascending phase occupies 20% of the flight time, the descending phase takes much longer, a consequence of the action of air viscosity at microscales. This friction is also responsible for the modest maximum height ($H = 740$ μm) reached by the drop after less than 6 ms. The Reynolds number in air is $\mathrm{Re} = \rho_a U R/\eta_a$, with U the jumping velocity, ρ_a and η_a the air density and viscosity. At microscales, Re is smaller than unity and Stokes drag $F = 6\pi\eta_a R\dot{z}$ is the main source of friction [24]. Hence the successive phases of rise and descent can be expressed by a balance between drag, inertia, and gravity, which yields the speed $\dot{z}$ as a function of time t:

$$\dot{z}(t) = (U + g\tau_a)e^{-t/\tau_a} - g\tau_a, \tag{3}$$

where the braking time τ_a is equal to $(2/9)\rho R^2/\eta_a$ [36]. Microdrops ballistics markedly differs from that of drops larger than 100 μm. For these, the drag force becomes negligible, which classically yields the parabolic motion resulting from a balance between inertia and gravity. The inset in Fig. 3(a) shows it for a drop with radius $R = 287 \pm 3$ μm departing at $U = 11 \pm 1$ cm/s, together with its parabolic fit drawn in red.

From our observations, we can also extract a useful, practical quantity, namely the maximum height H reached by the drop and plotted in Fig. 3(b) [27–29]. Integrating Eq. (3) yields $z(t) = \tau_a(U + g\tau_a)(1 - e^{-t/\tau_a}) - g\tau_a t$, whose maximum is:

$$H = U\tau_a - g\tau_a^2 \ln\left(1 + \frac{U}{g\tau_a}\right). \tag{4}$$

The main parameter in the last equation is the radius R, both contained in the departing velocity U [Eq. (1)] and in the braking time τ_a [Eq. (3)]. At microscales, τ_a is small so that H increases with R, as $R^{3/2}$. Equation (4) predicts that $H(R)$ reaches a maximum around $R \approx 50$ μm, a size larger than that of condensing drops. Drawn with a dashed line in Fig. 3(b) without adjustable parameter, Eq. (4) nicely describes the data. In the presence of a wind, in the range of 1–10 m/s, the air boundary layer at a centimeter size solid surface expelling dew has a thickness of about 100 μm, showing that most drops can escape this layer and be entrained by the wind (an interesting property if the substrate is horizontal for avoiding the redeposition of dew). For vertical substrates,

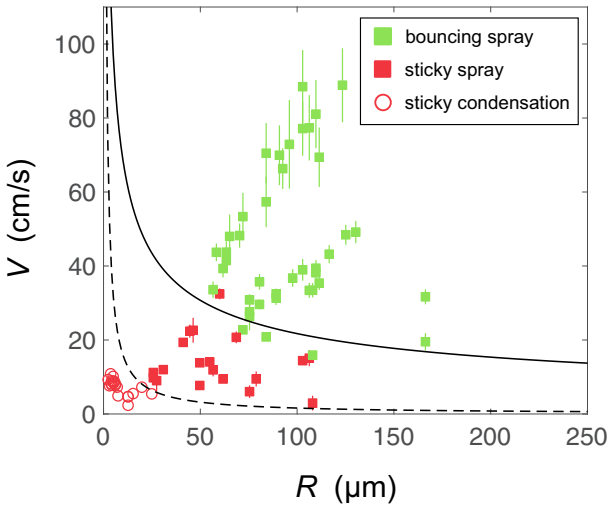

FIG. 4. Phase diagram of droplets at landing. The drop radius and velocity are denoted as R and V. Green color indicates bouncing and red color indicates sticking. Dots and squares mean that drops are made from condensation or from a spray, respectively. The solid line expresses the balance between adhesion and inertia [Eq. (5)]. The dashed line represents the threshold of bouncing dictated by viscosity $V^* \approx \eta/\rho R$.

H is the typical distance of ejection, after which droplets can fall under the action of gravity. This quantity is also useful to size the so-called phase-change thermal diodes (rectifying heat transfer [37]) by fixing the maximum gap for which jumping drops can be collected by a solid plate above the jumping stage.

On descent, drops quickly reach their terminal velocity V, plotted in Fig. 3(c) as a function of the radius R and compared to the prediction $V = g\tau_a$ (dashed line). The fit is convincing except at small radius ($R \leqslant 8\,\mu$m) where V can be as much as ten times larger than predicted. This discrepancy may originate from a charge effect [38] adding an electrostatic attractive contribution to the force balance, which is dominant at small substrate distances (i.e., at small R). This supplementary attraction is found to become significant at a distance of about 200 μm, which corresponds [in Fig. 3(b)] to a radius of about 7.5 μm, the size below which the gravitational prediction does not apply.

Droplets finally return to the substrate, which they impact at the velocity V. We study the landing for both condensed drops ($2.7\ \mu\text{m} \leqslant R \leqslant 22.7\,\mu\text{m}$ and $2\ \text{cm/s} \leqslant V \leqslant 15\ \text{cm/s}$) and water sprayed onto the surface ($25\ \mu\text{m} \leqslant R \leqslant 160\,\mu\text{m}$ and $2\ \text{cm/s} \leqslant V \leqslant 100\ \text{cm/s}$), and report in Fig. 4 the behavior of drops after impact: Either they bounce (green data), as expected on a repellent material, or they stick [red data split between sprayed (squares) and condensed droplets (empty circles)]. Only drops with large size R and velocity V are observed to bounce. Conversely, none of the droplets formed by condensation get reflected by the material from which they were ejected: Dew repellency is found to be more demanding than dew ejection, on which we now comment.

Our experiments probe the very unusual situation of microdrops impacting a solid at a small velocity (red circles). The corresponding Reynolds number $\text{Re} = \rho R V/\eta$ is of order unity or even smaller. Therefore, even in the limit of a strictly nonadhesive material ($\theta_r = 180^\circ$), drops should stick when the viscous dissipation at impact exceeds the kinetic energy. $\text{Re} = 1$ provides the threshold $V^* = \eta/\rho R$ above which we leave this regime. This frontier is marked with a dashed line in Fig. 4 and it is found to enclose all the data for dew. Being above this dashed line does no guarantee bouncing either. The Weber number $We = \rho V^2 R/\gamma$ controlling liquid deformation at impact in this domain remains modest, on the order of 0.1. Hence, for the sake of simplicity we consider that impacting water contacts the substrate with a radius of order R, with a contact line dissipation of order $\pi R^2\gamma(1 + \cos\theta_r)$. Drops will stick if this quantity exceeds the kinetic energy at impact $2\pi R^3\rho V^2/3$. The balance between these two energies yields a minimum velocity V^*

required for repellency:

$$V^* \approx \sqrt{\frac{3\gamma}{2\rho R}(1+\cos\theta_r)}. \tag{5}$$

Drawn with a solid line in Fig. 4, Eq. (5) nicely captures the frontier between bouncing and sticking. More generally, if we model the behavior of droplets after ejection using Eq. (3), we find $g\tau_a > V^*$ as a criterion for bouncing. Both the dependencies of τ_a and V^* with R being known, we deduce a minimum radius for bouncing $R^* = [243\,\eta_a^2\,\gamma\,(1+\cos\theta_r)/8\rho^3 g^2]^{1/5}$, a quantity around 60 μm. Such drops are larger than that obtained after condensation, which confirms the unability of condensed drops to bounce. It may seem surprising that an antifogging surface is unable to reflect the water ejected from it, but this is mainly a consequence of their slowness at impact. The only possibility for such a drop to bounce is to meet another one at impact [39,40].

V. SUMMARY

In summary, we provide quantitative measurements of the jumping velocity of coalescing droplets with radii ranging from 1 μm to 1 mm. Experiments at small scales are made possible by the use of highly nonadhesive materials, which enables water to remain mobile even at microscale. We report that the jumping velocity obeys the classical inertiocapillary scaling down to 5 μm, below which strong deviations are observed and interpreted as a consequence of viscous dissipation. The asymmetry of merging is shown to be another cause of reduced jumping efficiency. We characterize the flight, maximum height, descent kinetics, and landing of jumping microdroplets. Air viscosity rapidly stops ejected drops that later fall so slowly that they cannot bounce after impact. Our findings might help to design new antifogging properties where condensation produces drops large enough to be efficiently evacuated from the surface. The coupling of this motion with a lateral wind would be interesting to study, as well as the case where drops take off with solid particles (contamination or ballistospore) [41–44]. Another natural development of this study would be to understand how more than two drops merging on the surface are ejected.

ACKNOWLEDGMENTS

We thank Julien Husson and Alexandra Zak for the fabrication of the glass microneedles. Research carried out at Brookhaven National Laboratory is supported by the US Department of Energy, Office of Basic Energy Sciences, under Contract No. DE-AC02-98CH10886 and used resources of the Center for Functional Nanomaterials, which is a U.S. DOE Office of Science Facility. P.L. thanks the Ecole polytechnique for the financial support (Monge Fellowship). T.M. thanks the Direction Générale de l'Armement (DGA) for contributing to the financial support, Rose-Marie Sauvage and Thierry Midavaine for their constant interest, and Thales for cofunding this project. Finally, we thank Romain Labbé for help in the design of the experiments.

[1] D. L. Hu, B. Chan, and J. W. M. Bush, The hydrodynamics of water strider locomotion, Nature **424**, 663 (2003).

[2] X. Gao and L. Jiang, Biophysics: water-repellent legs of water striders, Nature **432**, 36 (2004).

[3] J. W. M. Bush and D. L. Hu, Walking on water: biolocomotion at the interface, Annu. Rev. Fluid Mech. **38**, 339 (2006).

[4] R. Blossey, Self-cleaning surfaces—virtual realities, Nat. Mater. **2**, 301 (2003).

[5] J. C. Bird, R. Dhiman, H.-M. Kwon, and K. K. Varanasi, Reducing the contact time of a bouncing drop, Nature **503**, 385 (2013).

[6] Y. Liu, L. Moevius, X. Xu, T. Qian, J. M. Yeomans, and Z. Wang, Pancake bouncing on superhydrophobic surfaces, Nat. Phys. **10**, 515 (2014).
[7] C. Shi, X. Cui, X. Zhang, P. Tchoukov, Q. Liu, N. Encinas, M. Paven, F. Geyer, D. Vollmer, Z. Xu, H.-J. Butt, and H. Zeng, Interaction between air bubbles and superhydrophobic surfaces in aqueous solutions, Langmuir **31**, 7317 (2015).
[8] W. A. Calder, Temperature relations and underwater endurance of the smallest homeothermic diver, the water shrew, Comp. Biochem. Physiol. **30**, 1075 (1969).
[9] M. R. Flynn and J. W. M. Bush, Underwater breathing: the mechanics of plastron respiration, J. Fluid Mech. **608**, 275 (2008).
[10] A. Balmert, H. F. Bohn, P. Ditsche-Kuru, and W. Barthlott, Dry under water: Comparative morphology and functional aspects of air-retaining insect surfaces, J. Morphol. **272**, 442 (2011).
[11] C. Cottin-Bizonne, J.-L. Barrat, L. Bocquet, and E. Charlaix, Low-friction flows of liquid at nanopatterned interfaces, Nat. Mater. **2**, 237 (2003).
[12] J. Ou, B. Perot, and J. P. Rothstein, Laminar drag reduction in microchannels using ultrahydrophobic surfaces, Phys. Fluids **16**, 4635 (2004).
[13] A. Tuteja, W. Choi, M. Ma, J. M. Mabry, S. A. Mazzella, G. C. Rutledge, G. H. McKinley, and R. E. Cohen, Designing superoleophobic surfaces, Science **318**, 1618 (2007).
[14] A. Steele, I. Bayer, and E. Loth, Inherently superoleophobic nanocomposite coatings by spray atomization, Nano Lett. **9**, 501 (2008).
[15] J. B. Boreyko and C.-H. Chen, Self-Propelled Dropwise Condensate on Superhydrophobic Surfaces, Phys. Rev. Lett. **103**, 184501 (2009).
[16] K. M. Wisdom, J. A. Watson, X. Qu, F. Liu, G. S. Watson, and C.-H. Chen, Self-cleaning of superhydrophobic surfaces by self-propelled jumping condensate, Proc. Natl. Acad. Sci. U.S.A. **110**, 7992 (2013).
[17] C. Lv, P. Hao, Z. Yao, Y. Song, X. Zhang, and F. He, Condensation and jumping relay of droplets on lotus leaf, Appl. Phys. Lett. **103**, 021601 (2013).
[18] F. Liu, G. Ghigliotti, J. J. Feng, and C.-H. Chen, Numerical simulations of self-propelled jumping upon drop coalescence on non-wetting surfaces, J. Fluid Mech. **752**, 39 (2014).
[19] F.-C. Wang, F. Yang, and Y.-P. Zhao, Size effect on the coalescence-induced self-propelled droplet, Appl. Phys. Lett. **98**, 053112 (2011).
[20] R. Enright, N. Miljkovic, J. Sprittles, K. Nolan, R. Mitchell, and E. N. Wang, How coalescing droplets jump, ACS Nano **8**, 10352 (2014).
[21] M.-K. Kim, H. Cha, P. Birbarah, S. Chavan, C. Zhong, Y. Xu, and N. Miljkovic, Enhanced jumping-droplet departure, Langmuir **31**, 13452 (2015).
[22] T. Mouterde, G. Lehoucq, S. Xavier, A. Checco, C. T. Black, A. Rahman, T. Midavaine, C. Clanet, and D. Quéré, Antifogging abilities of model nanotextures, Nat. Mater. **16**, 658 (2017).
[23] M. D. Mulroe, B. R. Srijanto, S. F. Ahmadi, C. P. Collier, and J. B. Boreyko, Tuning superhydrophobic nanostructures to enhance jumping-droplet condensation, ACS Nano **11**, 8499 (2017).
[24] F. Liu, G. Ghigliotti, J. J. Feng, and C.-H. Chen, Self-propelled jumping upon drop coalescence on Leidenfrost surfaces, J. Fluid Mech. **752**, 22 (2014).
[25] Z. Liang and P. Keblinski, Coalescence-induced jumping of nanoscale droplets on super-hydrophobic surfaces, Appl. Phys. Lett. **107**, 143105 (2015).
[26] H. Cha, C. Xu, J. Sotelo, J. M. Chun, Y. Yokoyama, R. Enright, and N. Miljkovic, Coalescence-induced nanodroplet jumping, Phys. Rev. Fluids **1**, 064102 (2016).
[27] B. Peng, S. Wang, Z. Lan, W. Xu, R. Wen, and X. Ma, Analysis of droplet jumping phenomenon with lattice Boltzmann simulation of droplet coalescence, Appl. Phys. Lett. **102**, 151601 (2013).
[28] G. S. Watson, M. Gellender, and J. A. Watson, Self-propulsion of dew drops on lotus leaves: a potential mechanism for self cleaning, Biofouling **30**, 427 (2014).
[29] G. S. Watson, L. Schwarzkopf, B. W. Cribb, S. Myhra, M. Gellender, and J. A. Watson, Removal mechanisms of dew via self-propulsion off the gecko skin, J. R. Soc., Interface **12**, 20141396 (2015).

[30] J. Liu, H. Guo, B. Zhang, S. Qiao, M. Shao, X. Zhang, X.-Q. Feng, Q. Li, Y. Song, L. Jiang, and J. Wang, Guided self-propelled leaping of droplets on a micro-anisotropic superhydrophobic surface, Angew. Chem. **128**, 4337 (2016).
[31] A. Checco, A. Rahman, and C. T. Black, Robust superhydrophobicity in large-area nanostructured surfaces defined by block-copolymer self assembly, Adv. Mater. **26**, 886 (2014).
[32] T. Mouterde, T.-V. Nguyen, H. Takahashi, C. Clanet, I. Shimoyama, and D. Quéré, How merging droplets jump off a superhydrophobic surface: Measurements and model, Phys. Rev. Fluids **2**, 11200 (2017).
[33] B. Zhang, X. Chen, J. Dobnikar, Z. Wang, and X. Zhang, Spontaneous wenzel to cassie dewetting transition on structured surfaces, Phys. Rev. Fluids **1**, 073904 (2016).
[34] H. Vahabi, W. Wang, S. Davies, J. M. Mabry, and A. K. Kota, Coalescence-induced self-propulsion of droplets on superomniphobic surfaces, ACS Appl. Mater. Interfaces **9**, 29328 (2017).
[35] R. Eiswirth, H.-J. Bart, A. Ganguli, and E. Kenig, Experimental and numerical investigation of binary coalescence: Liquid bridge building and internal flow fields, Phys. Fluids **24**, 062108 (2012).
[36] See Supplemental Material at http://link.aps.org/supplemental/10.1103/PhysRevFluids.4.013601 for the related content and supplementary movies.
[37] J. B. Boreyko, Y. Zhao, and C.-H. Chen, Planar jumping-drop thermal diodes, Appl. Phys. Lett. **99**, 234105 (2011).
[38] N. Miljkovic, D. J. Preston, R. Enright, and E. N. Wang, Electrostatic charging of jumping droplets, Nat. Commun. **4**, 2517 (2013).
[39] C. Lv, P. Hao, Z. Yao, and F. Niu, Departure of condensation droplets on superhydrophobic surfaces, Langmuir **31**, 2414 (2015).
[40] X. Chen, R. S. Patel, J. A. Weibel, and S. V. Garimella, Coalescence-induced jumping of multiple condensate droplets on hierarchical superhydrophobic surfaces, Sci. Rep. **6**, 18649 (2016).
[41] J. Turner and J. Webster, Mass and momentum transfer on the small scale: How do mushrooms shed their spores? Chem. Eng. Sci. **46**, 1145 (1991).
[42] A. Pringle, S. N. Patek, M. Fischer, J. Stolze, and N. P. Money, The captured launch of a ballistospore, Mycologia **97**, 866 (2005).
[43] X. Noblin, S. Yang, and J. Dumais, Surface tension propulsion of fungal spores, J. Exp. Biol. **212**, 2835 (2009).
[44] F. Liu, R. L. Chavez, S. Patek, A. Pringle, J. J. Feng, and C.-H. Chen, Asymmetric drop coalescence launches fungal ballistospores with directionality, J. R. Soc., Interface **14**, 20170083 (2017).

nature COMMUNICATIONS

ARTICLE

https://doi.org/10.1038/s41467-019-09456-8 OPEN

Two recipes for repelling hot water

Timothée Mouterde[1,2], Pierre Lecointre[1,2], Gaëlle Lehoucq[3], Antonio Checco[4], Christophe Clanet[1,2] & David Quéré[1,2]

Although a hydrophobic microtexture at a solid surface most often reflects rain owing to the presence of entrapped air within the texture, it is much more challenging to repel hot water. As it contacts a colder material, hot water generates condensation within the cavities at the solid surface, which eventually builds bridges between the substrate and the water, and thus destroys repellency. Here we show that both "small" (~100 nm) and "large" (~10 μm) model features do reflect hot drops at any drop temperature and in the whole range of explored impact velocities. Hence, we can define two structural recipes for repelling hot water: drops on nanometric features hardly stick owing to the miniaturization of water bridges, whereas kinetics of condensation in large features is too slow to connect the liquid to the solid at impact.

[1] Physique et Mécanique des Milieux Hétérogènes, UMR 7636 du CNRS, ESPCI, PSL Research University, 75005 Paris, France. [2] LadHyX, UMR 7646 du CNRS, École polytechnique, 91128 Palaiseau, France. [3] Thales Research and Technology, Route Départementale 128, 91767 Palaiseau, France. [4] Department of Mechanical Engineering, Light Engineering Lab, Stony Brook, New York 11794-2300, USA. These authors contribute equally: Timothée Mouterde, Pierre Lecointre. Correspondence and requests for materials should be addressed to T.M. (email: timothee.mouterde@polytechnique.org) or to D.Qéré. (email: david.quere@espci.fr)

When brought in contact with water, hydrophobic microfeatures on solids trap air, which lubricates the solid/liquid contact and renders water much more mobile than on conventional solids. As a consequence, most rough, hydrophobic materials repel rain in a dry atmosphere, resulting in spectacular rebounds after impact[1–3]: owing to its inertia, the impinging water first spreads as it would on plastic or glass, but the subjacent air then allows it to recoil and take off after a contact time of typically 10 ms. In contrast, humid conditions or dew repellency are much more challenging[4,5], as water nuclei condensing in the texture are then at the scale of the solid cavities, which fills the lubricating air layer and thus destroys superhydrophobicity. Many natural hierarchical surfaces, such as lotus leaves or artificial substrates covered by waxy microposts, indeed fail at repelling water in such conditions[6–8]. This limitation was recently circumvented by using nanopillars[9–11], whose scale can minimize the force of adhesion of water with the nuclei present in the nanocavities. This size effect can be amplified by making the nanopillars conical, a shape found to favour the jumping of condensing microdroplets as they coalesce[10,12–18].

In this context, it is not surprising that hydrophobic microtextures most often lose their superhydrophobicity when impacted by hot drops[19,20], except if the solid itself is hot[21]. The contact, even short, of hot water with a colder substrate promotes condensation within the microcavities at the solid surface, so as to bridge the incoming water to the substrate. How to repel hot water is an issue that has been poorly addressed despite its importance in industrial processes[22] such as clothing, coating, painting or windshield design[23]. This class of questions also includes the early stages of ice formation and accretion[24,25], potentially leading to serious damage to aircrafts, power lines, dams or wind turbines, when the typical time for phase change becomes shorter than the contact time of the impinging water. Hence, the idea to shorten the contact, which was achieved by tailoring large surface "defects"[26,27].

We wonder here how just the texture size may control the behaviour of hot water at impact and evidence two classes of texture able to robustly repel it. A first recipe consists in placing nanometric features (~100 nm) at the solid surface, which limits the size of water bridges and thus weakens the drop adhesion. A second recipe consists in having relatively "large" features (~10 µm), for which the construction of bridges is too slow to induce sticking during the brief contact at impact. We also explore the case of intermediate feature size, allowing us to test our model and to provide quantitative specifications for designing materials that can reflect hot water.

Results

Repellency failure. Experiments are performed with model texture with size ranging from 100 nm to 10 µm. We use silica or silicon sculpted with cylindrical pillars (radius a, height h) disposed on a square lattice with pitch p (Fig. 1a). All textures having a comparable geometry ($a \sim 0.1\,h$ and $p \sim h$), our materials are characterized by their pillar height, of respectively ~100 nm, ~1 µm and ~10 µm. The corresponding samples A, B and C, and

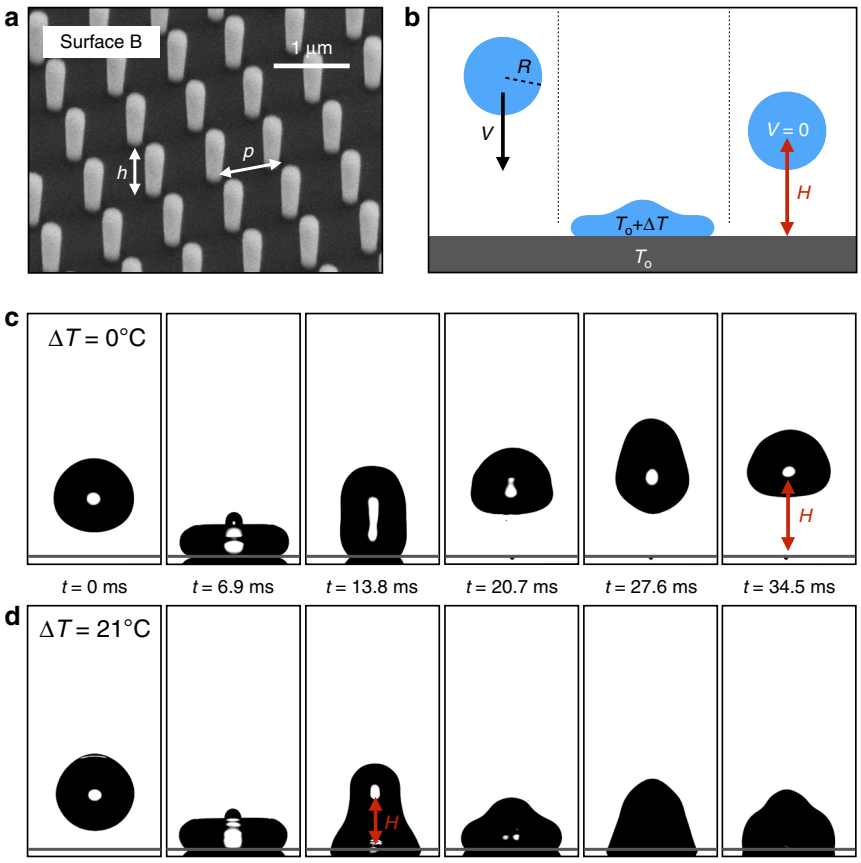

Fig. 1 Impact of hot drops on textured solids. **a** Scanning-electron viewgraph of substrate B. It is covered by pillars with height $h = 900$ nm spaced by $p = 840$ nm. Scale bar, 1 µm. **b** Schematic of the experiment: a water drop with radius R and temperature $T_o + \Delta T$ impacts at velocity V a superhydrophobic substrate kept at T_o. We measure the height H reached after impact, from which we deduce the restitution coefficient ε of the shock. **c**, **d** Snapshots of water drops ($R = 1.4$ mm) impacting the substrate B at $V = 40$ cm s^{-1}. Images are separated by 6.9 ms and the temperature difference ΔT between the drop and the substrate is either 0°C (**c**) or 21 °C (**d**). Water bounces in the first case and gets stuck in the second case

their fabrication[10,28] are described in the Methods section. Pillars make surfaces rough and we classically define the roughness factor $r = 1 + 2\pi ah/p^2$ as the ratio of total to apparent surface areas. Texture is finally rendered hydrophobic by vapour deposition of 1H,1H,2H,2H-perfluorodecyltrichlorosilane and such treatment on flat silicon provides an advancing angle θ_a for water of 120° ± 2°, which jumps to $\theta_a = 167°$, 168° and 169° (± 2°) on the rough materials A, B and C, respectively. The corresponding receding angles are $\theta_r = \theta_a - \Delta\theta = 140°$, 143° and 152° (± 3°), providing contact angle hysteresis $\Delta\theta_A = 27°$, $\Delta\theta_B = 25°$ and $\Delta\theta_C = 17°$.

Our goal is to determine how water repellency is affected by condensation at impact, which we control through the temperature of impinging drops. Water is brought to a temperature $T_o + \Delta T$ and dispensed from a syringe kept at the same temperature, so as to form drops with a radius $R = 1.40 \pm 0.05$ mm (a second radius is tested in the Supplementary Information). Water does not cool down during its fall, the dispensing height $L \approx 1$ cm being such that the falling time $(2L/g)^{1/2} \approx 40$ ms is negligible compared with the thermalizing time $\rho C_p R/H_T \approx 40$ s, where $\rho = 1000$ kg m^{-3} and $C_p = 4180$ J kg^{-1} K^{-1} are the density and thermal capacity of water, respectively, and $H_T \approx 100$ W m^{-2} K^{-1} is the heat transfer coefficient. Substrates kept at $T_o = 24 \pm 1$ °C and in a hygrometry of 32 ± 2% are impacted by drops impacting at a velocity $V = 40 \pm 5$ cm s^{-1} (Fig. 1b) and we display in Fig. 1c,d high-speed snapshots of impacts on surface B ($h = 900$ nm).

Without temperature difference ($\Delta T = 0$ °C, Fig. 1c), water bounces off the solid, as also observed for all of our samples (Fig. 2a and Supplementary Movie 1). This regular superhydrophobic behaviour[1,2,29] can be understood by comparing the water dynamic pressure ρV^2 and the Laplace pressure γ/p opposing the penetration in pillars, where γ is the water surface tension. This comparison entails a local Weber number $\rho V^2 p/\gamma$, a quantity always smaller than 0.01 in our experiments. The impacting liquid remains at the pillar tops, which makes rebounds possible and limits air compression within the pillars. The situation is quite different when elevating the temperature of water. As seen in Fig. 1d, an impinging drop brought to 45 °C ($\Delta T = 21$ °C) sticks to the sample B after impact, as revealed by the modest elevation H of its centre of mass ($H \approx R$): the surface fails at repelling hot water.

Texture repelling hot water. However, hot water can be repelled by other texture. As seen in Fig. 2a–c and in Supplementary Movies 2 and 3, drops with $\Delta T = 21$ °C and $\Delta T = 40$ °C are reflected by materials A and C, on which rebounds are similar to that at $\Delta T = 0$ °C (Fig. 2a). We also report in the Fig. 2a–c the behaviour of a fourth sample, called A', where the texture is still nanometric yet larger than for A (210 nm instead of 88 nm, see details in the Methods section). Drops still bounce on this sample for $\Delta T = 21$ °C but cease to be repelled for $\Delta T = 40$ °C, confirming that repellency depends in a non-trivial way on the texture scale and water temperature, which we further explore in this study.

We quantify the ability of a solid to repel hot water by introducing the restitution coefficient ε of the impacting drops, a quantity known for $\Delta T = 0$ °C to be fixed at a value ε_0 function of the impact velocity and contact angle hysteresis[30]. Before impact, the kinetic energy of a drop with mass $M = (4\pi/3)\rho R^3$ is $E_b = (1/2)MV^2$. When a drop bounces, its centre of gravity rises to a height

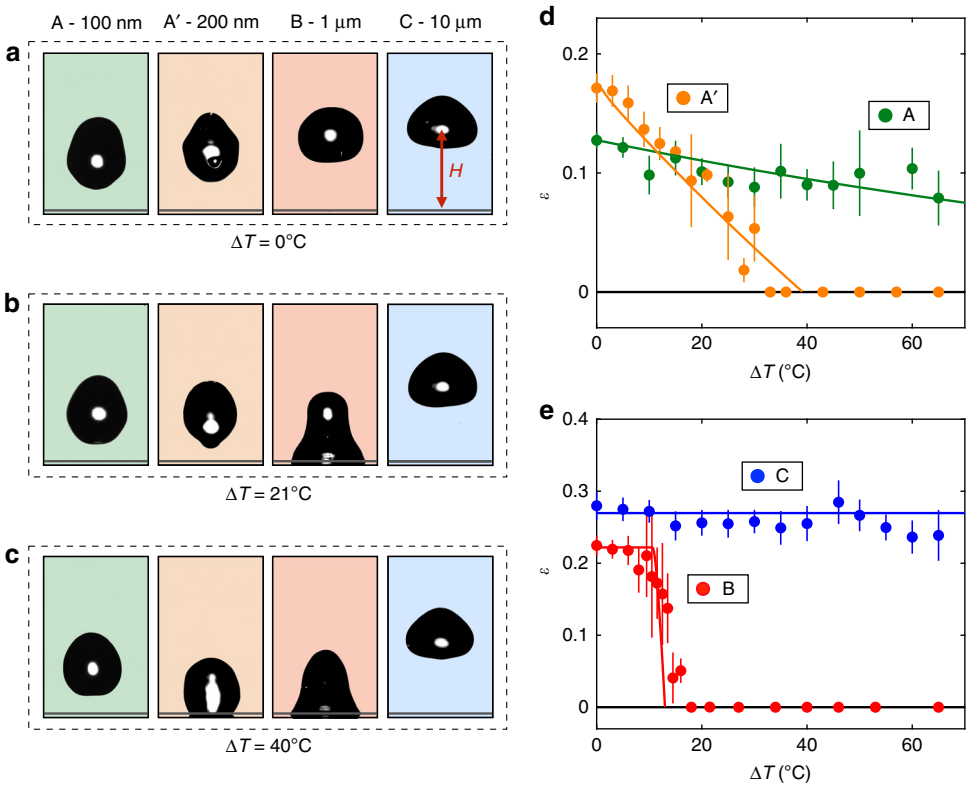

Fig. 2 Bouncing behaviour of hot drops. **a**–**c** Impacting water drops ($R = 1.4$ mm and $V = 40$ cm s^{-1}) at their maximum bouncing height H for $\Delta T = 0$°C (**a**), $\Delta T = 21$ °C (**b**) and $\Delta T = 40$ °C (**c**) on materials A, A', B and C with respective pillar heights of about 100 nm, 200 nm, 1 µm and 10 µm. **d**, **e** Coefficient of restitution ε of the rebound as a function of the temperature difference ΔT between water and the solid surface ($R = 1.4$ mm, $V = 40$ cm s^{-1}). For the sake of clarity, we separate data on nanometric features (**d**) from data on micrometric features (**e**). Water bounces on samples A and C at all drop temperatures, while it gets trapped ($\varepsilon = 0$) on A' and B when ΔT exceeds ~40 °C and ~15 °C, respectively. Solid lines show equation (5). Error bars represent uncertainty of the measurement

$H > R$ and we express the potential energy after take-off as $E_a = Mg(H - R)$. The bouncing efficiency is then quantified by the coefficient $\varepsilon = E_a/E_b$, a quantity which is taken null when drops stick to the substrate ($H \approx R$). Our goal is to see how we deviate from the value ε_0 when water is hot, i.e., when condensation can take place during the impact.

We report the variation of ε with ΔT in Fig. 2d,e for the surfaces A, A', B and C. We split the data in two graphs, to distinguish the behaviour on nano and microfeatures, which highlights the different nature of repellency in these two cases. Much information can be extracted from these plots: (1) At $\Delta T =$ 0 °C (where condensation effects are marginal), the coefficient of restitution slightly varies with the texture (of slightly different contact angle hysteresis), with a typical value $\varepsilon_0 \approx 0.2$ characteristic of superhydrophobic rebounds at such impact velocity[30]. (2) On the smallest features (green data, $h \approx 100$ nm), drops systematically bounce. However, we observe that ε slowly decreases with ΔT, showing a small, continuous loss of kinetic energy at take-off as water gets warmer. This effect is amplified when using larger features (orange data, $h \approx 200$ nm), for which the decrease of ε with ΔT becomes strong enough to intercept the abscissa axis in the range of explored temperature: drops hotter than 60 °C do not bounce on the substrate A'. (3) Observations are quite different with a micrometric texture. On the largest one (blue data, $h \approx$ 10 µm), ε is quasi-independent of ΔT ($\varepsilon = 0.27 \pm 0.04$) in the whole range of explored temperatures, $0 < \Delta T < 65$ °C. This is a surprising result, as we expect condensation to stick water all the more efficiently as ΔT increases. At smaller scale (red data, $h \approx 1$ µm), the behaviour is markedly different: after a small plateau, ε tumbles around $\Delta T_c \approx 15$ °C and water sticks to the surface above this value, as already seen in Fig. 1c,d.

Discussion

Contrasting with static situations where the smaller the texture, the better the water repellency in humid conditions[10], the fact that hot water bounces on 10 µm features reveals an original dynamical mechanism. When hot water contacts a colder superhydrophobic material, water nuclei form and grow within the texture (Fig. 3a). If they fill the elementary cells enclosed by neighbouring pillars, the resulting water bridges connect and stick the drop to its substrate (Fig. 3b). The formation of a bridge requires a time τ that can be evaluated. We assume that condensation is driven by a diffusive flux of water from the evaporating interface to the growing nucleus, whose respective vapour mass concentrations are $c_{sat}(T_o + \Delta T)$ and $c_{sat}(T_o)$. Denoting $\Delta c_{sat}(\Delta T) = c_{sat}(T_o + \Delta T) - c_{sat}(T_o)$, the diffusive flow rate scales as $D\Delta c_{sat}/h$, where $D \approx 20$ mm^2 s^{-1} is the diffusion coefficient of vapour in air. Integrating this rate over the cell surface area p^2 and time τ gives the mass $\rho h p^2$ of the filled cell, which yields:

$$\tau \sim \rho h^2 / D\Delta c_{sat} \quad (1)$$

As it hits the solid and spreads along it at a velocity V, the impinging water draws vapour within and along the texture, which adds a convective term to the diffusive growth of the nucleus. The typical velocity U of this vapour flow is deduced from the balance of viscous stresses at the liquid/vapour interface below the drop. Denoting η and η_v as the water and vapour viscosities, we simply write this balance as: $\eta V/R \sim \eta_v U/h$, where we neglect the friction of vapour around the pillars and thus slightly overestimate the convective flux. A vapour speed U scaling as $(\eta h/\eta_v R)$ V is maximum for the tallest features ($h = 10$ µm), where it typically reaches 10 cm s^{-1}. Hence, the Péclet number $Pe = Uh/D$ comparing convective and diffusive flux is found to be at most 0.1 for $h = 10$ µm and much smaller for shorter features, which justifies our assumption of diffusive growth for the nucleus.

In usual conditions ($T_o \approx 24$ °C) and for $\Delta T \approx 10$ °C, we have $\Delta c_{sat} \approx 10$ g m^{-3}, which leads to $\tau \sim 1$ ms for $h \approx 1$ µm. τ increases by four orders of magnitude as h rises from 100 nm to 10 µm, and it can be compared with the contact time τ_r of bouncing drops. τ_r being the response time of a spring with mass ρR^3 and stiffness γ, we have[31]: $\tau_r \sim (\rho R^3/\gamma)^{1/2}$, whose weak dependency on ρ and γ allows us to neglect its variation with temperature. The time τ_r is on the order of 10 ms for millimetric drops and thus possibly comparable to τ: There is a texture height, in the range of a few micrometres, for which we expect the two times to be equal, which eventually allows us to model the different impacts.

When the condensation time τ is larger than the bouncing time τ_r, water nuclei are smaller than the roughness height h (Fig. 3c) and thus do not connect the impacting drop to the substrate: ε is constant and equal to ε_0, its value at $\Delta T = 0$ °C:

$$\varepsilon = \varepsilon_0 \quad (2)$$

This mechanism explains the observations for the material C in Fig. 2d, a case where the large height of the pillars implies $\tau > \tau_r$. Hence, a material with a tall texture can dynamically repel hot

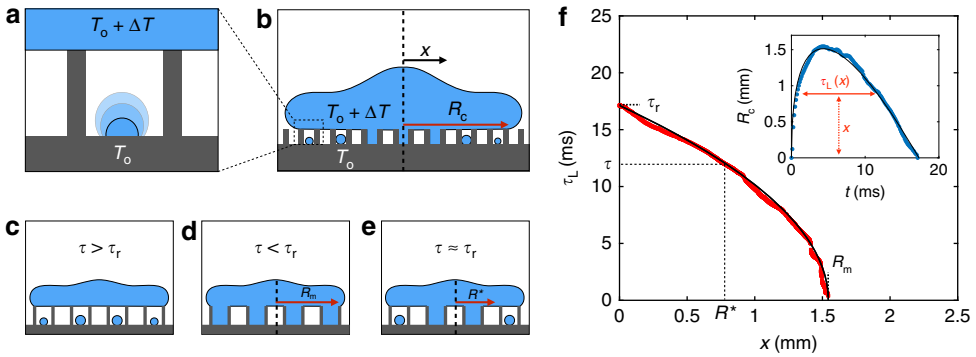

Fig. 3 Dynamics of adhesion. **a** Elementary cell containing a growing condensation nucleus fed by the hot water above. **b** Sketch of the spreading drop. x is the radial distance from the impact point and condensation nuclei are larger at small x, due to a higher local contact time τ_L. **c**–**e** Pinning mechanism as a function of τ and τ_r, the condensation and bouncing times. In the first case (**c**, $\tau > \tau_r$), there is no bridge between the substrate and the drop; in the second case (**d**, $\tau \ll \tau_r$), bridges form with a probability N below the drop; in the third case (**e**, $\tau \approx \tau_r$), bridges (with the same probability N) only connect the drop on a radius $R^* < R_m$, the maximum contact radius at impact. **f** Local contact time τ_L as a function of the distance x for a drop bouncing on surface B ($R = 1.4$ mm and $V = 40$ cm s^{-1}). The solid line shows equation (4), with $\tau_r = 17.4$ ms and $R_m = 1.55$ mm. For $\tau_L > \tau$, the drop is bridged to the surface on a disk with radius $x = R^*(\tau)$. Insert: contact radius R_c as a function of time for the same experiment. The solid fit $R_c(t) \approx 2(RVt)^{1/2} - (3\gamma/2\rho R)^{1/2} We^{1/4} t$ is discussed in the text

water, whereas it would lose its superhydrophobic character if exposed longer to humidity.

The opposite limit ($\tau < \tau_r$) concerns short pillars, when cavities enclosing a condensation droplet instantaneously fill at impact (Fig. 3d). As for hot water sitting on a cold texture[10], the adhesion force is $F \approx 4\pi R_m \gamma N$, where R_m is the maximum contact radius (sketched in Fig. 3d) and N is the probability of having a water nucleus in a cell. If we denote n as the number of nuclei per unit area, N is just $\min(nrp^2, 1)$, where the increase of n with ΔT ($n \approx 0.06\ \Delta T\ \mu m^{-2}$) can be determined by static measurements[10]. The energy E_{adh} induced by condensation and dissipated during bouncing is given by the work of F on the radius R_m, which yields $E_{adh} = 2\pi\gamma {R_m}^2 \min(nrp^2, 1)$. Hence, we deduce the coefficient $\varepsilon = \varepsilon_0 - E_{adh}/E_b$:

$$\varepsilon = \varepsilon_0 - 4\pi\gamma R_m^2 \min\left(nrp^2, 1\right)/MV^2 \quad (3)$$

At small nucleus density ($n(\Delta T) < 1/rp^2$), n linearly varies with ΔT and equation (3) predicts a linear decrease of ε with temperature, as seen with sample A. For a small texture, we have $nrp^2 < 1$, which yields: $\varepsilon = \varepsilon_0 - 4\pi\gamma {R_m}^2 rp^2 n/MV^2$. Drawn with a green line in Fig. 2d for the experimental value $R_m = 1.55$ mm, this law is found to quantitatively fit the data, explaining the persistence of bouncing at any water temperature and the slight decay of ε with ΔT. Three parameters in the model, namely γ, ρ and n, depend on temperature but the weak variations of γ and ρ with T make negligible their influence on the fit. The model also explains the behaviour observed with the sample A' (orange data), whose texture is twice larger than A. Then, we expect a stronger decrease of the function $\varepsilon(\Delta T)$ (sensitive to the quantity rp^2) and even strong enough to intercept the axis $\varepsilon = 0$. Hence, we quantitatively understand the transition to sticking for the orange data in Fig. 2d and more generally what is the feature size limit for repelling hot water with a nanotexture (see Supplementary Information for details).

The final case concerns the transition regime where both timescales have comparable magnitude ($\tau \approx \tau_r$). As sketched in Fig. 3e, condensation is favoured close to the impact point: water spends there more time than at the drop periphery, where it comes later and recedes earlier. We can introduce a local contact time $\tau_L(x)$, denoting x as the distance from the drop centre (Fig. 3b). By definition, τ_L is the contact time τ_r at the impact point ($\tau_L(0) = \tau_r$) and it vanishes at the drop periphery ($\tau_L(R_m) = 0$). If we denote R^* as the distance where the local contact time τ_L and the condensation time τ are equal, $\tau_L(R^*) = \tau$, we can distinguish two zones (Fig. 3e): for $x > R^*$, condensation is too slow to connect the drop to the solid and this area does not contribute to adhesion; for $x < R^*$, condensation bridges the material to the drop on a disk with radius R^* and the adhesion energy E_{adh} is determined by replacing in equation (3) R_m by R^*, the radius of the adhesive area.

As seen in Fig. 3f, the function $\tau_L(x)$ can be deduced from the time evolution of the contact radius R_c (insert in the figure). It can be also modelled by assuming that the contact dynamics can be divided in two phases: (1) at small time, the drop "sinks" at velocity V in the solid with the shape of a truncated sphere[32–34], which provides a Hertzian scaling: $R_c(t) \sim (RVt)^{1/2}$. This relationship was found to hold all along the spreading[32], with a numerical factor of ~2. (2) The recoiling drop[35] is a pancake with thickness z (Fig. 3a) that dewets at the Taylor–Culick velocity $(2\gamma/\rho z)^{1/2}$. Considering that the average height z of this pancake is given by a balance between inertia and surface tension[36], i.e., $z \approx (4R/3)We^{-1/2}$ (with $We = \rho V^2 R/\gamma$), we eventually get in this regime $R_c(t) \sim -(3\gamma/2\rho R)^{1/2} We^{1/4} t$. We finally assume that both contributions are additive, which yields: $R_c(t) \approx 2(RVt)^{1/2} - (3\gamma/2\rho R)^{1/2} We^{1/4} t$, a function drawn with a solid line in the insert of Fig. 3f where it nicely fits the data at all times. This description is valid at modest Weber number We, when no rim forms[37], similar to here where we have $We \approx 3$. The non-monotonic character of $R_c(t)$ implies that the equation $R_c = x$ has two solutions in time for $0 < x < R_m$, which we denote as t_1 and t_2 ($t_1 < t_2$). By definition, we have $\tau_L(x) = t_2 - t_1$, a quantity that can be extracted analytically from the expression of $R_c(t)$. We find:

$$\tau_L(x) \approx a(1 - x/b)^{1/2} \quad (4)$$

where $a = (8/3)\ (\rho R^3/\gamma)^{1/2} \approx \tau_r$ and $b = RWe^{1/4} \approx R_m$ (see the Supplementary Information for details). Equation (4) is drawn in Fig. 3f and observed to fit the data for $a \approx 17.4$ ms and $b \approx 1.6$ mm, i.e., the experimental values of τ_r and R_m that themselves nicely compare with the expected ones, $a \approx 15.9$ ms and $b \approx 1.8$ mm. From the explicit expression $\tau_L(x) \approx \tau_r\ (1 - x/R_m)^{1/2}$, we deduce the adhesion radius and find $R^* = R_m\ [1 - (\tau/\tau_r)^2]$ for $\tau \le \tau_r$, and $R^* = 0$ for $\tau > \tau_r$. Combining these equations with equation (3) in the transition regime, $\varepsilon = \varepsilon_0 - 4\pi\gamma {R^*}^2 \min(nrp^2, 1)/MV^2$, we get a general expression for the coefficient of restitution ε:

$$\varepsilon = \varepsilon_0 - 4\pi\gamma R_m^2 \max^2([1 - (\tau/\tau_r)^2], 0) \min\left(\mathrm{nrp}^2, 1\right)/\mathrm{MV}^2 \quad (5)$$

In order to compare this prediction with our data, we estimate Δc_{sat} using Rankine formula (see details in the Methods section). The only adjustable parameter is the numerical factor α in equation (1), $\tau = \alpha\rho h^2/D\Delta c_{sat}$. Drawn with solid lines in Fig. 2d,e with $\alpha = 8$, equation (5) is found to describe the whole ensemble of data. We recover the two limit cases, $\tau > \tau_r$, where condensation does not affect bouncing (equation (2), sample C and sample B at small ΔT), and $\tau < \tau_r$, where condensation is instantaneous (equation (3), samples A and A'), a regime sensitive to temperature. Moreover, equation (5) predicts the failure of repellency at intermediate pillar height (sample B). The transition is indeed found to be abrupt and to occur at the temperature given by the equality $\tau(\Delta T_c) = \tau_r$. Drops then cease to bounce, which we indicate by the line $\varepsilon = 0$. It is noteworthy that our test of equation (5) for another drop radius confirms its ability to describe all the regimes (Supplementary Fig. 1). We also studied the influence of the impact velocity (up to 1 m s^{-1}) and ambient hygrometry, and found again that the model is robust enough to capture the ensemble of data (Supplementary Figs 2, 3 and 4).

The predictive character of equation (5) eventually allows us to construct a phase diagram based on the temperature difference ΔT and pillar height h, fixing the other parameters (homothetic samples with $p = h$, $a = h/6$, $r \approx 2$, $\varepsilon_0 = 0.2$, $R = 1.4$ mm and $V = 40$ cm s^{-1}, all values comparable to that in our experiments). In the resulting phase diagram (Fig. 4), green and red colours distinguish bouncing from sticking. As found experimentally, the sticking region is indeed observed at intermediate pillar height and for $\Delta T > \Delta T_c$, where ΔT_c is given by $\varepsilon(\Delta T_c) = 0$ in equation (5) (solid line in the figure). Comparison with experiments can be refined by marking whether drops bounce or stick using green or red symbols. Experiments are performed with the samples A, A', B and C, to which we add data obtained with a fifth surface B' where pillar characteristics are $a = 100$ nm, $h = 600$ nm and $p = 560$ nm ($r \approx 2.2$). For samples A and C only (extreme values of h, $h = 88$ nm and $h = 10\ \mu$m), we remain in the bouncing regime whatever the water temperature, whereas bouncing/sticking transitions are observed at intermediate texture size (samples A', B' and B). The location of the transition is in good agreement with the prediction for ΔT_c, confirming for instance the non-monotonic character of ΔT_c with the pillar height. The two extreme values h_1 and h_2 below and above which rebounds are observed at all ΔT (dashes in the figure) can be expressed explicitly from equation (5), as shown in the Supplementary Discussion.

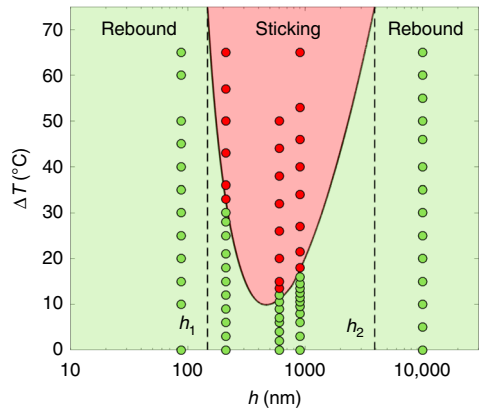

Fig. 4 Phase diagram for hot water impacting hydrophobic texture. The two control parameters are the water/substrate temperature difference ΔT and the pillar height h. The critical temperature ΔT_c defining the frontier between bouncing (green region) and sticking (red region) is calculated by solving $\varepsilon = 0$ in equation (5), with $p = h$, $a = h/6$, $r \approx 2$, $\varepsilon_0 = 0.2$, $R = 1.4$ mm and $V = 40$ cm s^{-1}, all values comparable to that in our experiments. The lower and upper bounds h_1 and h_2 for which bouncing is observed whatever the drop temperature are stressed with vertical dashes. Observations (green and red symbols for bouncing and sticking, respectively) are made for the five tested samples (A, $h = 88$ nm; A′, $h = 210$ nm; B′, $h = 600$ nm; B, $h = 900$ nm; C, $h = 10$ µm) and found to be in good agreement with the model

Our study shows the existence of two structural recipes for repelling hot water on a hydrophobic, textured material. (1) Tall features dynamically prevent the texture filling and the formation of water bridges between impacting drops and the solid material. (2) Small features miniaturize the bridges and thus their sticking abilities. In both cases, repellency is robust, as it is observed in the whole range of explored impact velocity and water temperature. The existence of two scenarii of repellency is reflected by differences in the repellency itself: although rebounds are found to be nearly unsensitive to water temperature in case 1, warmer drops are repelled slightly slower in case 2, due to the multiplication of water bridges when the impacting water is hotter. It would be interesting to mix the two kinds of texture to see what is the dominant scenario in such a case. On a more fundamental note, playing with the texture size gives access to the dynamics of condensation at submicrometric scales, a measure known to be particularly challenging. Our findings imply to consider the feature scale when developing new design able to reduce the bouncing time[26–28] for anti-icing or anti-fogging properties. However, the scale is not the only geometrical parameter: for instance, modifying (at constant height) the distance between the features or their order (square, hexagonal, etc.) should be alternative ways to design materials that repel hot water. It would finally be worth exploring what happens when water impacts repellent materials at room temperature in a rarefied atmosphere. Both the evaporation rate[38] and impact characteristics[39] are dramatically affected in a low-pressure environment, which might modify water repellency[40]. Non-condensable gases in air act as a neutral medium in our experiment. Replacing them by pure vapour should favour water condensation, whereas an increased rate of evaporation can conversely induce self-taking off (trampolining) of water, i.e., an increase of repellency[38]. On the whole, the interplay of impact at low pressure with the texture geometry and scale should be a subject of interest for the future.

Methods

Surface A. This surface is fabricated by combining block-copolymer self-assembly with anisotropic plasma etching in silicon, which provides large-area (cm^2) textures with ~10 nm feature size and long-range order. Posts have a radius $a = 15$ nm and a height $h = 88$ nm, and they are disposed on a rhombus network with side $p = 52$ nm. The roughness factor r is $r_A \approx 4.5$, and the water advancing and receding angles are $\theta_a = 167 \pm 2°$ and $\theta_r = 140 \pm 2°$, respectively.

Surface A′. The texture is a square lattice of pillars fabricated by electron-beam lithography and anisotropic plasma etching in silica. The pillar radius, height and spacing are respectively $a = 35$ nm, $h = 210$ nm and $p = 140$ nm. The pillar density and aspect ratio are ~20% and $h/2a = 3$, respectively, and the roughness factor is $r_A' \approx 3.4$. The water advancing and receding angles are $\theta_a = 155 \pm 3°$ and $\theta_r = 132 \pm 3°$, respectively.

Surface B. The texture is a square lattice of pillars fabricated by electron-beam lithography and anisotropic plasma etching in silica. The pillar size, height and spacing are respectively $a = 150$ nm, $h = 900$ nm and $p = 840$ nm. The pillar density and aspect ratio are ~10% and $h/2a = 3$, respectively, and the roughness factor is $r_B \approx 2.2$. The water advancing and receding angles are $\theta_a = 168 \pm 2°$ and $\theta_r = 143 \pm 2°$, respectively. Surface B' (used in Fig. 4) is made the same way, with $a = 100$ nm, $h = 600$ nm and $p = 560$ nm.

Surface C. This surface fabricated by photolithography and deep reactive ion etching is a square lattice of pillars. The pillar size, height and spacing are respectively $a = 1.25$ µm, $h = 10$ µm and $p = 10$ µm. The pillar density and aspect ratio are ~5% and $h/2a = 4$, respectively, and the roughness factor is $r_B \approx 1.8$. The water advancing and receding angles are $\theta_a = 169 \pm 2°$ and $\theta_r = 152 \pm 2°$, respectively.

Thermodynamic quantities. The water vapour concentration $c_{sat}(T)$ at temperature T is given by Dalton's law: $c_{sat}(T) = \rho_{sat}(M_w/M_{air})(P_{sat}(T)/P_0)$, where M_w and M_{air} are the respective molar masses of water and air, $P_{sat}(T)$ is the saturated vapour pressure of water at temperature T and P_0 is the atmospheric pressure. $P_{sat}(T)$ is given by the empirical Rankine formula: $P_{sat}(T) = P_0 \exp(13.7 - 5120/T)$. With this relation, we can estimate c_{sat} at temperatures T_o and $T_o + \Delta T$, a useful information in equation (1).

Data availability

The data that support the plots within this paper and other findings of this study are available in the main text and in the Supplementary Information. Additional information is available from the authors upon reasonable request.

Received: 24 October 2018 Accepted: 21 February 2019
Published online: 29 March 2019

References

1. Papadopoulos, P., Mammen, L., Deng, X., Vollmer, D. & Butt, H. J. How superhydrophobicity breaks down. *Proc. Natl Acad. Sci. USA* **110**, 3254–3258 (2013).
2. Blossey, R. Self-cleaning surfaces - virtual realities. *Nat. Mater.* **2**, 301–306 (2003).
3. Xia, F. & Jiang, L. Bio-inspired, smart, multiscale interfacial materials. *Adv. Mater.* **20**, 2842–2858 (2008).
4. Cheng, Y. T. & Rodak, D. E. Is the lotus leaf superhydrophobic? *Appl. Phys. Lett.* **86**, 1–3 (2005).
5. Wier, K. A. & McCarthy, T. J. Condensation on ultrahydrophobic surfaces and its effect on droplet mobility: ultrahydrophobic surfaces are not always water repellant. *Langmuir* **22**, 2433–2436 (2006).
6. Cheng, Y. T., Rodak, D. E., Angelopoulos, A. & Gacek, T. Microscopic observations of condensation of water on lotus leaves. *Appl. Phys. Lett.* **87**, 1–3 (2005).
7. Dorrer, C. & Rühe, J. Condensation and wetting transitions on microstructured ultrahydrophobic surfaces. *Langmuir* **23**, 3820–3824 (2007).
8. Narhe, R. D. & Beysens, D. Growth dynamics of water drops on a square-pattern rough hydrophobic surface. *Langmuir* **23**, 6486–6489 (2007).
9. Enright, R., Miljkovic, N., Al-Obeidi, A., Thompson, C. V. & Wang, E. N. Superhydrophobic condensation: the role of length scale and energy barriers. *Langmuir* **40**, 14424–14432 (2012).
10. Mouterde, T. et al. Antifogging abilities of model nanotextures. *Nat. Mater.* **16**, 658–663 (2017).
11. Lau, K. K. S. et al. Superhydrophobic carbon nanotube forests. *Nano. Lett.* **3**, 1701–1705 (2003).
12. Boreyko, J. B. & Chen, C. H. Self-propelled dropwise condensate on superhydrophobic surfaces. *Phys. Rev. Lett.* **103**, 2–5 (2009).

13. Cha, H. et al. Coalescence-induced nanodroplet jumping. *Phys. Rev. Fluids* **1**, 064102 (2016).
14. Miljkovic, N., Preston, D. J., Enright, R. & Wang, E. N. Electrostatic charging of jumping droplets. *Nat. Commun.* **4**, 1–9 (2013).
15. Mulroe, M. D., Srijanto, B. R., Ahmadi, S. F., Collier, C. P. & Boreyko, J. B. Tuning superhydrophobic nanostructures to enhance jumping-droplet condensation. *ACS Nano* **11**, 8499–8510 (2017).
16. Wang, Q., Yao, X., Liu, H., Quéré, D. & Jiang, L. Self-removal of condensed water on the legs of water striders. *Proc. Natl Acad. Sci. USA* **112**, 47–52 (2015).
17. Tian, J. et al. Efficient self-propelling of small-scale condensed microdrops by closely packed ZnO nanoneedles. *J. Phys. Chem. Lett.* **5**, 2084–2088 (2014).
18. Lv, C. et al. Condensation and jumping relay of droplets on lotus leaf. *Appl. Phys. Lett.* **103**, 1–5 (2013).
19. Liu, Y., Chen, X. & Xin, J. H. Can superhydrophobic surfaces repel hot water? *J. Mater. Chem.* **19**, 5602–5611 (2009).
20. Shiri, S., Murrizi, A. & Bird, J. C. Trapping a hot drop on a superhydrophobic surface with rapid condensation or microtexture melting. *Micromachines* **9**, 566–576 (2018).
21. Yu, Z. J. et al. How to repel hot water from a superhydrophobic surface? *J. Mater. Chem. A* **2**, 10639 (2014).
22. Shiri, S. & Bird, J. C. Heat exchange between a bouncing drop and a superhydrophobic substrate. *Proc. Natl Acad. Sci. USA* **114**, 6930–6935 (2017).
23. Dorrer, C. & Rühe, J. Some thoughts on superhydrophobic wetting. *Soft Matter* **5**, 51–61 (2009).
24. Kulinich, S. A., Farhadi, S., Nose, K. & Du, X. W. Superhydrophobic surfaces: are they really ice-repellent? *Langmuir* **27**, 25–29 (2011).
25. Nath, S., Ahmadi, S. F. & Boreyko, J. B. A review of condensation frosting. *Nanoscale Microsc. Thermophys. Eng.* **21**, 81–101 (2017).
26. Bird, J. C., Dhiman, R., Kwon, H.-M. & Varanasi, K. K. Reducing the contact time of a bouncing drop. *Nature* **503**, 385–388 (2013).
27. Liu, Y. et al. Pancake bouncing on superhydrophobic surfaces. *Nat. Phys.* **10**, 515–519 (2014).
28. Checco, A., Rahman, A. & Black, C. T. Robust superhydrophobicity in large-area nanostructured surfaces defined by block-copolymer self assembly. *Adv. Mater.* **26**, 886–891 (2014).
29. Bartolo, D. et al. Bouncing or sticky droplets: impalement transitions on superhydrophobic micropatterned surfaces. *Europhys. Lett.* **74**, 299–305 (2006).
30. Biance, A. L., Chevy, F., Clanet, C., Lagubeau, G. & Quéré, D. On the elasticity of an inertial liquid shock. *J. Fluid. Mech.* **554**, 47–66 (2006).
31. Rayleigh, L. On the capillary phenomena of jets. *Proc. R. Soc. Lond.* **29**, 71–97 (1879).
32. Roisman, I. V., Rioboo, R. & Tropea, C. Normal impact of a liquid drop on a dry surface: Model for spreading and receding. *Proc. R. Soc. A Math. Phys. Eng. Sci.* **458**, 1411–1430 (2002).
33. Rioboo, R., Marengo, M. & Tropea, C. Time evolution of liquid drop impact onto solid, dry surfaces. *Exp. Fluids* **33**, 112–124 (2002).
34. Vadillo, D. C., Soucemarianadin, A., Delattre, C. & Roux, D. C. D. Dynamic contact angle effects onto the maximum drop impact spreading on solid surfaces. *Phys. Fluids* **21**, 1–8 (2009).
35. Bartolo, D., Josserand, C. & Bonn, D. Retraction dynamics of aqueous drops upon impact on non-wetting surfaces. *J. Fluid. Mech.* **545**, 329–338 (2005).
36. Clanet, C., Béguin, C., Richard, D. & Quéré, D. Maximal deformation of an impacting drop. *J. Fluid. Mech.* **517**, 199–208 (2004).
37. Eggers, J., Fontelos, M. A., Josserand, C. & Zaleski, S. Drop dynamics after impact on a solid wall: theory and simulations. *Phys. Fluids* **22**, 1–13 (2010).
38. Schutzius, T. M. et al. Spontaneous droplet trampolining on rigid superhydrophobic surfaces. *Nature* **527**, 82–85 (2015).
39. Xu, L., Zhang, W. W. & Nagel, S. R. Drop splashing on a dry smooth surface. *Phys. Rev. Lett.* **94**, 184505 (2005).
40. Herminghaus, S. Roughness-induced non-wetting. *Europhys. Lett.* **52**, 165–170 (2000).

Acknowledgements

We thank Direction Générale de l'Armement (DGA) for contributing to the financial support, Rose-Marie Sauvage for her constant interest, Mathilde Reyssat, Stéphane Xavier, Atikur Rahman and Charles Black for their help in microfabrication, and Thales for cofunding this project. P.L. thanks the Ecole polytechnique for the financial support (Monge Fellowship).

Author contributions

T.M. conceived the project. T.M., P.L., C.C. and D.Q. designed the project. G.L. and A.C. provided samples and discussed the project. T.M. and P.L. performed experiments and analyses. T.M., P.L., C.C. and D.Q. built the model. T.M., P.L. and D.Q. wrote the manuscript with inputs from all other authors.

Additional information

Supplementary Information accompanies this paper at https://doi.org/10.1038/s41467-019-09456-8.

Competing interests: The authors declare no competing interests.

Reprints and permission information is available online at http://npg.nature.com/reprintsandpermissions/

Journal peer review information: *Nature Communications* thanks Sanjeev Chandra and the other anonymous reviewers for their contribution to the peer review of this work. Peer reviewer reports are available.

Publisher's note: Springer Nature remains neutral with regard to jurisdictional claims in published maps and institutional affiliations.

Bibliography

[1] Timothée Mouterde. *Matériaux multifonctions: antipluie, antibuée, antireflets*. PhD thesis, Paris Saclay, 2017.

[2] `https://www.futura-sciences.com/sciences/actualites/chimie-surprise-gouttelettes-eau-produisent-spontanement-peroxyde-hydrogene-77398/`. Accessed: 2019-09-02.

[3] `https://d1p2aimeyx6kdr.cloudfront.net/wp-content/uploads/2019/06/27171707/foule-monde-population-gens.jpg`. Accessed: 2019-09-02.

[4] `https://fr.m.wiktionary.org/wiki/Fichier:Fakir_on_bed_of_nails_Benares_India_1907.jpg`. Accessed: 2019-08-13.

[5] `https://documystere.com/histoires-legendes/moise-explique-par-la-science/`. Accessed: 2019-08-13.

[6] David L Hu, Brian Chan, and John WM Bush. The hydrodynamics of water strider locomotion. *Nature*, 424:663–666, 2003.

[7] John WM Bush and David L Hu. Walking on water: biolocomotion at the interface. *Annual Review of Fluid Mechanics*, 38:339–369, 2006.

[8] Thomas Young. III. An essay on the cohesion of fluids. *Philosophical Transactions of the Royal Society of London*, (95):65–87, 1805.

[9] David Quéré. Wetting and roughness. *Annual Review of Materials Research*, 38:71–99, 2008.

[10] Robert N Wenzel. Resistance of solid surfaces to wetting by water. *Industrial & Engineering Chemistry*, 28(8):988–994, 1936.

[11] Robert N Wenzel. Surface roughness and contact angle. *The Journal of Physical Chemistry*, 53(9):1466–1467, 1949.

[12] ABD Cassie and S Baxter. Wettability of porous surfaces. *Transactions of the Faraday Society*, 40:546–551, 1944.

[13] Wilhelm Barthlott and Christoph Neinhuis. Purity of the sacred lotus, or escape from contamination in biological surfaces. *Planta*, 202(1):1–8, 1997.

[14] Stephen J Wilson and Mike C Hutley. The optical properties of 'moth eye' antireflection surfaces. *Optica Acta: International Journal of Optics*, 29(7):993–1009, 1982.

[15] Stephan Herminghaus. Roughness-induced non-wetting. *Europhysics Letters*, 52(2):165, 2000.

[16] Anish Tuteja, Wonjae Choi, Minglin Ma, Joseph M Mabry, Sarah A Mazzella, Gregory C Rutledge, Gareth H McKinley, and Robert E Cohen. Designing superoleophobic surfaces. *Science*, 318:1618–1622, 2007.

[17] Xu Deng, Lena Mammen, Hans-Jürgen Butt, and Doris Vollmer. Candle soot as a template for a transparent robust superamphiphobic coating. *Science*, 335(6064):67–70, 2012.

[18] Christian Dorrer and Juergen Ruehe. Wetting of silicon nanograss: from superhydrophilic to superhydrophobic surfaces. *Advanced Materials*, 20:159–163, 2008.

[19] Denis Richard and David Quéré. Bouncing water drops. *Europhysics Letters*, 50(6):769, 2000.

[20] Mathilde Reyssat, Anne Pépin, Frédéric Marty, Yusen Chen, and David Quéré. Bouncing transitions on microtextured materials. *Europhysics Letters*, 74(2):306, 2006.

[21] Denis Bartolo, Farid Bouamrirene, Emilie Verneuil, Axel Buguin, Pascal Silberzan, and Sébastien Moulinet. Bouncing or sticky droplets: Impalement transitions on superhydrophobic micropatterned surfaces. *Europhysics Letters*, 74(2):299, 2006.

[22] Glen McHale, Sanaa Aqil, Neil J Shirtcliffe, Michael I Newton, and Yildirim H Erbil. Analysis of droplet evaporation on a superhydrophobic surface. *Langmuir*, 21(24):11053–11060, 2005.

[23] Aurélie Lafuma and David Quéré. Superhydrophobic states. *Nature Materials*, 2(7):457, 2003.

[24] Dimo Kashchiev. *Nucleation*. Elsevier, 2000.

[25] Chunfeng Mu, Jingjing Pang, Qiaoyu Lu, and Tianqing Liu. Effects of surface topography of material on nucleation site density of dropwise condensation. *Chemical Engineering Science*, 63(4):874–880, 2008.

[26] Yang-Tse Cheng and Daniel E Rodak. Is the lotus leaf superhydrophobic? *Applied Physics Letters*, 86(14):144101, 2005.

[27] Yang-Tse Cheng, Daniel E Rodak, Anastasios Angelopoulos, and Ted Gacek. Microscopic observations of condensation of water on lotus leaves. *Applied Physics Letters*, 87(19):194112, 2005.

[28] Kevin A Wier and Thomas J McCarthy. Condensation on ultrahydrophobic surfaces and its effect on droplet mobility: ultrahydrophobic surfaces are not always water repellant. *Langmuir*, 22(6):2433–2436, 2006.

[29] Ryan Enright, Nenad Miljkovic, Ahmed Al-Obeidi, Carl V Thompson, and Evelyn N Wang. Condensation on superhydrophobic surfaces: the role of local energy barriers and structure length scale. *Langmuir*, 28(40):14424–14432, 2012.

[30] Konrad Rykaczewski, William A Osborn, Jeff Chinn, Marlon L Walker, John Henry J Scott, Wanda Jones, Chonglei Hao, Shuhuai Yao, and Zuankai Wang. How nanorough is rough enough to make a surface superhydrophobic during water condensation? *Soft Matter*, 8:8786–8794, 2012.

[31] Nenad Miljkovic, Ryan Enright, and Evelyn N Wang. Effect of droplet morphology on growth dynamics and heat transfer during condensation on superhydrophobic nanostructured surfaces. *ACS Nano*, 6(2):1776–1785, 2012.

[32] Megan D Mulroe, Bernadeta R Srijanto, Farzad S Ahmadi, Patrick C Collier, and Jonathan B Boreyko. Tuning superhydrophobic nanostructures to enhance jumping-droplet condensation. *ACS Nano*, 11(8):8499–8510, 2017.

[33] Jonathan B Boreyko and Chuan-Hua Chen. Self-propelled dropwise condensate on superhydrophobic surfaces. *Physical Review Letters*, 103(18):184501, 2009.

[34] Xuefeng Gao, Xin Yan, Xi Yao, Liang Xu, Kai Zhang, Junhu Zhang, Bai Yang, and Lei Jiang. The dry-style antifogging properties of mosquito compound eyes and artificial analogues prepared by soft lithography. *Advanced Materials*, 19(17):2213–2217, 2007.

[35] Katrina M Wisdom, Jolanta A Watson, Xiaopeng Qu, Fangjie Liu, Gregory S Watson, and Chuan-Hua Chen. Self-cleaning of superhydrophobic surfaces by self-propelled jumping condensate. *Proceedings of the National Academy of Sciences*, 110:7992–7997, 2013.

[36] Timothée Mouterde, Gaëlle Lehoucq, Stéphane Xavier, Antonio Checco, Charles T Black, Atikur Rahman, Thierry Midavaine, Christophe Clanet, and David Quéré. Antifogging abilities of model nanotextures. *Nature Materials*, 16(6):658, 2017.

[37] Konrad Rykaczewski, Adam T Paxson, Sushant Anand, Xuemei Chen, Zuankai Wang, and Kripa K Varanasi. Multimode multidrop serial coalescence effects during condensation on hierarchical superhydrophobic surfaces. *Langmuir*, 29(3):881–891, 2013.

[38] Doekele G Stavenga, S Foletti, G Palasantzas, and K Arikawa. Light on the moth-eye corneal nipple array of butterflies. *Proceedings of the Royal Society B: Biological Sciences*, 273(1587):661–667, 2005.

[39] Yi-Fan Huang, Surojit Chattopadhyay, Yi-Jun Jen, Cheng-Yu Peng, Tze-An Liu, Yu-Kuei Hsu, Ci-Ling Pan, Hung-Chun Lo, Chih-Hsun Hsu, Yuan-Huei Chang, et al. Improved broadband and quasi-omnidirectional anti-reflection properties with biomimetic silicon nanostructures. *Nature Nanotechnology*, 2(12):770, 2007.

[40] Antonio Checco, Atikur Rahman, and Charles T Black. Robust superhydrophobicity in large-area nanostructured surfaces defined by block-copolymer self assembly. *Advanced Materials*, 26(6):886–891, 2014.

[41] Debbie Stokes. *Principles and practice of variable pressure/environmental scanning electron microscopy (VP-ESEM)*. John Wiley & Sons, 2008.

[42] Ray F Egerton, Peng Li, and Marek Malac. Radiation damage in the TEM and SEM. *Micron*, 35(6):399–409, 2004.

[43] Zahava Barkay. Dynamic study of nanodroplet nucleation and growth using transmitted electrons in ESEM. In *Nanodroplets*, pages 51–72. Springer, 2013.

[44] Daniel Aronov, Gil Rosenman, and Zahava Barkay. Wettability study of modified silicon dioxide surface using environmental scanning electron microscopy. *Journal of Applied Physics*, 101(8):084901, 2007.

[45] Daniel Aronov, Michel Molotskii, and Gil Rosenman. Electron-induced wettability modification. *Physical Review B*, 76(3):035437, 2007.

[46] F Bozso and Phaedon Avouris. Thermal and electron-beam-induced reaction of disilane on Si (100)-(2×1). *Physical Review B*, 38(6):3943, 1988.

[47] Paddy Royall, Brad L Thiel, and Athene Donald. Radiation damage of water in environmental scanning electron microscopy. *Journal of Microscopy*, 204(3):185–195, 2001.

[48] Athene Donald and S Kitching. Beam damage of polypropylene in the environmental scanning electron microscope: an FTIR study. *Journal of Microscopy(UK)*, 190(3):357–365, 1998.

[49] Debbie J Stokes, Brad L Thiel, and Athene Donald. Dynamic secondary electron contrast effects in liquid systems studied by environmental scanning electron microscopy. *Scanning*, 22(6):357–365, 2000.

[50] Joseph I Goldstein, Dale E Newbury, Joseph R Michael, Nicholas WM Ritchie, John Henry J Scott, and David C Joy. *Scanning electron microscopy and X-ray microanalysis*. Springer, 2017.

[51] Frieder Mugele and Jean-Christophe Baret. Electrowetting: from basics to applications. *Journal of physics: condensed matter*, 17(28):R705, 2005.

[52] Konrad Rykaczewski, John Henry J Scott, and Andrei G Fedorov. Electron beam heating effects during environmental scanning electron microscopy imaging of water condensation on superhydrophobic surfaces. *Applied Physics Letters*, 98(9):093106, 2011.

[53] Konrad Rykaczewski and John Henry J Scott. Methodology for imaging nano-to-microscale water condensation dynamics on complex nanostructures. *ACS Nano*, 5(7):5962–5968, 2011.

[54] Konrad Rykaczewski. Microdroplet growth mechanism during water condensation on superhydrophobic surfaces. *Langmuir*, 28(20):7720–7729, 2012.

[55] Lakshminarayanan Mahadevan and Yves Pomeau. Rolling droplets. *Physics of Fluids*, 11(9):2449–2453, 1999.

[56] Edgar J Lobaton and Todd R Salamon. Computation of constant mean curvature surfaces: Application to the gas–liquid interface of a pressurized fluid on a superhydrophobic surface. *Journal of Colloid and Interface Science*, 314(1):184–198, 2007.

[57] Frank Schellenberger, Noemí Encinas, Doris Vollmer, and Hans-Jürgen Butt. How water advances on superhydrophobic surfaces. *Physical Review Letters*, 116(9):096101, 2016.

[58] `http://matharguments180.blogspot.com/2014/06/day-134-medieval-ballistics.html`. Accessed: 2019-07-23.

[59] Niccolò Tartaglia. *Nova Scientia*. 1588.

[60] Fangjie Liu, Giovanni Ghigliotti, James J Feng, and Chuan-Hua Chen. Self-propelled jumping upon drop coalescence on leidenfrost surfaces. *Journal of Fluid Mechanics*, 752:22–38, 2014.

[61] Ryan Enright, Nenad Miljkovic, James Sprittles, Kevin Nolan, Robert Mitchell, and Evelyn N Wang. How coalescing droplets jump. *ACS Nano*, 8:10352–10362, 2014.

[62] Cunjing Lv, Pengfei Hao, Zhaohui Yao, Yu Song, Xiwen Zhang, and Feng He. Condensation and jumping relay of droplets on lotus leaf. *Applied Physics Letters*, 103(2):021601, 2013.

[63] Feng-Chao Wang, Fuqian Yang, and Ya-Pu Zhao. Size effect on the coalescence-induced self-propelled droplet. *Applied Physics Letters*, 98:053112, 2011.

[64] Fangjie Liu, Giovanni Ghigliotti, James J Feng, and Chuan-Hua Chen. Numerical simulations of self-propelled jumping upon drop coalescence on non-wetting surfaces. *Journal of Fluid Mechanics*, 752:39–65, 2014.

[65] Hyeongyun Cha, Chenyu Xu, Jesus Sotelo, Jae Min Chun, Yukihiro Yokoyama, Ryan Enright, and Nenad Miljkovic. Coalescence-induced nanodroplet jumping. *Physical Review Fluids*, 1(6):064102, 2016.

[66] Zhi Liang and Pawel Keblinski. Coalescence-induced jumping of nanoscale droplets on super-hydrophobic surfaces. *Applied Physics Letters*, 107:143105, 2015.

[67] Timothée Mouterde, Thanh-Vinh Nguyen, Hidetoshi Takahashi, Christophe Clanet, Isao Shimoyama, and David Quéré. How merging droplets jump off a superhydrophobic surface: measurements and model. *Physical Review Fluids*, 2:11200, 2017.

[68] Lord Rayleigh. On the capillary phenomena of jets. *Proc. R. Soc. London*, 29(196-199):71–97, 1879.

[69] Moon-Kyung Kim, Hyeongyun Cha, Patrick Birbarah, Shreyas Chavan, Chen Zhong, Yuehan Xu, and Nenad Miljkovic. Enhanced jumping-droplet departure. *Langmuir*, 31:13452–13466, 2015.

[70] Hamed Vahabi, Wei Wang, Seth Davies, Joseph M Mabry, and Arun K Kota. Coalescence-induced self-propulsion of droplets on superomniphobic surfaces. *ACS Applied Materials & Interfaces*, 9(34):29328–29336, 2017.

[71] Joseph D Paulsen, Justin C Burton, and Sidney R Nagel. Viscous to inertial crossover in liquid drop coalescence. *Physical Review Letters*, 106(11):114501, 2011.

[72] Joseph D Paulsen, Justin C Burton, Sidney R Nagel, Santosh Appathurai, Michael T Harris, and Osman A Basaran. The inexorable resistance of inertia determines the initial regime of drop coalescence. *Proceedings of the National Academy of Sciences*, 109(18):6857–6861, 2012.

[73] René T Eiswirth, Hans-Jörg Bart, Arijit A Ganguli, and Eugeny Y Kenig. Experimental and numerical investigation of binary coalescence: Liquid bridge building and internal flow fields. *Physics of Fluids*, 24:062108, 2012.

[74] Caroline Cohen. *La Physique du Sport*. PhD thesis, Ecole Polytechnique, 2014.

[75] Christophe Clanet. Sports ballistics. *Annual Review of Fluid Mechanics*, 47:455–478, 2015.

[76] Nenad Miljkovic, Daniel J Preston, Ryan Enright, and Evelyn N Wang. Electrostatic charging of jumping droplets. *Nature Communications*, 4:2517, 2013.

[77] Benli Peng, Sifang Wang, Zhong Lan, Wei Xu, Rongfu Wen, and Xuehu Ma. Analysis of droplet jumping phenomenon with lattice boltzmann simulation of droplet coalescence. *Applied Physics Letters*, 102:151601, 2013.

[78] Gregory S Watson, Marty Gellender, and Jolanta A Watson. Self-propulsion of dew drops on lotus leaves: a potential mechanism for self cleaning. *Biofouling*, 30:427–434, 2014.

[79] Gregory S Watson, Lin Schwarzkopf, Bronwen W Cribb, Sverre Myhra, Marty Gellender, and Jolanta A Watson. Removal mechanisms of dew via self-propulsion off the gecko skin. *Journal of the Royal Society Interface*, 12:20141396, 2015.

[80] Cunjing Lv, Pengfei Hao, Zhaohui Yao, and Fenglei Niu. Departure of condensation droplets on superhydrophobic surfaces. *Langmuir*, 31:2414–2420, 2015.

[81] Xuemei Chen, Ravi S Patel, Justin A Weibel, and Suresh V Garimella. Coalescence-induced jumping of multiple condensate droplets on hierarchical superhydrophobic surfaces. *Scientific Reports*, 6:18649, 2016.

[82] Logan S McCarty and George M Whitesides. Electrostatic charging due to separation of ions at interfaces: contact electrification of ionic electrets. *Angewandte Chemie International Edition*, 47(12):2188–2207, 2008.

[83] Chuanshan Tian and Yuen-Ron Shen. Structure and charging of hydrophobic material/water interfaces studied by phase-sensitive sum-frequency vibrational spectroscopy. *Proceedings of the National Academy of Sciences*, 106(36):15148–15153, 2009.

[84] Emma Cunningham. On the velocity of steady fall of spherical particles through fluid medium. *Proceedings of the Royal Society of London. Series A, Containing Papers of a Mathematical and Physical Character*, 83(563):357–365, 1910.

[85] Kenneth KS Lau, José Bico, Kenneth BK Teo, Manish Chhowalla, Gehan AJ Amaratunga, William I Milne, Gareth H McKinley, and Karen K Gleason. Superhydrophobic carbon nanotube forests. *Nano Letters*, 3(12):1701–1705, 2003.

[86] Kyoo-Chul Park, Hyungryul J Choi, Chih-Hao Chang, Robert E Cohen, Gareth H McKinley, and George Barbastathis. Nanotextured silica surfaces with robust superhydrophobicity and omnidirectional broadband supertransmissivity. *ACS Nano*, 6(5):3789–3799, 2012.

[87] Jean Louis Viovy, Daniel Beysens, and Charles M Knobler. Scaling description for the growth of condensation patterns on surfaces. *Physical Review A*, 37(12):4965, 1988.

[88] Van P Carey. *Liquid vapor phase change phenomena: an introduction to the thermophysics of vaporization and condensation processes in heat transfer equipment*. CRC Press, 2018.

[89] Wei Xu, Zhong Lan, Benli Peng, Rongfu Wen, and Xuehu Ma. Heterogeneous nucleation capability of conical microstructures for water droplets. *RSC Advances*, 5(2):812–818, 2015.

[90] Wei Xu, Zhong Lan, Benli Peng, Rongfu Wen, and Xuehu Ma. Effect of nano structures on the nucleus wetting modes during water vapour condensation: From individual groove to nano-array surface. *RSC Advances*, 6(10):7923–7932, 2016.

[91] Jeetain Mittal and Gerhard Hummer. Static and dynamic correlations in water at hydrophobic interfaces. *Proceedings of the National Academy of Sciences*, 105(51):20130–20135, 2008.

[92] Sapna Sarupria and Shekhar Garde. Quantifying water density fluctuations and compressibility of hydration shells of hydrophobic solutes and proteins. *Physical Review Letters*, 103(3):037803, 2009.

[93] Rahul Godawat, Sumanth N Jamadagni, and Shekhar Garde. Characterizing hydrophobicity of interfaces by using cavity formation, solute binding, and water correlations. *Proceedings of the National Academy of Sciences*, 106(36):15119–15124, 2009.

[94] Suruchi Prakash, Erte Xi, and Amish J Patel. Spontaneous recovery of superhydrophobicity on nanotextured surfaces. *Proceedings of the National Academy of Sciences*, 113(20):5508–5513, 2016.

[95] Françoise Brochard-Wyart, Jean Marc Di Meglio, David Quére, and Pierre Gilles De Gennes. Spreading of nonvolatile liquids in a continuum picture. *Langmuir*, 7(2):335–338, 1991.

[96] Pierre-Gilles De Gennes, Françoise Brochard-Wyart, and David Quéré. *Capillarity and wetting phenomena: drops, bubbles, pearls, waves*. Springer Science & Business Media, 2013.

[97] Uwe Thiele, Michael Mertig, and Wolfgang Pompe. Dewetting of an evaporating thin liquid film: Heterogeneous nucleation and surface instability. *Physical Review Letters*, 80(13):2869, 1998.

[98] José M Fernández-Varea and Rafael Garcia-Molina. Hamaker constants of systems involving water obtained from a dielectric function that fulfills the f sum rule. *Journal of Colloid and Interface Science*, 231(2):394–397, 2000.

[99] Antonio Checco, Benjamin M Ocko, Atikur Rahman, Charles T Black, Mykola Tasinkevych, Alberto Giacomello, and Siegfried Dietrich. Collapse and reversibility of the superhydrophobic state on nanotextured surfaces. *Physical Review Letters*, 112:216101, 2014.

[100] Bo Zhang, Xuemei Chen, Jure Dobnikar, Zuankai Wang, and Xianren Zhang. Spontaneous Wenzel to Cassie dewetting transition on structured surfaces. *Physical Review Fluids*, 1:073904, 2016.

[101] Rongfu Wen, Zhong Lan, Benli Peng, Wei Xu, Ronggui Yang, and Xuehu Ma. Wetting transition of condensed droplets on nanostructured superhydrophobic surfaces: coordination of surface properties and condensing conditions. *ACS Applied Materials & Interfaces*, 9(15):13770–13777, 2017.

[102] Xuemei Chen, Jun Wu, Ruiyuan Ma, Meng Hua, Nikhil Koratkar, Shuhuai Yao, and Zuankai Wang. Nanograssed micropyramidal architectures for continuous dropwise condensation. *Advanced Functional Materials*, 21(24):4617–4623, 2011.

[103] Ling Schneider, Milan Laustsen, Nikolaj Mandsberg, and Rafael Taboryski. The influence of structure heights and opening angles of micro-and nanocones on the macroscopic surface wetting properties. *Scientific Reports*, 6:21400, 2016.

[104] Il Woong Park, Maria Fernandino, and Carlos A Dorao. Wetting state transitions over hierarchical conical microstructures. *Advanced Materials Interfaces*, 5(5):1701039, 2018.

[105] Wenwu Ding, Maria Fernandino, and Carlos A Dorao. Conical micro-structures as a route for achieving super-repellency in surfaces with intrinsic hydrophobic properties. *Applied Physics Letters*, 115(5):053703, 2019.

[106] Neelesh A Patankar. On the modelling of hydrophobic contact angles on rough surfaces. *Langmuir*, 19(4):1249–1253, 2003.

[107] Yuyang Liu, Xianqiong Chen, and JH Xin. Can superhydrophobic surfaces repel hot water? *Journal of Materials Chemistry*, 19(31):5602–5611, 2009.

[108] Samira Shiri, Armela Murrizi, and James Bird. Trapping a hot drop on a superhydrophobic surface with rapid condensation or microtexture melting. *Micromachines*, 9(11):566, 2018.

[109] Zhe-Jun Yu, Jieyi Yang, Fang Wan, Quan Ge, Long-Lai Yang, Zun-Liang Ding, De-Quan Yang, Edward Sacher, and Tayirjan T Isimjan. How to repel hot water from a superhydrophobic surface? *Journal of Materials Chemistry A*, 2(27):10639–10646, 2014.

[110] James C Bird, Rajeev Dhiman, Hyuk-Min Kwon, and Kripa K Varanasi. Reducing the contact time of a bouncing drop. *Nature*, 503(7476):385, 2013.

[111] Yahua Liu, Lisa Moevius, Xinpeng Xu, Tiezheng Qian, Julia M Yeomans, and Zuankai Wang. Pancake bouncing on superhydrophobic surfaces. *Nature Physics*, 10(7):515, 2014.

[112] Anaïs Gauthier, Sean Symon, Christophe Clanet, and David Quéré. Water impacting on superhydrophobic macrotextures. *Nature Communications*, 6:8001, 2015.

[113] Pierre Chantelot, Ali Mazloomi Moqaddam, Anaïs Gauthier, Shyam S Chikatamarla, Christophe Clanet, Ilya V Karlin, and David Quéré. Water ring-bouncing on repellent singularities. *Soft Matter*, 14(12):2227–2233, 2018.

[114] Samira Shiri and James C Bird. Heat exchange between a bouncing drop and a superhydrophobic substrate. *Proceedings of the National Academy of Sciences*, 114(27):6930–6935, 2017.

[115] Christophe Josserand and Sigurdur T Thoroddsen. Drop impact on a solid surface. *Annual Review of Fluid Mechanics*, 48:365–391, 2016.

[116] Denis Bartolo, Farid Bouamrirene, Emilie Verneuil, Axel Buguin, Pascal Silberzan, and Sébastien Moulinet. Bouncing or sticky droplets: Impalement transitions on superhydrophobic micropatterned surfaces. *Europhysics Letters*, 74(2):299, 2006.

[117] Periklis Papadopoulos, Lena Mammen, Xu Deng, Doris Vollmer, and Hans-Jürgen Butt. How superhydrophobicity breaks down. *Proceedings of the National Academy of Sciences*, 110(9):3254–3258, 2013.

[118] Anne-Laure Biance, Frédéric Chevy, Christophe Clanet, Guillaume Lagubeau, and David Quéré. On the elasticity of an inertial liquid shock. *Journal of Fluid Mechanics*, 554:47–66, 2006.

[119] Denis Bartolo, Christophe Josserand, and Daniel Bonn. Retraction dynamics of aqueous drops upon impact on non-wetting surfaces. *Journal of Fluid Mechanics*, 545:329–338, 2005.

[120] Pierre Chantelot. *Rebonds spéciaux de liquides*. PhD thesis, Paris Saclay, 2018.

[121] Ilia V Roisman, Romain Rioboo, and Cameron Tropea. Normal impact of a liquid drop on a dry surface: model for spreading and receding. *Proceedings of the Royal Society of London. Series A: Mathematical, Physical and Engineering Sciences*, 458(2022):1411–1430, 2002.

[122] Romain Rioboo, Marco Marengo, and Cameron Tropea. Time evolution of liquid drop impact onto solid, dry surfaces. *Experiments in Fluids*, 33(1):112–124, 2002.

[123] Damien C Vadillo, Arthur Soucemarianadin, Cyril Delattre, and Denis CD Roux. Dynamic contact angle effects onto the maximum drop impact spreading on solid surfaces. *Physics of Fluids*, 21(12):122002, 2009.

[124] Anne Mongruel, Virginie Daru, François Feuillebois, and Svoboda Tabakova. Early post-impact time dynamics of viscous drops onto a solid dry surface. *Physics of Fluids*, 21(3):032101, 2009.

[125] Guillaume Riboux and José Manuel Gordillo. Experiments of drops impacting a smooth solid surface: a model of the critical impact speed for drop splashing. *Physical Review Letters*, 113(2):024507, 2014.

[126] Christophe Clanet, Cédric Béguin, Denis Richard, and David Quéré. Maximal deformation of an impacting drop. *Journal of Fluid Mechanics*, 517:199–208, 2004.

[127] Jens Eggers, Marco A Fontelos, Christophe Josserand, and Stéphane Zaleski. Drop dynamics after impact on a solid wall: theory and simulations. *Physics of Fluids*, 22(6):062101, 2010.

[128] Guillaume Lagubeau, Marco A Fontelos, Christophe Josserand, Agnès Maurel, Vincent Pagneux, and Philippe Petitjeans. Spreading dynamics of drop impacts. *Journal of Fluid Mechanics*, 713:50–60, 2012.

[129] Denis Richard, Christophe Clanet, and David Quéré. Surface phenomena: Contact time of a bouncing drop. *Nature*, 417(6891):811, 2002.

[130] Ko Okumura, Frédéric Chevy, Denis Richard, David Quéré, and Christophe Clanet. Water spring: A model for bouncing drops. *Europhysics Letters*, 62(2):237, 2003.

[131] Pierre-Brice Bintein. *Dynamiques de gouttes funambules: applications à la fabrication de laine de verre*. PhD thesis, 2015.

[132] Steven Bryant and Anna Johnson. Wetting phase connectivity and irreducible saturation in simple granular media. *Journal of Colloid and Interface Science*, 263(2):572–579, 2003.

[133] Torsten Gröger, Ugur Tüzün, and David M Heyes. Modelling and measuring of cohesion in wet granular materials. *Powder Technology*, 133(1-3):203–215, 2003.

[134] Felipe Pacheco-Vázquez, Florian Moreau, Nicolas Vandewalle, and Stéphane Dorbolo. Sculpting sandcastles grain by grain: Self-assembled sand towers. *Physical Review E*, 86(5):051303, 2012.

[135] Guillaume Saingier, Alban Sauret, and Pierre Jop. Accretion dynamics on wet granular materials. *Physical Review Letters*, 118(20):208001, 2017.

[136] Lucija Boskovic, Igor E Agranovski, and Roger D Braddock. Filtration of nanosized particles with different shape on oil coated fibres. *Journal of Aerosol Science*, 38(12):1220–1229, 2007.

[137] Shahriar Nick Niakin. High capacity hybrid multi-layer automotive air filter, November 2 2004. US Patent 6,811,588.

[138] Thilo K Müller, Jörg A Meyer, E Thébault, and Gerhard Kasper. Impact of an oil coating on particle deposition and dust holding capacity of fibrous filters. *Powder technology*, 253:247–255, 2014.

[139] Mathilde Reyssat, Laetitia Y Sangne, Ernst A Van Nierop, and Howard A Stone. Imbibition in layered systems of packed beads. *Europhysics Letters*, 86(5):56002, 2009.

[140] Lev Landau and Veniamin Levich. Dragging of a liquid by a moving plate. *Acta Physicochimica U.R.S.S.*, 17(1-2):42–54, 1942.

[141] Élise Lorenceau, Christophe Clanet, and David Quéré. Capturing drops with a thin fiber. *Journal of Colloid and Interface Science*, 279(1):192–197, 2004.

[142] Namiko Mitarai and Franco Nori. Wet granular materials. *Advances in Physics*, 55(1-2):1–45, 2006.

[143] Richard Lucas. Ueber das zeitgesetz des kapillaren aufstiegs von. *Flussigkeiten, Kolloid*, (1918):23.

[144] Edward W Washburn. The dynamics of capillary flow. *Physical Review*, 17(3):273, 1921.

[145] Philip Crosbie Carman. Fluid flow through granular beds. *Transactions of the Institution of Chemical Engineers*, 15:150–166, 1937.

[146] Manuel Alonso, Enrique Sainz, Félix A Lopez, and Kunio Shinohara. Void-size probability distribution in random packings of equal-sized spheres. *Chemical Engineering Science*, 50(12):1983–1988, 1995.

[147] `http://equiperecherchescientifique.over-blog.fr/2015/11/mouton-de-panurge-legende-ou-realite.html`. Accessed: 2019-08-15.

[148] Alan P Kirman. *Complex Economics: Individual and Collective Rationality*. Routledge, 2010.

[149] Jean-Philippe Bouchaud. Crises and collective socio-economic phenomena: simple models and challenges. *Journal of Statistical Physics*, 151(3-4):567–606, 2013.

[150] Philip W Anderson. More is different. *Science*, 177(4047):393–396, 1972.

[151] Alan P Kirman. Whom or what does the representative individual represent? *Journal of Economic Perspectives*, 6(2):117–136, 1992.

[152] Eugen E Slutsky and O Ragusa. On the theory of the budget of the consumer. *Giornale degli Economisti e Annali di Economia*, 71(2/3):173–200, 2012.

[153] Martin Browning and Pierre-André Chiappori. Efficient intra-household allocations: A general characterization and empirical tests. *Econometrica*, pages 1241–1278, 1998.

[154] Jean-Philippe Bouchaud and Marc Potters. Financial applications of random matrix theory: a short review. *arXiv preprint arXiv:0910.1205*, 2009.

[155] Vilfredo Pareto. *Cours d'économie politique*, volume 1. Librairie Droz, 1964.

[156] Benoit Mandelbrot. The Pareto-Levy law and the distribution of income. *International Economic Review*, 1(2):79–106, 1960.

[157] Adrian Drăgulescu and Victor M Yakovenko. Exponential and power-law probability distributions of wealth and income in the United Kingdom and the United States. *Physica A: Statistical Mechanics and its Applications*, 299(1-2):213–221, 2001.

[158] James CR Turner and John Webster. Mass and momentum transfer on the small scale: How do mushrooms shed their spores? *Chemical Engineering Science*, 46:1145–1149, 1991.

[159] Anne Pringle, Sheila N Patek, Mark Fischer, Jessica Stolze, and Nicholas P Money. The captured launch of a ballistospore. *Mycologia*, 97:866–871, 2005.

[160] Xavier Noblin, Sylvia Yang, and Jacques Dumais. Surface tension propulsion of fungal spores. *Journal of Experimental Biology*, 212:2835–2843, 2009.

[161] Fangjie Liu, Roger L Chavez, Sheila N Patek, Anne Pringle, James J Feng, and Chuan-Hua Chen. Asymmetric drop coalescence launches fungal ballistospores with directionality. *Journal of The Royal Society Interface*, 14:20170083, 2017.

[162] Warren M Rohsenow, James P Hartnett, Young I Cho, et al. *Handbook of heat transfer*, volume 3. McGraw-Hill New York, 1998.

[163] Thomas M Schutzius, Stefan Jung, Tanmoy Maitra, Gustav Graeber, Moritz Köhme, and Dimos Poulikakos. Spontaneous droplet trampolining on rigid superhydrophobic surfaces. *Nature*, 527(7576):82, 2015.

[164] Lei Xu, Wendy W Zhang, and Sidney R Nagel. Drop splashing on a dry smooth surface. *Physical Review Letters*, 94(18):184505, 2005.

Titre : À la recherche de la texture hydrophobe, et quelques effets collectifs dans les milieux granulaires et en économie

Mots clés : antibuée, superhydrophobe, gouttes, condensation, milieux granulaires, économie

Résumé : Une buée ou de l'eau chaude peuvent détruire le caractère superhydrophobe d'une surface texturée, du fait de la condensation à l'intérieur des textures. Néanmoins, il a été observé que des matériaux couverts de cônes nanométriques peuvent résister à la buée, les gouttes issues de la condensation étant éjectées à l'occasion de leur coalescence. Nous montrons tout d'abord expérimentalement par des images de microscopie électronique que la forme conique des textures permet bien aux gouttelettes d'eau d'être en "état fakir", y compris à très petite échelle. Nous étudions ensuite différentes familles de surfaces à cônes en variant l'espacement et la hauteur des textures. Aux nanoéchelles, nous montrons que l'effet anti-buée est peu influencé par la taille des textures, et que ses limites proviennent plutôt des propriétés de l'eau elle-même, sa viscosité en particulier. Aux microéchelles, nous décrivons des situations nouvelles où l'on observe l'éjection spontanée de la buée, malgré un piégeage local de l'eau. Nous étudions ensuite la trajectoire des gouttes de buée éjectées et confirmons que la viscosité joue un rôle majeur dans leur balistique. Enfin, nous nous intéressons à la capacité des surfaces superhydrophobes à repousser des gouttes d'eau chaude, montrant l'existence de deux recettes distinctes pour parvenir à un tel effet. Dans la seconde partie de la thèse, nous abordons le problème du pouvoir de capture de poussière de fibres mouillées d'huile. Nous montrons que la quantité de particules capturées est seulement influencée par la quantité d'huile déposée sur la fibre et non par la configuration adoptée par l'huile (film ou goutte), contrairement à la dynamique de croissance de l'agrégat, au cours de laquelle, de larges différences apparaissent entre les deux configurations. La dernière partie de la thèse est consacrée à l'équation de Slutsky, communément rencontrée dans le domaine de la microéconomie. Nous décrivons comment la matrice de Slutsky est modifiée en présence d'hypothèses non rencontrées en économie classique telles que l'irrationalité, l'interaction entre produits ou l'hétérogénéité des agents ; et comment celles-ci font apparaître des résultats surprenants non prédits par la théorie classique du consommateur. Les trois parties peuvent être abordées de manière indépendante.

Title : Texture-induced hydrophobicity, and some collective effects in granular matter and economics

Keywords : antifogging, superhydrophobic, drops, condensation, granular matter, economics

Abstract : Fog or hot water can destroy the superhydrophobic properties of a textured surface owing to the condensation inside the texture. However, it was recently shown that such surfaces covered with cones at a scale of hundred nanometers could resist fog : condensed droplets can be ejected during their coalescence. We first experimentally show by electronic microscopy that a conical texture enables water drops to remain in a "fakir state", even at a very small scale. We then study different families of cone-textured surfaces by varying the spacing and the texture height. At the nanoscale, we show that the texture size has a low influence on the antifogging efficiency whose limits rather lie in the water properties themselves, especially its viscosity. At the microscale, we describe new situations where spontaneous ejection of condensed drops occurs despite a local trapping of water. We also study the trajectory of expelled drops on such surfaces and confirm that viscous effects play a major role in their ballistics. Finally, we focus on the ability of superhydrophobic surfaces to repel hot water, a challenging situation for which we identify two independent recipes. In the second part of the thesis, we study the ability of wetted fibers to capture dust. We show that the quantities of captured particles is only influenced by the quantity of oil deposited on the fiber and not by its configuration (film or drop) on the fiber, unlike the growth kinetics of the aggregate where large differences are observed between the two configurations. The last part of the thesis focuses on the Slutsky equation, a classical equation encountered in microeconomics. We describe how the Slutsky matrix is modified when challenging classical economics hypotheses such as irrationality, interactions between goods or agents' heterogeneity, and how it exhibits surprising features not predicted by consumer choice theory. The three parts can be addressed independently.

Institut Polytechnique de Paris
91120 Palaiseau, France